

Sigurd Aamot

A Geochemical and Petrological Analysis of the Klemetsaunet Rhyodacite, Central Norwegian Caledonides

Unraveling the Rock's Origin, Mineral Alteration,
and Deformation Patterns

Master's thesis in Geology
Supervisor: Bjørn Eske Sørensen
Co-supervisor: Steinar Løve Ellefmo
June 2023

Sigurd Aamot

A Geochemical and Petrological Analysis of the Klemetsaunet Rhyodacite, Central Norwegian Caledonides

Unraveling the Rock's Origin, Mineral Alteration, and
Deformation Patterns

Master's thesis in Geology
Supervisor: Bjørn Eske Sørensen
Co-supervisor: Steinar Løve Ellefmo
June 2023

Norwegian University of Science and Technology
Faculty of Engineering
Department of Geoscience and Petroleum



Abstract

The Klemetsaunet rhyodacite is one of three felsic intrusions that was emplaced in oceanic crust at 481 ± 5 Ma. The location of the study area is in the northern parts of the Bymarka ophiolite, Trondheim, Norway, situated in the Upper Allochthon in the Central Scandinavian Caledonides. In the late Silurian to early Devonian the Scandinavian Caledonides were formed through the continent-continent collision between Baltica and Laurentia, forming a subducting complex. Resulting in Baltica being subducted underneath the Laurentian continent, which was followed with the closing of the Iapetus Ocean.

The research shows that the Klemetsaunet rhyodacite exhibits a significant variation of lithologies altered through post-magmatic processes, showcasing its complex nature. Detailed mapping and photogrammetric 3D-modelling of the Klemetsaunet rhyodacite reveals localised ductile deformation and brecciation, with the discovery of a phyllonitic shear zone, a garnet-biotite shear zone, and a breccia. Geochemical and petrological analyses indicates that the rhyodacite share characteristics that align with the calc-alkaline series, commonly observed in subduction zones where the source melt originates from partial melting in an oceanic setting. Dehydration of the subduction slab has led to the mixing of melts and introducing volatiles into the system, promoting oxidizing conditions.

Within the Klemetsaunet area, the predominant lithologies include rhyodacite, mafic dikes, and the Byneset trondhjemite. Additionally, localised areas of chalcophile enrichment, shear zones, and brecciation can be observed in the rhyodacite. With kinematic indicators from the shear zones, showing a dominant shear sense with the top to the WNW, while in the phyllonitic shear zone also shows a shear sense towards SSW. The rhyodacite outcrops display a matrix characterized by an aphanitic texture, accompanied by porphyroclasts of garnet and hornblende. These porphyroclasts are distributed throughout the outcrops, displaying variations in concentration, type, and occasionally exhibiting a nematoblastic texture. Based on the observed mineral assemblages, it is proposed that hydrothermal activity has played a crucial role in shaping the distinctive paragenesis of these lithologies. Resulting in the matrix to be predominantly composed of a combination of quartz and neocrystalline albite.

The primary objective of the thesis was to document and analyse localised deformation zones along with their geochemical characteristics. The presence of hydrothermal fluids has resulted in the mobilization of major and trace elements. The shear zones and breccia exhibit enrichment in K_2O , MgO , Na_2O , Fe_2O_3 , Zn , Ga , Rb , Sr , Nb , Ba , while displaying depletion in SiO_2 , Cr , and W . By utilizing scanning electron microscopy and electron microprobe analysis, several minerals have been investigated, with the emphasis on garnet. Garnet grains found at Klemetsaunet exhibits a porphyroclastic- and poikilitic texture, with albite overgrowth and quartz inclusions. There are two identified garnet phases: almandine and Mn- and Ca-enriched almandine. Large prograde almandine grains display zonation with a transition from a Mn- and Ca-enriched core with depletion of Mn towards the rim. The zonation pattern is suspected to be diffusion limited, with a slow diffusion rate of major elements from the surrounding matrix relative to the mineral growth. Smaller grains are heterogeneous mixture of the two almandine phases, suggesting their immaturity.

Based on the analysis of geochemical and mineralogical data, it is evident that the rhyodacite in the study area has undergone regional metamorphism into a transitional stage between greenschist- and amphibolite facies. The observations reveal two distinct

sets of pressure-temperature (P-T) estimates. The peak metamorphic conditions are estimated to be in the range of 6-9.5 kbar at 520-580°C. During this stage, dynamic recrystallization of quartz occurred, characterized by grain boundary migration, and the formation of syn-kinematic garnet, muscovite, and biotite. Subsequently, retrograde chloritization took place under cooler conditions, approximately 365-393°C, correlating to greenschist facies. Since it's evident of retrograde chloritization of garnet in the shear zones, it poses problems for reliability of P-T estimates including garnet.

Sammendrag

Klemetsaunet ryodacitten er en av tre felsiske intrusjoner som ble dannet i oseansk skorpe for om lag 481 ± 5 millioner år siden. Studieområdet ligger i de nordlige delene av Bymarka-ofiolitten i Trondheim, Norge, og er plassert i den øvre allokton i den sentrale delen av den Skandinaviske fjellkjeden. I sen-Silur til tidlig-Devon ble den Skandinaviske fjellkjeden formet ved en kollisjon mellom kontinentplatene til Baltica og Laurentia, som dannet et subduksjonskompleks. Dette førte til subduksjon av Baltica under Laurentia, etterfulgt av lukkingen av Iapetus-havet.

Forskningen viser at Klemetsaunet ryodacitten har en betydelig variasjon i litologier som er endret gjennom post-magmatiske prosesser, dette fremhever Klemetsaunet ryodacittens kompleksitet. Detaljert kartlegging og fotogrammetrisk 3D-modellering av Klemetsaunet ryodacitten avdekker lokalisert duktil deformasjon og breksjedannelse, med oppdagelsen av en fyllonittisk skjæringsone, en granat-biotitt skjæringsone og en breksie. Geokjemiske og petrologiske analyser indikerer at ryodacitten deler egenskaper som samsvarer med kals-alkalisk serier, som ofte observeres i subduksjonssoner der smelten har opphav fra delvis smelting i et oseanisk miljø. Dehydrering av kontinental skorpen under subduksjon har ført til blanding av smelter og introdusert fluidfaser i systemet, som fremmer oksiderende forhold.

Innenfor Klemetsaunet området består de dominerende litologiene av ryodacitt, mafiske ganger og Byneset trondhemitten. I tillegg kan lokaliserte områder med kalkofile berikning, skjærsoner og breksie observeres i ryodacitten. Kinematiske indikatorer fra skjærsonene viser en dominerende skjæringsretning med toppen mot vest-nordvest, mens i den fyllonittiske skjærsonen viser også en skjæringsretning mot sør-sørvest. Matrixen til ryodacitten viser en aphanittisk tekstur, sammen med porfyroklaster av granat og hornblende. Disse porfyroklastene er fordelt over hele blottningen og viser variasjoner i konsentrasjon, type, og av og til en nematoblastisk tekstur. Basert på de observerte mineral selskapene, tolkes det at hydrothermal aktivitet har spilt en avgjørende rolle i utformingen av den distinkte paragenesen til disse litologiene. Dette resulterer i at matrixen hovedsakelig består av en kombinasjon av kvarts og neokrystallinsk albitt.

Hovedmålet med oppgaven var å dokumentere og analysere lokaliserte deformasjonssoner sammen med deres geokjemiske egenskaper. Tilstedeværelsen av hydrothermale væsker har ført til mobilisering av hoved- og sporelementer. Skjærsoner og breksien viser berikning i K_2O , MgO , Na_2O , Fe_2O_3 , Zn , Ga , Rb , Sr , Nb , Ba , samtidig som de viser utarming av SiO_2 , Cr og W . Ved bruk av SEM og EPMA er flere mineraler blitt undersøkt, med hovedvekt på granat. Granatkornene som er funnet i Klemetsaunet viser en porfyroblastisk og poikilitisk tekstur, med overvekst av albitt og kvartsinneslutninger. Det er identifisert to faser av granat: almandin og Mn- og Ca-beriket almandin. Større prograde almandinkorn viser sonering med en overgang fra en Mn- og Ca-beriket kjerne med utarming av Mn mot kanten. Soneringsmønsteret antas å være diffusjonsbegrenset, med en langsom diffusjonsrate av hovedelementer fra den omkringliggende matrixen i forhold til mineralveksten. Mindre korn har en heterogen blanding av de to almandinfasene, noe som antyder deres umodenhet.

Basert på analysen av geokjemiske og mineralogiske data, er det tydelig at ryodacitten har gjennomgått regional metamorfose og befinner seg i en overgangsfase mellom grønnskifer facies og amfibolitt facies. Observasjonene avslører to distinkte sett med trykktemperatur (P-T) estimer. De maksimale metamorfe forholdene anslås å være i området 6-9,5 kbar ved 520-580°C. I løpet av denne fasen skjedde dynamisk rekrystallisering av kvarts, preget av reorganisering av kornegrensener, og dannelse av syn-kinematiske granatkorn, muskovitt og biotitt. Deretter fant retrograd klorittisering sted under kjøligere

forhold, omtrent 365-393°C, som korresponderer til grønnskifer facies. Siden det er tydelig at retrograd klorittisering av granat forekommer i skjærsonene, kan det føre til problemer med påliteligheten av P-T-estimer som inkluderer granat.

Foreword

This master thesis has been carried out at the Department of Geoscience and Petroleum (IGP) at the Norwegian University of Science and Technology (NTNU). I would like to thank my main supervisors Dr. Bjørn Eske Sørensen and Dr. Steinar Løve Ellefmo for their support and guidance in the project.

I am grateful to all the faculty members at the IGP who have supported me by providing equipment and teaching me various geochemical analyses methods. I would like to thank the thin section lab and MiMaC lab for their assistance with thin sections, SEM, and EPMA. Where Jostein Røstad, Stefanie Lode, and Kjetil Eriksen have contributed greatly to the possibility for this project. From the geochemical lab I want to thank Torill Sørløkk for helping me with sample preparation and XRF, and Laurentius Tjihuis for helping me with XRD and ICP-MS. I'm grateful for Knut Olav Solem for providing me with the Nikon camera, Lars Johan Sandvik for IT-support and Mehmet Ali Gücer for providing the excel spreadsheet used for chlorite thermometry.

Finally, I would like to thank my classmates and professors that have been a part of my journey at NTNU. Big shout-out to Lapis for boosting my morale, especially, dirigentus Axel Holmen for handling the logistics of beer. Thanks to Maarten Felix for his field course in England, to this day it's the most challenging and treasured field course that I have been a part of. These years have been wonderful, and the memories will remain forever.

Sigurd Aamot

04.06.15, Trondheim

Table of contents

List of figures	xiv
List of tables	xv
List of general abbreviations and symbols	xvi
List of mineral abbreviations and symbols	xvii
1 Introduction	1
The Study Area	2
2 Regional geology	3
2.1 Caledonides	3
2.2 Bymarka Ophiolite	5
3 Theory	7
3.1 Geochemistry	7
3.2 Deformation mechanism and -style	7
3.3 Metamorphism, P-T	10
3.4 Photogrammetry	12
4 Methods	13
4.1 Gathering of information and planning	13
4.2 Field work & drone survey	14
4.3 Post-processing of field data/ Photogrammetry and 3D-modelling	19
4.4 Geochemical and mineralogical analyses	20
4.4.1 Sample preparation	21
4.4.2 Thin sections/Petrology/Bulk mineralogy	26
4.4.3 Image analyses of thin sections	28
4.4.4 Whole-rock geochemistry	29
4.4.5 Electron microscopy	29
4.4.6 Mineral Chemistry	30
5 Results	32
5.1 Field observations and samples	32
5.1.1 Klemetsaunet Rhyodacite	35
5.1.2 Byneset Trondhjemite	37
5.1.3 Mafic Dikes	38
5.1.4 Phyllonitic Shear Zone	38
5.1.5 Garnet-Biotite Shear Zone	40
5.1.6 Breccia Zone	41
5.2 Petrography	44
5.2.1 Modal Mineralogy	44

5.2.2	Least deformed sample, rhyodacite protolith	49
5.2.3	Phyllonitic shear zone	51
5.2.4	Garnet-Biotite shear zone.....	55
5.2.5	Breccia zone	58
5.3	3D-model	62
5.4	Mineral chemistry	64
5.5	Whole-rock geochemistry	69
5.6	Tectonic origin	75
5.7	P-T	77
6	Discussion.....	81
6.1	3D-modelling, Data, and Alternative Methods	81
6.1.1	3D-modelling	81
6.1.2	Data	81
6.1.3	Alternative methods	82
6.2	Scanning Electron Microscope and MicroProbe Analysis	83
6.3	Geochemistry	83
6.4	Mineral Chemistry of Garnet	84
6.5	Magmatic Evolution	85
6.6	Deformation	87
6.7	Metamorphism.....	88
6.8	Metasomatism and Mineral Alteration.....	91
7	Conclusion	94
8	Further work	96
9	Disclaimer for the Thesis.....	97
10	References	98
	Appendix	103
	Appendix A: Overview of samples and which have been analysed	104
	Appendix B: Description of hand specimen.....	110
	Appendix C: Thin sections.....	112
	Appendix D: Modal mineralogy	125
	Appendix E: XRD diffractograms	127
	Appendix F: XRF, Major elements	137
	Appendix G: XRF, Trace elements	139
	Appendix H: ICP-MS.....	140
	Appendix I: EBS-images and mineral maps from SEM	141
	Appendix J: EPMA, data and stoichiometry	147
	Appendix K: Quartz analysis, grain size and angles	153

List of figures

Figure 1: Satellite images of Trondheim.	2
Figure 2: The Scandinavian Caledonides.	4
Figure 3: The Støren group and the Bymarka ophiolite emplaced onto the Gula complex	4
Figure 4: Ophiolite sequence in Oman and a geological map of the Bymarka ophiolite....	6
Figure 5: Geological map of Bymarka from NGU.	6
Figure 6: Deformation mechanism transition with depth in the crust and related metamorphic facies for specific depths..	8
Figure 7: Dynamic recrystallization as a reaction to temperature under deformation	9
Figure 8: Tectonic growth of porphyroblasts	9
Figure 9: Classification for types of metamorphism and some of their sub-categories....	10
Figure 10: Chloritization of biotite and hornblende.	11
Figure 11: Control points used in drone survey	15
Figure 12: Sampling locations.	17
Figure 13: All collected samples from Klemetsaunet.	18
Figure 14: Classification chart of rocks based on deformation style/mechanism and matrix content	19
Figure 15: Flow chart for "gentle" sample preparation	23
Figure 16: Billets of samples.	24
Figure 17: Reorientation of in-situ sample to produce the thin sections.	27
Figure 18: Display of symbology for annotating the parameters of the thin sections....	28
Figure 19: Overview of analysis points for EPMA.	31
Figure 20: Lithological 2D map of Klemetsaunet	33
Figure 21: Observations of different types of garnets and hornblende	36
Figure 22: Rhyodacite sample with the least alteration and deformation	37
Figure 23: Samples from the phyllonitic shear zone	39
Figure 24: Sample 6 from the garnet-biotite shear zone	40
Figure 25: Samples from the breccia zone	42
Figure 26: Thin section of the garnet-biotite shear zone	45
Figure 27: The mineral assemblage based on XRD-analysis from bulk samples.	46
Figure 28: Mineral assemblage of mineral maps scanned with SEM	48
Figure 29: Albite-quartz matrix from the phyllonitic shear zone, the breccia (b), and the garnet-biotite shear zone	49
Figure 30: Thin section 3 with mineral map..	50
Figure 31: Quartz showing GBM and deformation bands.	51
Figure 32: Thin section 2-2 with overview EDS-map	52
Figure 33: EBS-image and mineral map from the detailed map 2-2d1.	53
Figure 34: Chlorite with a 1.order brown interference colour, from the phyllonitic shear zone.	53
Figure 35: Kinematic indicators with dextral shear sense	54
Figure 36: Kinematic indicators of sinistral shear sense	54
Figure 37: Mineral maps of garnet-biotite shear zone	56
Figure 38: EBS-image and mineral map of 6A-2d.	57
Figure 39: Kinematic indicators of biotite mica fishes	57
Figure 40: Hornblende grains displaying dextral shear sense.	58
Figure 41: Comparison of hand specimen and the produced thin section	59
Figure 42: Thin section 5A-2 with mineral map	59
Figure 43: Thin section 4A-1 showing chlorite with masked interference colour.	60

Figure 44: Two phases in the breccia from thin section 4A-1	61
Figure 45: Thin section 5C showing several veins	62
Figure 46: 3D-map of Klemetsaunet	63
Figure 47: Cross section of geological model at Klemetsaunet.	63
Figure 48: Heatmaps of garnet in the phyllonitic shear zone	65
Figure 49: Heatmaps of of foliated matrix in the phyllonitic shear zone	66
Figure 50: Heatmap of garnet in garnet-biotite shear zone	67
Figure 51: Ternary garnet diagram	67
Figure 52: Ternary feldspar diagram	69
Figure 53: Classification of chlorite	69
Figure 54: Classification diagrams of fine-grained volcanic rocks	71
Figure 55: Variation diagrams for all geochemical data.....	73
Figure 56: Variation diagrams	74
Figure 57: Spider plots.....	75
Figure 58: Tectonic discrimination diagrams for granitic rocks.	76
Figure 59: AFM-diagrams	78
Figure 60: Boxplot of geothermometers for chlorite	79
Figure 61: AFM diagram displaying internal variation between the Klemetsaunet samples	86
Figure 62: Summary of shear sense indicators.	87
Figure 63: Metamorphic facies diagram	89
Figure 64: Classification of chlorite, figure from Slenes (2016)	90
Figure 65: Diagram for mineral assemblages during regional metamorphism	91

List of tables

Table 1: Equipment used during the field work and their specific information.	13
Table 2: The different types of software used for surveying and modelling.....	19
Table 3: Overview of the samples and analysis methods	22
Table 4: Material loss percentage.	25
Table 5: Settings for the SEM and Mineralogic (software)	30
Table 6: List of overview- and detailed mineral maps and the reclassification process ...	30
Table 7: List of the analysed minerals and which elements that were measured	31
Table 8: Samples collected from field work at Klemetsaunet.	34
Table 9: Ratios for comparison in variation of main occurring minerals for all bulk samples from XRD.	47
Table 10: Average mineral formulas of minerals analysed with EPMA.	68
Table 11: Summary for the different methods used for estimating P-T conditions	80

List of general abbreviations and symbols

AMS	Automated Mineralogy System
BX51	Olympus BX51 Thin Section Scanner
CP	Control Point
DSM	Digital Surface Model
E600	Nikon E600 Spot Image Camera Meters
EBS	Electron Backscatter Diffraction
EDS	Energy Dispersive Spectroscopy
EPMA	Electron Probe MicroAnalysis
GSPO	Grain Shape Preferred Orientation
HFSE	High Field Strength Elements
HREE	Heavy Rare Earth Elements
ICP-MS	Inductively Coupled Plasma Mass Spectrometry
IGP	Department of Geoscience and Petroleum
IGRF	International Geomagnetic Reference Field
LILE	Large-ion Lithophile Elements
LREE	Light Rare Earth Elements
MASL	Meters Above Sea Level
MTFC	Møre-Trøndelag fault complex
NTNU	Norwegian University of Science and Technology
PPL	Plane Polarized Light
REE	Rare Earth Elements
RFL	Reflected Light
SC	Scandinavian Caledonides
SEM	Scanning Electron Microscope
SFM	Structure-from-Motion
XPL	Cross Polarized Light
XRD	X-ray Diffraction
XRF	X-ray Fluorescence

List of mineral abbreviations and symbols

Ab	Albite
Alm	Almandine
Amp	Amphibole
Ap	Apatite
Bt	Biotite
Cal	Calcite
Ccp	Chalcopyrite
Chl	Chlorite
Dol	Dolomite
Ep	Epidote
Fsp	Feldspar
Grt	Garnet
Hbl	Hornblende
Mag	Magnetite
Mgs	Magnesite
Ms	Microcline
Ms	Muscovite
Opq	Opaque mineral
Or	Orthoclase
Pl	Plagioclase
Po	Pyrrhotite
Py	Pyrite
Qz	Quartz

Mineral abbreviations used in the Master's Thesis are taken from the article "Abbreviations for names of rock-forming minerals" Whitney and Evans (2010).

1 Introduction

This Master's Thesis represents independent research conducted at the Department of Geoscience and Petroleum (IGP) at the Norwegian University of Science and Technology (NTNU). The Klemetsaunet rhyodacite, located within the Bymarka ophiolite complex, is an intrusion with an estimated age of 481 ± 5 Ma (Roberts et al., 2002). The rock has been classified as an ocean ridge granite, exhibiting characteristics that align with the calc-alkaline series, commonly observed in subduction zones. Therefore, it has been interpreted that the source melt likely stems from the partial melting of a mixture of magmas and volatiles in an oceanic setting. The rhyodacite melt was derived from dehydration of a subduction slab migrating into basalts and subsequently evolved into its felsic composition. It's evident that the Klemetsaunet rhyodacite has undergone regional metamorphism, correlating to a transitional stage between greenschist- and amphibolite facies. An abundance of hydrothermal activities has altered the rhyodacite by initial neomattic albization of a feldspar rich matrix, followed by localised ductile deformation zones and brecciation. These hydrothermal processes have played a significant role in the evolution of the Klemetsaunet rhyodacite.

The primary focus of this thesis is to investigate the occurrence of post-magmatic processes and deformation within the Klemetsaunet rhyodacite. The examination of metamorphic mineral assemblages and mineral chemistry within localised deformation zones will be used to estimate the local temperature and pressure conditions during formation. To comprehend the petrography of the area and estimate the metamorphic conditions, a range of geochemical and mineralogical analysis methods have also been utilized. This research aims to better understand the characteristic paragenesis of metasomatic processes and deformation, which play a crucial role in limiting factors for mineral growth. Additionally, there will be investigated whether mineral alteration is attributed to solid-state reactions, partial melting, and/or hydrothermal activity. There will be discussed how the physicochemical conditions varies between hydrothermal alteration of the rocks. Where mineral textures and mineral assemblages will be applied to assess the validity of P-T estimates. A more detailed study of garnet has been carried out where the patterns of mineral growth has been linked to the mineral chemistry and distribution of major elements. By examining these relationships, a better understanding of the evolving conditions within the metamorphic process can be obtained.

During the fieldwork, sample preparation, and post-processing, various approaches were tested, some of which may offer advantages over traditional methods. Photogrammetry will be employed to generate a 3D model of the outcrop. This model will serve as the basis for further modelling and the creation of a comprehensive database using Leapfrog Geo software. The primary objective is to facilitate documentation and enhance reusability by providing future researchers with easy access to high-resolution models and clear information regarding observations and sampling locations. It is worth noting that the focus of the thesis shifted midway through its duration, transitioning from 3D-modelling and documentation into gathering of geochemical- and mineralogical data. The shift late in the theses work resulted in delay of the thesis and leaving insufficient time to recalibrate and reanalyse data from (SEM and EPMA), which would have yielded improved results.

The Study Area

The study area Klemetsaunet depicted in Figure 1, is situated at the northern end of Bymarka, which is in Trondheim, Trøndelag, Norway. The relevant area is wedged between the road (Fv715) and the fjord, the area experiences a humid climate. The study area consists of one single outcrop that extends approximately 90 m along the shoreline and curves slightly around the landmasses. On the east end of the outcrop there is stream which is a plausible fresh water source and can be used for cooling motorised equipment. The terrain slopes downward towards the water and is littered with blocks likely originating from the road cut of Fv715. Accessibility to the outcrop is significantly influenced by tide and weather conditions, which can pose challenges for traversing, particularly when the surface is wet. Moreover, extensive portions of the outcrop are covered with a weathered black surface and/or overgrowth, which hinders observations and limits the visibility of the rocks. Due to the steep terrain of Bymarka, direct sunlight on the outcrop can be scarce. This can make ideal conditions for photography by limiting the shadow contrast, but it also leads to premature freezing. Ice covering the outcrop is a risk factor that can occur early in October. As long temperature reaches the freezing point, then the outcrop will remain frozen for a long time.

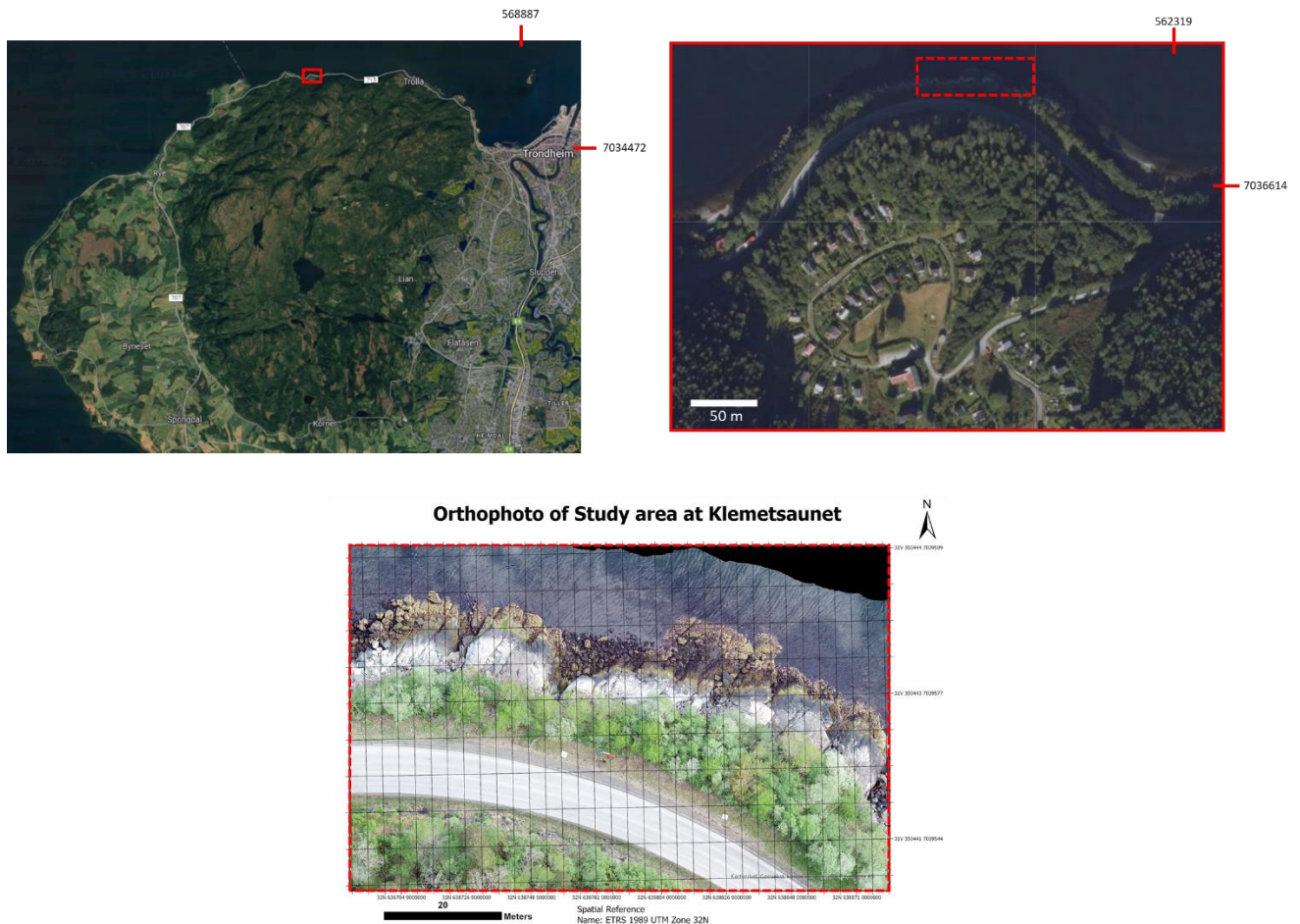


Figure 1: Satellite images of Trondheim to the left, with Klemetsaunet displayed of the right side. The bottom image is a self-produced orthophoto of the study area, projected coordinate system: WGS 84 / UTM zone 32N.

2 Regional geology

2.1 Caledonides

The majority of the Trøndelag county is characterized by rocks from the Central Scandinavian Caledonides, which was a defining tectonic event for Norway's geological history. The Scandinavian Caledonides (SC) consists of a series of thrust sheets that are stacked upon one another. These sheets are divided into four main units; Lower-, Middle-, Upper-, and Uppermost Allochthon (Osmundsen et al., 2006, Braathen et al., 2000) (Figure 2). The orogenesis of the SC lasted from Late Silurian to Early Devonian by the continent-continent collision between Baltica and Laurentia, creating a subducting complex. Baltica was subducted underneath the Laurentian continent, which was followed with the closing of the Iapetus Ocean. Subsequent episodes of divergence and convergence led to the accumulation and deformation, forming the terranes. In the late Silurian, slices of Baltica's basement and terranes were thrust south-eastwards on top of the Baltoscandian margin, shortening the continental margin and forming the Caledonian Allochthones (Stephens et al., 1985, Terry et al., 2000, Seranne, 1992).

Of the four major allochthones, Trondheim is situated in the Upper Allochthon, which is mainly composed of ophiolitic fragments, both primitive and evolved magmatic arcs, and marginal basins. In the Trondheim Nappe complex, there is a number of subdivisions of smaller groups such as the Støren group, the Hovin group, the Gula complex, and the ophiolitic greenstone complex (Gee, 1977, Gee et al., 2010, Gasser et al., 2022, Grenne et al., 1999, Roberts et al., 2002). The Trondheim area in the Upper Allochthon experienced a significant geological event referred to as the "Trondheim disturbance" (Holtedahl, 1920). This event is one of the four major transgressive events that occurred during the formation of the Scandinavian Caledonides and is characterized by regional metamorphic deformation. As a result of this event, ophiolite fragments and parts of the basement were obducted onto the landmasses. Resulting in regional metamorphism subjecting the Upper allochthon to a prograde greenschist- to amphibolite facies (Hacker and Gans, 2005). The metamorphic facies of fragments from the basement has been identified as blueschist facies according to Eide and Lardeaux (2002).

Figure 3 illustrates the obduction of the ophiolite complex, connecting both Bymarka ophiolite (part of the ophiolitic greenstone complex) and the Støren group, onto the Gula complex. Generally, the Upper Allochthon have been shaped by deformation conditions of high temperature and pressure (Hacker and Gans, 2005). Where both brittle and ductile faulting have been documented in the Trondheim region. One of these is the Møre-Trøndelag fault complex (MTFC), which is a ductile sinistral shear zone trending to ENE-WSW, that cuts through the SC in central Norway. The MTFC is a post-Caledonian tectonic event that has a great importance for the formation of Devonian sedimentary basins in the Hitra and Fosen area (Braathen et al., 2000; Osmundsen et al., 2006; Seranne, 1992).

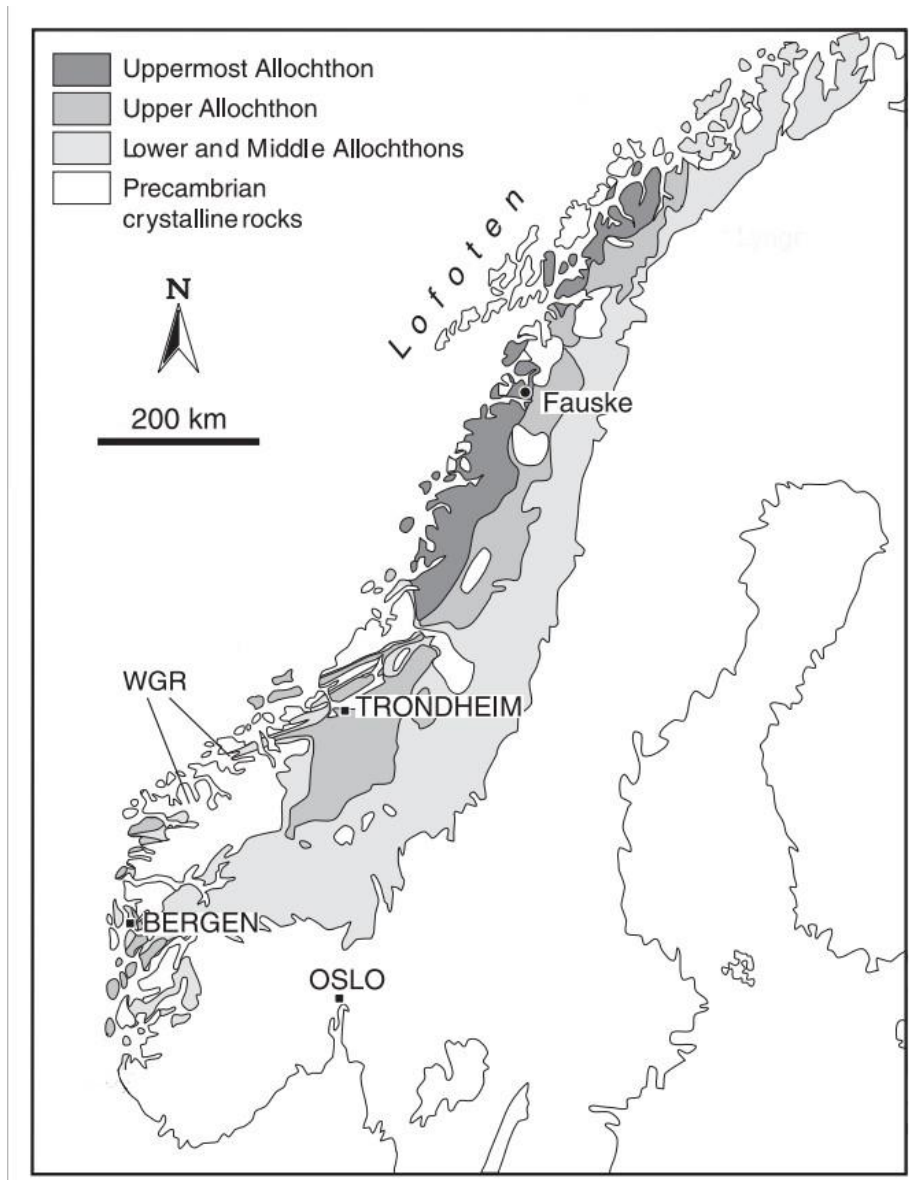


Figure 2: Simplified map of the four Allochthon of the Scandinavian Caledonides from Roberts (2003).

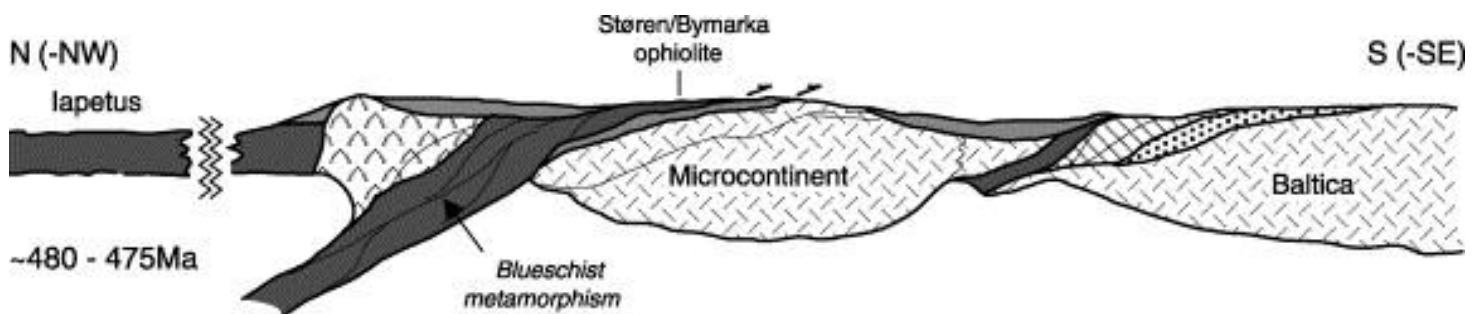


Figure 3: Sketch of how the Støren group and the Bymarka ophiolite was emplaced onto the Gula complex, from Roberts (2003).

2.2 Bymarka Ophiolite

An ophiolite is oceanic crust that have been obducted onto a landmass. The Bymarka and its felsic intrusions have been researched in detail in several articles and masters' theses. Mentionable research of the Bymarka ophiolite and its felsic intrusions:

- Slagstad (2001) has published a field guide that includes the locations of pillow lavas, sheeted dikes, gabbro, and the three felsic intrusions in Bymarka.
- Roberts et al. (2002) conducted U-Pb age dating of zircon to determine the geochronological formation ages of the three felsic intrusions in the Bymarka ophiolite.
- Slagstad (2003) investigated the geochemistry of the felsic intrusions of Bymarka, using trace element analyses to establish the magmatic origin of these felsic intrusions.
- Vedeler (2013) carried out mapping and geochemical analyses of the Klemetsaunet rhyodacite.
- Granseth (2015) has mapped and performed geochemical analyses of the Fagervika trondhjemite. Focusing on deformation and element mobilisation of the granitoid rocks and investigating a localised phyllonitic shear zone.
- Slenes (2016) performed mapping and geochemical analyses of the Klemetsaunet rhyodacite, with emphasis on metamorphic alteration and element mobilisation.

In Trondheim, the ophiolite consists of basalt with greenschist facies and meta-gabbros, which has retained a significant degree of preservation despite the deformation events it has undergone. The ophiolite sequence is visible, oriented with its uppermost part towards the SE. Slagstad (2001) provides a description of the locations where remnants of pillow lava, sheeted dikes, and meta-gabbros can be found. However, these features have limited exposure and have been strained (Slagstad, 2003). The gabbros and sheeted dikes are in the northwestern part of Bymarka, whereas the pillow lavas are situated to the southeast. The ophiolite is intruded by three felsic dikes: the Fagervika trondhjemite, the Byneset trondhjemite, and the Klemetsaunet rhyodacite (Figure 4). Within the Ophiolite greenstone complex, the geochemical characteristics of Bymarka are associated with those of Løkken and Vassfjellet. Notably, the Klemetsaunet rhyodacite exhibits a similar rare earth elements (REE) geochemical pattern to the plagiogranite of Løkken (Slagstad, 2003). In Bymarka there are registered both ductile- and brittle faults, with varying dip-directions. From Figure 5 it can be seen that brittle faults dips towards North, South, East, and South-East, while a ductile shear zone has a generally trending dip direction towards East. According to Roberts et al. (2002) and Slagstad (2001) the Byneset trondhjemite is the youngest felsic intrusion in Bymarka. Concluded with U-Pb age dating of all three felsic intrusions, where the age of the Byneset trondhjemite is ca. 423 Ma, compared to Klemetsaunet's rhyodacite which is dated to be 482 ± 5 Ma and the Fagervika trondhjemite age of 481 ± 5 Ma. The observation of the Byneset Trondhjemite cutting the Klemetsaunet rhyodacite by Slenes (2016) supports the conclusive age dating, that the Byneset trondhjemite must be younger than the Klemetsaunet rhyodacite. There occur smaller mafic dikes that intrude the Klemetsaunet rhyodacite, and their geochemical compositions are like the mafic rocks in the Bymarka ophiolite. Compared to the Fagervika- and Byneset trondhjemite, Klemetsaunet rhyodacite exhibits unique characteristics with the occurrence of large euhedral porphyroblasts of garnet and hornblende, and a flat REE-pattern unlike the other felsic intrusions (Roberts et al., 2002, Slagstad, 2003, Slagstad, 2001).

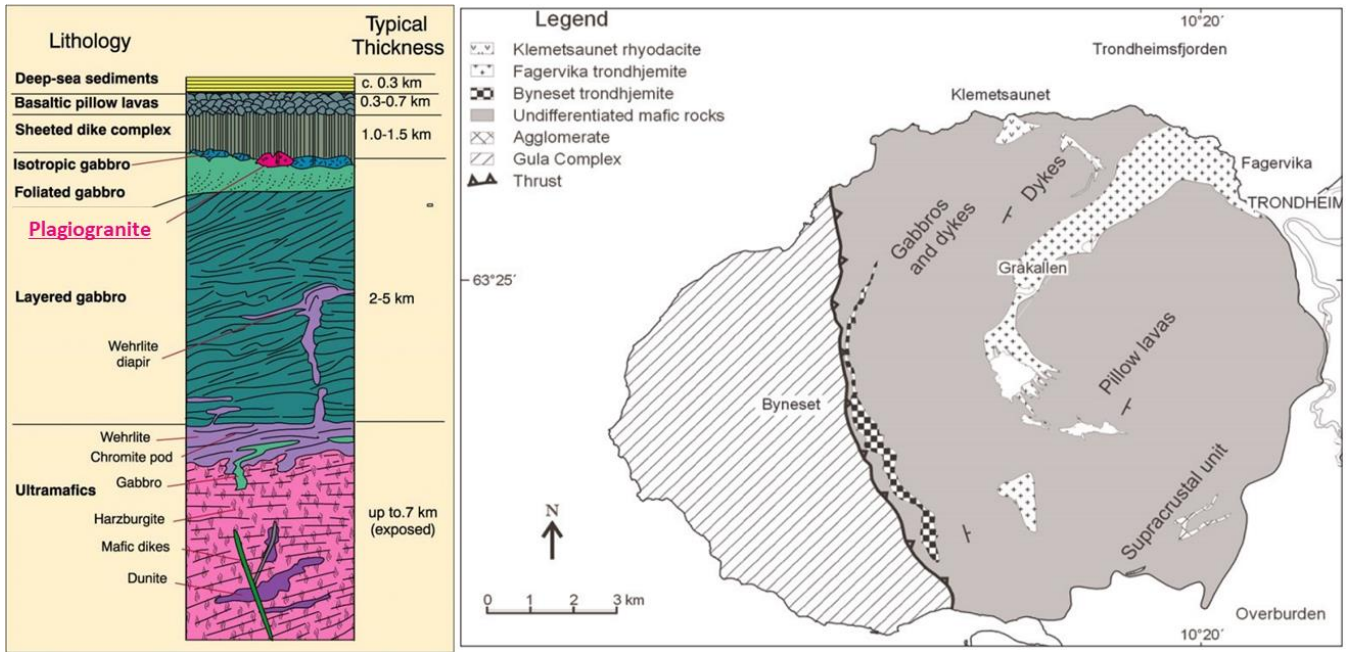


Figure 4: To the left is a sketch of the Samail Ophiolite in Oman (Winter, 2013). On the right side is a geological map of the Bymarka ophiolite complex from Slagstad (2003).

Geological map of Bymarka, Trondheim

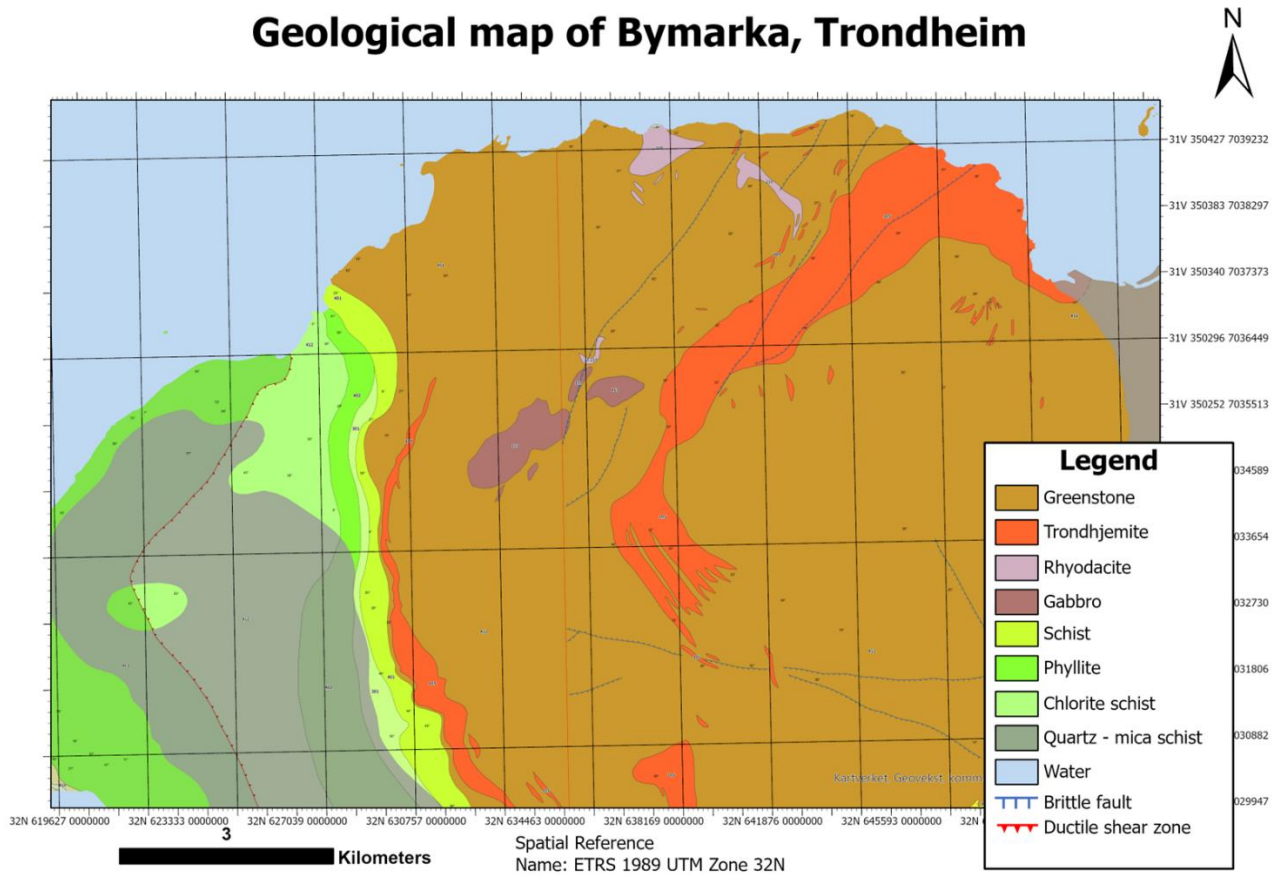


Figure 5: Detailed geological map of Bymarka based on data from NGU (2023) showing multiple different deformation styles in Bymarka.

3 Theory

3.1 Geochemistry

In geology a rock's chemical composition is essential for understanding under which processes that it formed. With this information it's possible to classify and interpret the origin and evolution of a geological system. The chemistry of a rock divides its elements into two groups depending on their abundance: major elements and trace elements. Major elements are typically presented as oxides and makes up more than 0.1 wt. % of a rock. SiO_2 , Al_2O_3 , MgO , CaO , Na_2O , K_2O , FeO and Fe_2O_3 are typical examples, and these elements play a crucial role in the formation of minerals and rocks. Trace elements, on the other hand, are the elements that constitutes of less than 0.1 wt. % of a rock's composition. These values are commonly given as a single element and often in ppm. Their rarity makes them valuable for detecting relatively rapid changes in their involvement in forming- and altering processes (Winter, 2013, Rollinson, 2014, Best, 2013). The relationship for the amount of a trace element present in a rock or mineral is described in Equation 1. Trace element's partition coefficient is dependent on whether the element has a greater affinity for the solid phase or the liquid phase.

Equation 1: Partition coefficient after Henderson (2013).

$$D = \frac{\text{Concentration in solid}}{\text{Concentration in melt/fluid}}$$

The partition coefficient, D is a descriptive value for trace element's preference to participate in either a solid- or liquid phase. If the D-value is greater than 1 then the trace elements prefer to partake in a solid phase, and this property defines a compatible element. In contrast if the D-value is less than 1 then the element favours a liquid phase and is defined as an incompatible element (Henderson, 2013, Rollinson, 2014, Winter, 2013). However, there are other factors that influence the participation of an element in a phase system. Such as accessibility to hard- and soft ligands in a hydrothermal system, such as Cl^- , OH^- , F^- , Br^- , O^{2-} , etc. Where the ionic potential (charge/ionic radius) is detrimental for dissolving metals and bonding with the ligands.

3.2 Deformation mechanism and -style

There are two main styles of deformation, brittle and plastic. They are differentiated by their deformation mechanism and their grade of ductility. To distinguish between deformation styles by looking at the relevant deformation mechanisms as shown in Figure 6. The style of deformation is dependent of the deformation mechanism, where a brittle deformation occurs under high stress conditions and low temperatures, with minimal plastic deformation of the rock. Resulting in fracturing of the rock, creating incontinuous layers of the broken rock. The brittle deformation style is associated with tectonic activity at shallow depths. Whereas ductile deformation style occurs at greater depths, which correlates to higher temperatures. A high temperature changes the physical properties of the rock, enabling it to be plastically deformed straining the rock by keeping it intact (Ragan and Ragan, 1985, Fossen, 2016).

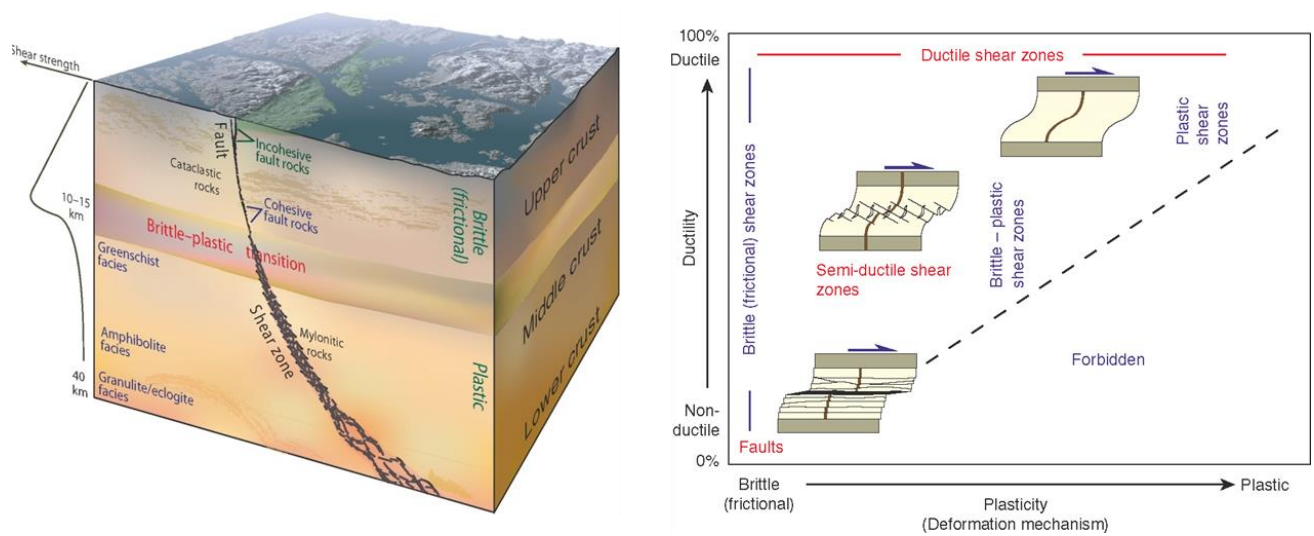


Figure 6: Illustration to the left by Fossen (2016) of how deformation mechanisms transitions with depth in the crust and relatable metamorphic facies to specific depths. On the right side there is a diagram on how deformation styles are correlated to -mechanisms.

During ductile deformation, silicate minerals can experience dynamic recrystallization of its grain boundaries. Defining the recrystallization process is dependent on the scale of the observation. At a microscopic level, dynamic recrystallization occurs by mobilization of the atoms in the crystal lattice (Lloyd and Freeman, 1994). Quartz is a mineral that can be used as a deformation thermometer. By looking at microstructures and the type of recrystallization of a mineral is one of the methods to determine a range for deformation temperature (Figure 7). There are two ductile crystallographic textures that results from grain size reduction during dynamic deformation: subgrain rotation and grain boundary migration. These textures occur at different temperatures and arises at different ranges for specific minerals. Typically, quartz is a suitable temperature indicator for low- to high temperature conditions.

There can be retrieved valuable information from studying porphyroblastic minerals in metamorphic rocks. The formation of porphyroblasts often reveal deformation patterns by studying inclusion patterns, that relates to the metamorphic growth conditions (Passchier and Trouw, 2005a). Figure 8 shows the different types of deformation pattern that porphyroblasts might display, including pre-tectonic, inter-tectonic, syn-tectonic, and post-tectonic (Passchier and Trouw, 2005b).

- Pre-tectonic porphyroblasts are uncommon in areas affected by regional metamorphism, the inclusion pattern is irregular showing no indication of deformation direction. However, the surrounding matrix will deflect around the grain.
- Inter-tectonic porphyroblasts forms during early stages of deformation and preserve only the initial deformation pattern. Later stages of deformation can commonly be seen in the matrix, were it warps around the porphyroblast.
- Syn-tectonic porphyroblasts has formed during deformation were the inclusion pattern typically curves due to the gradual growth of the grain while being rotated, where the matrix usually folds into the grain.
- Post-tectonic porphyroblasts typically preserves all deformation patterns and the matrix does not deflect off the mineral grain.

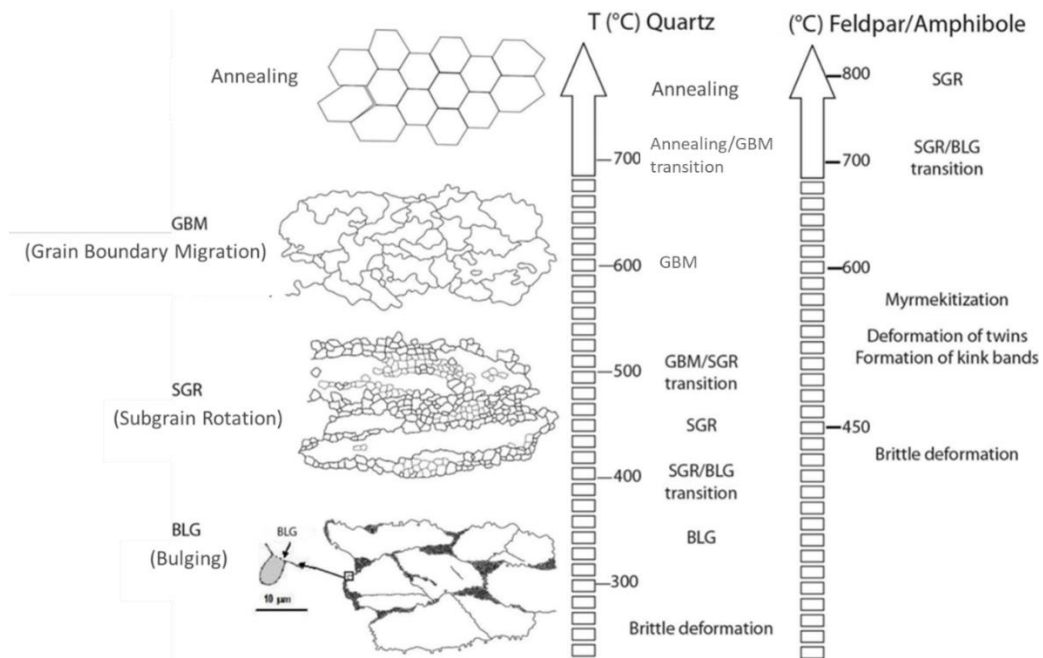


Figure 7: Dynamic recrystallization as a reaction to temperature under deformation from Owona et al. (2013).

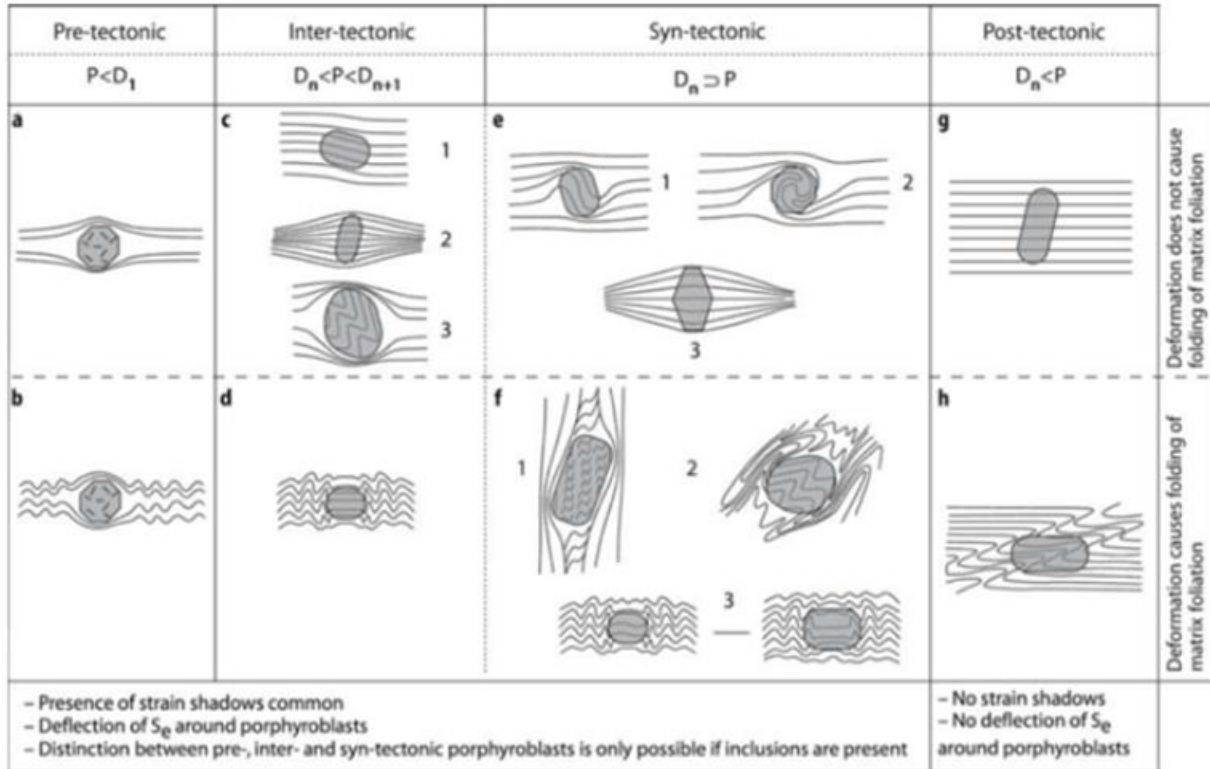


Figure 8: Figure from Passchier and Trouw (2005b) that shows the different types of tectonic growth of porphyroblasts. The scenarios depend on when the porphyroblast grew and if the deformation caused folding or not, this will result in different patterns (Passchier and Trouw, 2005a).

3.3 Metamorphism, P-T

The metamorphic alteration of a rock is the geological process of changing the mineralogy, geochemical composition, and structure of a rock. Metamorphism can be divided into two main categories: regional- and local metamorphism. Within these brackets they branch out into many under categories, these subdivisions can be useful for classifying between the different types of metamorphism Figure 9. The change in a protolith is driven by the shift in physicochemical conditions (Bucher and Grapes, 2011).

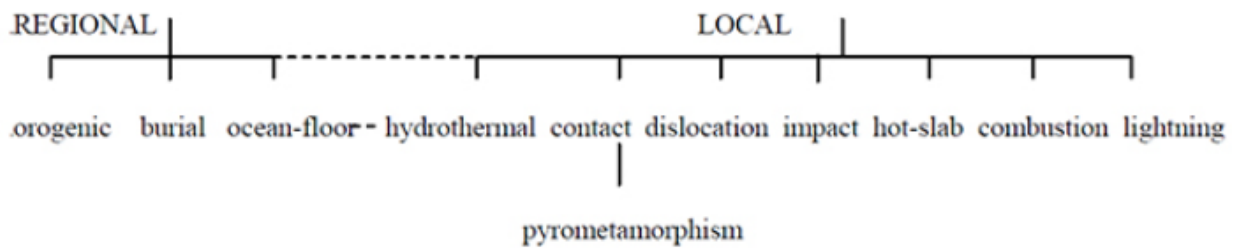


Figure 9: The main classifications of the different types of metamorphism and some of their sub-categories.

Local metamorphism is a specific type of metamorphism that occurs within a limited area or volume. This type of metamorphism can be directly attributed to a localised cause, such as magmatic intrusion, faulting, or meteorite impact. A metamorphic process can be further classified depending on the changes in temperature. If metamorphism is followed by either an increase or decrease in temperature, then they are referred to as either prograde- and retrograde metamorphism. Prograde metamorphism is characterized by continuous series of chemical reactions between a rock's minerals and any present fluid phase. These reactions occur as pressure and temperature increase, resulting in the formation of new and stable mineral assemblages. The opposite metamorphic process of this process is retrograde metamorphism. Retrograde metamorphism is a type of metamorphism that results in the formation of minerals that are typical of a lower grade, than the previous phase assemblage. This reversal can occur due to cooling in temperature (Winter, 2013).

Metamorphism is heavily linked to the temperature and pressure conditions which are related to depth of the protolith during metamorphism. To uncover the circumstances for pressure and temperature both mineral texture and -chemistry can be applied. There are many proxies that can be viable as thermobarometers depending on the specific conditions for co-existing mineral assemblages during deformation (Bucher and Grapes, 2011).

Garnets is a resilient mineral that preserves both major- and trace elements in zonation, which is useful for establishing P-T estimates for the changes in formation conditions. The occurrence of zoning within garnets is a typical phenomenon during the growth process where element concentrations differ as a reflection in change of physicochemical conditions (pressure, temperature, reactive mineral assemblage, fluid phases, etc.) (Moore et al., 2013). This is why garnet compositions with preserved zoning are highly used for estimation of formation conditions. In general, garnets are classified as nesosilicates and can be described by the formula $X_3Y_2(SiO_4)_3$. The X site is commonly occupied by divalent cations like Ca^{2+} , Mg^{2+} , or Fe^{2+} , while the Y site is usually containing trivalent cations such as Al^{3+} , Fe^{3+} , or Cr^{3+} . The overall structure consists of an octahedral/tetrahedral

framework, with $[\text{SiO}_4]^{4-}$ ions occupying the tetrahedra. The unique classifications of garnet is differentiated by either having calcium in the X site, or aluminium in the Y site, which gives these possible mineral compositions (Howie et al., 1992). Garnet is divided into 2 series: pyrope (pyrope, almandine, and spessartine) and ugrandite (uvarovite, grossular, and andraite). Often there can be continuous variation within a series, but there is typically not any continuous variation between the two series (Howie et al., 1992). Compositional variations within a mineral during formation and subsequent growth, helps understanding the mechanisms involved in metamorphic process. Trace elements tend to be more resilient to being reset by diffusional re-equilibration during high grade metamorphic processes, than major elements. Keeping them from redistributing across the zonation in a mineral (Hermann and Rubatto, 2003). According to Atherton (1968) garnet interacts with melt or hydrothermal phases when outside its stability field, enabling formation of secondary phases. Thus, only garnets that remain unchanged can be used to establish P-T estimates (Spear, 1993, Caddick et al., 2010), e.g. retrograde metamorphism. can alter the minerals needed for the estimate. Figure 10 shows an example chloritization which is one of the retrograde processes that can unable a P-T estimate. According to Yuguchi et al. (2015) chloritization of hornblende and biotite is related to hydrothermal activity. Fluid phases brings an influx of water and dissolved elements, which promotes the decomposition of biotite and hornblende. Chlorite replaces the minerals and leads to element mobilisation and restructures the crystal system.

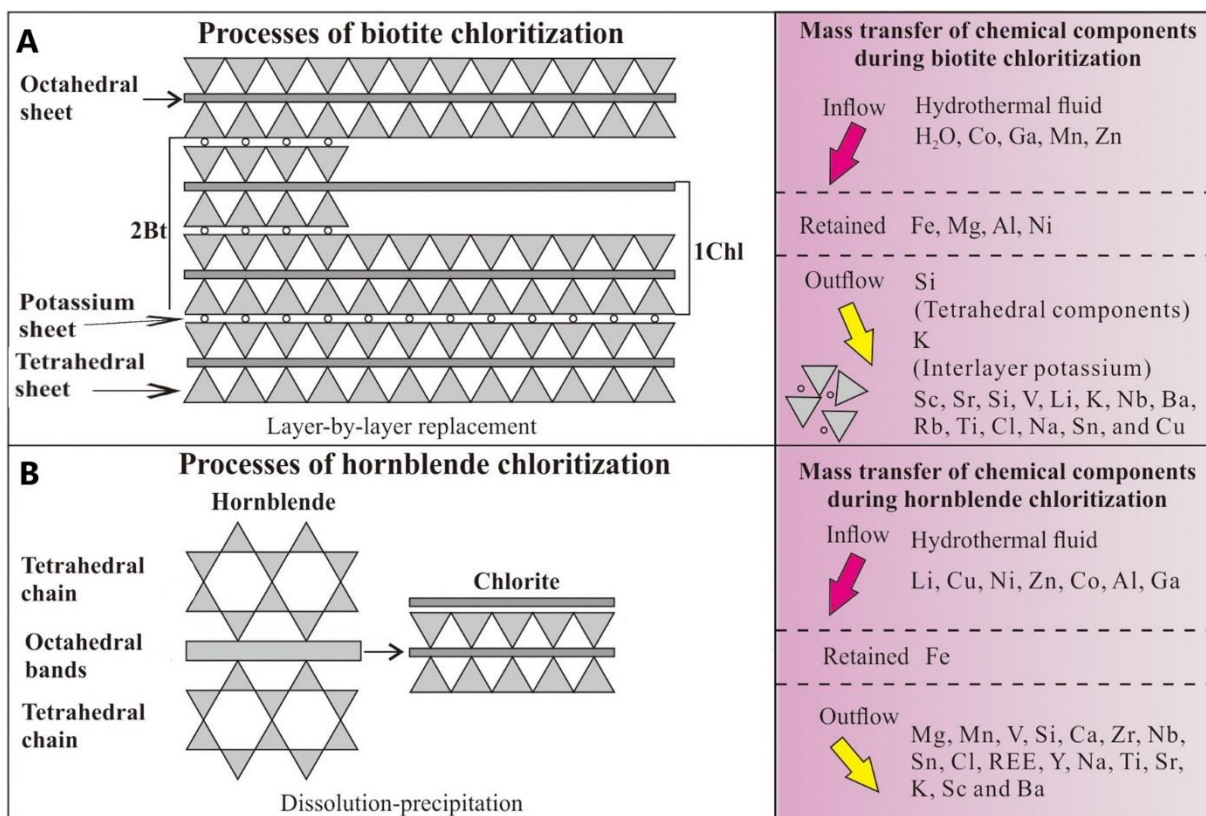


Figure 10: Schematic figure modified after Yuguchi et al. (2015) showing how alteration in crystal structure and mass transfer of elements during chloritization of biotite (A) and hornblende (B).

3.4 Photogrammetry

Photogrammetry is a technique that extracts 3D information from 2D images, allowing to determine the shape, size, and position of objects as well as their spatial relationships. The method uses the algorithm Structure-from-Motion (SfM) which generates 3D-surfaces of an object from overlapping images. This enables the creation of precise 3D models and reconstructions without the need for physical measurements or direct contact with the object or environment, making it a useful tool across various industries (Linder and Linder, 2009, Westoby et al., 2012).

The process of photogrammetry typically involves:

- **Image Acquisition:** Multiple photographs or images of the object or scene are captured from different angles or viewpoints. These images can be taken using traditional cameras, drones, or specialized photogrammetry systems.
- **Image Processing:** The acquired images are processed to identify common points or features that are visible in multiple images. These points serve as reference points for the reconstruction process.
- **Triangulation:** By analysing the locations of common points in different images, the photogrammetry software calculates the relative positions and orientations of the camera used to capture the images.
- **Point Cloud Generation:** Using the triangulation information, the software creates a 3D point cloud, which is a collection of 3D coordinates representing the surface of the object or scene. Each point in the point cloud corresponds to a location on the object or scene.
- **Mesh Generation:** The point cloud is then used to create a mesh, which is a connected network of triangles that approximate the surface of the object. The mesh provides a more detailed representation of the object's shape.
- **Texture Mapping:** The original images are mapped onto the 3D mesh, giving the object its visual appearance and texture.

A 3D-model will be relative in size and location without the addition of known locations within the model. To give this spatial relation to the real-world it's needed to either have the coordinates of the images recorded or use control points (CPs). A CP is a point with a known location in three-dimensional space (X, Y, Z), set out before the photography takes place. In photogrammetry, ground control points are established to accurately align the images with real-world coordinates and dimensions, enabling precise spatial referencing and measurements in the photogrammetric process. For a 3D-model it's needed at least three CPs distributed within the confined area, where multiple images overlap the CPs. To gain a better precision it's recommended to use more than three CPs and spread them out as much as possible to get a greater accuracy and less standard deviation in spatial relations. Also, the images themselves should overlap each other be taken at different distances, and from different angles, ideally from a vertical and tilted viewpoints at the target. Agisoft (2014) suggests that a minimum overlap of 80 % is adequate for forward aerial imagery, while a 60 % overlap is recommended for side images. Which will result in improvement of both the resolution and offset (Róg and Rzonca, 2021, Micheletti et al., 2015, Bemis et al., 2014).

4 Methods

4.1 Gathering of information and planning

Prior to the field trips to the study area, essential preparations were carried out by conducting online surveys to gather geological data and information relating to Klemetsaunet. This was a crucial step in determining what had already been researched. The discovery of relevant yet previously poorly documented features in the outcrop significantly influenced the decision-making process regarding the direction of the thesis investigation. It became apparent that the available open-source data on Klemetsaunet was inadequate. Typically, publicly accessible websites such as "Norge I Bilder" (www.norgebilder.no), provide orthophotos that serve as suitable basemaps. These websites offer georeferenced, high-resolution satellite and aerial photographs of Norway. The most recent aerial photograph which covers the study area, is the "Trondheim kommune MOF 2022". It has a high resolution of 0.1 m, with a standard deviation of 0.7 m. After considering the resolution in relation to the size of the area, it was concluded that a higher resolution image was wanted. This led to the idea of using a drone to capture photos of the entire area and creating a 3D model from those images. This tool could then be used to assist with field mapping, documentation, and modelling.

As part of the project, it was decided to explore alternative software options for digital mapping during fieldwork. In cooperation with supervisors, I opted to use the mobile app "StraboSpot mobile," which is specifically designed for documenting geological fieldwork. The objective was to assess whether this app would be easier to use and/or more suitable for detailed mapping compared to other commonly used software, such as ArcGIS Field maps. Table 1 provides a list of the equipment used during the fieldwork. Although a tablet was originally intended for digital mapping, technical issues prevented this option from being possible. As a result, a personal mobile phone was used for digital mapping, and the data was subsequently refined and adjusted after the fieldwork.

Table 1: Equipment used during the field work and their specific information.

Type of equipment	Name	Properties
RTK drone	DJI – Phantom 4 RTK	Focal length: 8.8 mm F-Stop: f/3.2 Exposure time: 1/40 sec
Field controller (RTK GPS)	Leica CS20	
Antenna (RTK GPS)	LEICA GS16 GNSS	
Phone	Huawei Mate 20Pro	Focal length: 5.58 mm F-Stop: f/1.8 Exposure time: 1/15 sec
Camera	Nikon D3200	Focal length: 18 mm F-Stop: f/3.5 Exposure time: 1/40 sec

Compass	Brunton - Geo Transit Pocket	Calibrated for declination by 4° 32' E
Rock-saw		Motorized, water-cooling system
Sledgehammer		
Chisel		

4.2 Field work & drone survey

The field work was carried out in multiple stages from May to November in 2022. During this period surveying, mapping, measuring, and sampling took place. In the beginning the focus was on mapping the geology and surveying the area with a drone. By using a RTK drone to take photos of the area it enabled georeferencing the images since the drone records the coordinates in its metadata. Which made it possible to create my own orthophoto, digital surface model (DSM) and 3D-model of the outcrop. The first flight in May was meant to gain experience with drone surveys and could be used to produce basemaps which was used for field mapping and being able to study the outcrop in a 3D-model. The process of field work and post-processing the field data was an intertwined process. I was continually updating basemaps and observations from post-processing and then using the new data in the field to improve the data gathering process in the next field session.

Two drone surveys were carried out during the field work, the first in the end of May and the second in start of September. Originally the first flight was meant to be used as a crude test project and to enable creating an orthophoto to use as a basemap. The first survey was flown at an altitude which only considered the highest parts of the topography, resulting in a constant flight height of 85 meters above sea level (MASL). The pictures taken in the initial drone survey was taken automatically in a program set up by the pilot in advance of the flight. The photographs were taken while the drone was moving, which can affect the quality of the images depending on the speed of the drone and shutter speed of the camera. To improve the accuracy of the georeferencing even further, control points were measured before the flight. Were a combination of the field controller and antenna that is listed in Prior to the field trips to the study area, essential preparations were carried out by conducting online surveys to gather geological data and information relating to Klemetsaunet. This was a crucial step in determining what had already been researched. The discovery of relevant yet previously poorly documented features in the outcrop significantly influenced the decision-making process regarding the direction of the thesis investigation. It became apparent that the available open-source data on Klemetsaunet was inadequate. Typically, publicly accessible websites such as "Norge I Bilder" (www.norgeibilder.no), provide orthophotos that serve as suitable basemaps. These websites offer georeferenced, high-resolution satellite and aerial photographs of Norway. The most recent aerial photograph which covers the study area, is the "Trondheim kommune MOF 2022". It has a high resolution of 0.1 m, with a standard deviation of 0.7 m. After considering the resolution in relation to the size of the area, it was concluded that a higher resolution image was wanted. This led to the idea of using a drone to capture photos of the entire area and creating a 3D model from those images. This tool could then be used to assist with field mapping, documentation, and modelling.

As part of the project, it was decided to explore alternative software options for digital mapping during fieldwork. In cooperation with supervisors, I opted to use the mobile app

"StraboSpot mobile," which is specifically designed for documenting geological fieldwork. The objective was to assess whether this app would be easier to use and/or more suitable for detailed mapping compared to other commonly used software, such as ArcGIS Field maps. Table 1 provides a list of the equipment used during the fieldwork. Although a tablet was originally intended for digital mapping, technical issues prevented this option from being possible. As a result, a personal mobile phone was used for digital mapping, and the data was subsequently refined and adjusted after the fieldwork.

Table 1 was used to measure the CPs. To avoid problems with ambiguity for the XYZ-axis of a 3D-model there was 3 CPs distributed on the outcrop (Figure 11) in a manner so that they didn't line up and had different XYZ-coordinates. If there is too small a difference between the coordinates for the CPs, for one of the axes. E.g., if every point is perfectly aligned, then a 3D-model that is based on these points can be pivoted into different angles while remaining at those points.

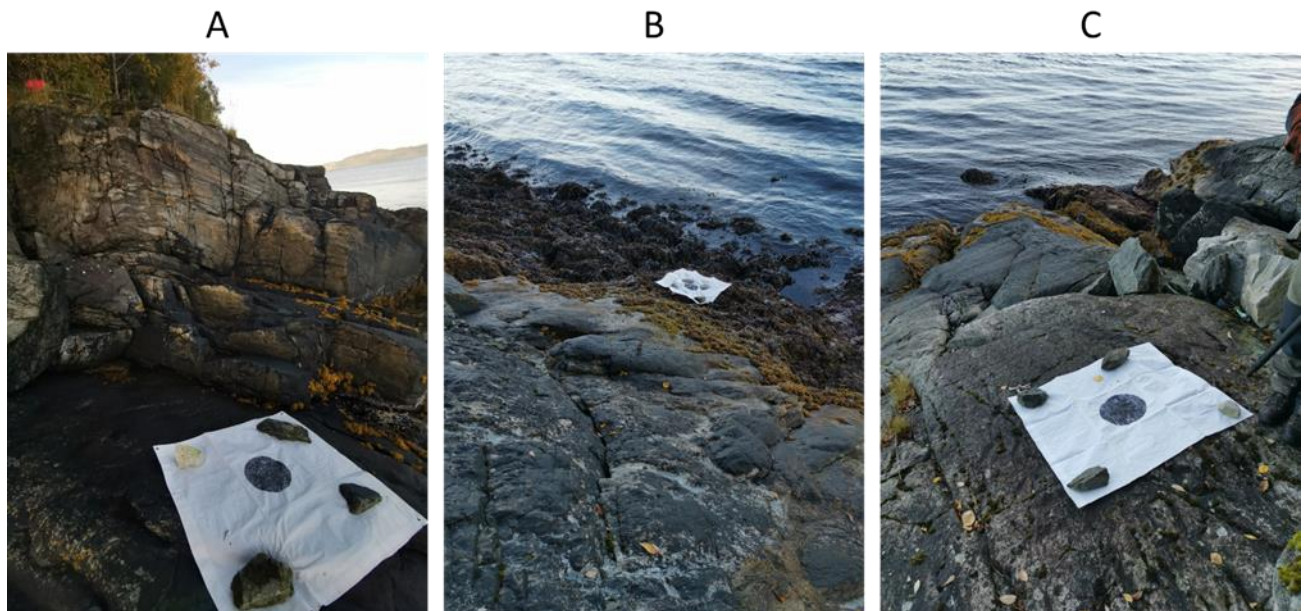


Figure 11: The control points used in the second drone survey, the black centre in each sheet is used as the georeferenced point. (A) Control point 1, (B) Control point 2 and (C) Control point 3.

The geological mapping was done digitally in a 2D-map to georeference geological boundaries, observations, and target interesting areas within the unit. The mapping consisted of segregating rhyodacite into segments, where the differential factors being visible changes on a macro level. These factors being matrix colour, the absence, presence, and/or alternation of phenocrysts consisting of garnets and hornblende. By observing how these minerals changed with respect to their size, colour and their interaction with the surrounding granular mass was also factored into the segregation. Areas in the rhyodacite which are penetrated by dikes was also remarked.

Later into the field work a new drone survey had to be carried out and samples were taken from the outcrop. The second survey had to be done to compensate for the low resolution of the photographs from the first drone survey which was flown at a constant altitude

above the sea level of an initially larger area. The new flight was flown manually only over the outcrop along the shoreline, with varying heights when respecting the distance to the topography of the outcrop. Therefore, the photographs were taken from varying altitudes from 8–40 MASL.

My gathered data was used together with the data I had available from previous work (Slenes, 2016, Vedeler, 2013) to influence where I wanted to collect my samples. The areas where I spent the most time on were geological features that deviates from the rest of the unit and has not been well documented. In Figure 12 it shows which parts of the outcrop I wanted to further investigate, and which became my sampling locations. I decided sample these areas based on observations of where there were geological “anomalies” in the rhyodacite and had not been sampled yet. This led to sampling of areas that had either a pronounced schistosity, mineralization of secondary veins and/or visible changes in the colour of the matrix. Before cutting out the samples from the outcrop, the desired sampling area was then marked and then the orientation of the in-situ rock was measured in dip and dip-direction. The equipment that was used for sampling was mainly a handheld motorized rock-saw with a water-cooling system. Then the sledgehammer and chisel were used gently to remove the slabs if the remained fastened to the outcrop. The samples were then bagged and labelled according to the order they were sampled, thus from 1 to 6 (Figure 13). Within those numbers there was given subgroup names depending on if the cut-out slabs were broken into fragments. This complete labelling of hand specimens sampled from Klemetsaunet is shown in Appendix A. To supplement the main 3D-model meant for the whole outcrop it was decided to take new photos of all sampling locations. All sampling locations were then photographed with a handheld camera after the sampled material was removed. During the field work it was also measured structure geological measurements for bedding and sampling locations for the lithologies. However, the number of measurements was limited due to safety reasons, being accessibility to the measurable areas. Also, many features have already been measured in previous work and the topography of the outcrop can give misleading effects of some structure’s orientation. The compass that was used was calibrated with respect to the calculated magnetic declination of Trondheim according to the International Geomagnetic Reference Field (IGRF) (National Oceanic and Atmospheric Administration, n.d.).

A



B



C



D



Figure 12: Sampling location, (A) is the locality where sample 1, 2 and 3 were from. (B) is sample 4 still in-situ, while (c) is the area where sample 5 resided, but the sample is removed in the image. (D) is the last sampled location; sample 6, still in-situ.

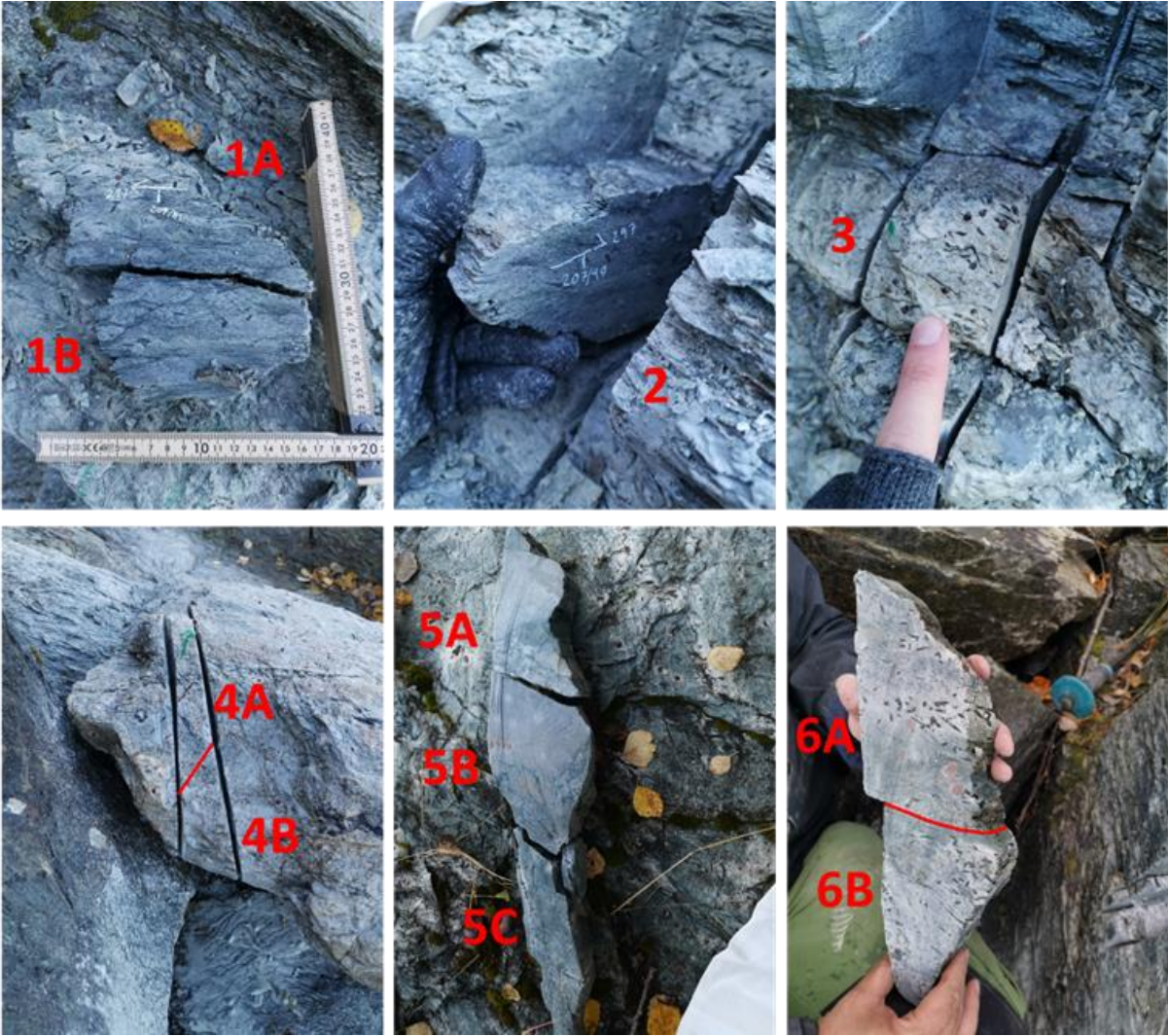


Figure 13: All collected samples from Klemetsaunet. Only sample 1 and 2 has their orientation written on them, but all the samples had their orientation recorded in StraboSpot.

The samples were then classified according to Figure 14 after being progressively studied. This classification was used at both macro- and micro levels and remained relevant throughout all analyses that gave textural information about the rocks.

Brittle		←Deformation style→				Ductile		% matrix and grain-size	
Frictional flow		←Dominant deformation mechanism→				Plastic flow			
Non-cohesive		Secondary cohesion		Primary cohesion					
		Cemented HB	Indurated HB		> 50% phyllosilicate	< 50% phyllosilicate			
Hydraulic breccia (HB)	Breccia series	Proto-breccia	Cemented proto-breccia	Indurated proto-breccia	Cataclasite series	Proto-cataclasite	Proto-phylionite	Proto-mylonite	0-50% matrix
		Breccia	Cemented breccia	Indurated breccia		Cataclasite	Phyllonite	Mylonite	50-90% matrix
		Ultra-breccia	Cemented ultra-breccia	Indurated ultra-breccia		Ultra-cataclasite	Ultra-phylionite	Ultra-mylonite	90-100% matrix
	Gouge	Cemented gouge	Indurated gouge				Blastomylonite	Sub-microscopic matrix	
Pseudotachylyte									

Figure 14: Classification chart of rocks based on deformation style/mechanism and matrix content by Braathen et al. (2004).

4.3 Post-processing of field data/ Photogrammetry and 3D-modelling

When I returned from the field work, then I had the opportunity to work with the gathered data and edit them on a more suitable hardware than my mobile phone. In Table 2 it is shown the different software that I had to use before gaining the final digital result.

Table 2: The different types of software used for surveying and modelling the study area.

Name of software	Purpose
ContextCapture	3D-modelling with photographs taken with both drone and handheld camera.
ArcGIS Pro	Editing and fine-tuning field data collected with StraboSpot mobile.
Leapfrog Geo	Building a database compatible with all obtained data and measuring structural data.

All acquired photographs taken with the drone was put into the software ContextCapture to be first aerotriangulated. To ensure that the coordinates of the images had a high accuracy, the three CPs were used for georeferencing. This was done by manually identifying where the centre of a CP was in at least three images for each CP and including their measured coordinates. For good measure it was decided to use more than three images to verify the CP's location and ideally use the same image for multiple CPs if possible. The output format of the 3D-model was a 3D-mesh as an .OBJ-file, but there was also produced a DSM and an orthophoto which replaced the old basemaps in the StraboSpot app. The process of manually georeferencing was repeated for each of the four sampling locations, which were smaller local areas within the already existing 3D-model. However, the images were taken with a handheld camera that does not have an inbuilt

GPS and did not contain any of the control points. Therefore, these 3D-models had to be georeferenced based on the already georeferenced 3D-model. To create new control points, it was necessary to select easily recognizable spots in the 3D-model and use their coordinates. Thereafter these new control points had to be found in the images and manually select where these control points should be. By manually selecting at least three images and finding the most precise position to a control point and accepting the new position as a reference to the control point.

The field data from StraboSpot was then imported into ArcGIS Pro to ensure the spatial accuracy of the data and its quality. The geological 2D map, sampling locations, and observed features were adjusted to more correct and detailed spots. Then the data had to be converted into another coordinate system, since the default coordinates units in StraboSpot are given in longitude and latitude which are not compatible in Leapfrog Geo. The data was converted into the UTM system specifically WGS 84/UTM zone 32N (EPSG:32632), then exported. All 3D-models from ContextCapture were then manually moved in Leapfrog, due to loss of coordinates at importing the models, but the null point/origin in the spatial reference system was accessible in the metadata of each model. At last, all data from ArcGIS Pro such as, lithological units, bedding, sampling locations, and observations were added and draped onto the model to create a database of Klemetsaunet.

4.4 Geochemical and mineralogical analyses

To be able to classify and map the chemical composition, mineralogy, and P-T conditions of the rock samples and thus deformation events. A set analyses methods were used, were all sample preparations and analyses were performed at NTNU's Department of Geology and Mineralogical Resources Engineering:

- Thin sections were prepared to study microstructures and mineralogy.
- X-ray diffraction (XRD) was used to estimate bulk mineralogy.
- X-ray fluorescence (XRF) to assess abundance of major- and trace elements.
- Inductively coupled plasma mass spectrometry (ICP-MS) to enable a more precise measurement for a broader spectrum of trace elements.
- Scanning Electron Microscope (SEM) and automated mineralogy for mapping mineral classification and element concentrations.
- Electron Probe MicroAnalysis (EPMA) to analyse mineral chemistry.

The material used for the different analyses for a sample were taken from the same area within that sample. The pathway for selecting which samples to investigate went from a large scale and gradually stepwise towards a smaller scale. Samples that kept being interesting was investigated further and proceeded to the next analysis method. The order of which an analysis have been described also relates to the chronological order of when they were performed and the results from those analyses were used to supplement the next analysis method. To do so was to study the hand specimens on a macrolevel, with the intent of targeting areas which can give the most useful information about the facies. Therefore, structure geological features have also been taken into consideration, this way boundaries between to facies, veins and secondary minerals can be studied. This way some samples are more suited for analysis methods that focuses on specific areas and not the whole rock chemistry. Since the amount of material that can be analysed is limited to the time and money available, only some samples could be analysed.

4.4.1 Sample preparation

Preparing and studying the material were done according to Table 3 and Figure 15, which describes the unique steps taken for each analysis. By initially cutting the samples into crosscuts, I could see more than just the outer weather-exposed material of the slabs. When representative areas were located, they were cut into billets, as shown in Figure 16. Then out of the remaining pieces, material was selected for preparation to other analyses methods. This preparation workflow was influenced by and Henriksen (2022), where her work tested if the perseverance of swelling minerals could be improved with a gentler approach to sample preparations. By avoiding the use of a disc mill to obtain the wanted grain size and rather crush the material stepwise with a jaw crusher. This methodology focuses on removing ambiguity from XRD-analysis, where quantification of some minerals proves to be difficult, e.g., "weak" minerals due to their disintegration during sample preparation (Selen et al., 2020). Phyllosilicates or sheet silicates goes under this definition of "weak minerals", where their flaky morphology can be problematic (Ruessink and Harville, 1992). Within that group, micas and chlorite are relevant minerals for the material that I sampled.

Table 3: Overview of the samples and which of them was analysed with the different analyses-methods. The cells that are contain information and are highlighted with the lightest colour shades of either blue, yellow and/or green indicates which samples have been relevant for an analysis. Samples that are not highlighted wasn't inspected further than at a macro level after they was sampled from the field.

Sample ID				Thin sections and analyses preformed on them					Geochemical- and mineralogical analyses on crushed samples						
Field ID	Location (WGS 84 / UTM zone 32N (EPSG:32632))			Thin section ID	Type	SEM		EPMA	ID		XRF, Major	XRF, Trace	XRD	ICP-MS	
	X	Y	Z (m)			Overview	Detailed		Personal ID	Journal number					
1A	562215.335	7036675.285	2.775												
1B	562215.338	7036675.28	2.768												
2	562215.4	7036675	2.737	2-1	Polished				2	220899	x	x	x	x	
				2-1B	Polished										
				2-2	Polished	x	2-2d1 & 2-2d2								
3	562215.437	7036675.2	2.673	3	Polished	x			3	220900	x	x	x	x	
4A	562187.6	7036679	3.462	4A-1	Polished	x		x	4A	220901	x	x	x	x	
				4A-1B	Polished										
				4A-2	Polished	x									
4B	562187.729	7036679.266	3.451												
5A	562190.2	7036679	3.377	5A-1	Polished				5A-A	220902	x	x	x	x	
				5A-1V	Liquid										
				5A-2	Polished	x	5A-2d	x	5A-B	220903	x	x	x	x	
5B	562190.134	7036679.454	3.314												
5C	562190.01	7036679.528	3.23	5C	Polished	x			5C	220905	x	x	x	x	
6A	562202.8	7036677	3.085	6A-1	Polished	x			6A-A	220906	x	x	x	x	
				6A-2	Polished	x	6A-2d	x	6A-B	220907	x	x	x	x	
				6A-2B	Polished										
				6A-3	Polished				6A-C	220908	x	x	x	x	
6B	562202.859	7036676.45	3.026												
6-XRD	562202.783	7036676.519	3.059												

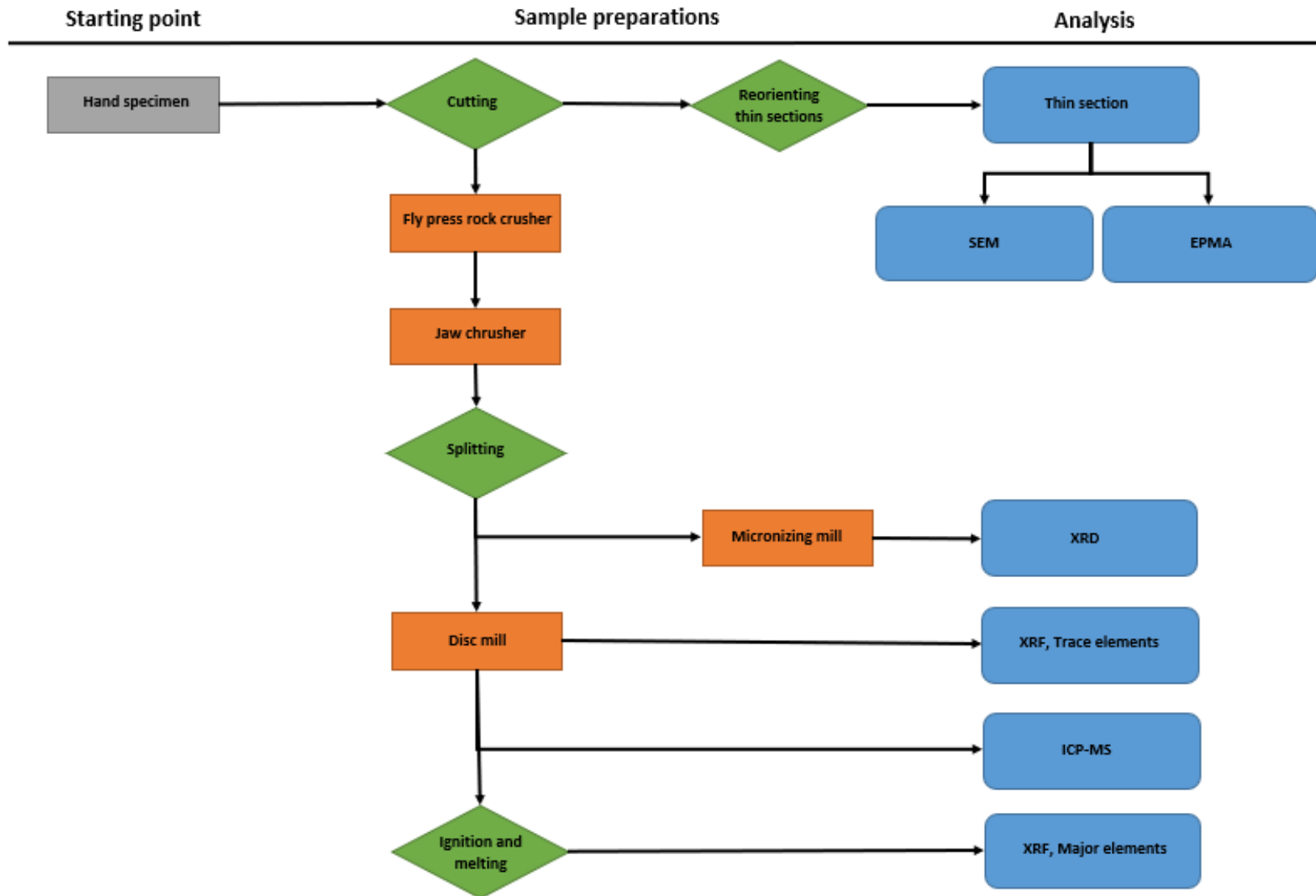


Figure 15: Flow chart for “gentle” sample preparation, general steps in the process shown in green boxes. The name of unique equipment is shown in orange boxes and the name of analyses methods is displayed with the blue boxes.

The following procedure was to crush the samples that didn't fit into the opening of the Jaw crusher, while avoiding damaging the minerals and keeping the loss of material as low as possible. This was done with the "Fly Press Rock Crusher", where every sample except 6A-A, 6A-B, and 6A-C had to be crushed into an adequate grain size.

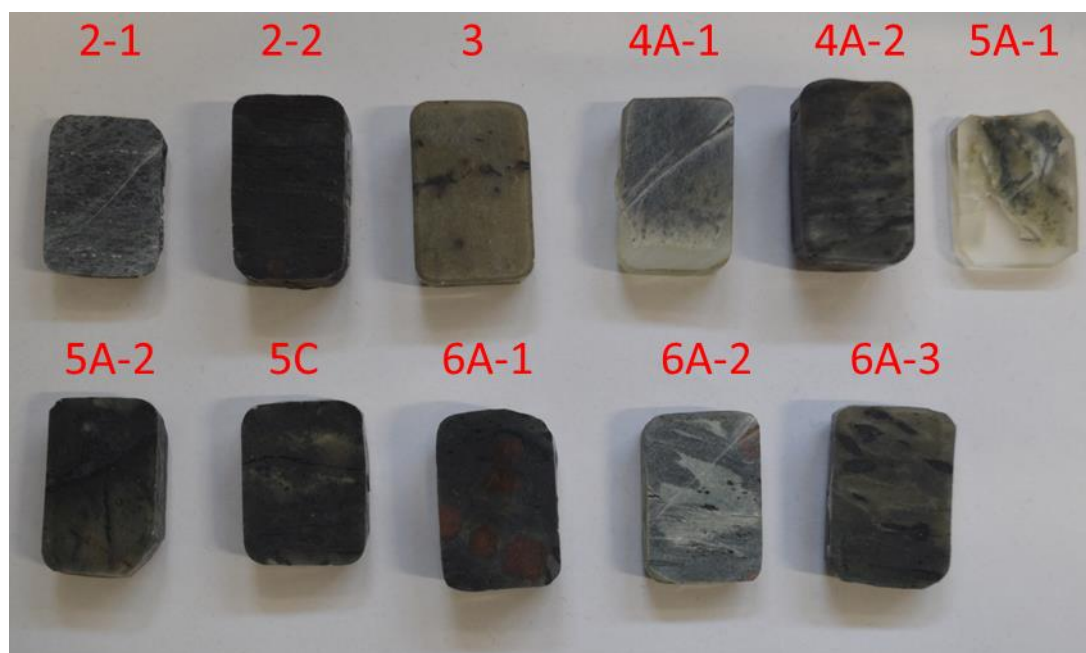


Figure 16: Billets of the selected sample material to produce thin sections.

The settings for the Jaw crusher were used to obtain a fine-grained material while causing as little damage as possible to the grains. The speed was consistently set to 700 rpm and the crushing process was repeated in several intervals with reducing the gap width after each step. The gap width was decided depending on the grain size after crushing the samples with the "Fly press rock crusher". For most samples the first round of crushing had a gap width of 5 mm, then 2 mm and to obtain the finished product the gap width was set to 0 mm and this step was repeated an additional time for good measure. Between each cycle the equipment was cleaned to remove any possible residue of the previous sample. The cleaning process consisted of first dismantling the equipment, then vacuuming all the parts that have been in contact with the sample. Then the parts wiped down with fine paper and alcohol, thereafter they were cleaned by using compressed air and the finishing touch was to use a dry fine paper to see if the equipment was clean or not. If the equipment was clean, then all the parts would be reassembled, and I could continue with the next sample.

The use of the Jaw crusher was important due to the XRD-analysis, where the quality of the analysis is dependent on the grains being as small as 10 μm , well-rounded, and undamaged to quantify correctly. In contrast the XRF-analysis which does not require the same quality of roundness of the grains. Therefore, the use of a disc mill is sufficient to reduce the grain size to proximally 40 μm , but the instrument risks grinding the grains into tabular shapes which can damage the original crystal habitus. Thus, all the material had to be crushed first with the Jaw crusher and not directly put into the disc mill.

After the material had been crushed it was split several times to gain a representative and evenly distributed sample. The splitting was done depending on the necessity to gain enough material that was satisfactory for performing the intended analyses. Approximately

3-5 g of material from each sample was kept for XRD and three times of that amount was hold on to as a back-up. The loss of material during crushing is depicted in Table 4.

Most of the kept XRD-material was then put into a plastic cylinder that was loaded with agate pellets and mixed with at least 10 mL of alcohol. Then the cylinder was put into a micronization mill and shaken for 2 minutes and thereafter the mixture was dumped into glass tray. The mixture was then dried overnight in an oven at 60 °C, then the dry material was scraped out of its container and pulverized before transferring it into the sample holder for the XRD-analysis. The remaining powdered XRD-material that wasn't put into the sample holder was then quickly tested for magnetic minerals before being stored away. This was done by dragging a paper with the powder along a basic lab magnet and observing if there were any magnetic minerals.

For the remaining material that wasn't used for XRD-analysis was then split into smaller batch sizes that are wanted for being processed in a disc mill. To avoid under- or overgrinding the material its needed to have an amount of approximately 30,0 ± 5,00 g, with setting the settings of the disc mill to 1200 rpm for 2 minutes. This way the obtained product should have a grain size of 40 µm.

The milled material was then used to produce an analysis for XRF trace elements. By combining 9,6 g of material with 2,4 g of Licowax in a closed container with a glass ball. The container was then shaken by a machine for at least 2 minutes to mix the material thoroughly. Thereafter the ball was removed from the container and the mix was pressed into a powder pellet in a press with a force of 200 kN.

To analyse major elements with XRF it was measured as close as possible to 2,5 g of milled material from each sample. The material was then heated in an oven at 1000 °C for one hour. Then 0,5000 ± 0,0002 g of ignited material was placed into crucible made of platinum and mixed with 5,0000 ± 0,0002 g of lithium borate and 120 µL of lithium iodide. As the final step for the XRF major element preparations the mixture was smelted into glass wafers in a furnace a 1000°C for 24 minutes.

The remaining disc milled material was then used as an additional assay for trace elements by performing an ICP-MS analysis. The next steps for preparing the material and the analysis itself was done by the operator.

Table 4: Weight of material before and after crushing and material loss percentage.

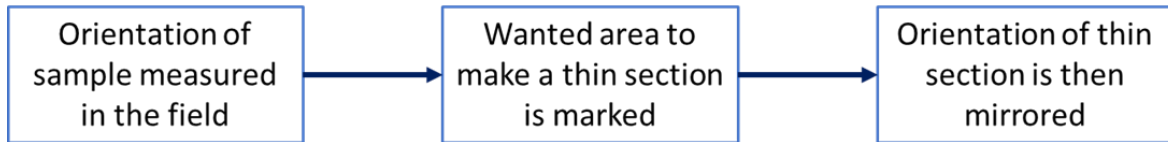
<i>Samples</i>	<i>2</i>	<i>3</i>	<i>4A</i>	<i>5A-A</i>	<i>5A-B</i>	<i>5C</i>	<i>6A-A</i>	<i>6A-B</i>	<i>6A-C</i>
<i>Before crushing (g)</i>	128.1	82.2	139.2	57.6	166.7	169.4	31.1	34	76.2
<i>After crushing (g)</i>	124.1	80.4	136.3	56.4	163	165.6	30.6	32.7	75
<i>Material loss (%)</i>	3.12	2.19	2.08	2.08	2.22	2.24	1.61	3.82	1.57

4.4.2 Thin sections/Petrology/Bulk mineralogy

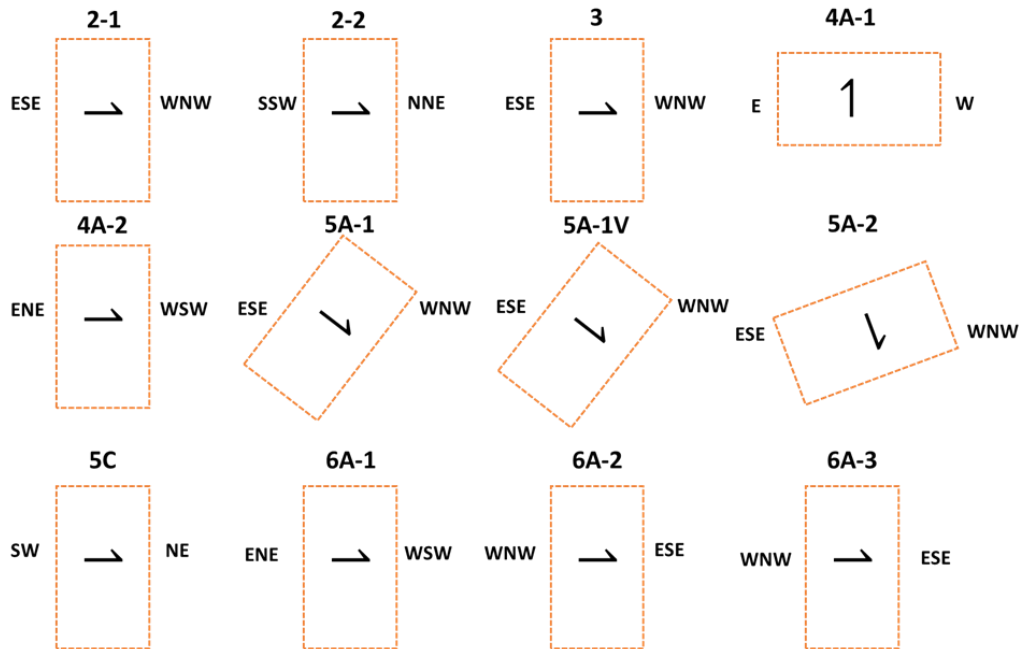
Thin sections and XRD-analysis were produced and used to observe and measure the mineral assemblages and mineral textures within some of the sampled rocks. These methods were used to supplement each other and to gain a better understanding of the alteration of the original host rock. The purpose of XRD-analysis was to gain bulk data that is representative for the sampled rocks, with a qualitative and quantitative measurement of the mineralogy. The XRD recognizes the minerals "signature" and measures the quantity of those minerals by the intensity of the signal in the diffractograms (Dutrow and Clark, 2012). The used material was chosen to overlap with the areas of the thin sections and in a few cases even target the exact same area as some thin sections. The fitted signal from the produced diffractograms were later adjusted if new minerals were found and assumed to make up at least 1 wt. % of the sample, since this is the detection limit of machine.

The thin sections had to be reoriented in several steps to keep track of the directions relevant for each thin section (Figure 17). This process documents the all the steps taken to ensure that the final orientations in the thin sections are correct. Areas within the cut samples which showed diverse mineralogical textures and a heterogenic mineral assemblage were marked into rectangular billets with dimensions of 28x48 mm. These targets were used for producing thin sections; one doubly polished fluid inclusion thin section and eleven polished thin sections. The thickness of the material on top of the thin section are at 30 μm , except for thin section 5A-1. Which was problematic and has a decreasing thickness as it goes to the right side, which reduces the interference colours. I did get three additional thin sections from the same order, that are parallel to the originals, adding up to a total of fourteen polished thin sections. These additional thin sections are denoted with the letter "B" at the end of the thin section name. An overview of the thin sections can be found in Appendix C.

All the polished thin sections were then scanned with a microscope, Olympus BX51 Thin Section Scanner (BX51), to gain overview images. All scans were consistently scanned with an objective lens with a zoom of x5, which fields a scale bar of 2 mm which is displayed in the upper right corner of each image. My standard for scanning a thin section was always done first with plane polarized light (PPL). Then again with PPL, but also rotating the polarizer from 0° to 90°. Thereafter the scanning proceeded with cross polarized light (XPL) with the polarizer at 0° and rotating the analyser until the edges in the thin section became fully extinguished. Next XPL scan was taken by rotating the polarizer to 45° and rotating the analyser until the edges was extinguished. For thin sections with a considerable amount of opaque minerals were scanned with reflected light (RFL) and some images were scanned with the lambda plate inserted with XPL and with the polarizer with an angle of 45°. In Figure 18 it is displayed what the settings are for each thin section image scanned only with the BX51. For photographing specific areas within the thin sections, it was used another microscope, Nikon E600 Spot Image Camera (E600). This is a faster process and takes up a lesser amount of data. This method easily captures particles and textures that are small, while if an image was cropped from the scans taken with the BX51 then it could have a lousy resolution. The final step was to make duplicates from the BX51 images with a reduced file size, by using the software InfranView 64. The original images had a file size from 300 – 450 MB, which was reduced to 1 – 2 MB by limiting the images to 10 % for both length and width of the originals.



Thin section placement on hand specimen



Corrected orientation of thin sections

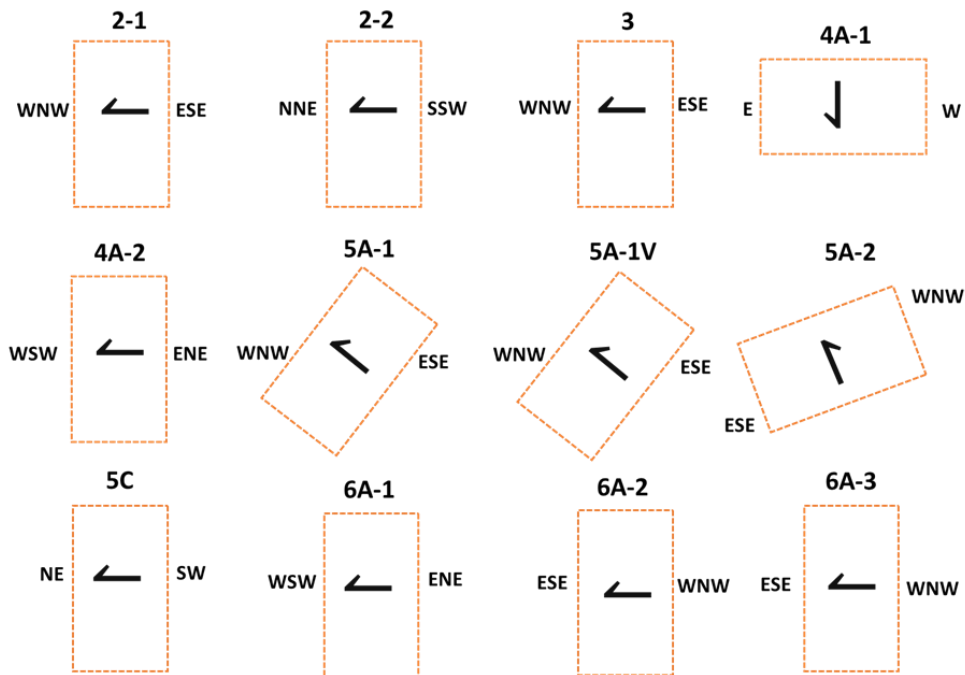


Figure 17: The steps taken from measuring the orientation of the in-situ rock before sampling, followed by the orientation of wanted thin sections onto the hand specimen. Lastly is the corrected orientation due to the mirrored effect from the billets being used to produce the thin sections.

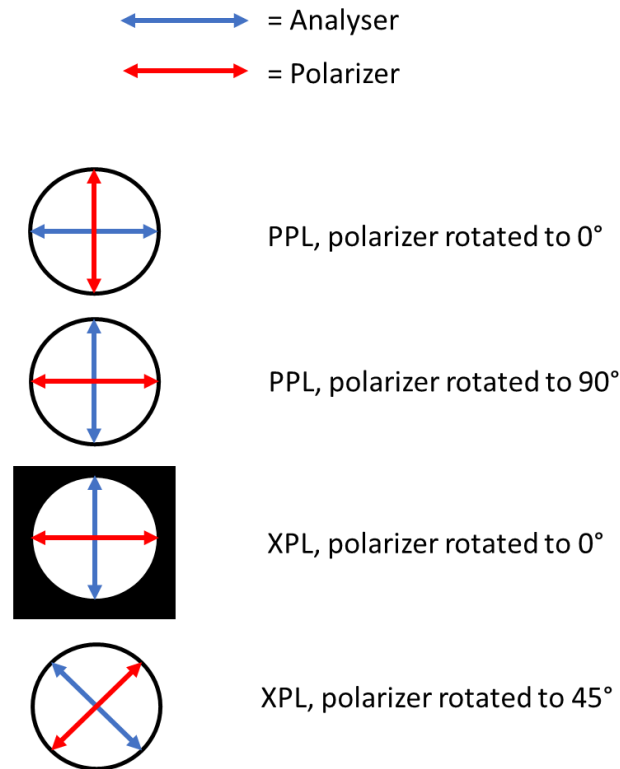


Figure 18: Display of symbology for annotating the parameters of the thin sections scanned with the BX51. Images of thin sections taken with the E600 do not follow this rule. The focus for those images was to capture feature in the best way of smaller specific areas, e.g., displaying pleochroism of a grain.

4.4.3 Image analyses of thin sections

It was carried out image analyses of the thin section scans taken with the BX51 in an open-source software called Fiji-ImageJ. The software can be used to measure physical properties of a selected area based on the pre-set settings for the measured parameters. In my case I wanted to select the circumference of recrystallized grains, either by using an auto-selection tool called "Magic wand" or by manually tracing the grain's boundary. I mainly used the auto-selection tool, which bases its selection on the colour contrast in the image. If there occurred difficulties auto selecting a mineral, then either the sensitivity of the auto-selection tool could be adjusted, or a manual tracing tool had to be used. This prioritisation of selecting methods within the images was chosen to quicken the data gathering process and ensure the quality of the data. The analyses consisted of uploading the XPL-scans with the polarizer at an angle of 45°. This version of the scans was chosen to create the simplest method to distinguish between the minerals, where quartz grains is the mineral that I wanted to measure. To ensure correct measurements it was necessary to define the scale bar for the whole image. This was done by drawing a line along the original scale bar in the image, then defining it in the software. When I defined that the drawn line's real length was 2 mm, then the software calculated the length of a pixel in the image. This is the main way to quantify the textural data. To ensure reliable data for estimating the P-T conditions it was avoided to measure grains located near strain shadows (Speciale et al., 2022). Other aspects that I tried to avoid would be grains that have not been deformed or affected by post-tectonic events that could result in mineral growth without the grains being strained. Features that can indicate an undeformed grain are even grain boundaries, 120° triple junctions and/or straight extinction of the grains. Post-

tectonic deformation that can accrue from high temperature as a form for static recrystallization called annealing, which enables the healing of dislocations in the crystal lattice, crystal growth, and possibly recovering the original crystal structure as an undeformed grain (Owona et al., 2013).

4.4.4 Whole-rock geochemistry

To classify the samples, it was applied geochemical data to the uncover differences between the sampled areas. The data was obtained from the XRF-analyses for both major- and trace elements, and ICP-MS. I plotted the geochemical data in the software R-4.1.3 and utilized the package, GCDkit, to create graphs. Additionally, I compared the XRF-results of my own data with the external datasets from previous master's theses (Vedeler, 2013, Slenes, 2016). The different diagrams that were used to create standard classifications of felsic igneous rocks, geotectonic origin, and spider diagrams of HREE/LREE. These diagrams will be used to distinguish subtle, but defining and segregating features that can indicate enrichment or depletion by look at the abundance of mobile or immobile elements.

4.4.5 Electron microscopy

A ZEISS Sigma 300VP FE scanning electron microscope was with the assistance of NTNU's Electron microscopy-laboratory leader used to automatically identify the mineralogy and elemental concentrations of the thin sections. The relevant parameters used for the analysis are listed in Table 5 were I produced two types of mineral maps. The overview category means that the whole thin section was mapped, while detailed means that a specified segment of the thin section was mapped with a higher resolution. In Appendix C it is displayed where the areas of the detailed maps were taken in the relevant thin sections.

With the software Mineralogic and Mineralogic Explorer, I modified the output data from the raw SEM analysis (

Table 6) by editing the chosen default mineral list that has its perimeters predefined. The editing process was done by adjusting the qualification for the element content of a particle to either be included or excluded in the classification as a specific mineral. The manipulation for the criteria of classification was done by lowering or increasing the threshold of an allowed element within the mineral. To get a most out of the data it was important to preview and compare the mineralogic maps generated by the Automated Mineralogy System (AMS)/Energy Dispersive Spectroscopy (EDS) and the backscatter (BS) images. This way it's possible to reduce the amount of unclassified or wrongly classified pixels. For each time I renewed the mineral list I would reclassify the original output data from the SEM with the new mineral list. Thereafter I would tweak the mineral list even further and rerun the reclassification until I obtained a satisfactory low percentage of unclassified minerals, while keeping the amount of wrongly classified minerals to be insignificant. At last, I would create heatmaps of the detailed mineral maps (except for 5A-2d) to observe how certain elements were distributed in the scanned areas. In the case of 6A-2d it was necessary to create a montage of all particle images then apply a filter that replaces the mineral list and focuses only on a single specified element.

Table 5: Settings for the SEM and Mineralogic (software) for the different mineralogic maps.

	Vacuum	Acceleration energy	Field overlap	Step Size
Overview	High	15 kV	8 %	20 μm
Detailed	High	15 kV	8 %	2 μm

Table 6: List of overview- and detailed mineral maps and the reclassification process for reducing the area % of unclassified minerals within every scan.

Overview map	Raw area % unclassified minerals	Area % unclassified minerals after reclassification
2-2	7.86	3.16
3	4.45	1.41
4A-1	8.22	2.81
4A-2	7.69	1.96
5A-2	5.88	1.95
5C	8.82	4.21
6A-1	8.34	3.40
6A-2	9.81	5.11
Detailed map	Raw area % unclassified minerals	Area % unclassified minerals after reclassification
2-2d1	24.61	4.95
2-2d2	33.56	3.52
5A-2d	26.85	1.73
6A-2d	42.13	5.26

4.4.6 Mineral Chemistry

A simplified geochemical analysis of the most common minerals above 0.8 wt. % or a corresponding cumulative sum of alterations of a mineral was extracted from the SEM analysis. However, to establish an accurate analysis of the mineral chemistry it was decided to additionally use EPMA, specifically a JEOL Electron Probe Microanalyzer JXA-8530FPlus. Certain minerals were measured to confirm if those minerals coexisted under an equilibrium and possibly use their chemical data to estimate P-T conditions based on several geothermometers. The EPMA analysis was chosen because it is a non-destructive analysis method, especially when using a defocused beam. Among these non-destructive methods it, has the highest resolution and the lowest detection limits (Batanova et al., 2018). The settings used during the analysis were the same for analysed minerals, the analysis used high vacuum with 15 kV acceleration voltage, a defocused beam with a diameter of 5 μm , and a beam current of 20 nA.

The minerals that were to be analysed was garnet, biotite, muscovite, chlorite, albite, calcite, and dolomite in three separate thin sections. The relevant thin sections are shown in Figure 19 where 188 points were distributed for the analysis (Appendix J) and were chosen to gain a broader grasp of the metamorphic conditions of Klemetsaunet. Therefore, thin section thin section 4A-1, 5A-2, and 6A-2 were selected out of the three available spots on the EPMA-holder. To gain good quality of the data, all points were selected prior to the analysis with a Leica DM4M Point Logger. By firstly defining three reference points on the thin section holder, it's possible to create a grid, where all points

defined and classified by me has their X- and Y-coordinates preserved. Thereafter, before starting the analysis I personally redefined the correct Z-coordinates for each point by adjusting the focus of an optical lens with crosshairs, which should yield the correct height for that point. And if necessary then I also relocated points that turned out to have badly suited locations. Reasons for this could be due to the possibility of measuring inclusions or impurities along fractures or boundaries of other grains. Then lastly it was important to choose appropriate standard samples for both correction and comparison of the samples to be measured (Table 7). These standards were chosen and readjusted by the technician of the EPMA, who took this responsibility and only conferred with me what I wanted to analyse and what I already had classified the minerals as.

Table 7: List of the analysed minerals and which elements that were measured with respect to the minerals, lastly is the correction for water content in the minerals.

MINERALS	ELEMENT LIST
MICAS	Fe + Mg + Mn + Ca + Na + K + Al + Si + Ti + Cl + F + Sr + Ba
GARNET	Fe + Mg + Mn + Ca + Al + Si + Ti
ALBITE	Ca + Na + K + Al + Si + Sr + Ba
CARBONATES	Fe + Mn + Mg + Ca + Sr + C

After the EPMA-analysis was completed the thin section holder to the EPMA, was scanned with the BX51. To do so a costume made plate had to be made to fit the EPMA thin section holder, since the BX51 is meant for having thin sections directly placed on its table. The purpose of this scan was to allow automatic georeferencing all 188-analysis point, that were selected with the Leica DM4m Point Logger.

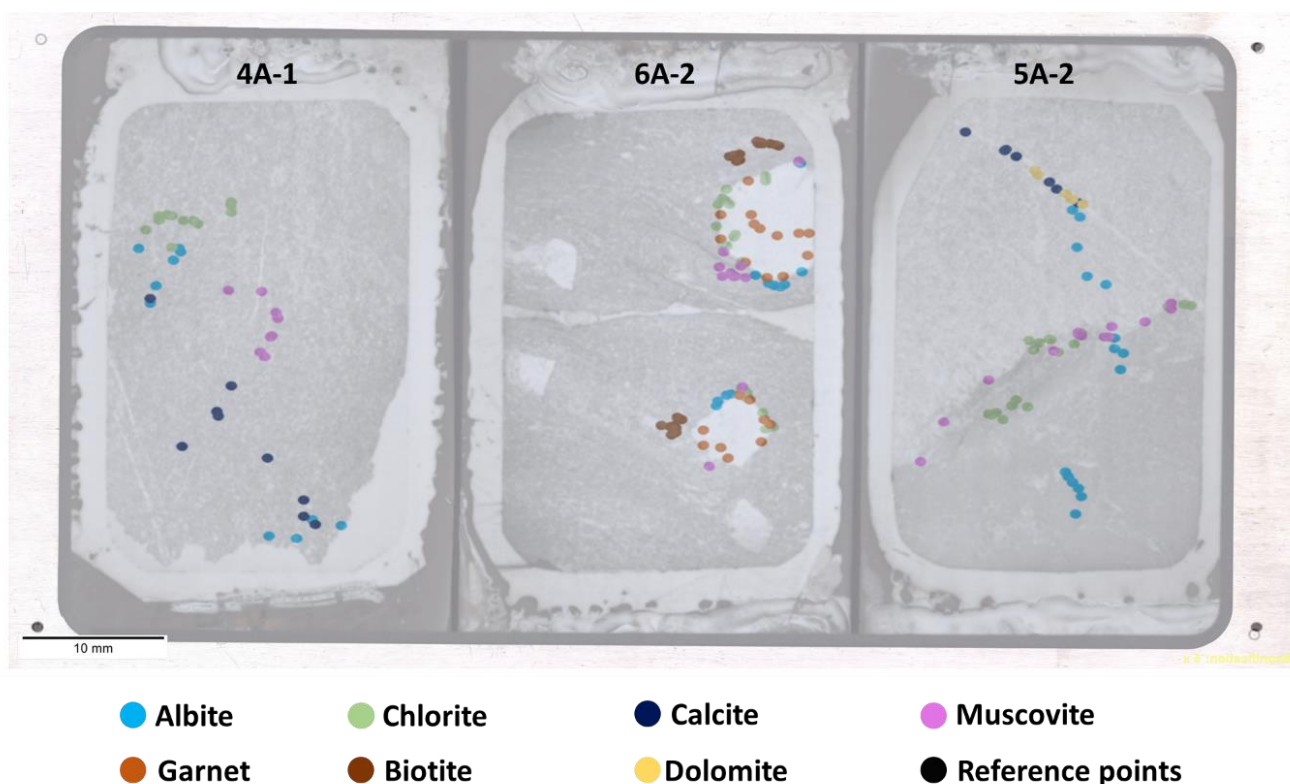


Figure 19: Overview with the scan of the custom made EPMA holder with thin sections fitted above scatter plot of analysis-points for mineral chemistry. Beware that the thin sections are mirrored.

5 Results

5.1 Field observations and samples

To gain insight to the geological history of the Klemetsaunet locality and how the Klemetsaunet's rhyodacite was formed and deformed it is important to note and map what features are present. Figure 20 shows the resulting map interpreting the area that has been divided into several lithologies, including 1. Klemetsaunet rhyodacite/protolith, 2. Byneset trondhjemite, 3. Mafic dikes, 4. Phyllonitic shear zone, 5. Breccia zone, 6. Garnet-biotite dominated shear zone. These segments often have a gradual transition between the boundaries with exception of a few areas where the outcrop is penetrated by dikes. Most of the transitions are obscured due to overgrowth of dark algae covered surfaces, especially the parts closest to the ocean. In the following subsections the observed lithologies are described in more detail.

Samples were collected from the unique lithologies where all analysis have been based on this material. Sample 1 and 2 were gathered from the phyllonitic shear zone, where parts of the hand specimen 1 fractured into smaller pieces. Resulting into sample 1 being divided into sample 1A and 1B. Additionally, both sample 1 and 2 disintegrated upon being removed from the outcrop. Sample 3 consists of a solid piece of rhyodacite with minor signs of alteration. A hornblende vein can be seen cutting through this hand specimen, else it looks like a typical rhyodacite found at Klemetsaunet. Therefore, sample 3 is referred to as Klemetsaunet rhyodacite and as the protolith. In the breccia zone sample 4 and 5 were retrieved, both samples were fractured when collected from the outcrops, resulting in grouping them as sample 4A, 4B, 5A, 5B, and 5C. At last, from the garnet-biotite dominated shear zone sample 6 was also fractured, resulting in hand specimen 6A and 6B. Additional material was collected from the outcrop sample 6-XRD, but this hand specimen has not been used any further. The samples from the garnet-biotite dominated shear zone will be referred to as the garnet-biotite shear zone in the thesis. An overview table of the collected samples are shown in Table 8, a more detailed description is included in the lithological subsections. A more thorough description can be found in Appendix B.

Lithological map of Klemetsaunet

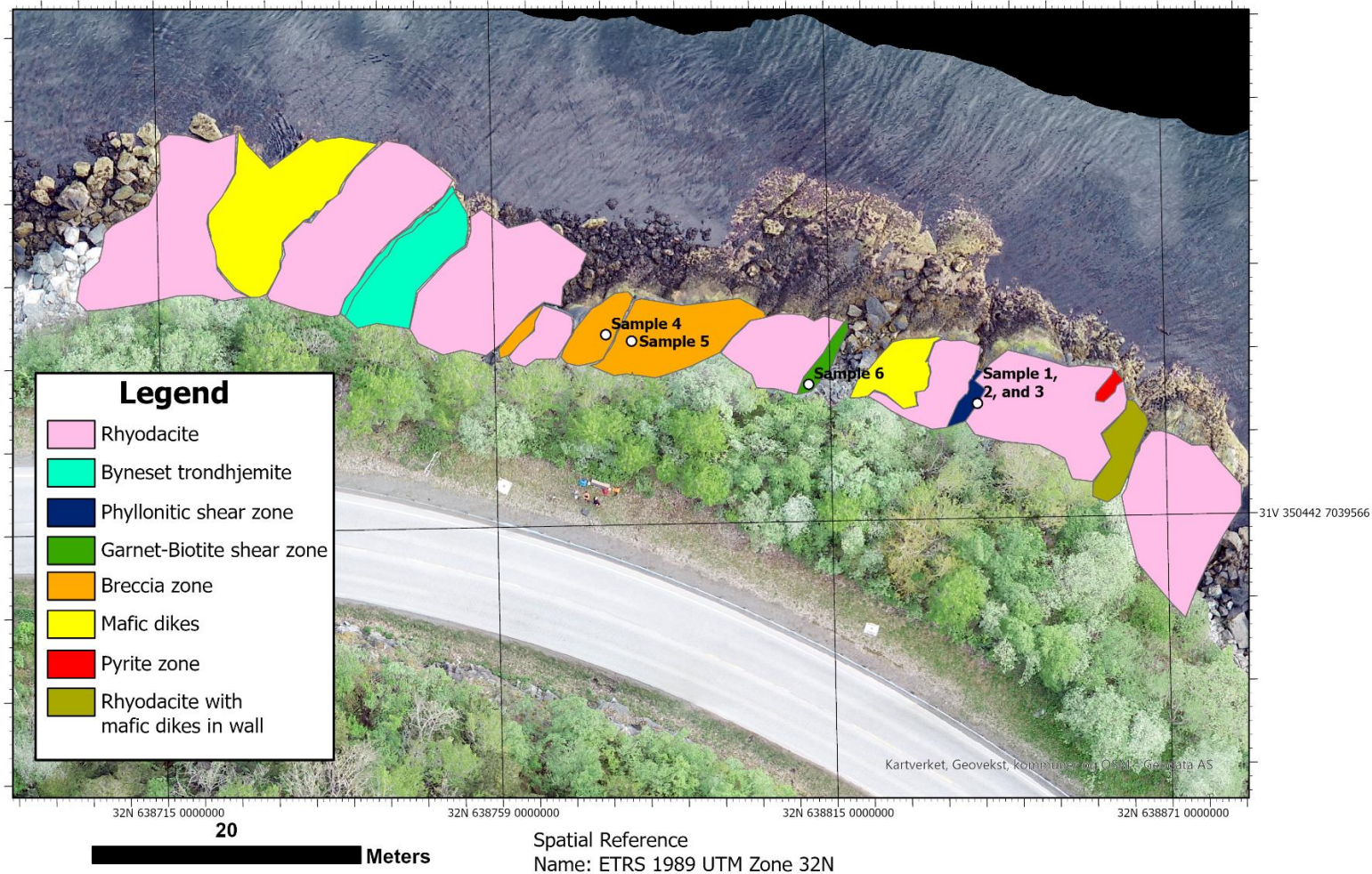
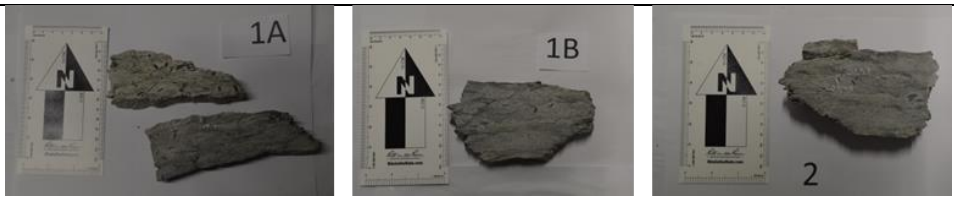
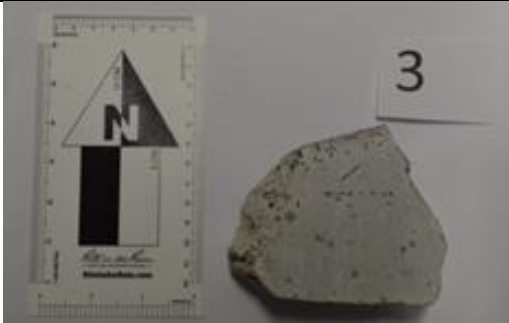

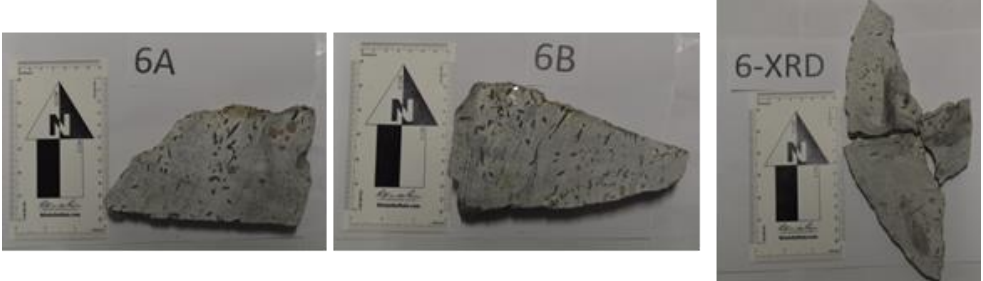


Figure 20: Lithological 2D map of the studied outcrop at Klemetsaunet. Unclassified rocks were either concealed by blocks, overgrowth, or are submerged due to the tide.

Table 8: Samples collected from field work at Klemetsaunet.

Lithology	Samples		
Phyllonitic shear zone			
Protolith			
Breccia zone			
Garnet-biotite shear zone			

The several observations of the area reveal that Klemetsaunet's rhyodacite is a lot more complex than it initially may appear. Field observations documents internal variability in the rhyodacite matrix and intrusions by multiple dikes in several places. From previous work it is stated that one of the major intrusive dikes is the Byneset Trondhemite (Slenes, 2016), the dike's surface is contaminated by overgrowth which makes it difficult to distinguish between other dikes on a macrolevel.

5.1.1 Klemetsaunet Rhyodacite

General observations are that the outcrops of the Klemetsaunet rhyodacite is packed with phenocrysts/porphyroblasts of garnet and hornblende which stands out, compared to the other tonalitic intrusions in the Bymarka area which lack this feature. The matrix is aphanitic with a common grey to blue colour. However, the matrix still has variability in its colour where certain areas it appears whiter, other areas the matrix is specked with an orange/red tint. And for some parts of the outcrop the matrix has a blue-green-greyish colour. Garnet grains are scattered in a great abundance throughout the whole outcrop, but they do vary in type and concentration. Figure 21 display the variations of garnet in aspects such as size, colour, crystal habitus, clustering, interaction to its matrix and so on. Their traits occur in specific areas, suggesting that the different types of garnet stems from localised variations in physicochemical conditions during mineral growth and alteration. Depletion halos are observed in certain garnet grains, while others exhibit no such halos, indicating their localised occurrence. Additionally, some garnet grains show signs of oxidation, indicated by the presence of rust accumulation around the grain, and these oxidized garnets tend to cluster together. Occasionally, garnets can be found aligned in relation to each other, forming string-like structures. At the eastern end of the outcrop by the rhyodacite wall with mafic dikes, there was an area that was packed full of small garnets, that were black in colour and had a perfect crystal habitus. Their dark colour is not known if it's natural or a result from a weathering of the surface. To identify if these were garnets or perhaps magnetite crystals it was used a susceptibility meter. It measured the mineral to have a susceptibility with an average value of $35 \times 10^{-3} \text{ Si}$, which is why it was classified as garnet. Hornblende grains share similar variations as the garnet grains, except for the variety in colour. Often, they appear to be randomly scattered in the outcrops, with absence of grain shape preferred orientation. While other hornblende grains cluster together and form string-like structures, which are typically accompanied by depletion halos. It was determined that the least altered rhyodacite sample relates the most to the protolith, where such an example is shown in Figure 22. The hand specimen contained porphyroblasts of garnet and hornblende, where the latter displays a string-like structure that cuts through the sample. Else, the hand specimen is solid and has a bright grey-white colour, with an absence of deformation indicators,

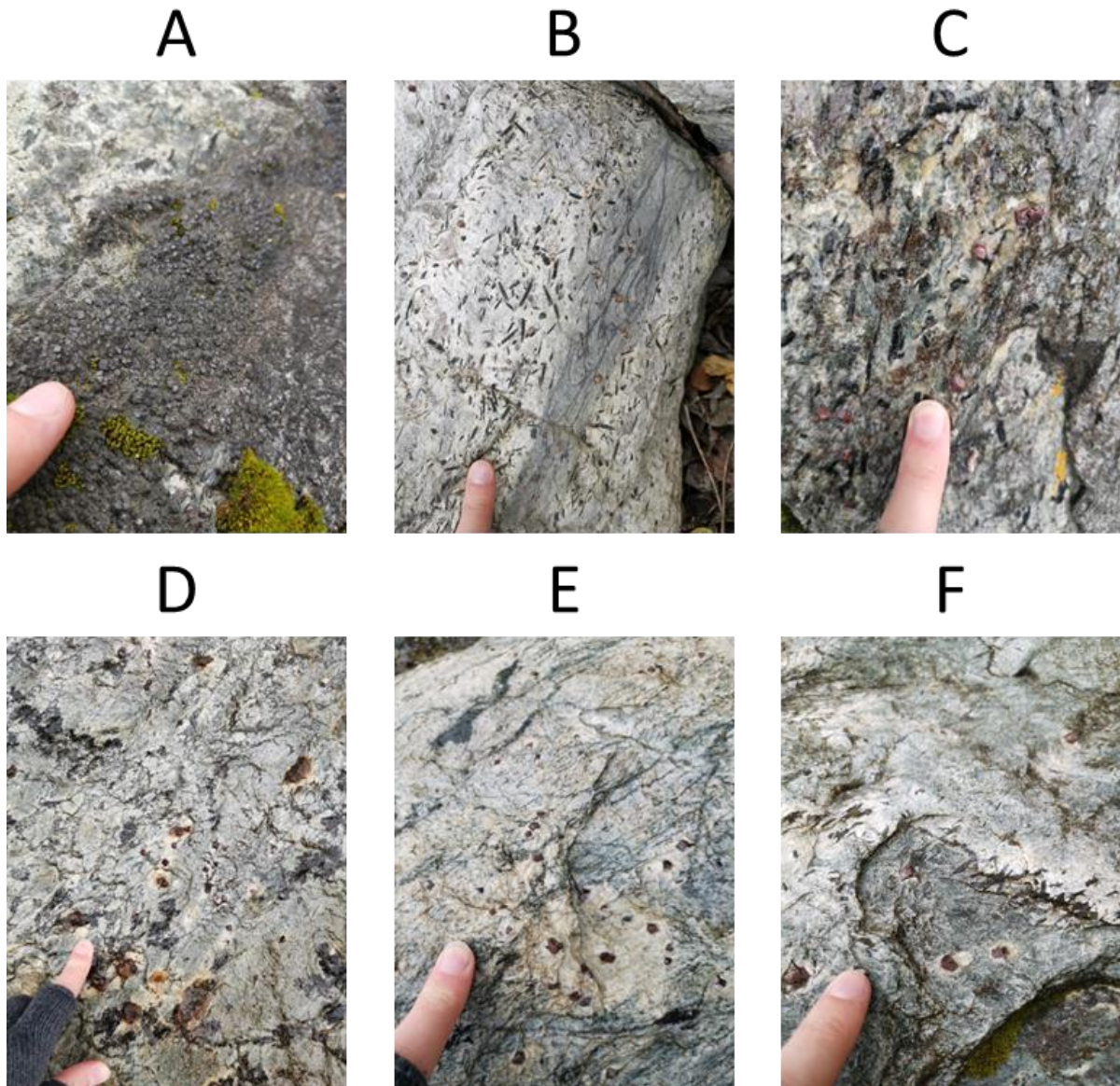


Figure 21: Observations of different types of garnets and hornblende found at Klemetsaunet. (A) Shows the black garnets that were suspected to be magnetite crystals. (B) Mafic dike through rhyodacite with garnets within and outside of the dikes area, while hornblende grains are mostly on the outside. (C) Garnets and hornblende in depleted matrix, which has a lighter white colour in contrast to the usual grey matrix. (D) Garnets with depletion halos and some aligned garnets that cluster together and has been oxidized, resulting to the rust. (E) Garnets within larger depleted areas from the breccia (F) Depletion halos around garnets and hornblende grains that align along a plane.



Figure 22: Rhyodacite sample with the least alteration and deformation, thus referred to as the protolith of Klemetsaunet. The in-situ location of the retrieved hand specimen is just underneath the phyllonitic shear zone.

5.1.2 Byneset Trondhjemite

In the field, the distinguishing features that set it apart from other interpreted mafic dikes are its well-preserved contact with the host rock and absence of cavities from weathered carbonates. However, prior research by Slenes (2016) reports the mineral composition and geochemistry of the trondhjemite. Therefore, the element composition and its leucocratic character (65-95 % felsic minerals) has been used to set it apart from the mafic dikes. The boundary is sharp and from it it's possible to roughly measure the orientation of the intrusion. Another factor is that the mafic dikes contain a lot of cavities that accrue due to weathering of carbonate minerals on the surface, and the Byneset Trondhjemite don't share this feature. The Byneset Trondhjemite has an opposing dip direction (SE) compared to the general trend of other lithologies within Klemetsaunet.

5.1.3 Mafic Dikes

The mafic dikes intrude the Klemetsaunet rhyodacite in several places. Their appearance tends to be dark grey-black in colour with a weathered surface, leaving cavities in the rock. These cavities are likely the result of weathering of carbonates as described by Slenes (2016). The lithological boundaries between the intrusions and host rock are abrupt, and the surfaces of the mafic dikes are usually altered due to erosion, resulting in difficulties to distinguish the thickness of the layers to the mafic dikes. In some places they are as thin as 1 cm, where other places the dikes disappear into the soil, which makes their actual thickness questionable, but it's assumed to be greater than the 1 cm layers. At the Eastern end of Klemetsaunet, there are multiple thinner mafic dikes that intertwine into the rhyodacite, this area have not been focused on in this thesis, however extensive research of this area have been carried out by Slenes (2016). In this area an extensive amount of smaller garnet grains (<0.5 cm) is packed together in string-like structures.

5.1.4 Phyllonitic Shear Zone

The phyllonitic shear zone occurs abruptly within the rhyodacite, where the shear zone is quite localised. The shear zone has a pronounced schistosity, porphyritic texture and with an aphanitic groundmass, that has a greenish-blue colour to it and a thickness of approximately 25 cm. The hand specimens depicted in Figure 23 were fragile, especially sample 1, were parts of them disintegrated when retrieved from the outcrop. There can be seen randomly oriented hornblende grains at the upper part of sample 1A, whereas the rest of the samples lack this mineral. However, the rest of the samples contains porphyroblasts of garnet and chalcophile minerals can be spotted. The garnet grain often displays a depletion halo and a cross-section of sample 2 shows that garnet grains with zonation. There is a flow pattern in the hand specimen that is visible due to foliation between layers with a bright grey colour and layers that have a darker hue to its grey colour. The crosscut of the sample reveals thinner layers that are more parallel to each other, forming a more regular flow pattern. Perpendicular to the foliation, towards 297°, dark layers warp around the brighter layers, which form strained lens shapes.

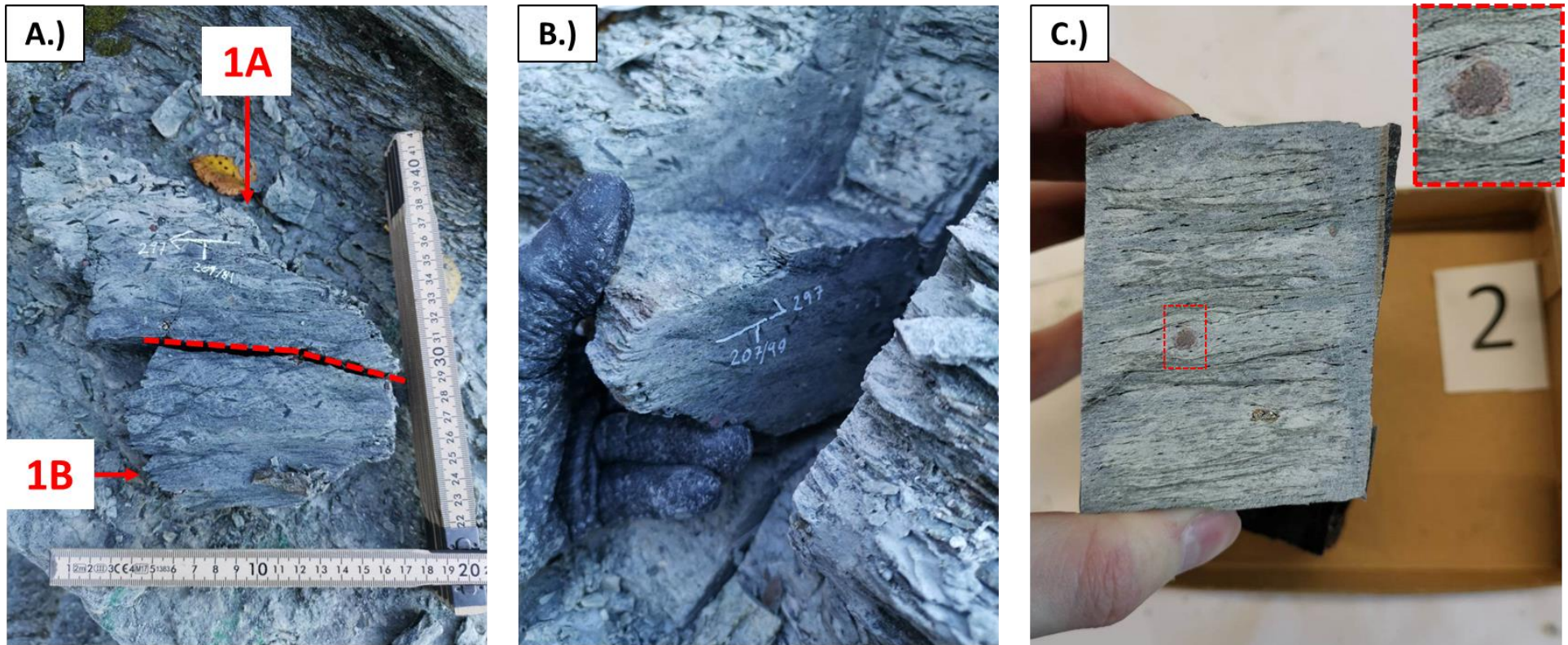


Figure 23: Samples collected from the phyllonitic shear zone. A.) Sample 1A and 1B gathered from the upper part of the shear zone. B.) Sample 2 from the centre of the shear zone being put back into in-situ with its sampled orientation written on it. C.) Displays a cross-section of sample 2 parallel to its foliation with visible chalcophile mineral, that is suspected to be pyrite. The highlighted area is a garnet grain with noticeable zonation at a macro level.

5.1.5 Garnet-Biotite Shear Zone

The garnet-biotite shear zone is similar to the phyllonitic shear zone, distinct by its localised occurrence. It displays a 20 cm thick, dark blue-grey coloured matrix at the centre of the hand specimen (Figure 24). This area contains lots of garnet- and few hornblende grains, where both minerals have depletion halos. A weak flow pattern of brighter layers within the matrix can be observed adjacent to the garnet. The slab is solid in contrast to the other shear zone, where disintegration of the sample occurred. Above and below the centre the concentration of hornblende grains increases by a lot, while the number of garnets diminishes, and the matrix gets a lighter white colour. Continuing further above and below within the hand specimen the grey coloured matrix returns, but without the presence of garnet.

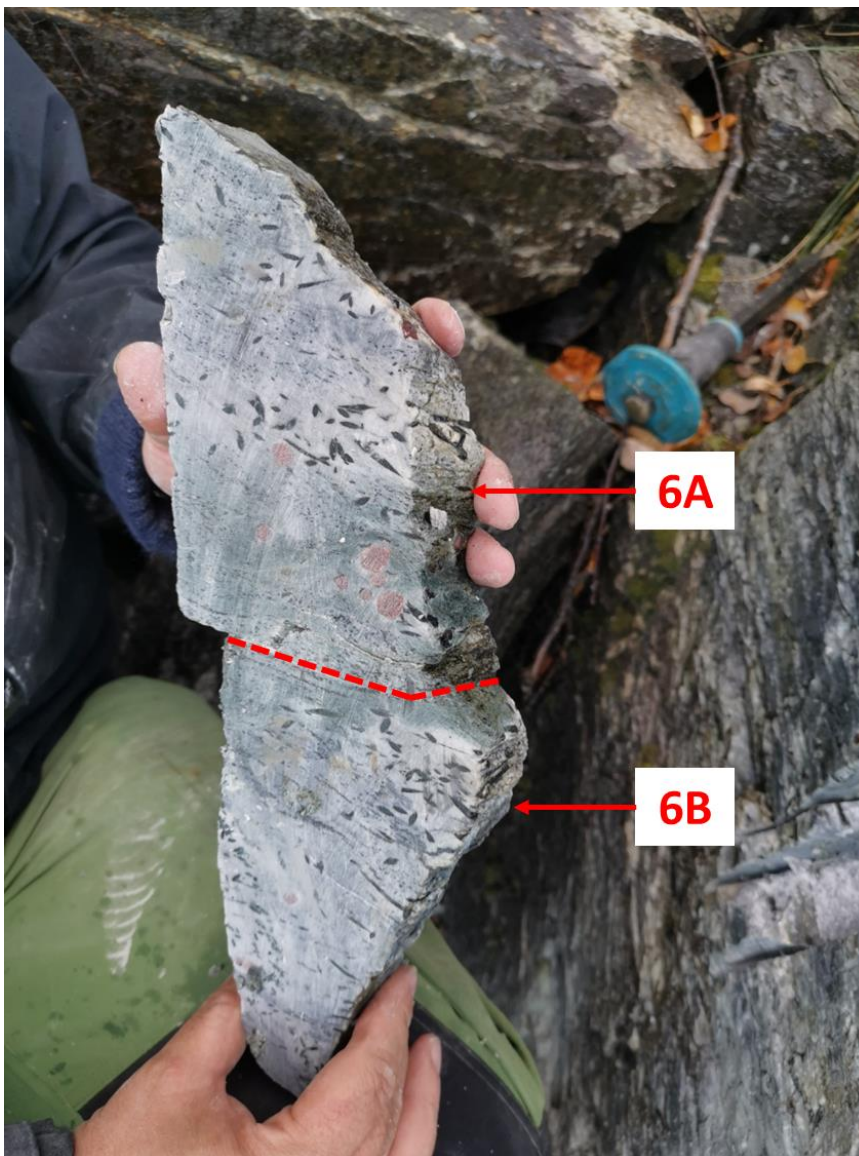


Figure 24: Sample 6 from the garnet-biotite shear zone is divided by occurring fracture upon retrieval. Sample 6A displays an abundance of garnet grains in the centre of the shear zone with a minor content of hornblende. In contrast to the upper part of the hand specimen which shows a depleted area with a great amount of hornblende forming a string-like structure. Followed by the almost complete disappearance of hornblende at the very top, where the rhyodacite has a typical blue-grey colour for its locality.

5.1.6 Breccia Zone

In the field the breccia is characterized by a spotted matrix, that alternates between an orange/red colour- and bright/dark grey coloured rhyodacite. There are numerous types of veins penetrating the outcrop, including muscovite-, hornblende-, and quartz-carbonate veins. In peculiar the quartz-carbonate veins display a brown/reddish colour, that likely stems from a high Fe content (See sample 5A in Appendix E). Garnet grains are typically accompanied with depletion halos or a layer of rust. The rusted garnet was not sampled, but the observation indicates that the garnet has oxidized likely to high Fe concentrations at the surface of the mineral grain. Which could relate to a Fe-rich rim, in zonation of garnets. The hand specimen, sample 4A and 4B shows two lithologies one looks like the typical rhyodacite commonly found at Klemetsaunet. However, this phase contains darker minerals forming an irregular pattern, almost like a webbing through the matrix and there are brown quartz-carbonate veins penetrating the rock. The other phase is a white rhyodacite with brown spots scattered around its matrix (Figure 25). Sample 5 show a cataclastic texture, with angular grey fragments in a dark grey matrix. Inside the sample it's larger pieces of rhyodacite that contains garnets with depletion halos. The pieces themselves has a brighter with colour, with a brown-reddish tint to them. There are also hornblende grains that align themselves along one plane, that also has a depleted area around those grains.

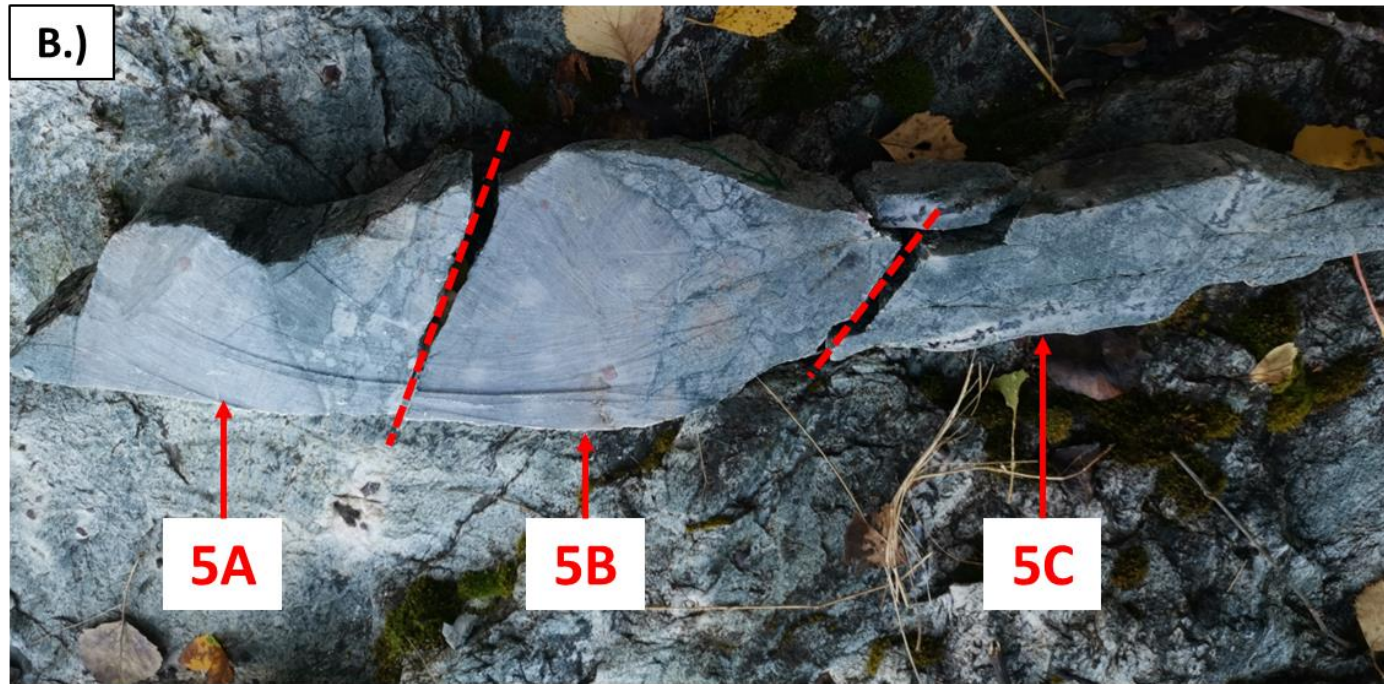
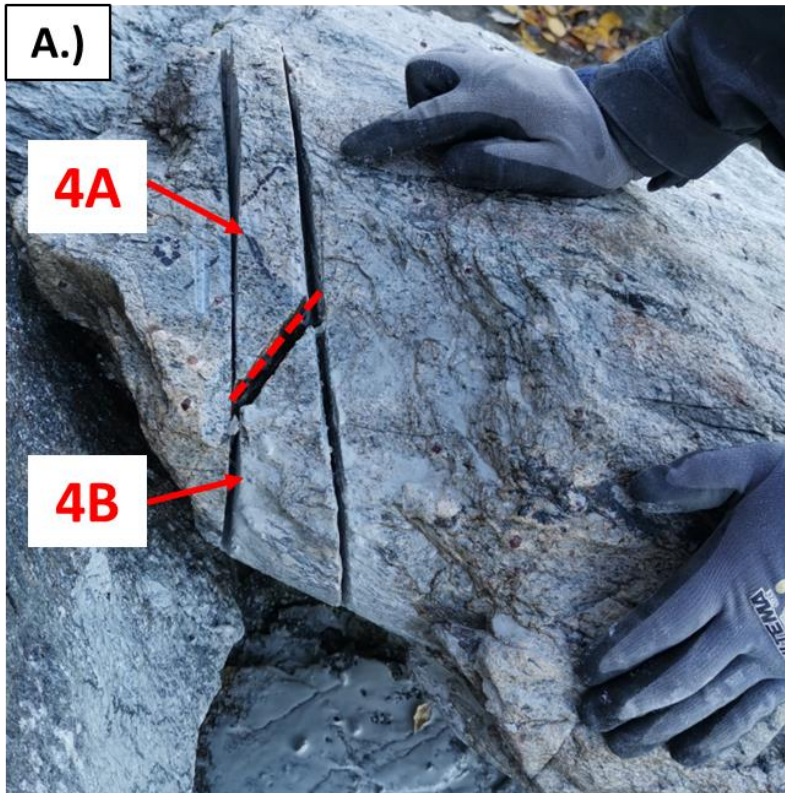


Figure 25: The retrieved samples from the breccia zone. A.) Sample 4A and 4B were separated due to a fracture. B.) Sample 5 displays clear brecciation, where carbonates occur in the matrix with a red-brown tint. There is a lack of hornblende in the samples, except for 5C, which contains a hornblende vein with depletion halos.

There were few if any kinematic indicators in the field. Mostly the bedding of the rock and veins were the measured structural features. Additionally, the terrain of Klemetsaunet limits the accessibility to areas where it could be possible to measure features at a perpendicular surface. This makes it so that the orientation of measured veins is viewed in 2D and the dip angle cannot be precisely measured.

5.2 Petrography

Shared attributes for all samples:

- Their matrix consists of quartz and albite.
- Grain boundary migration in quartz grains.
- Magnetite occurs, but with a varying abundance. Classified as Fe-oxides by the Mineralogic software.
- Few grains of apatite randomly found in all samples.

5.2.1 Modal Mineralogy

By analysing the observed XRD-diffractograms, examining the SEM results, and studying the available thin sections, an overview of typical mineralogy of all samples was created. Appendix D was constructed to highlight the predominant minerals found in the thin sections. However, it is important to note that not all these minerals are present in every thin section. Therefore, only a few basic properties are mentioned, but they are defining attributes for recognising a specific mineral. Notably, there appears to be a transition in the interference colour of the chlorite from the sampled areas. In the phyllonitic shear zone and the protolith, it's observed that the chlorite's interference colour is brown-pinkish, while in the second shear zone and breccia the chlorite has its characteristic masked dark blue interference colour (Figure 26).

In Figure 27, a bulk estimate has been made for the mineral assemblages based on the XRD-analysis. From these results, it occurs that the samples are similar in their proportions, where quartz and albite are the dominant minerals. Thereafter chlorite and muscovite are the subsequent most abundant minerals. One can look at these four minerals and their ratios to separate the samples from each other, as displayed in Table 9. The ratios show that albite combined with the class albite intermediate is the dominant mineral in all samples. The Ab/Qz-ratio for the protolith (sample 3) is the lowest and shows that the protolith consists of almost equal parts of those minerals. It also comes forth that the protolith has the greatest of albite and quartz in contrast to its mica content. Whereas the phyllonitic- and garnet-biotite shear zone are on the opposite side of the spectrum, with the highest mica contents. Additionally, they almost have a 2:1 ratio for chlorite to muscovite (except for 6A-A). The breccia has a significant amount of chlorite, with a respectively low amount of muscovite.

Figure 28 estimates the samples' mineral assemblages based on the thin sections. What is noteworthy is that the mineral assemblages in Figure 28 were analysed with SEM, which makes the estimate of quantities representable for only those represented areas (Appendix C). Were data from the analysis was extracted and all mineral percentages below 0.8 wt. % was removed. Here as well both quartz and albite are the dominant minerals for most thin sections, however the mineral maps that target garnets is not comparable for with the rest of the samples. Mainly the overview scans can be used for assessing the modal mineralogy of a thin section. Which are somewhat alike to the equivalent samples from the XRD-analysis. Else, it was observed during the sample preparation from the leftovers of crushed material it came up that the samples contained magnetic minerals and in varying quantities. In Appendix E, the hand specimens utilized for bulk chemistry analysis are presented to enhance clarity and facilitate relatable correlation. This crude test method established that the phyllonitic shear zone (sample 2), the breccia with carbonate spots (sample 4A), and the garnet-biotite shear zone outside with minimal hornblende and absence of garnet (sample 6A-C) had elevated quantities of magnetic minerals. In

comparison sample most fragmented breccia (5A-B) and the garnet-biotite shear zone with an abundance of garnet (6A-A) contained no minerals with magnetic properties were observed. As for the other samples they only contained few grains of an insignificant amounts. In Figure 29 the typical quartz and albite matrix is shown, were the garnet-biotite shear zone is the more unique with muscovite grains scattered into the matrix, exhibiting a strong grain shape preferred orientation (GSPO).

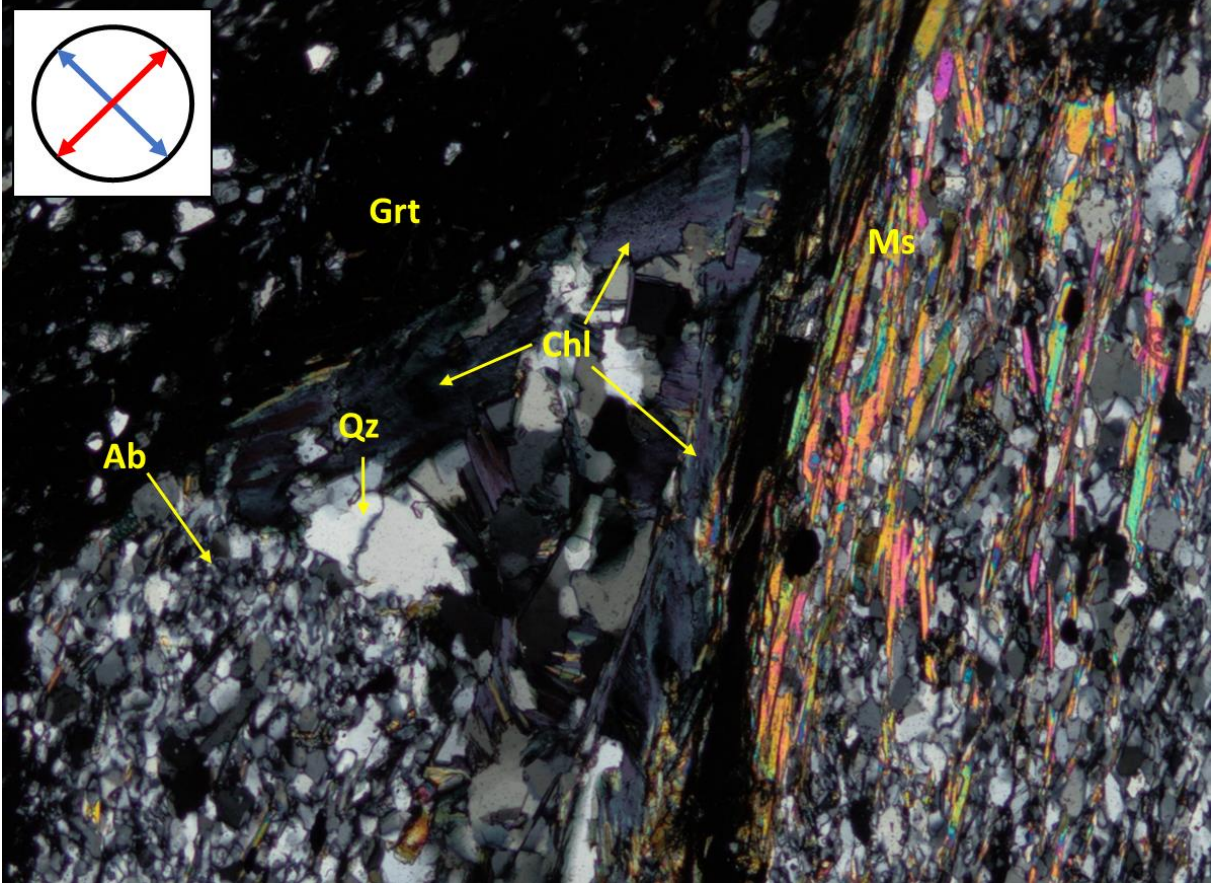


Figure 26: Thin section of the garnet-biotite shear zone (6A-2B) where chlorite displays a blue/violet masked interference colour.

Bulk analysis of mineral assemblage based on XRD-diffractiograms with detection limit of 1 wt. %

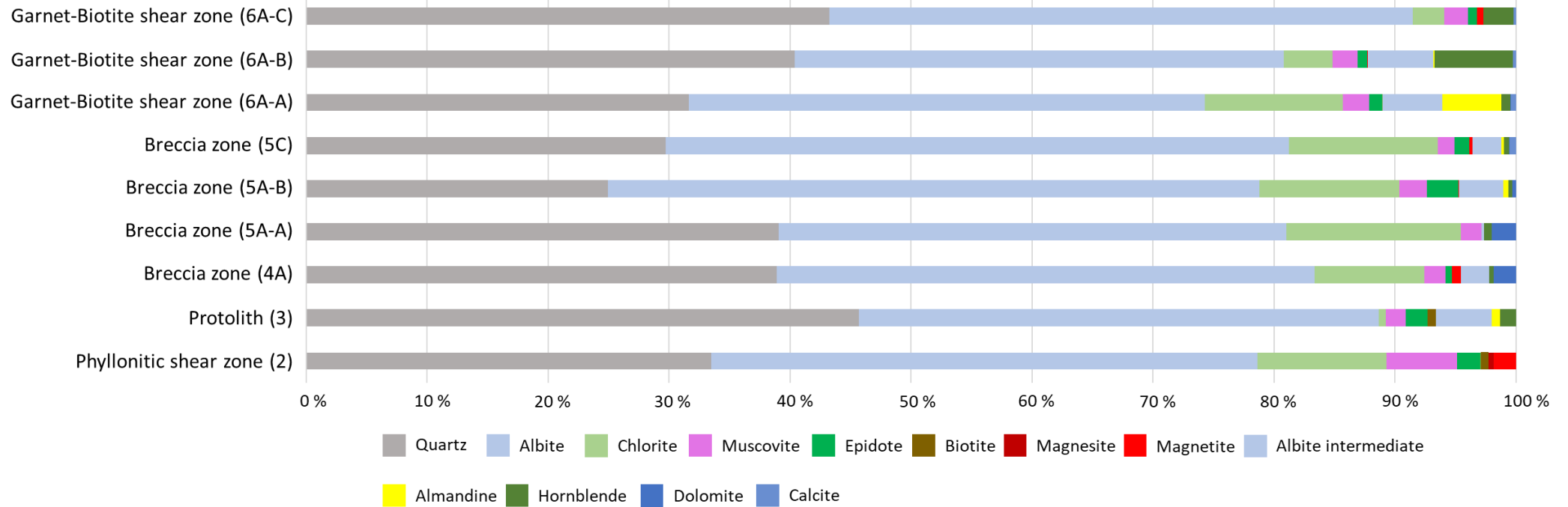


Figure 27: The mineral assemblage based on XRD-analysis from bulk samples.

Table 9: Ratios for comparison in variation of main occurring minerals for all bulk samples from XRD.

Sample	Ratio, albite/quartz	Ratio, chlorite/ muscovite	Ratio, Ab + Qz / Chl +Ms
Phyllonitic shear zone (2)	1,35	1,83	4,77
Protolith (3)	1,04	No Chl	56,89
Breccia zone (4A)	1,20	5,08	7,92
Breccia zone (5A-A)	1,08	8,49	5,02
Breccia zone (5A-B)	2,30	5,16	5,96
Breccia zone (5C)	1,81	8,96	6,13
Garnet-Biotite shear zone (6A-A)	1,50	5,26	5,83
Garnet-Biotite shear zone (6A-B)	1,13	1,99	14,14
Garnet-Biotite shear zone (6A-C)	1,12	1,34	19,88

Simplified mineral assemblage based on SEM results of thin sections with all values below 0.8 wt. % removed

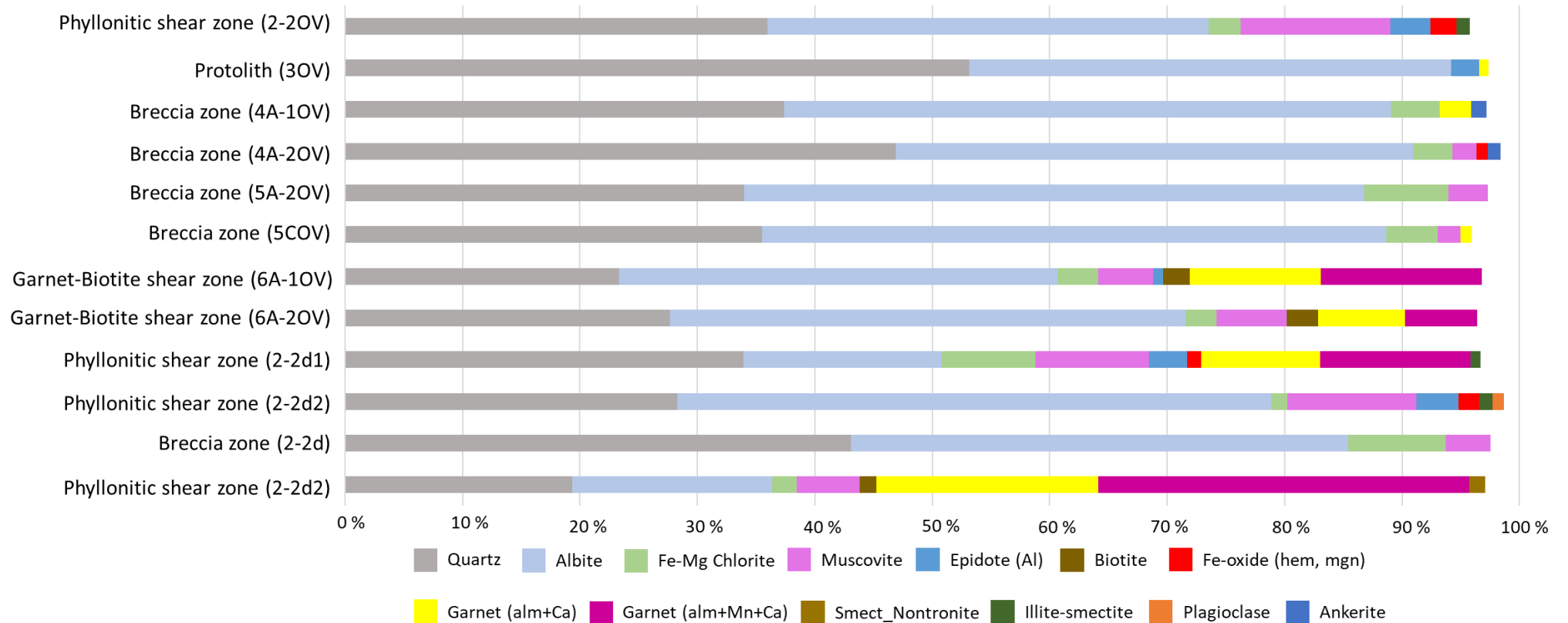


Figure 28: Mineral assemblage of mineral maps scanned with SEM for both overview maps and detailed maps. All values below 0.8 % was removed from the mineral list.

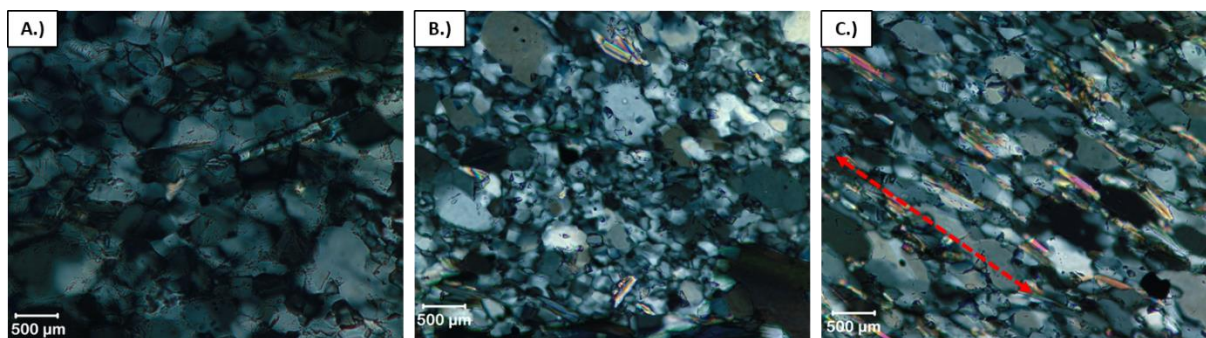


Figure 29: Albite-quartz matrix from the phyllonitic shear zone (A), the breccia (b), and the garnet-biotite shear zone (C). Muscovite with observed strong GSPO and an even distribution in the matrix is common for the garnet-biotite shear zone.

5.2.2 Least deformed sample, rhyodacite protolith

The matrix texture in the protolith has indications of a typical magmatic texture where the distribution of albite and quartz is evenly spread and quartz and feldspar grains are intergrown as shown by the SEM mineral map (Figure 30). However, in the optical cross polarized images it's seen that quartz and feldspar recrystallize, interlocking with each other. Reflecting signs of the original magmatic texture. The sample also displays a porphyroblastic texture with porphyroblasts of both hornblende and garnet. The garnets have a poikilitic texture with only quartz inclusions and displays a zonation from Mn- and Ca-rich almandine at its core, and a depleted almandine at the rim. It's observed that the garnet has overgrown the quartz and left no albite behind. It should be noticed that chlorite neither surrounds nor penetrates the garnets, but there is chloritization of the hornblende grains. The hornblende grains display a nematoblastic texture by aligning through the thin section, producing an L-fabric. Which represents a typical amphibole vein that can be seen at a macro level in the field.

There are no signs of foliation, kinematic indicators, flow patterns, or grain shape preferred orientation in the sample. Which supports earlier assumptions that the matrix hasn't been exposed to intense tectonic deformation after crystallization. However, there are indications of dynamic recrystallization and deformation of the quartz. It's observed that the grain boundaries of the quartz have been rearranged, displaying a wonky pattern having parts of their boundaries migrating into the neighbouring grains. Indicating grain boundary migration (Figure 31). There is also the occurrence of deformation bands as seen in Figure 31, which is also indicated by the quartz's undulose extinction. These findings prove defects in the quartz crystal lattice. According to Appendix K the average grain size of quartz is greater, by averaging a higher concentration of quartz grain greater than 130 μm , compared to that of the phyllonitic shear zone. These measurements were based on the image-analysis with Fiji-ImageJ, where only quartz in those two thin sections were quantified.

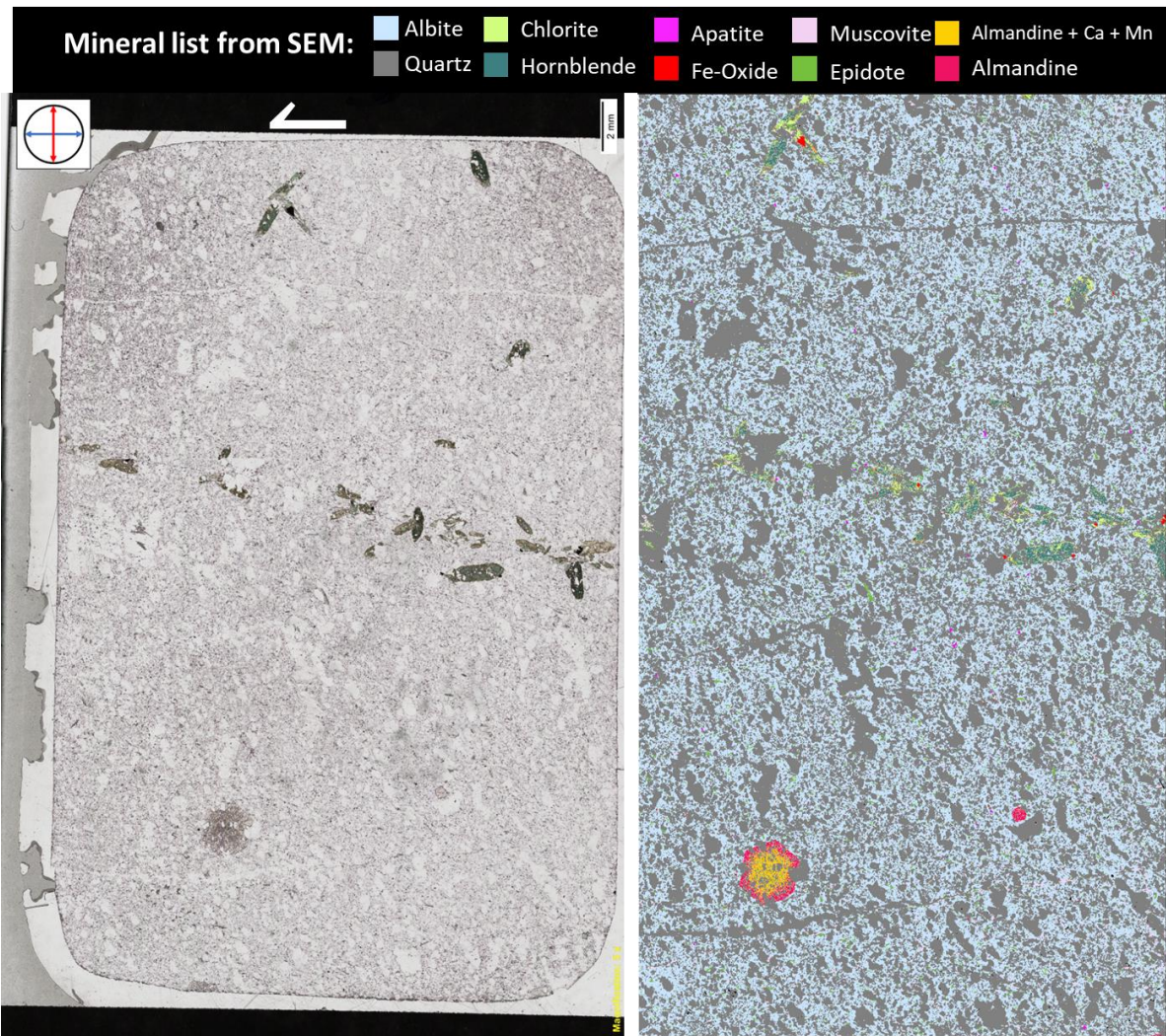


Figure 30: Thin section 3 with its mineral map. In the PPL image it's easy to see how a hornblende vein aligns through the sample.

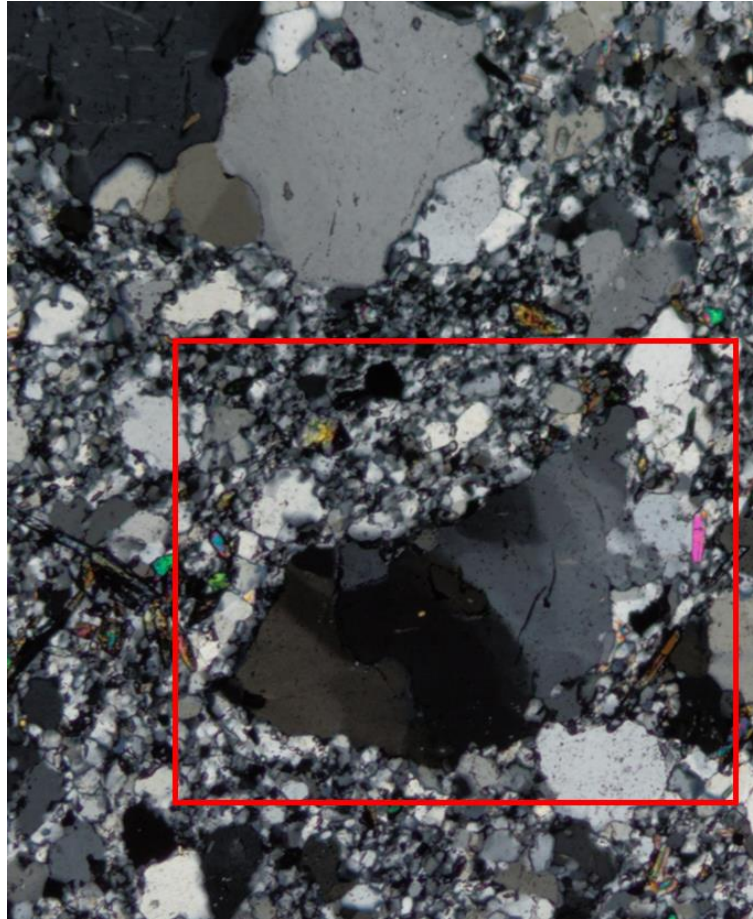


Figure 31: Quartz grain inside marked area shows GBM and deformation bands, which implies that there has been deformation under relatively high temperatures. The circumference of this large quartz grain is mainly surrounded by fine-grained albite.

5.2.3 Phyllonitic shear zone

The overview Figure 32 depicts how the minerals group together in the foliation of the phyllonitic shear zone. Micas bands run through the thin sections and warp around quartz lenses and porphyroclasts of garnet. Observations of the garnets shows the same zonation pattern as in the protolith, however there is chlorite that cuts into the core, which indicate that the chlorite is a result of retrograde metamorphism. The Mn- and Ca depleted rim does not follow these dents and maintains the original thickness of zonation all around the grain boundary (Figure 33). Suggesting chloritization after the growth of the garnets. The garnet has a porphyroclastic texture, exciding the common grain size for the rest of the grains. It also is poikilitic, with both quartz and chlorite inclusions. In Figure 34 there are multiple minerals and mineral interactions typical for the phyllonitic shear zone. Chlorite is commonly intergrown or overprinting biotite and has a 1.order brown interference colour. Epidote and muscovite are frequently scattered in an albite and quartz matrix, with a strong grain shape preferred orientation along either the foliation or the flow pattern around quartz lenses.

Based on sample 2 viewed in thin section 2-1, 2-1B and 2-2 indicates that the phyllonitic shear zone is phyllonitic with either a horizontal- or vague oblique foliation that indicates dextral movement (Figure 35). It can be assumed that the shear strength of the phyllonite is controlled by these mica bands and can be linked to the crumbling of the hand specimen. In 2-2 the dominant kinematic indicators show a top to the right movement, Figure 35

depicts some of the best examples of this dextral shear sense. In the images the garnet either displays inter-kinematic or syn-kinematic deformation with a gentle bend of the inclusions. Quartz outside the garnet curves around it and at the rim at both entry points and through its core the inclusions of quartz are linear. There is also a strain shadow behind the garnet relative to the movement where chlorite has grown. Most kinematic indicators in thus suggests that the shear plane went towards SSW with a dextral shear sense. However, in 2-1 and 2-1B the kinematic indicators indicate a sinistral shear sense. This is seen in mica fishes and folds (Figure 36) and they suggest that the deformation was sinistral towards WNW. The flow direction has most likely to been parallel with 2-2, since its mica bands are more linear and parallel to other mica bands within that thin section. While in 2-1 and 2-1B the mica bands are wavier and form irregular and less repeating patterns, which leads to less foliation. The quartz lenses' GSPO is angled in contrast to the mica bands (Appendix K), which are more horizontally oriented along the foliation. Patches and strings of relatively coarse-grained quartz form lenses, in the more fine-grained albite and quartz matrix. Some of these lenses are also plastically deformed having an asymmetrical boudinage geometry to them, typically pinching at its flanks.

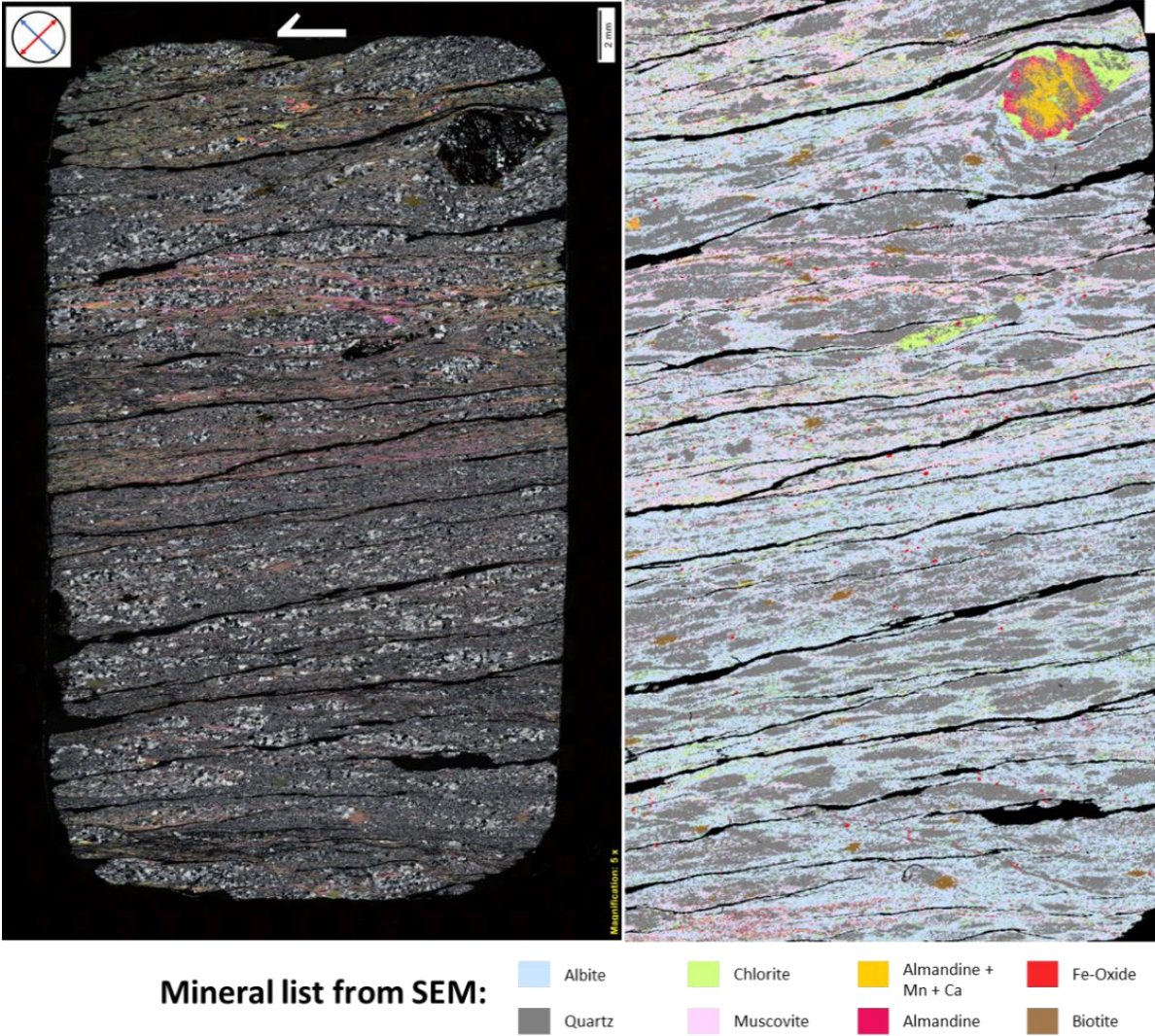


Figure 32: Thin section 2-2 with overview EDS-map, displaying the mineral assemblage and foliation in the sample. Garnet in the upper right corner has zonation and a strain shadow of chlorite behind it.

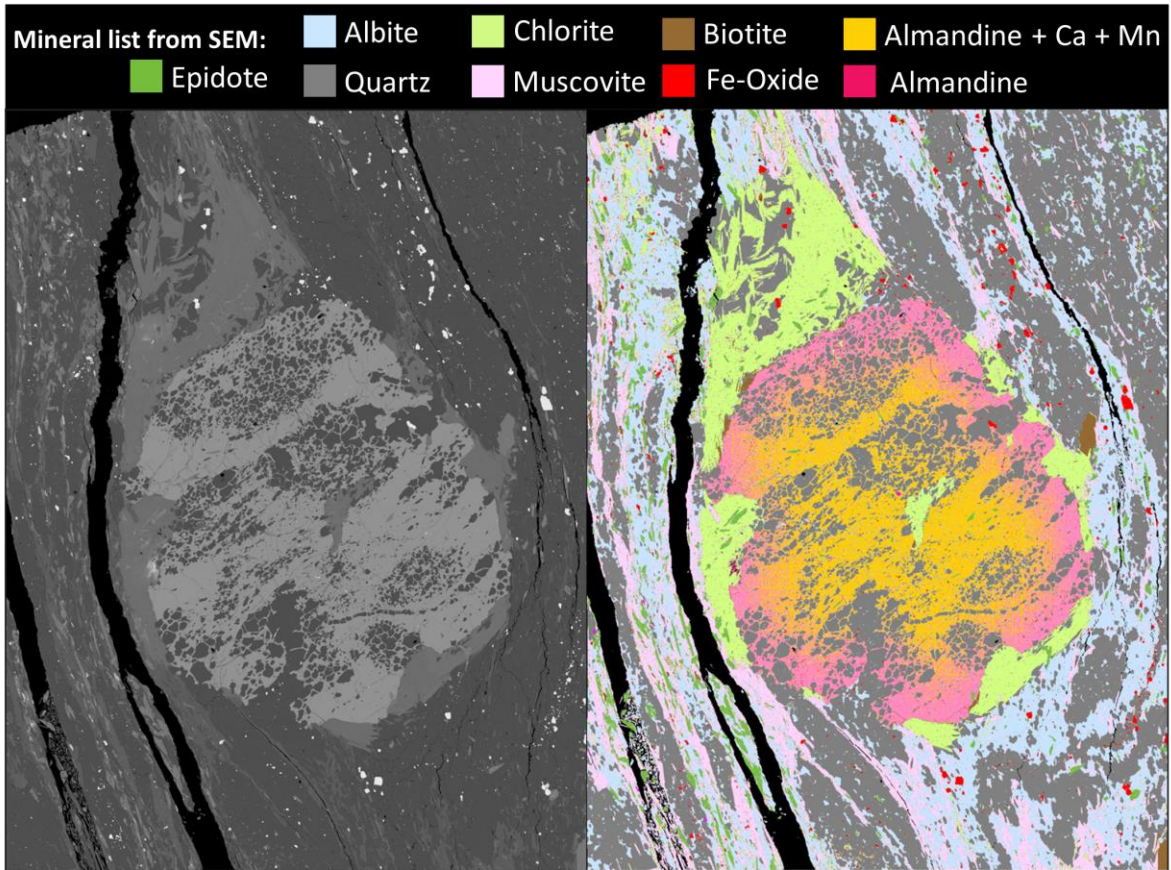


Figure 33: EBS-image to the left and mineral map to the right from the detailed map 2-2d1.

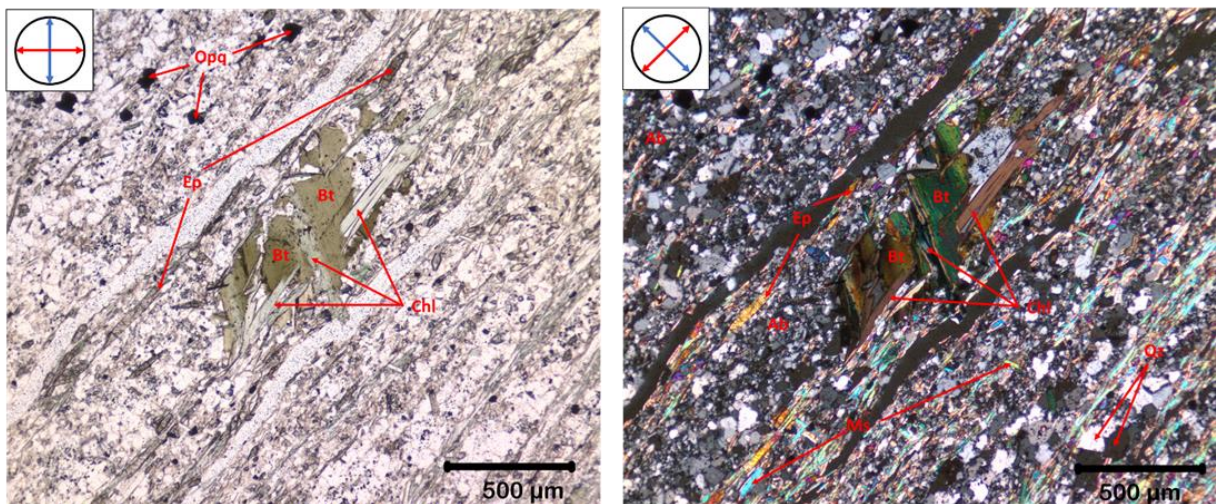


Figure 34: Chlorite with a 1.order brown interference colour, from thin section 2-1. Other showcased minerals are common for the mineral assemblage in the phyllonitic shear zone.

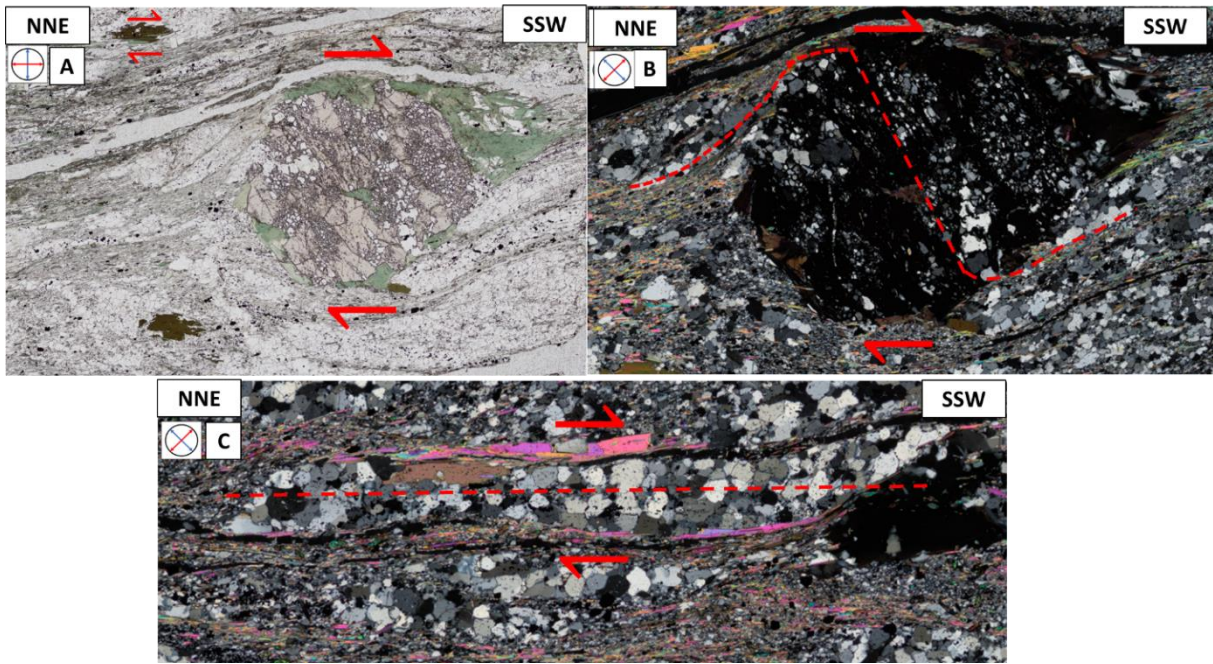


Figure 35: Kinematic indicators of dextral shear sense with top to the SSW in thin section 2-2. Image A.) shows a biotite mica fish and a strain shadow of chlorite. B.) shows either an inter-kinematic or syn-kinematic indicator by tracing the wings of a δ -clast and through its body. In C.) there is an example of a quartz lens that has an oblique foliation and ductile boudinage, were the red stippled line is parallel to the matrix foliation.

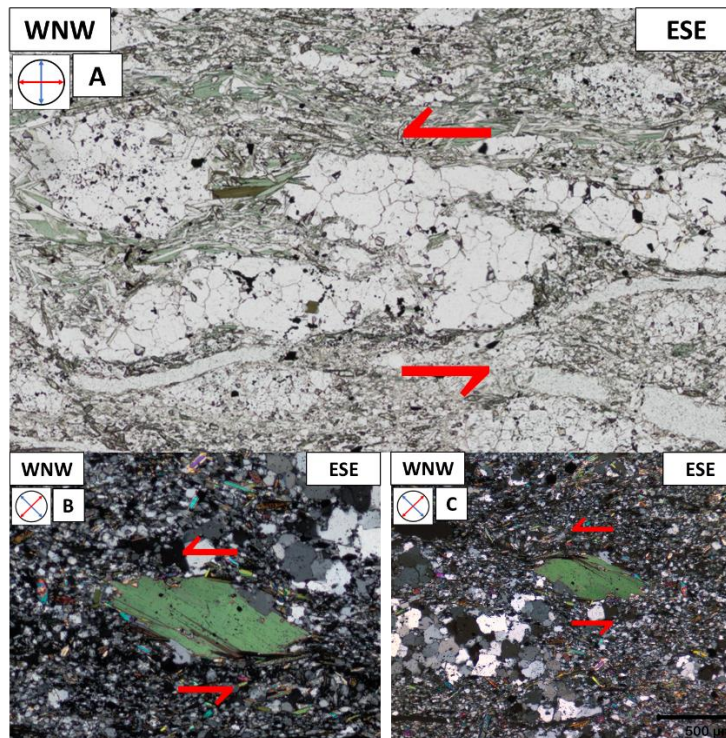


Figure 36: Kinematic indicators of sinistral shear sense with top to the WNW from thin section 2-1 and 2-1B. A.) shows a fold, whereas in B & C.) there are examples of mica fishes.

5.2.4 Garnet-Biotite shear zone

It can be seen in Figure 37 that there is a dispersion in the distribution of quartz and albite in the matrix. Mostly there is a consistent amount of quartz to albite, but the ratio seems to be disturbed in the flow pattern around the garnets. From both the thin sections and the SEM-analysis the garnet mapped in 6A-2d contains inclusion forming sigmoidal lines (Figure 38). This S-shape is a syn-kinematic indicator where the rolling pattern indicates dextral shear sense with top to the WNW. The garnets are therefore considered as poikiloblasts with a flow pattern of inclusions that formed during simultaneous rotation and growth of the crystal. However, the concentration of Mn and Ca gradually declines further away from the core in the larger garnets. In contrast to the smaller garnet grains where this transition is not as easily identified in the mineral maps, only the shift from rim to core is clear in those grains. Garnets and hornblende display the same porphyroclastic- and poikilitic texture as the garnets in the phyllonitic shear zone. Several mica-fishes of biotite in Figure 39 show a dextral shear sense with movement in the same direction as the garnets. Finally, there are hornblende grains exhibiting similar kinematic indicators (Figure 40). Resulting that the dominant shear sense in the thin section being dextral with top to the WNW. The general flow pattern in the thin sections is difficult to distinguish and there is not observed any clear foliation. Nonetheless, there are a lot of fine-grained mica, mostly muscovite that are evenly distributed through the matrix and has a strong GSPO along ESE-WNW. There are micas (biotite., chlorite and muscovite) which do form larger bands and cluster together. However, muscovite mostly they lay within the quartz and albite matrix. It's observed that the abundance of biotite is greater than the amount of chlorite, in contrast to the first shear zone. But there is minor chloritization of biotite, hornblende, and garnets, where chlorite is intertwined along the cleavages of the biotite grains, at the flanks of hornblende, and surrounding and penetrating the garnets. Quartz veins also penetrates a larger garnet in 6A-1, were they fold outside of garnet, being disrupted in the flow pattern.

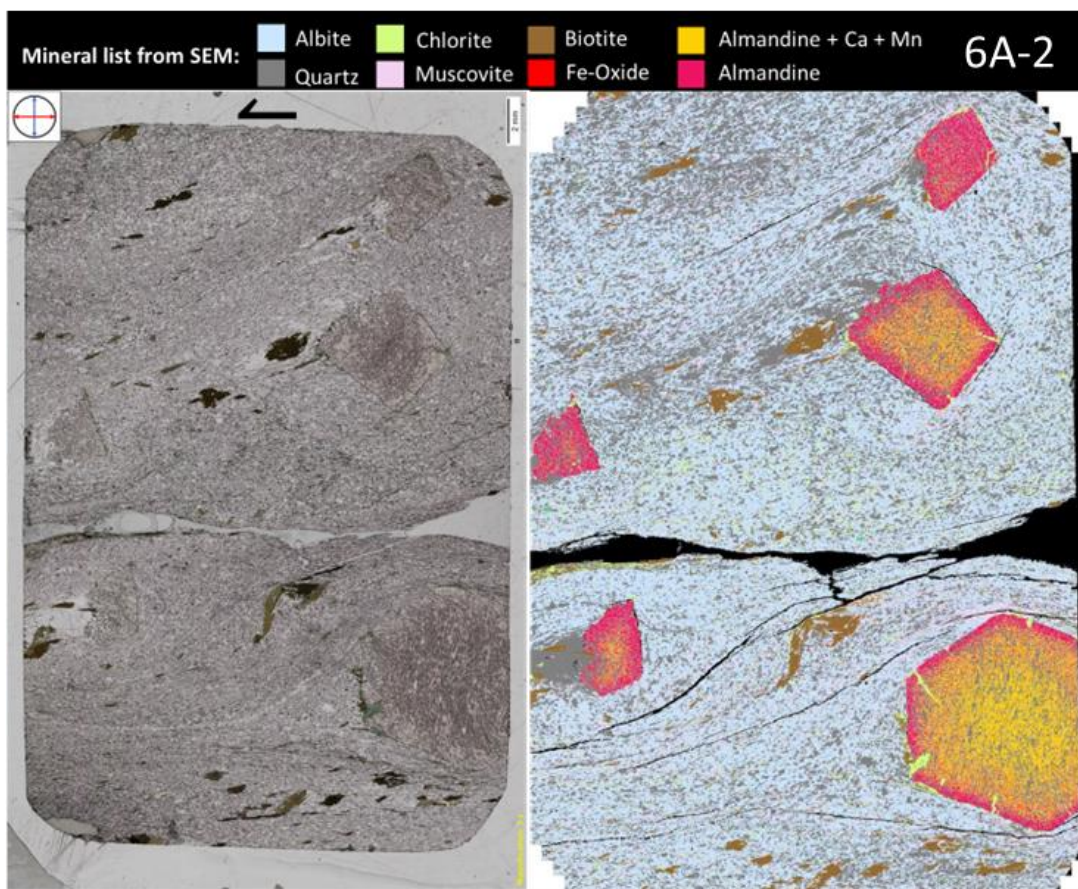
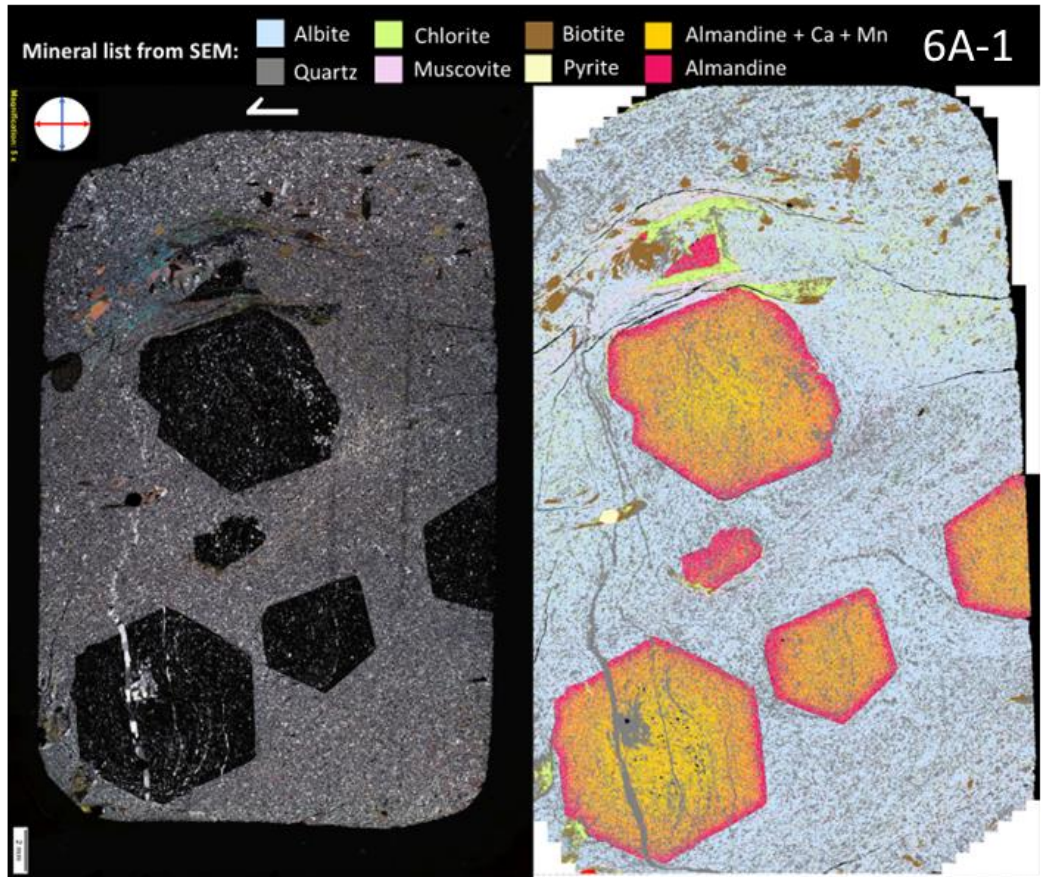


Figure 37: Mineral maps of garnet-biotite shear zone, where most garnets display a zonation with clear transition between the rim and core in the grains.

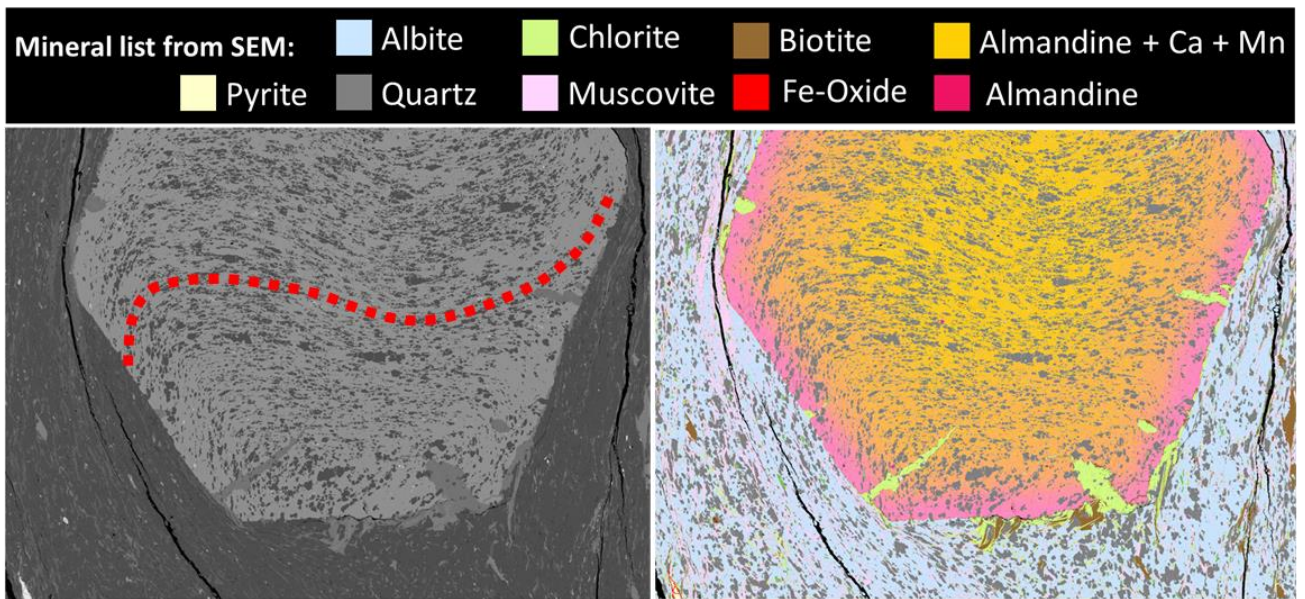


Figure 38: EBS-image and mineral map of 6A-2d. EBS-image has the S-shape drawn on to it, which shows the snowball garnet structure.

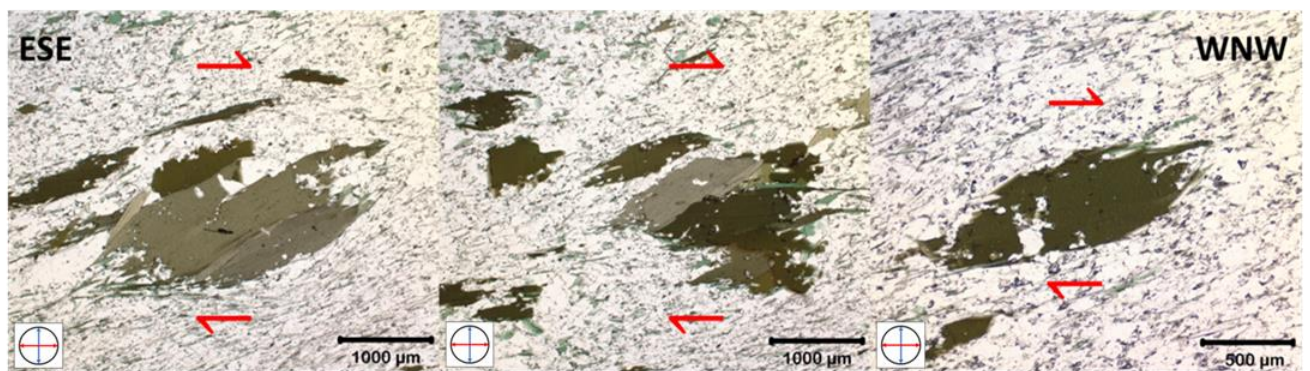


Figure 39: Kinematic indicators of biotite mica fishes with dextral shear sense with top to the WNW from thin section 6A-3.

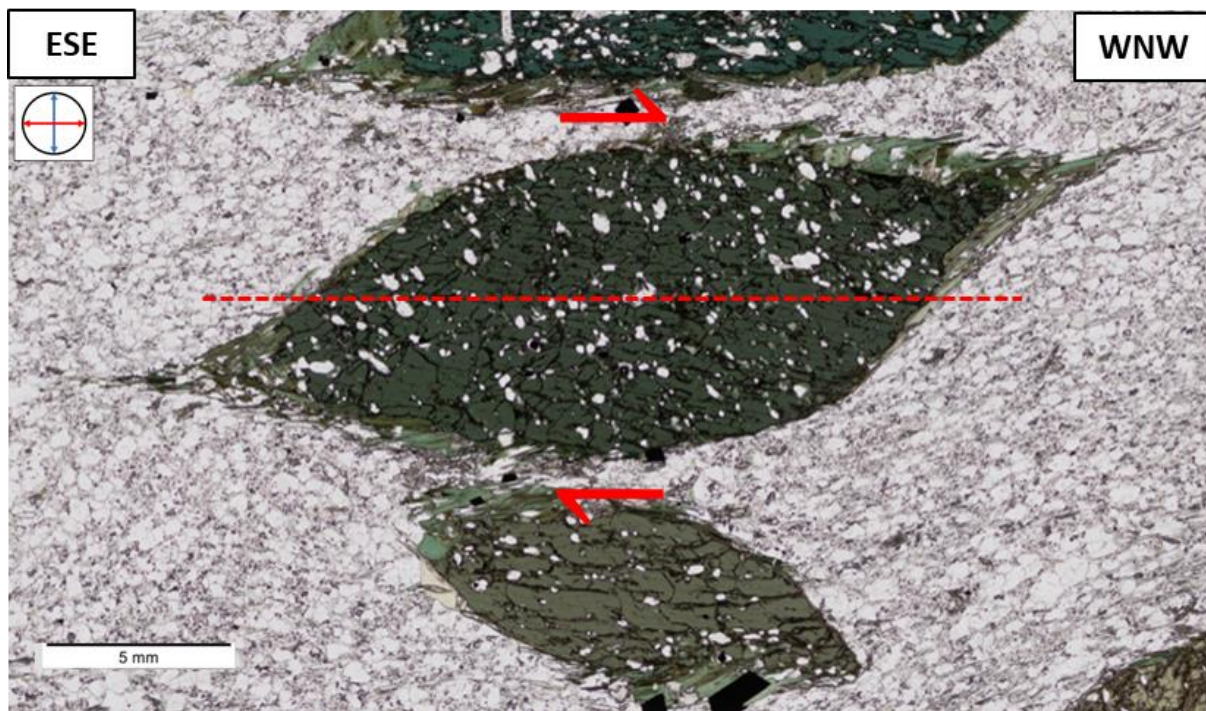


Figure 40: Hornblende grains from thin section 6A-3 displaying dextral shear sense, with top to the WNW.

5.2.5 Breccia zone

There are at least 3 phases found in the breccia that's distinguishable by textures and ratios in mineral assemblage. In most of the samples the dominant matrix is a mix of albite and quartz, which appears bright in colour in both PPL and at a macro level. As shown in Figure 41 the dark breccia clasts and infill is not the same lithology as the larger bright clast with the garnet in the hand specimen. The darker breccia in PPL consists mainly of larger albite clasts with few quartz inclusions, between the fragments there is an infill of quartz and chlorite that follows the fractures in the rock (Figure 42). All thin sections from the breccia share the feature of containing chlorite that have filled in fractures. There is also a high abundance of magnetite that is concentrated together with this chlorite which has a masked blue/violet interference colour (Figure 43). The breccia appears to be clast-born, especially in the darker and most fragmented lithology. These fractures do go into the lighter breccia but is cut a younger vein. The paragenesis of this vein consists of quartz, calcite, dolomite, muscovite, and Chlorite, and similar veins appears in other thin section such as 5A-1 and 5C. It can also be seen in that there are new phases within the breccia in Figure 44. Carbonates appears in the matrix with no other significant indication of change in the facies. The occurrence of carbonates is suspected to be the reasoning of the red-brown tint seen in the outcrop at a macro level. In Figure 45 there is a garnet grain which do not have a zonation in it. According to the EDS-map the dominant mineral is standard almandine, but there are cells that have been classified as Mn- and Ca enriched almandine mixed into the grain. However, what the EDS do not show but can be seen in the thin section of 5C is that there is a depletion halo around the garnet.

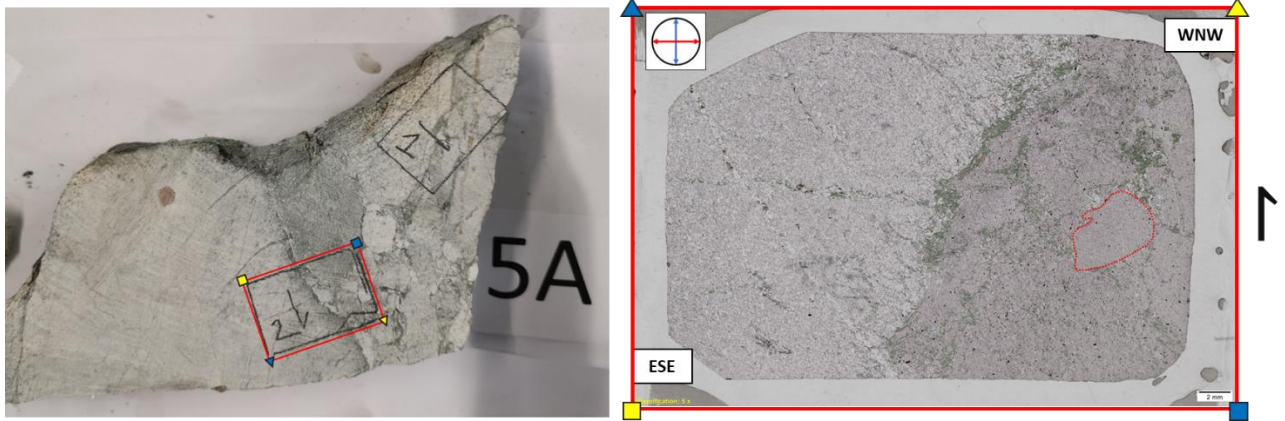


Figure 41: Comparison of hand specimen and the produced thin section. The breccia clasts appear darker and consists mostly of albite and is supported by other clasts. Chlorite and quartz have filled in the fractures. It can also be seen that the brown veins that contains carbonates penetrate both the large bright rhyodacite and the breccia clasts. The red line within the thin section traces the perimeter for one of these clasts.

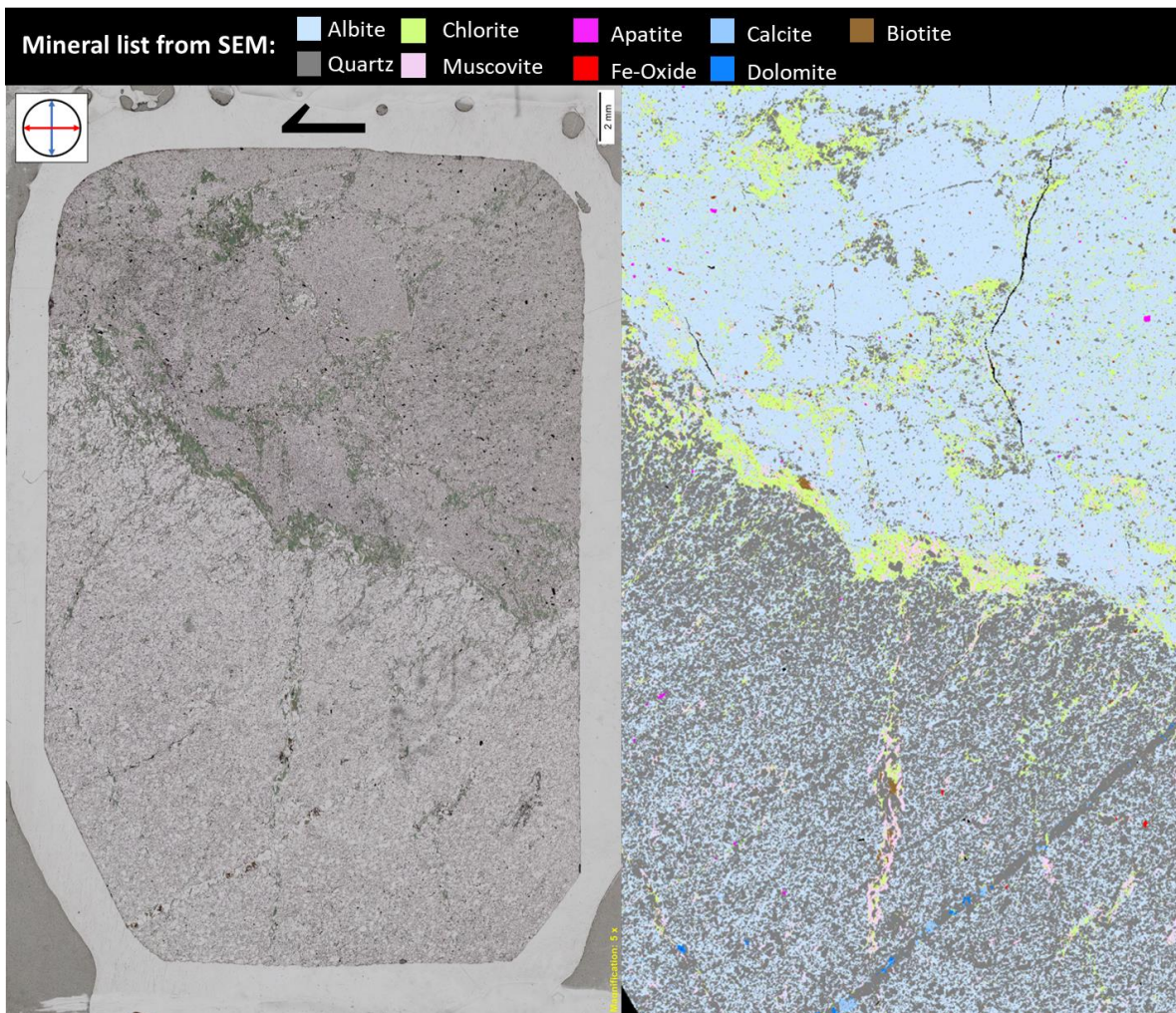


Figure 42: Thin section 5A-2 with its the mineral map showing the two phases. Massive chloritization along the border of the two phases, otherwise chlorite seems to be filling in cavities in the rock.

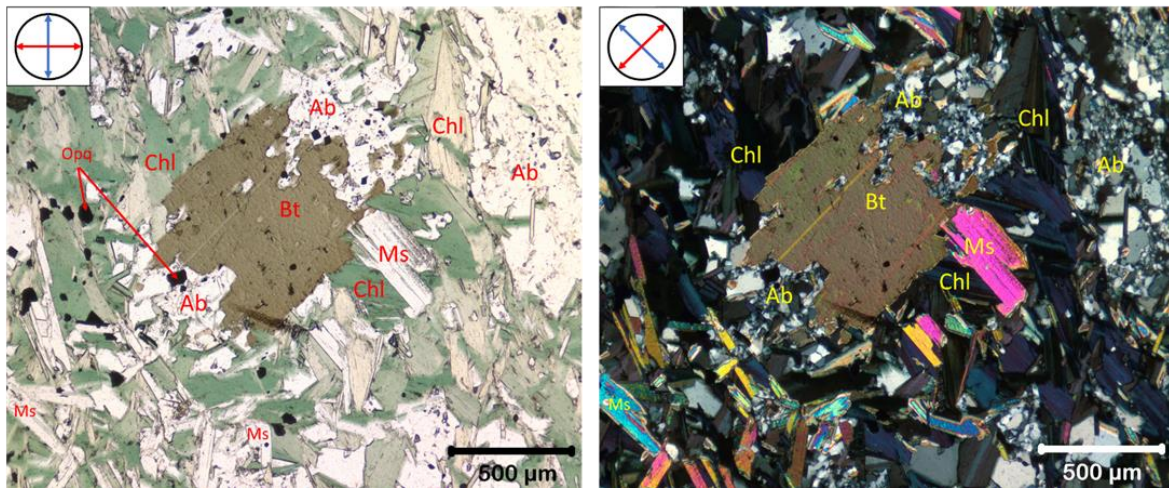


Figure 43: From thin section 4A-1, shows chlorite with dark blue masked interference colour.

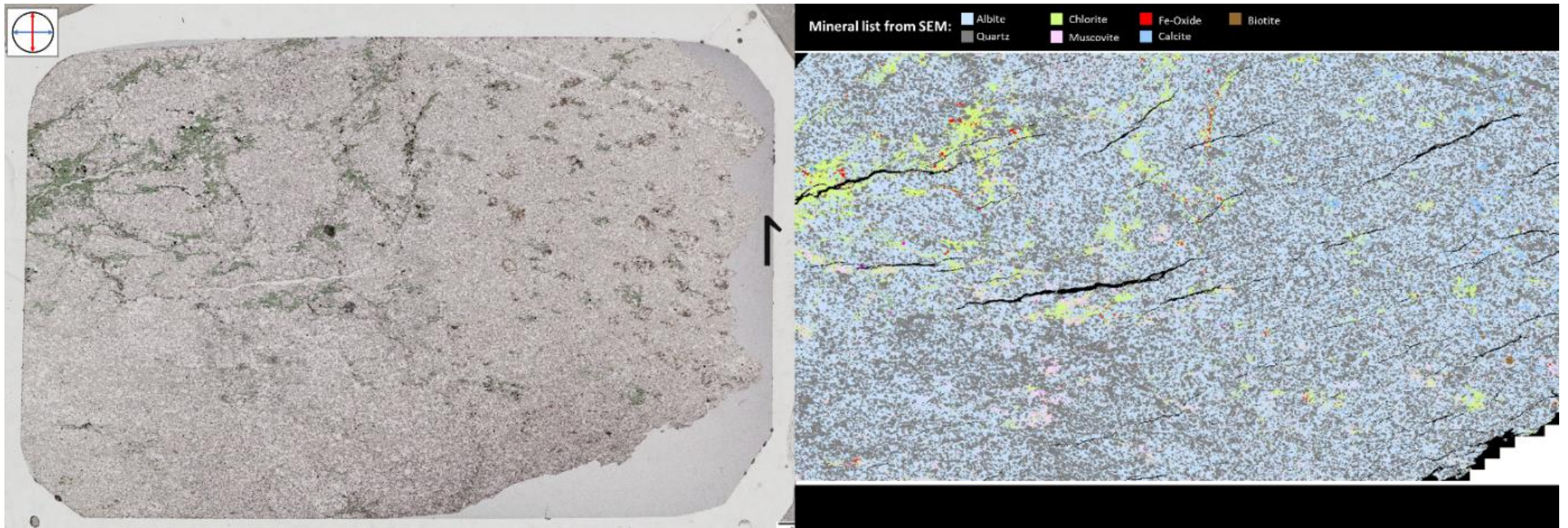


Figure 44: Two phases in the breccia from thin section 4A-1. On the left side there is more common breccia with a lot of fractures with chlorite and magnetite infill. Whereas of the right side the occurrence of carbonates scattered into the quartz and albite matrix.

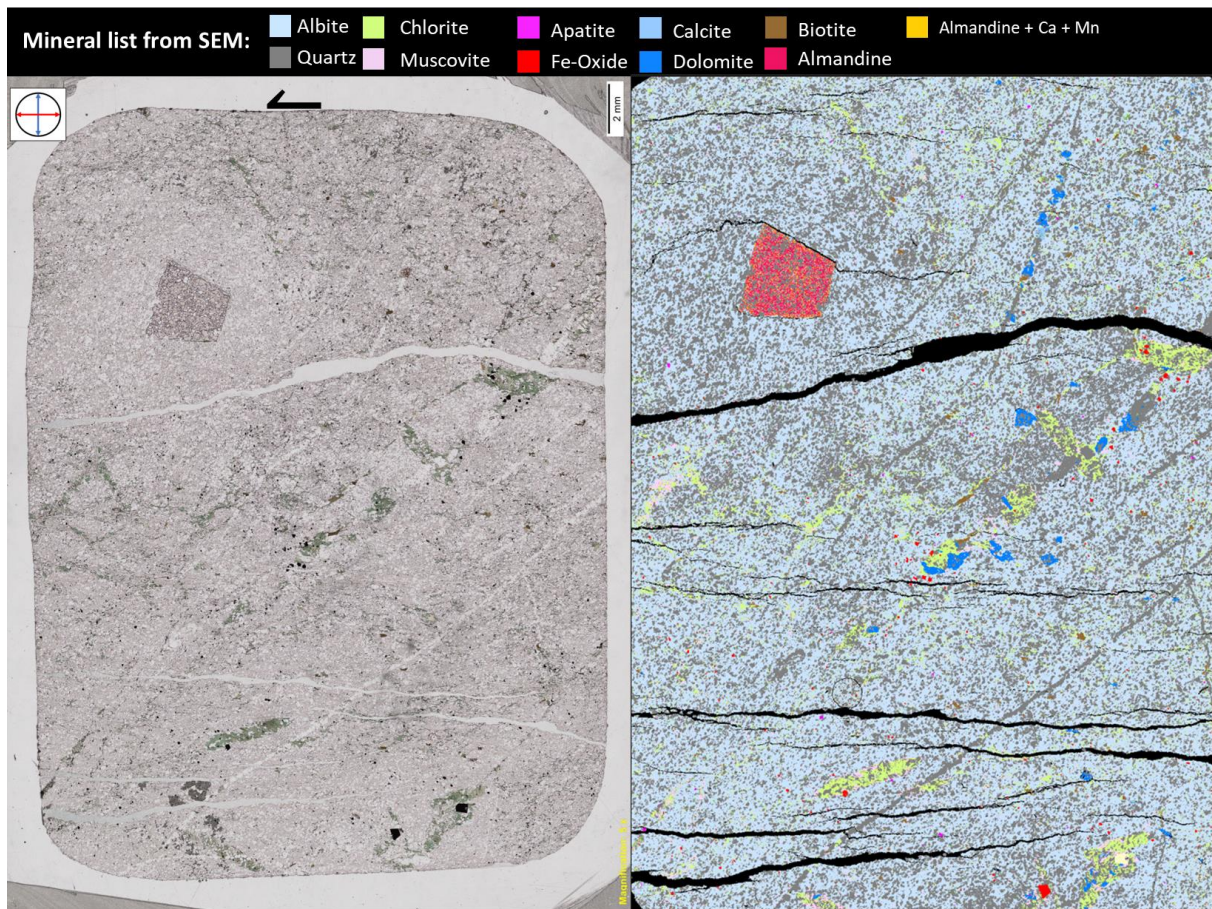


Figure 45: Thin section 5C showing several veins of mainly quartz, dolomite, and calcite penetrating the sample. In the PPL-image there can be seen a depletion halo surrounding the garnet.

5.3 3D-model

The accuracy of georeferenced sample locations is reliable and was determined by reconstructing higher resolution 3D-models from the photographs taken with a Nikon D3200. Control points have been self-identified and are based on easily recognisable points in both the main 3D-model and photos taken with the handheld camera. From the main 3D-model the coordinates for the CPs were determined, thereafter the sampling locations was found by using the coordinates in the new 3D-models. This can lead to a lower accuracy of georeferencing but shouldn't be significant. A reasonable assumption is an offset of ± 5 cm in the cartesian coordinate system, depending on the quality of triangulation between the three control points.

The general dip direction of the bedding at Klemetsaunet is shown in Figure 46, which is the 3D-model with all field observations from StraboSpot attached to it. The rhyodacite and mafic dikes falls towards Northwest with a dip of $14.7-28^\circ$, whereas the Byneset Trondhjemite which has an apparent dip-direction towards the Southeast with a dip of $54.7-75.2^\circ$. Most structure measurements were gathered in the field, except for some that was extracted from the 3D-model to supplement. The photogrammetric 3D-models of all sampling location can be found in Appendix A, while a cross-section of a plausible lithological model is shown in Figure 47.

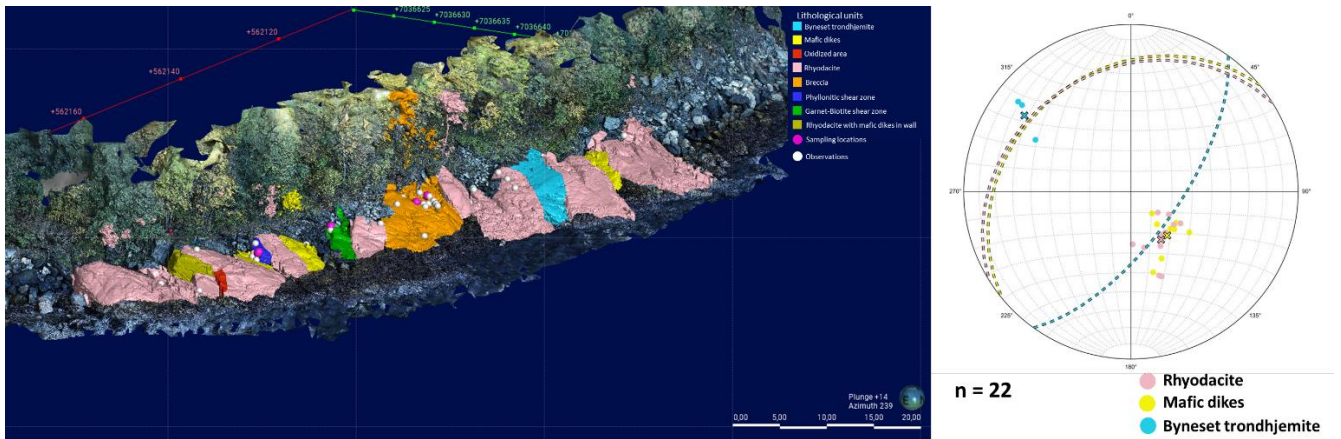


Figure 46: 3D-map of the mapped outcrop at Klemetsaunet with its lithologies, sampling locations, observation points, and a stereonet added to it. Scale units in meters.

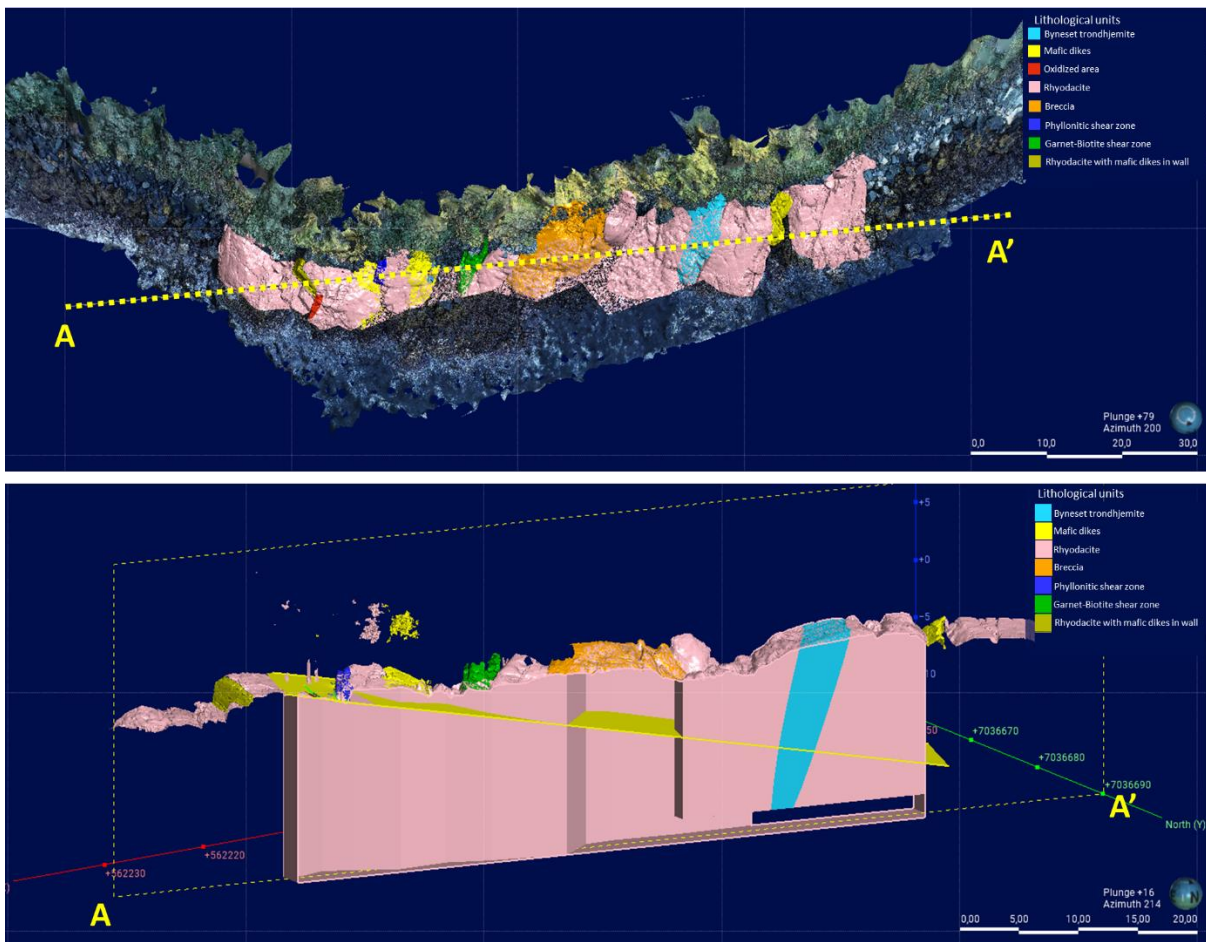


Figure 47: Cross section of the simplified geological model of Klemetsaunet, where one mafic dike has been extended. In this example the mafic dikes have been classified to be younger than the Byneset trondhjemite, even though there are no evidence for this.

5.4 Mineral chemistry

Mineral chemistry plays a crucial role in comprehending the formation and evolution of rocks in many aspects. By utilizing geochemical data it's possible to determine the petrological evolution, estimate undergone geodynamic processes, and effectively classify rocks. What will be presented in this chapter is:

- Heatmaps to uncover element distribution and association in minerals.
- Stoichiometry of minerals and classification.
- Apply element concentrations and stoichiometry to evaluate growth evolution.

Heatmaps were produced to visualize variations in the geochemical distribution within thin sections from the SEM-analysis. These heatmaps help identify specific minerals or textures based on element concentrations. Figure 48 the geochemical distribution of 2-2d1 shows some basic elements associated with the minerals included in that area. According to the EDS-maps the garnet is supposed to have a zonation from core to its rim. It comes forth that the zonation stems from elevated concentrations of Mn and Fe in the core and decreases towards the grain boundary. Notably is that magnetite, epidote, and chlorite is more enriched in Fe than the garnet, but the threshold is only up to 35 wt. % so magnetite grains are not shown. The Fe-content helps identifying chlorite as inclusions and surrounding the garnet grain. Especially when looking at the Mg-content, which mainly resides in the chlorite. With the two Ca-heatmaps it is possible to see that the garnet has up to 8 wt. % Ca, while epidote exceeds this amount with concentrations of 20-25 wt. %. Albite is the dominant holder of Na at 8-11 wt. %, whereas muscovite is the primary holder of K. These heatmaps makes it easier to distinguish where the mentioned minerals are situated in the EDS-map. As for the detailed EDS-map of a typical foliated area in thin section 2-2 (2-2d2), the heatmaps Figure 49 serve for the same purpose. Likewise, Na mainly resides in albite, K in muscovite and Ca in epidote. The highest Fe-values can be seen in the Fe-oxides, which are magnetite grains, then biotite has the subsequent highest concentration of Fe, then chlorite and the least amount resides in the epidote. The more detailed Mn-heatmap of 6A-2d shows how the zonation pattern transitions in a garnet from the garnet-biotite shear zone. The core has an average Mn concentration of 6.04 wt. %, compared to the rim of the garnets, where it lies around 2.57 wt. % until Mn is fully depleted at the edges of the rim. The lack of Mn in any other minerals makes the heatmap ideal for identifying inclusions and tracing the sigmoidal S-shape of the snowball garnet. This can also be seen in both Figure 50 and Table 10, where data from Appendix J have been used to calculate the stoichiometric formula for garnets found in shear zone been calculated. The stoichiometry of garnet is based on the general formula for garnet which can be expressed as $X_3Y_2(SiO_4)_3$. Ca^{2+} , Mn^{2+} , Mg^{+} , and Fe^{2+} typically occupies the X site, whereas Al^{3+} , Fe^{3+} , and Cr^{3+} fits into the Y site. Based on the ternary diagram (Figure 51), In Figure 51 the stoichiometric data of garnet has been applied to classify it, which yield that both the rim and core of garnets from the garnet-biotite shear zone classifies as almandine. The main segregating factor between the rim and core appears to be that the core is more enriched in Mn^{2+} , while the rims have a slither enrichment in Fe^{2+} . The rim shows a migration towards the spessartine field, while still falling within the almandine class.

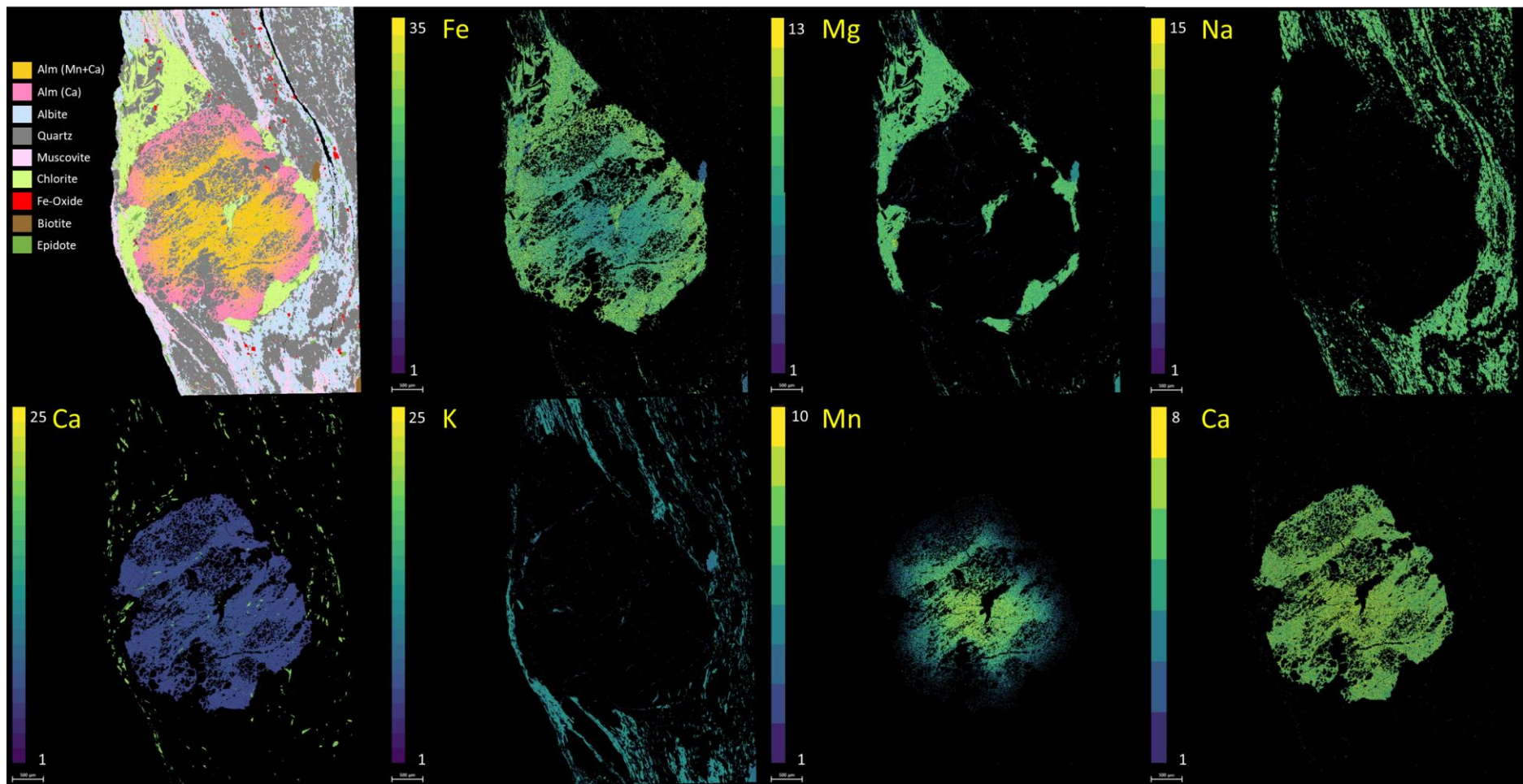


Figure 48: Heatmaps of detailed map of garnet in the phyllonitic shear zone (2-2d1) from SEM-analysis. The scale bar for element content in each heatmap is given as weight percentage. There was produced two heatmaps for Ca, the one with the lowest range was meant for detecting variation within the garnet.

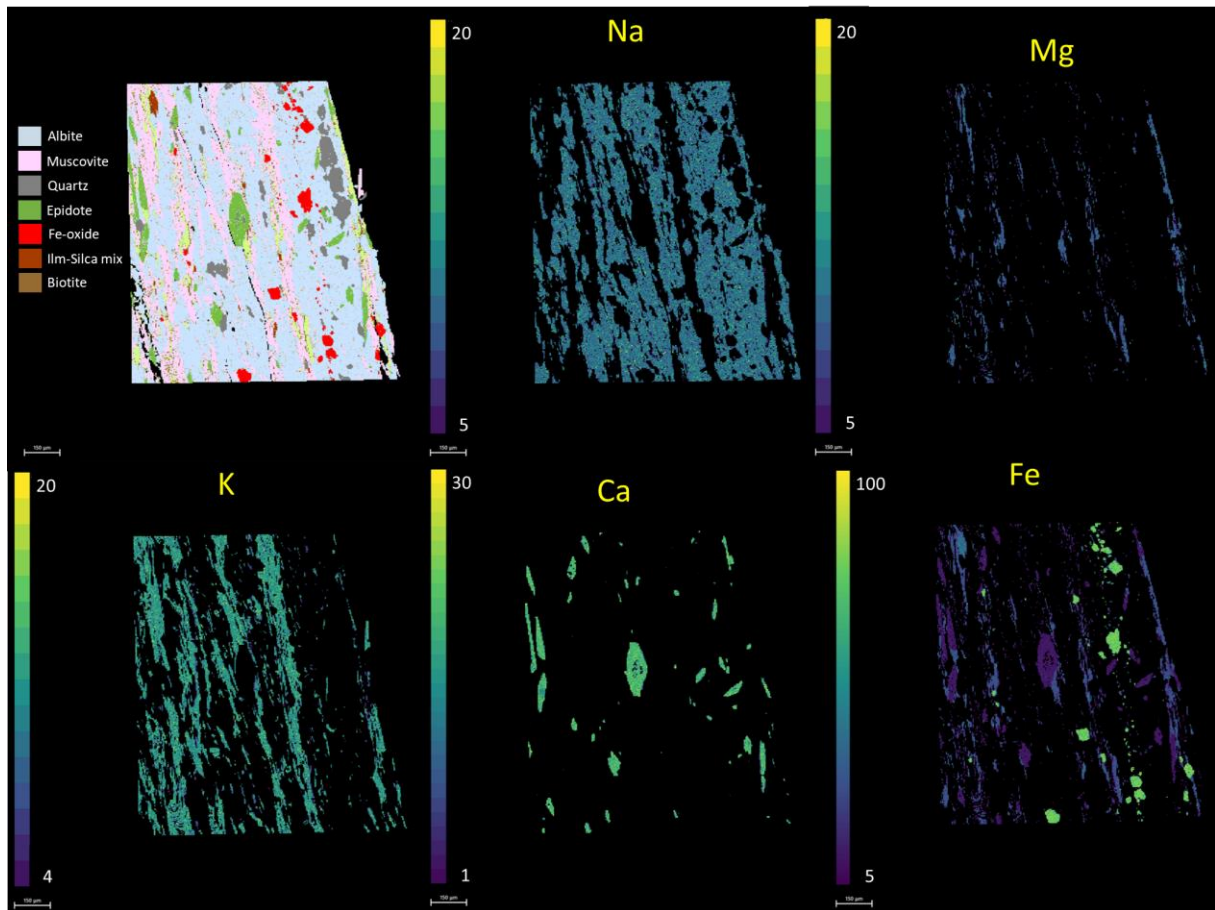


Figure 49: Heatmaps of detailed map of foliated matrix with mica bands (2-2d2) from SEM-analysis. The scale bar for element content in each heatmap is given as weight percentage. The maps represent foliated areas in sample 2.

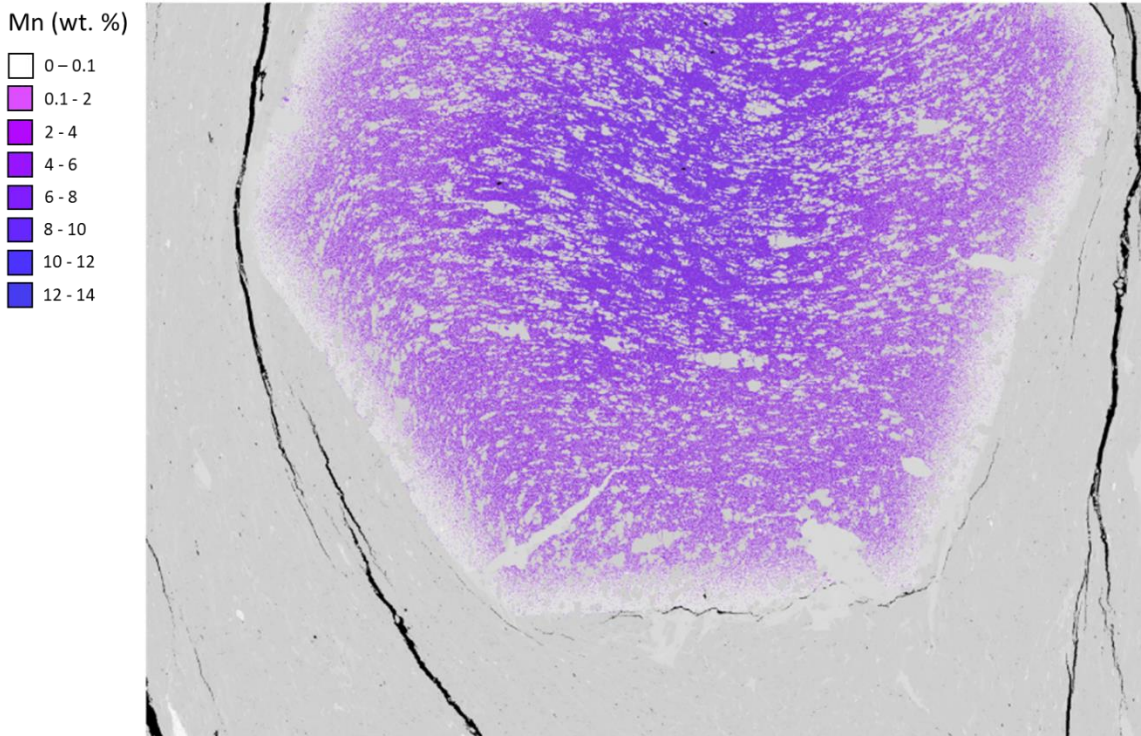


Figure 50: Heatmap of 6A-2d with its concentration of Mn. There is a gradual decrease in Mn from the core to the edges of the garnet and the lack of Mn in the inclusions shows the snowball structure well.

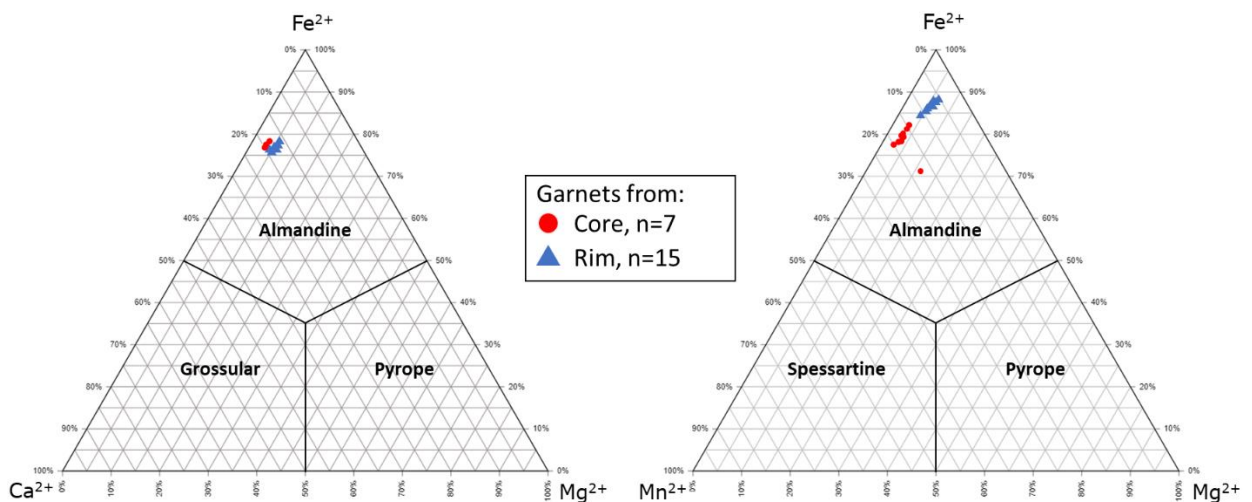


Figure 51: Ternary garnet diagram based on the mineral chemistry from the EPMA-analysis. Garnet samples from the garnet-biotite shear zone classifies as almandine, with only noticeable differences in the Mn^{2+} concentration between rim and core.

Generally, datapoints from the microprobe analysis that contained bad results were removed from to avoid staining the interpretation. The reasoning for bad data might be poor focus with the crosshair when determining the Z-height of surface mineral with the Point Logger. Other scenarios can be to misinterpretation of minerals when classifying them with the Point Logger, or inclusions within a grain being included in the measured point. Therefore, all datapoints (188) that has a sum of total weight percentage within the threshold 100.0 ± 2.5 Wt. % were the only ones that were included. To ensure correct estimation of cations for a mineral formula all elements' number of cations were

multiplied with their value of ionic charge. This sum should then be equal to the number of anions multiplied with oxygen's ionic charge of two negative. If these sums are equal, then the stoichiometry of a mineral should be adequate.

Table 10: Average mineral formulas of minerals for each thin section analysed with EPMA.

Mineral	Sample	Stoichiometry
Garnet, Rim	6A-2	$(Ca_{0.48}Fe_{2.10}Mg_{0.14}Mn_{0.17})(Al_{2.32})(Si_{2.82})O_{12}$
Garnet, Core	6A-2	$(Ca_{0.48}Fe_{1.94}Mg_{0.08}Ti_{0.01}Mn_{0.39})(Al_{2.31})(Si_{2.81})O_{12}$
Albite	6A-2	$(K_{0.01}Na_{0.92}Ca_{0.01})(Al_{1.01}Si_{3.01})O_8$
Albite	5A-2	$(Na_{0.96})(Al_{1.01}Si_{3.00})O_8$
Albite	4A-1	$(Na_{0.94})(Al_{1.00}Si_{3.01})O_8$
Chlorite	6A-2	$(Mg_{1.92}Fe_{2.87}Mn_{0.03})(Al_{2.55}Si_{2.67})O_{10}(OH_{7.99}F_{0.01})$
Chlorite	5A-2	$(Mg_{1.93}Fe_{2.76}Mn_{0.02}Ti_{0.01})(Al_{2.66}Si_{2.65})O_{10}(OH_{7.97}F_{0.03})$
Chlorite	4A-1	$(Mg_{1.97}Fe_{2.82}Mn_{0.02})(Al_{2.66}Si_{2.60})O_{10}(OH_{7.98}F_{0.02})$
Muscovite	6A-2	$(Na_{0.17}K_{1.74})(Mg_{0.35}Fe_{0.62}Ba_{0.02}Ti_{0.02})(Al_{4.75}Si_{6.44})O_{20}(OH_{3.97}F_{0.03}Cl_{0.01})$
Muscovite	4A-1	$(Na_{0.24}K_{1.70})(Mg_{0.31}Fe_{0.58}Ba_{0.01}Ti_{0.02})(Al_{4.83}Si_{6.42})O_{20}(OH_{3.93}F_{0.07})$
Biotite	6A-2	$(Na_{0.01}K_{0.94})(Mg_{0.95}Fe_{1.74}Mn_{0.01}Ba_{0.01}Ti_{0.09})(Al_{1.45}Si_{2.73})O_{10}(OH_{1.96}F_{0.04})$
Dolomite	5A-2	$Ca_{0.93}(Mg_{0.53}Fe_{0.50}Mn_{0.04})(CO_3)_2$
Dolomite	4A-1	$Ca_{0.95}(Mg_{0.48}Fe_{0.52}Mn_{0.04})(CO_3)_2$
Calcite	5A-2	$Ca_{1.73}(Mg_{0.08}Fe_{0.16}Mn_{0.02})(CO_3)_2$

To supplement the interpretation from the thin sections, XRD, and SEM, I calculated and plotted the composition of the plagioclase in Figure 52 based on the data from the microprobe analysis. From the previous analyses, I classified the plagioclase in the samples as albite and an intermediate state of albite from XRD. The EPMA data was used in a ternary diagram, but data with poor results had to be removed. This resulted in a sample size of 7 analysed points in thin section 6A-2, 10 points in 5A-2 and 3 in 4A-1. The results show that the feldspar in the analysed samples is relatively homogenous, and its composition mostly pure albite. Generally, the points gather around 98,6 – 99,4 % albite, apart from one outlier from 6A-2 which contains 97,2 % albite. To segregate the albite that is clustered together, it's possible to compare the ratio between orthoclase and anorthite. The samples from 6A-2 are slightly more enriched in orthoclase compared to 5A-2 which are more even in the ratio between orthoclase and anorthite. These are subtle differences that might be insignificant due to the limiting number of analysed points. As for 4A-1 there is a spread where it plots, but it's not responsible to draw any pattern from these values. The same was done for chlorite, but according to Hey (1954) in Figure 53 were all samples classified as ripidolite. Which is a hybrid between the endmembers clinocllore and chamosite. This ripidolite is a ferroan variety which will result in a violet or blue interference colour instead of a brown interference colour which is typical for Mg-rich chlorites (Howie et al., 1992).

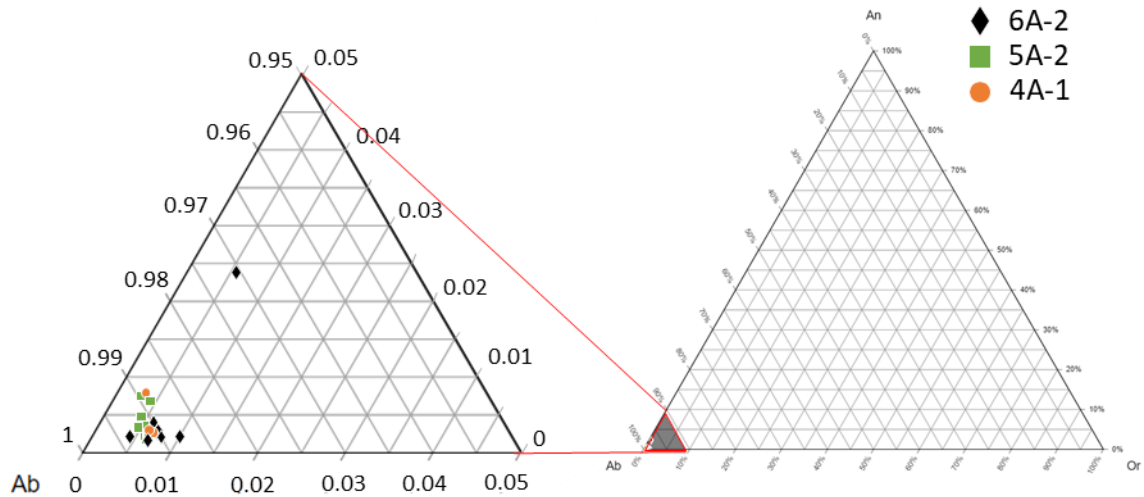


Figure 52: Ternary feldspar diagram based on the mineral chemistry from the EPMA-analysis. The calculation of the feldspar ratios was done with a spreadsheet from Science Education Resource Center (2009).

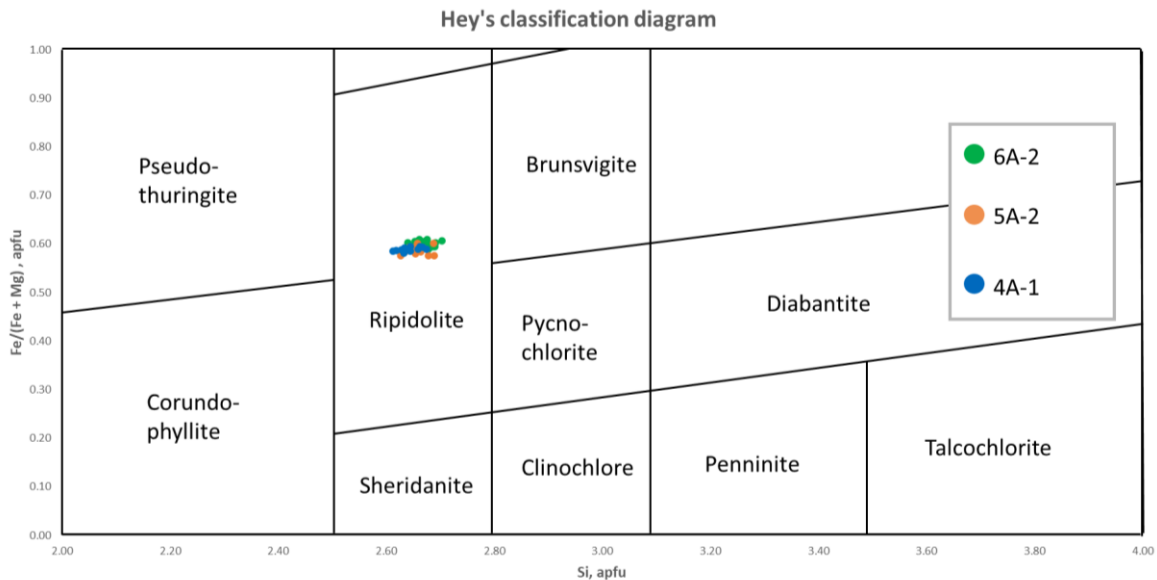
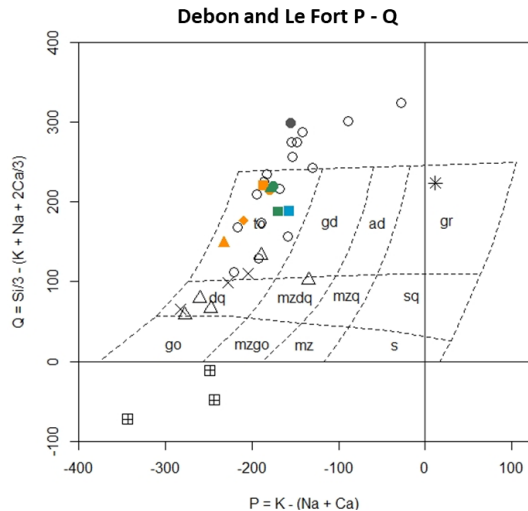
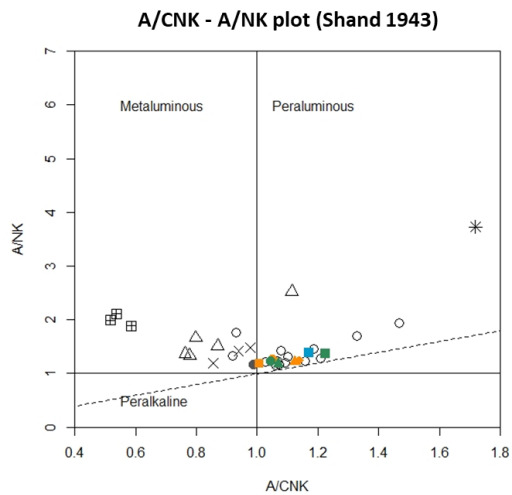


Figure 53: Classification of chlorite normalised to 18 oxygen according to diagram by Hey (1954). All samples from microprobe analysis fit into the ripidolite field.

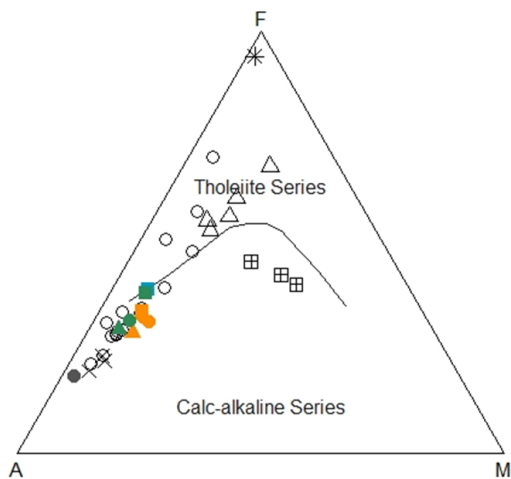
5.5 Whole-rock geochemistry

In this chapter all graphs have been based on geochemical data provided from XRF-analyses and ICP-MS. According to the classification diagrams in Figure 54 most of the felsic samples plots into the rhyolite field in the TAS (Middlemost 1994)-diagram due to the high SiO₂ content. In the feldspar triangle diagram by O'Connor 1965 uses the ratios between albite, orthoclase and anorthite. Where the dominant classification for the felsic rocks is within the quartz keratophyre field, which stems from the high albite content. Both the protolith and Byneset trondhjemite are similar in some respects such as being metaluminous and the most evolved based of the AFM-diagram. Which is implied by the high content of K₂O + Na₂O (A-corner) follow the calc-alkaline series and that the magmas are oxidized. Whereas the mafic dikes are the most primitive, which is reflected in the high MgO content, Plotting at starting point to the reference line relating to basaltic magmas

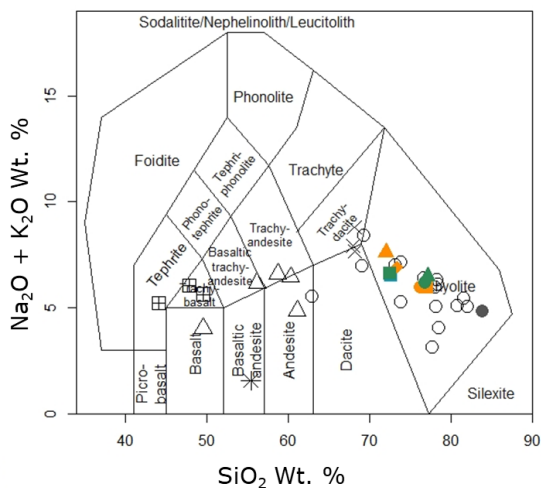
(Osborn, 1959, Rollinson et al., 2021). In contrast the breccia and shear zones are peraluminous and plots further away from the protolith due to a greater amount of Fe, but still following the same series. My samples in the Jensen (1976)-diagram plots between the rhyolite and dacite field still following the calc-alkaline series. The rhyodacite samples taken from the wall with mafic dikes in it, has a higher abundance of $Fe_{total} + TiO_2$. Resulting in them fitting into the andesite field in the tholeiitic series. In the Debon and Le Dort P-Q diagram the protolith and many rhyodacite samples from the external dataset plots outside the classification diagram. While the breccia and shear zones fit inside the tonalite/trondhjemite (to) field. This tells that the protolith does not correlate with one of the subdivision of cafemic and alumino-cafemic magmatic associations (Debon and Le Fort, 1988). The Byneset trondhjemites' classifies as both tonalite/trondhjemite, but as well into the quartz diorite/gabbro field.



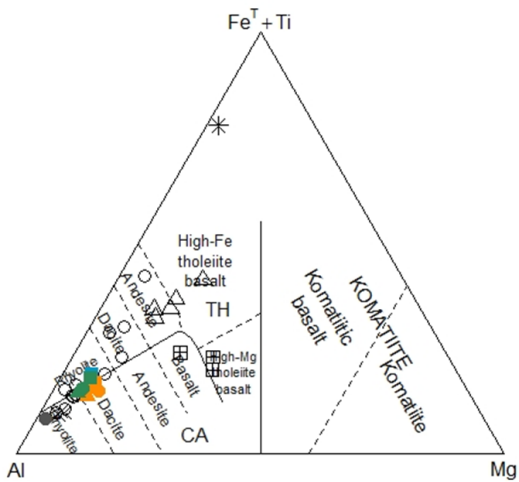
AFM plot (Irvine and Baragar 1971)



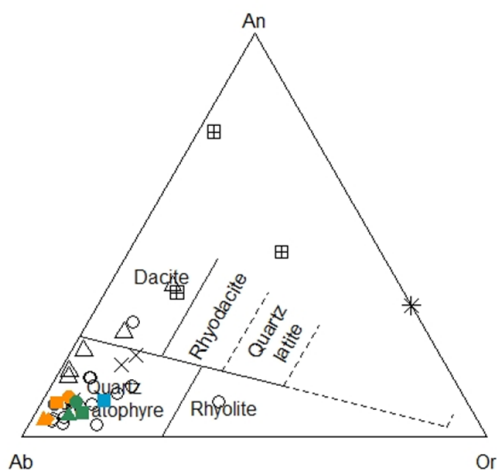
TAS (Middlemost 1994)



Jensen (1976)



CIPW-normative feldspar triangle (O'Connor 1965)



- | | | | |
|------------------------|---------------|---------------|------------|
| External data | Shear zone | Breccia | Rhyodacite |
| ○ Rhyodacite | ■ Sample 2 | ■ Sample 4A | ● Sample 3 |
| △ Mafic dike from wall | ■ Sample 6A-A | ○ Sample 5A-A | |
| □ Mafic dike | ● Sample 6A-B | △ Sample 5A-B | |
| × Byneset Trondhjemite | ▲ Sample 6A-C | ◇ Sample 5C | |
| * Pyrite zone | | | |

Figure 54: Classification diagrams of fine-grained volcanic rocks for lithologies, magmatic evolution, and melts' originating source.

From the discrimination diagrams in Figure 55 K_2O have been used as a standard for comparing changes in trace element content. Since K_2O is recognized as a proxy for valuating element behaviour in a hydrous environment (Marumo et al., 2003). Based on the K_2O content the breccia plots closest to the protolith in most of the variation diagrams. Then follows the garnet-biotite shear zone and finally the phyllonitic shear zone with the greatest amount of K_2O . It occurs that the protolith is relatively poor in all trace elements, except for CO, compared to my samples. Typically, the garnet-biotite shear zone usually has a greater concentration of trace elements than the breccia, whereas the phyllonitic shear zone exceeds the abundance of trace elements of the garnet-biotite shear zone. There is a clear positive trend for Rb, Nb, Ba, and V, extending from the protolith up to the phyllonitic shear, which indicates mobilisation of these elements. For Sn, Zn, and Ga there is a jump between the protolith and all my other samples. The trace elements content is low for the protolith, but Ga and Sn doubles in amount for the rest of the samples where they almost have a flat trend among themselves. As for Zn the difference between the protolith and the rest is at least a hundred times greater, with a negative trend between the breccias and shear zones. Figure 56 was made to see if element mobilisation was represented, which would be reflected in the scattering of datapoints. Thus, suggesting that TiO_2 , Rb, or Sr are immobile, whereas K_2O and Ba are mobile in my samples.

In Figure 57 only my samples from ICP-MS have been compared with results from Slagstad (2003). It appears that my samples follow the same REE-pattern for as his data for Klemetsaunet. Generally, the chondrite normalised spider plots the abundance of LREE (Light Rare Earth Elements) increases with each element until Sm at the peak. Furthermore, there is a notable Eu-anomaly observed in the REE-pattern, indicating a significant decrease in concentration. This anomaly suggests the substitution of Ca^{2+} for Eu^{2+} in plagioclase. This substitution implies that the partial melt originated from deeper sources where pyroxenes may have crystallized, incorporating Eu^{2+} into their mineral composition (Shearer and Papike, 1989). Then the REE-pattern transitions into a relatively flat trend of HREE (Heavy Rare Earth Elements), which matches prior data of Klemetsaunet. Both spider plots and variation diagrams highlight the dispersion of my data points, revealing distinct patterns. Notably, the samples obtained from the breccia exhibit significant variations. Sample 5A-A consistently exhibits the lowest concentrations of both LREE and HREE, whereas sample 5A-B consistently shows the highest enrichments among all the samples. Sample 5A-A corresponds to thin section 5A-1, characterized by numerous carbonate and silica veins penetrating it, while 5A-B is associated with the highly fragmented dark facies observed in thin section 5A-2. In the NMORB normalised spider plots the trace elements associated with Large-ion lithophile elements (LILE) and High field strength elements (HFSE) are added. The peaks and troughs of the REE-pattern are like those of Slagstad's which gives a good correlation between the rhyodacites and Løkken's plagiogranite.

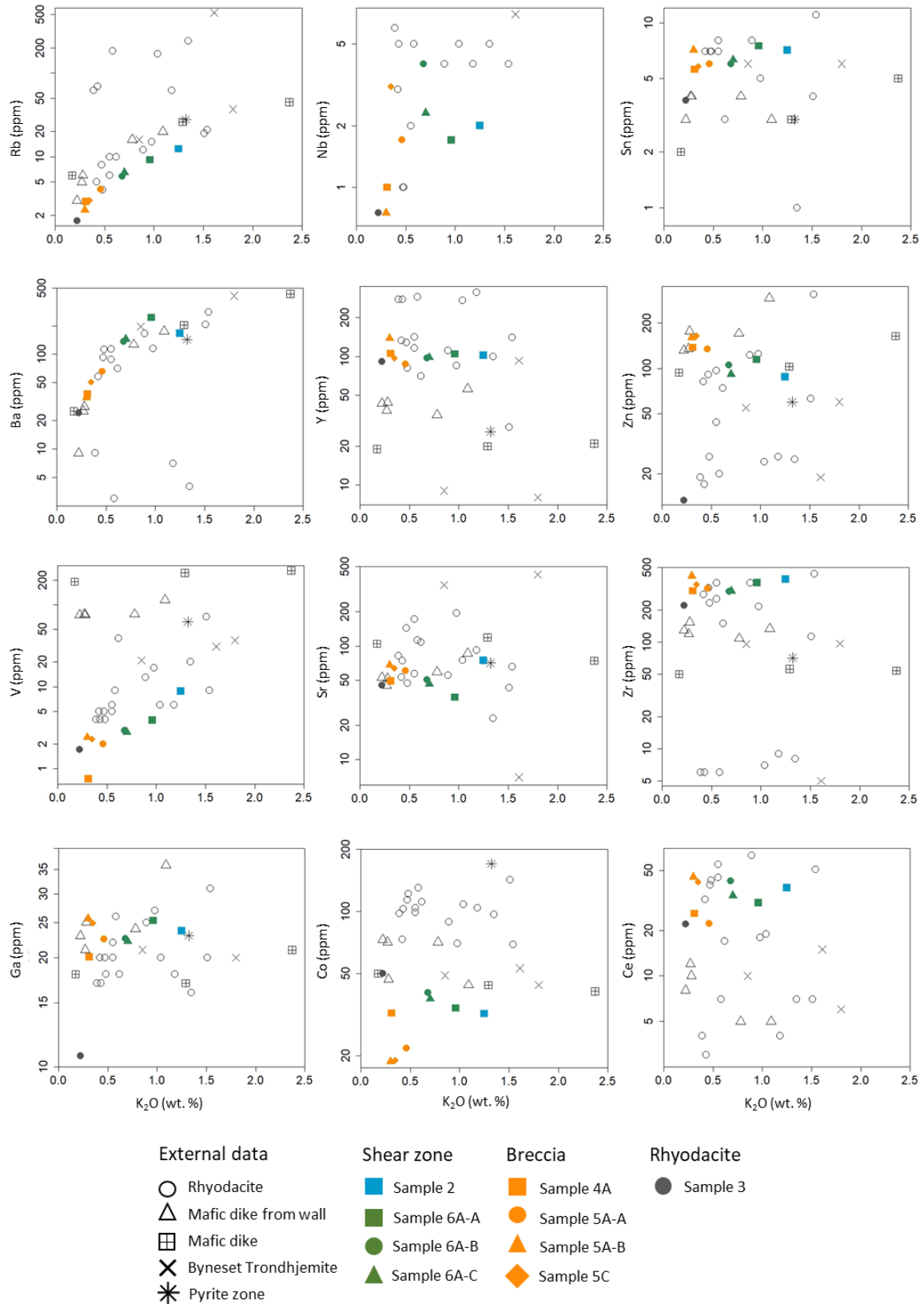


Figure 55: Variation diagrams for all geochemical data gained from XRF for both major- and trace elements. My own data is plotted with colours, while the data from the previous master's theses are displayed as black lines with a white filling.

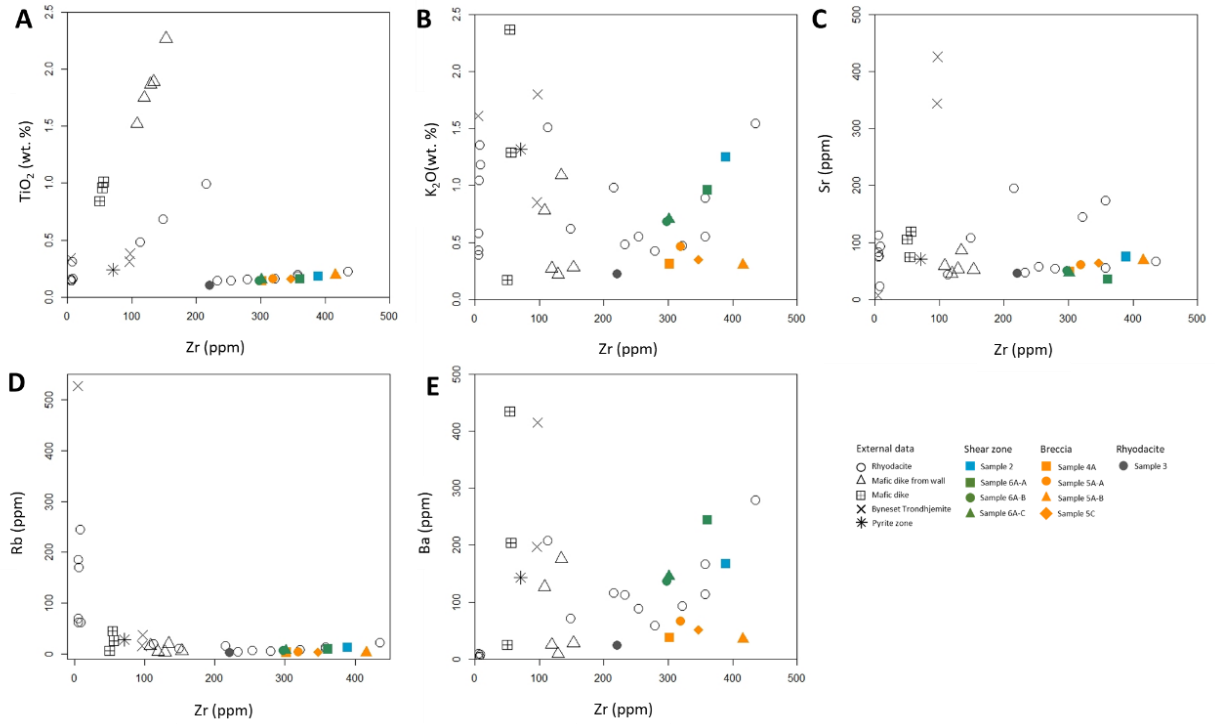


Figure 56: Variation diagrams A.) indicates that limited mobility of elements, since Zr and TiO₂ are used as a proxy and correlates well. B and E.) shows scattering which suggests mobility of these elements, while C and D.) does not, therefore Rb and Sr are immobile (Slagstad, 2003).

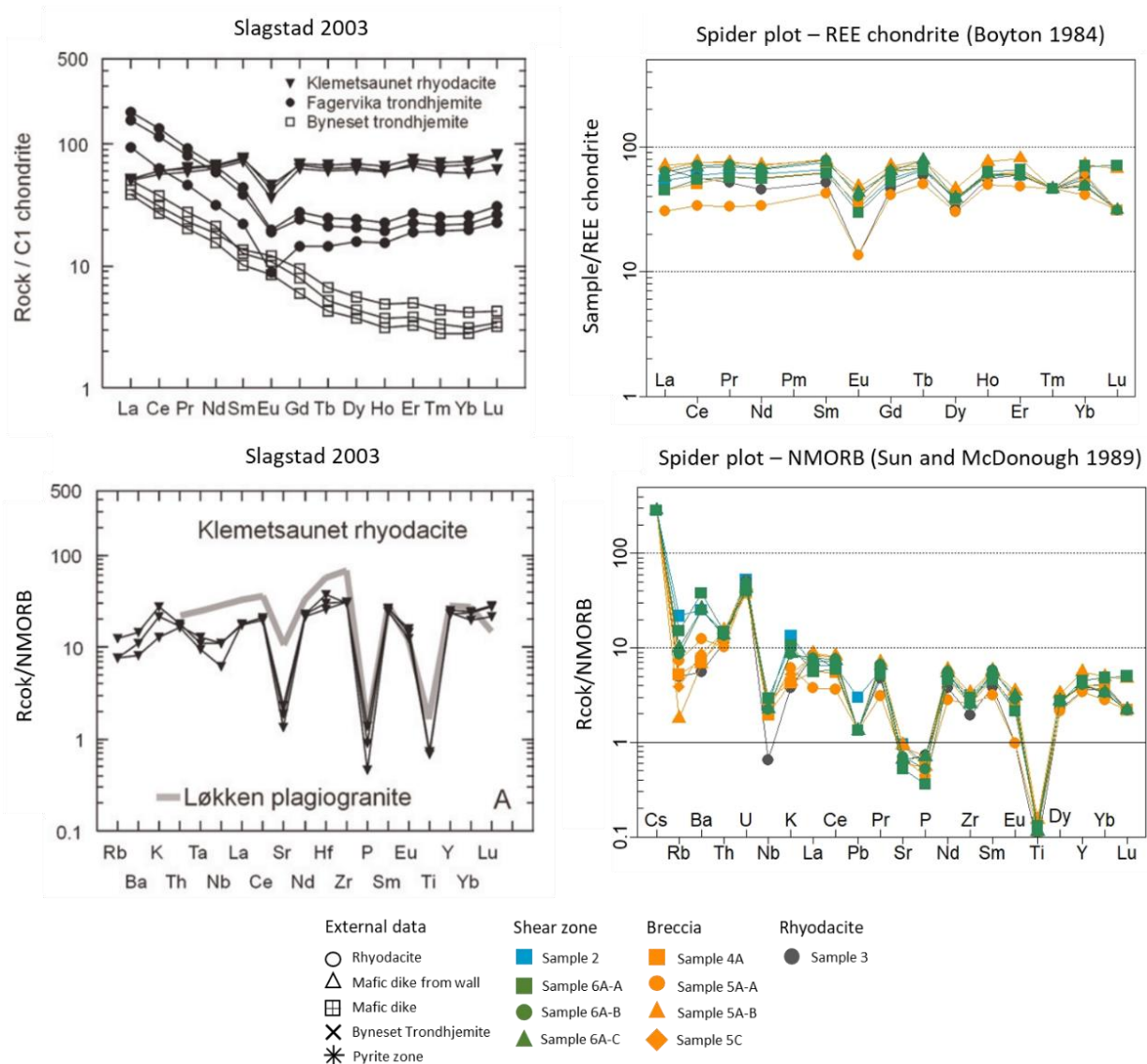


Figure 57: The two upper chondrite-normalised spider plots compare all three felsic intrusions in Bymarka, with my own data. Whereas the primitive mantle-normalised spider plots relate the plagiogranite of Løkken to the rhyodacite of Klemetsaunet. Beware that the order of elements in the X-axis of the NMORB spider plots are not equal.

5.6 Tectonic origin

The tectonic origin of the samples was determined by applying both major- and trace elements from XRF (Figure 58). The lower tectonic discrimination diagrams use abbreviations such as within plate granites (WPG), volcanic arc granites (VAG), collision granites (Syn-COLG), and ocean ridge granite (ORG). It can be observed from these diagrams that all my samples fall into the ORG category. The Byneset Trondhjemite samples, however, fit into the VAG field and VAG+Syn-COLG field. External data points show a wide range of variation in facies and mostly plot within the ORG, VAG, and Syn-COLG fields. The shear zones are indicated to be Fe-dominated (ferroan) or plots along the border, while all breccias are more Mg-rich (magnesian). The SiO₂ content of the protolith is too great to fit into discrimination diagrams by Frost and Frost. Other samples are scattered on both sides, except for those taken from the wall with mafic dikes, which are

categorized as ferroan. In terms of my samples, they exhibit a range from mainly calcic to alkalic-calcic compositions.

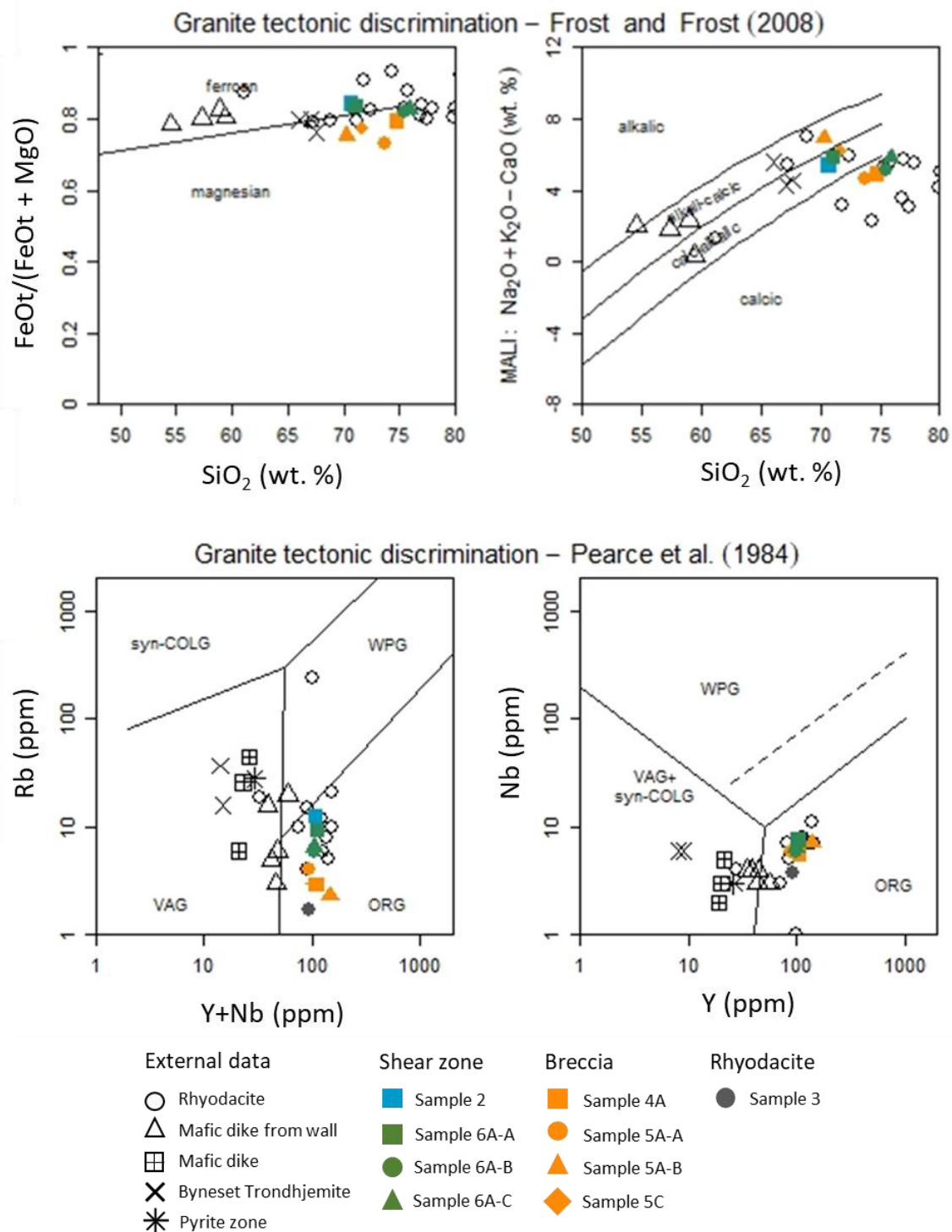


Figure 58: Tectonic discrimination diagrams for granitic rocks. The two upper diagrams, based on Frost and Frost (2008). Where the graph of the left side serves to distinguish between samples dominated by either Fe or Mg. On the right side, the diagram separates between alkalic and calcic controlled samples. The remaining two diagrams are based on Pearce, Harris et al.(1984) contributes to the classification of tectonic origin. While these diagrams share the same purpose, they employ different parameters.

5.7 P-T

To estimate the pressure and temperature conditions during the deformation of the rhyodacite, several analyses methods were applied. To do so the mineral chemistry from EPMA, mineral assemblages, and mineral textures observed in thin sections have been used to calculate and interpret the latest assumed deformation conditions. From the identified mineral assemblage within the thin sections, it is possible to find AFM diagrams from that fits the composition. These ternary graphs are used to represent the mineral assemblage in metamorphic facies and are mainly designed for pelitic rocks, but can still be applied (Spear and Cheney, 1989, Spear, 1993). To select plausible AFM-diagrams that fits the mineral assemblage it is necessary to assume that the minerals coexist at an equilibrium. If multiple diagrams fit a sample's mineral assemblage, then there will be a greater range of possible temperature and pressure for the metamorphic conditions. From Figure 59 the plausible P-T conditions ranges from slightly below 500°C at 1 kbar to 575°C at 9,5 kbar. The marked area indicates all plausible P-T conditions for the related mineral assemblage.

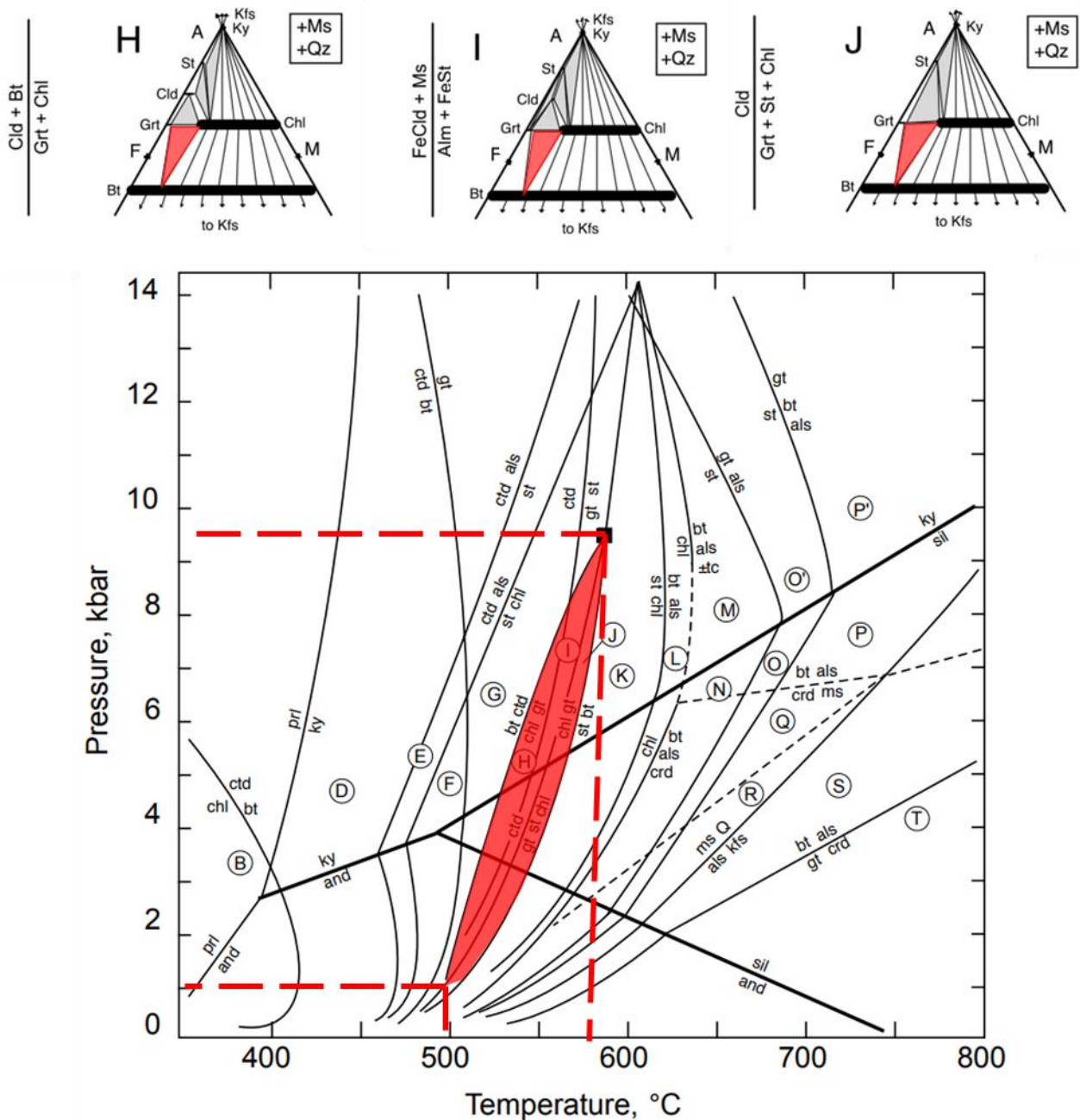


Figure 59: The three AFM-diagrams that fits the mineral assemblage concerns the co-existence of biotite, chlorite, and garnet at a stable equilibrium, with the P-T ranges plotted into the KFMASH-diagram (Spear and Cheney, 1989).

With the application of mineral chemistry, multiple geothermobarometers have been estimated. These estimates are calculated from microprobe data of chemical compositions in wt. % or stoichiometry by using Excel spreadsheets. The analysed samples stem from the garnet-biotite shear zone and the breccia therefore these estimates are only valid for these two segments. The used methods are:

- Biotite – muscovite thermobarometer (Wu, 2020).
- Chlorite thermometers (Cathelineau, 1988, Jowett, 2021).
- Garnet – biotite thermobarometer (Ferry and Spear, 1978).

The composition of chlorite can be used to estimate physical and chemical conditions under its formation. By looking at variations in the mineral chemistry of chlorite is dependent on parameters such as temperature, pressure, rock composition, fluid composition, and redox conditions (Xiao and Chen, 2020, Inoue et al., 2018, Vidal et al., 2001, Raza et al., 2021). From Raza et al. (2021) it's discussed several methods for estimating the formation temperature of chlorite. In Figure 60 the two methods I chose for estimating the formation temperature indicates that the chlorite crystallized between 365 – 393°C. The temperature ranges are lesser for the second shear zone. Since there is documented a chemical difference in the garnets' zonation from the stoichiometry. Data points for biotite were chosen from grains bordering or near garnets, while for the garnets themselves, only points within the rim were selected. It's likeable that there is a change in P-T conditions for the growth the garnets' core in contrast to the final growth of the rim. It must be assumed that the biotite and garnet rims formed under the same conditions for this estimate. The calculated temperatures were based on stoichiometry and an input for pressure conditions, where these pressures were inspired from the plausible conditions from the KFMASH-grid. Thus, resulting in a temperature range of 350-370°C, that is valid for pressures going from 1,5-9.5 kbar. A linear trend can be followed through these datapoints, making it possible to estimate other temperatures for pressure conditions exceeding or falling short to the used pressure. As for the temperature estimations for muscovite and biotite, they also were also calculated based on pressures from 1,5-9,5 kbar. Resulting in a temperature range of 506-571°C. All temperature and pressure estimates are summarised in Table 11.

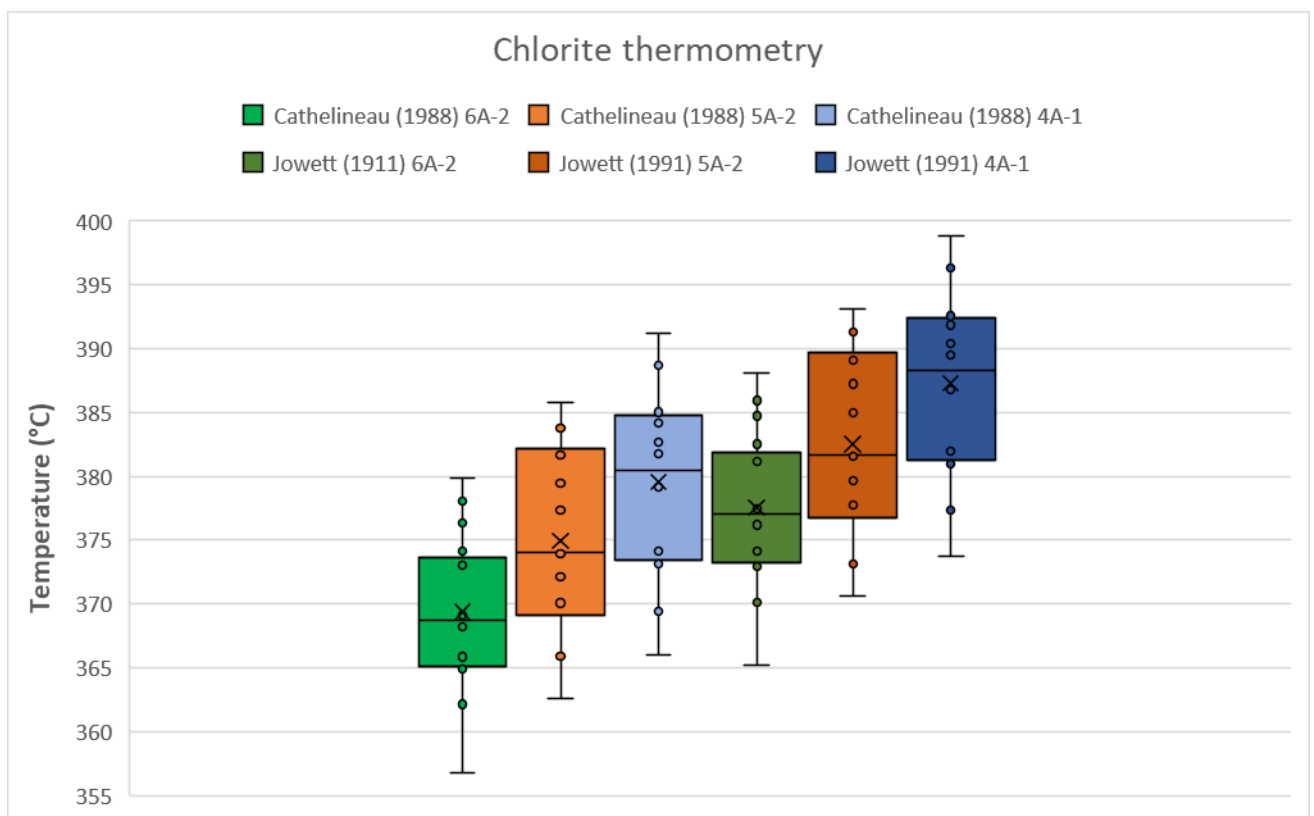


Figure 60: Boxplot of geothermometers that is constructed with microprobe data of chlorite from Ahmed (2014). Temperature estimates are based on Cathelineau (1988) & Jowett (2021). Sample 6A-2 relates to the garnet-biotite shear zone, while sample 4A-1 and 5A-2 relates to the breccia zone.

Table 11: Summary for the different methods used for estimating the P-T conditions.

Method	Source for method	Geothermometer	Geobarometer	Relevant areas
KFMASH-grid	Spear and Cheney (1989)	500-580°C	1-9.5 kbar	Phyllonitic- and garnet-biotite shear zone
GBM	Owona et al. (2013)	500-750°C		All
Biotite-Muscovite	Wu (2020)	506-571°C	1-9.5 kbar	Garnet-biotite shear zone
Garnet-Biotite	Ferry and Spear (1978)	350-370°C	1-9.5 kbar	Garnet-biotite shear zone
Chlorite	Cathelineau (1988)	365-385°C		Garnet-biotite shear zone & breccia zone
Chlorite	Jowett (2021)	373-393°C		Garnet-biotite shear zone & breccia zone

6 Discussion

6.1 3D-modelling, Data, and Alternative Methods

6.1.1 3D-modelling

The utilization of drone-based photogrammetry appears to be a suitable approach for the attempted 3D modelling of Klemetsaunet. Given the limited scale of the outcrop, obtaining a high-resolution representation using downloadable lidar data is unfeasible, thus rendering self-acquired data more advantageous. In retrospect, the intended level of resolution was not achieved despite manual drone flight and photography. The quality of resolution varied across different outcrops, with vegetation obstructing optimal angles for generating a more uniform 3D model. Consequently, the photogrammetric 3D model exhibited blurriness in areas such as the phyllonitic shear zone. Therefore, it was necessary to resort to photographing the outcrop using a handheld camera.

To enhance the 3D model, capturing photographs at a closer distance using the drone could potentially improve the resolution. In my subjective opinion, a distance of 5 meters would be recommended for areas of importance. However, it should be noted that this approach would significantly increase the amount of data for the software to process and handle. However, the post-processing of the data was limited to the creation of an early-stage database containing the field data, with further processing yet to be conducted. Figure 47 presents a simplified cross section of Klemetsaunet, which serves as an approximation rather than an accurate representation. The model's simplicity is due to limited data. Given the constraints of limited access to the outcrop and the absence of observed cross-cutting relationships between the mafic dikes and the Byneset trondhjemite, determining the relative age of the layers remains speculative. To address this challenge, suitable options for further refinement can be achieved with geophysical modelling and borehole investigations.

6.1.2 Data

The sample size of the data used in the results should be acknowledged as insufficient to achieve statistical significance. Due to the limited amount of sample material, the validity of my results is primarily applicable to the specific areas studied and may not adequately represent the metamorphic facies as a whole. Even when supplementing my data with previous work, there remains uncertainty regarding the quality of the data classified by others. The rhyodacite samples from the external sources are undifferentiated, apart from Slenes's Slenes (2016). These samples are classified based on various factors, including the presence or absence of hornblende, or mixing with mafic dikes.

Additionally, the georeferencing of these samples may not be precise enough to confidently align with their classifications. Therefore, data of questionable legitimacy has been excluded from the analysis. Furthermore, the samples from previous master's theses and my own research have undergone different preparation methods and were likely analysed using different machines. This is evident in the variation in detection limits, with older data tending to be less accurate as equipment and methods have been improved over time. I would recommend increasing the number of samples from the

studied areas to enhance the statistical significance of the data. This approach would allow for a representative study of each lithology, enabling the detection of outliers that can significantly impact the statistics, particularly in small sample sizes, leading to inadequate estimates (Kürzl, 1988).

The limitation of the sample size and lack of organization were factors that inspired the idea to build a database for Klemetsaunet, where all present and future data can be stored. However, due to the lack of time at the end of the project, this was deprioritized in favour of producing SEM- and EPMA data which were considered to be more important. In the datafile of Klemetsaunet only the locations of my samples were recorded in the model. To improve the value as a dataset I would recommend that the geochemical- and mineralogical data should be appended to the samples' attribute table and imported into Leapfrog Geo. Thereafter the other samples from the external data that can be georeferenced should also be added. This would decrease the used time of investigating what have been already investigated and enable easier spatial analyses in Leapfrog Geo. Further modelling of the outcrop and the surrounding lithologies would create a more complete model of Klemetsaunet, then expand the model further into Bymarka.

6.1.3 Alternative methods

The different techniques that have been tested in this project include, 1. StraboSpot, 2. Gentle sample preparation, 3. Fiji ImageJ.

1. StraboSpot: The use of StraboSpot made it easy to document geological features in the field. The app offers convenient built-in functions that allow for user-friendly classification of polygons, lines, and point features, with pre-set classes that can be customized. However, challenges arise when exporting the data to other software due to the inability to modify the coordinate system used in StraboSpot. This necessitates additional post-processing steps, such as importing the data into ArcGIS Pro to adjust positions and attributes of the datasets and match the coordinate system with the one used for the 3D model in Leapfrog Geo. Based on my experience, it appears that ArcGIS Online could be an equally or even better alternative, especially if it eliminates a post-processing step by utilizing ArcGIS's app. Therefore, while ArcGIS Online seems to be the preferred option, further testing of StraboSpot is warranted, considering my limited familiarity with the app.
2. Gentle sample preparation: The purpose of the new method was to prevent damage to phyllosilicates used for XRD analysis. Although the approach was more time-consuming compared to using a disc mill (old method) to reduce the grain size of the samples, the stepwise crushing with the jaw crusher provided better control over the process. After each cycle, the material was examined to ensure that the grain size was sufficiently fine before proceeding to the final grain size reduction using the micronizing mill. Ideally, both the old and new methods should have been applied to obtain comparable data from identical samples. According to Henriksen (2022), her research suggests that the new method may be more effective in preserving phyllosilicates. However, due to the limited sample size, a definitive conclusion could not be drawn. Since the new method doesn't delay the sample preparation process to greatly, I would recommend using and further testing of the method.

3. Fiji ImageJ: Fiji ImageJ offers extensive and efficient capabilities for image analysis. When utilizing the software for thin section image analysis, it is crucial to adopt a strategic approach. Selection of mineral grains necessitates both awareness and discipline, encompassing the avoidance of duplicates and not solely focusing on easily identifiable grains. Striking a balance between image resolution and grain size is essential to ensure compatibility and obtain data of adequate quality. Regrettably, most of the post-processing of the image analysis was discarded at the end of the project, limiting the ability to conduct a comprehensive evaluation of the process and its results. Qualitative image analysis holds significant potential in providing crucial data for a project. Thus, further experimentation is advised.

6.2 Scanning Electron Microscope and MicroProbe Analysis

When comparing the first produced different mineralogic maps to the electron backscatter diffraction images, it becomes evident that the percentage of unclassified or misclassified minerals can be significantly reduced. To achieve reliable classifications, several parameters must be taken into account, considering the inherent ambiguity of particle data. The SEM settings, such as acceleration voltage, beam focus, and step size, play a crucial role in this regard. Certain variables can become problematic to mineral classification, such as the interaction volume from neighbouring and underlying grains (El Azzouzi et al., 2017, Mohammed and Abdullah, 2018). Additionally, factors as the presence of mixed mineral phases can also influence classification accuracy. Areas exhibiting such uncertainties were categorized into a new class, defined as an alternative variant of the closely associated mineral. In addition to the equipment-related challenges, other factors such as grain fracturing, surface roughness of thin sections, cracks along the thin sections, and limited image resolution where adjacent minerals overlap a single pixel may pose additional difficulties.

A cross sectional through the Mn-zonation in Figure 50 using an EDS-diffractogram would exhibit a distinctive bell-shaped pattern in element concentration. This pattern is attributed to the fractional crystallization of garnet, which typically results in a gradual depletion of element concentration from the core towards the rim (Cygan and Lasaga, 1982). What should be made aware of is that upon comparing the mineral classification from SEM with the stoichiometry data from EPMA, it was observed that the SEM misclassified the carbonates. This was confirmed by the EPMA data, showcasing that dolomite, classified by the Mineralogic software, is in fact a Fe-Mg calcite, whereas calcite turns out to be ankerite.

6.3 Geochemistry

The data from the laboratory analyses plays a crucial role in understanding the lithological variations within Klemetsaunet. By unravelling the defining attributes for each studied lithologies it becomes possible to interpret both their shared traits and what sets them apart. Even though all lithologies share the same origin, their characterisation has been achieved through field observations, and differing concentrations in geochemistry, mineral assemblages, and mineral textures set them apart.

It is evident that the mineral assemblages in my samples are primarily characterized by subtle variations between albite and quartz. This observation holds true across multiple analytical methods, including thin section observations, XRD analysis, and SEM mineral maps. However, it is important to consider that only the XRD and XRF analysis is unbiased, as it represents bulk samples that are representative of the entire specimen. In contrast, the thin section observations and SEM mineral maps focus on specific areas selected for investigation based on desired features. It is worth noting that the XRD diffractograms were not updated with new mineralogical information obtained from other analyses. Incorporating this additional data might have provided a more accurate fit to the observed values. Furthermore, it should be acknowledged that XRD analysis may encounter challenges in differentiating between intermediate phases of feldspars (Xu et al., 2016). However, the EPMA analysis, which involved a "random" selection of albite grains, reveals minimal variation in the chemistry of albite (Figure 52). Hence, it is plausible that all albite and albite intermediates identified in the XRD analysis represent the same mineral with minor and insignificant variations. The samples generally exhibit a consistent flat REE-pattern with a negative Eu anomaly in Figure 57. This suggests that Eu^{2+} was removed from the system through fractional crystallisation of plagioclase at a greater depth prior to the ascent of the residual melt (Winter, 2013). Mobilization of elements has led to both depletion and enrichment. While the protolith typically shows low REE concentrations, one of the breccia samples displays depletion. The REE-pattern in the shear zones and other breccia samples follows the same trend as the Løkken plagiogranite, since they showcase similar trends as observed by Slagstad (2003). In contrast the Byneset trondhjemite has a characteristic primitive mantle-normalized pattern. The negatively trending slope exhibits an enrichment in LREE and gradually transitions into depletion of HREE, with a slightly positive Eu^{2+} anomaly (Slagstad, 2003).

I do need to be mindful when comparing my geochemical data with the two previous master's theses. Since the preparation methods for the XRF results have been performed differently and the analysis equipment is likely to be different and doesn't have the same precision and/or detection limits. Thus, it's vital to remember that one must be somewhat sceptical when assessing the data points. Also, much have been learned about the area since the first thesis was written. Which is relevant to how and what have been categorized as standard unaltered rhyodacite.

6.4 Mineral Chemistry of Garnet

The SEM- and EPMA analysis results indicate that the garnet found at Klemetsaunet is classified as almandine. Two classifications of almandine are used: regular almandine and Ca- and Mn-enriched almandine. Large garnet grains exhibit zonation, with a core enriched in Ca and Mn, while the rim is dominated by regular almandine. Smaller grains typically display a more even mixture of the two almandine phases. Both Figure 48 and Figure 50 display garnet zonation, with a transition from a Mn-enriched core to a depletion of Mn towards the rim. However, the rim is richer in Fe and Mg compared to the core. According to Müller and Schneider (1971) compositional zoning of garnet with Ca and Mn enriched core is a sign of prograde metamorphism. This suggests that zonation occurs during the growth of garnet and likely only takes place after a certain level of maturity. In early prograde stages, zonation of smaller grains may be lost due to slow diffusion of major elements (Caddick et al., 2010). The zonation might also be caused by retrograde metamorphism at a later stage, where growth evolution is reflected by different physicochemical conditions (Spear, 1993). However, based on the relationship with other mineral phases discussed in chapter 5.1.4. It seems likely that the

limiting factor for garnet growth is the maturity and absence of decomposing mineral phases, evident by depletion halos observed in the field. Suggesting that diffusion limited growth has been controlling factor as a solid-state reaction during prograde metamorphism. Which implies that the diffusion has been slow compared to the growth rate, with an influx of elements from the surrounding matrix (Skora et al., 2006).

Regarding the stoichiometry of garnet, it seems that the chosen standard for microprobe analysis may not be the best fit. According to Howie et al. (1992) the apfu of Si^{4+} should be precisely 3.00 when normalised to 12 oxygen. However, the Si^{4+} content for both the rim and core ranges from 2.80-2.83 apfu, which rises doubts about the suitability of the chosen standard. From observing the interaction between the garnets and chlorite in the thin sections, it's interpreted that chlorite is a retrograde metamorphic product formed under cooler conditions. The evident chloritization of garnet indicate that the garnet growth of both rim and core correlates to the same prograde stage, while chlorite is a retrograde product (Caddick et al., 2010). Where chlorite replaces the garnet around its rim and penetrating the core. Thus, garnet and chlorite does not co-exist at an equilibrium, which suggests that the measurement of other elements in garnet may also be inadequate.

6.5 Magmatic Evolution

It should be noted that even though the TAS diagram in Figure 54 is proposed for unaltered volcanic rocks. Therefore, classifying rocks that have experienced alteration, metamorphism, or weathering should be avoided. Since alkali elements are likely to be mobilized by such processes (Rollinson et al., 2021). According to the AFM diagram from chapter 5.5 the Klemetsaunet samples follow the calc-alkaline series, implying that the melt is more evolved than the primitive basalts. According to Kelley and Cottrell (2009) calc-alkaline rocks typically correlates to subduction zones, where dehydration of the subduction slab occurs with the interaction of the mantle wedge and the overriding plate. Resulting in mixing of melts and volatiles, promoting oxidizing conditions and facilitate the crystallization of ferric iron-bearing magnetite, which effectively removes Fe from the melt (Osborn, 1959). The metaluminous protolith is indicated to be the most evolved, suggesting that the source melt stems from partial melting under oxidizing conditions. Whereas the other samples are categorized as peraluminous and less evolved, likely due to the alteration of the host rock. Where the magnetite content contributes to the variation in the AFM diagram (Figure 61). For the mafic dikes I would have used another discrimination diagram that is more tailored for mafic rock, such as the Ti-Zr-Y diagram from Pearce and Cann (1973). This wasn't done because the mafic dikes of Klemetsaunet weren't the focus of this thesis, but was more observed by Slenes (2016). Else, it should be mentioned that post-tectonic granites have difficulties being identified due to the traits being dependent on factors such as melt composition and composition of the lithosphere (Pearce et al., 1984). Therefore, one should be aware of this constriction and the possibility of wrongly classifying post-tectonic granites as something else.

AFM plot (Irvine and Baragar 1971)

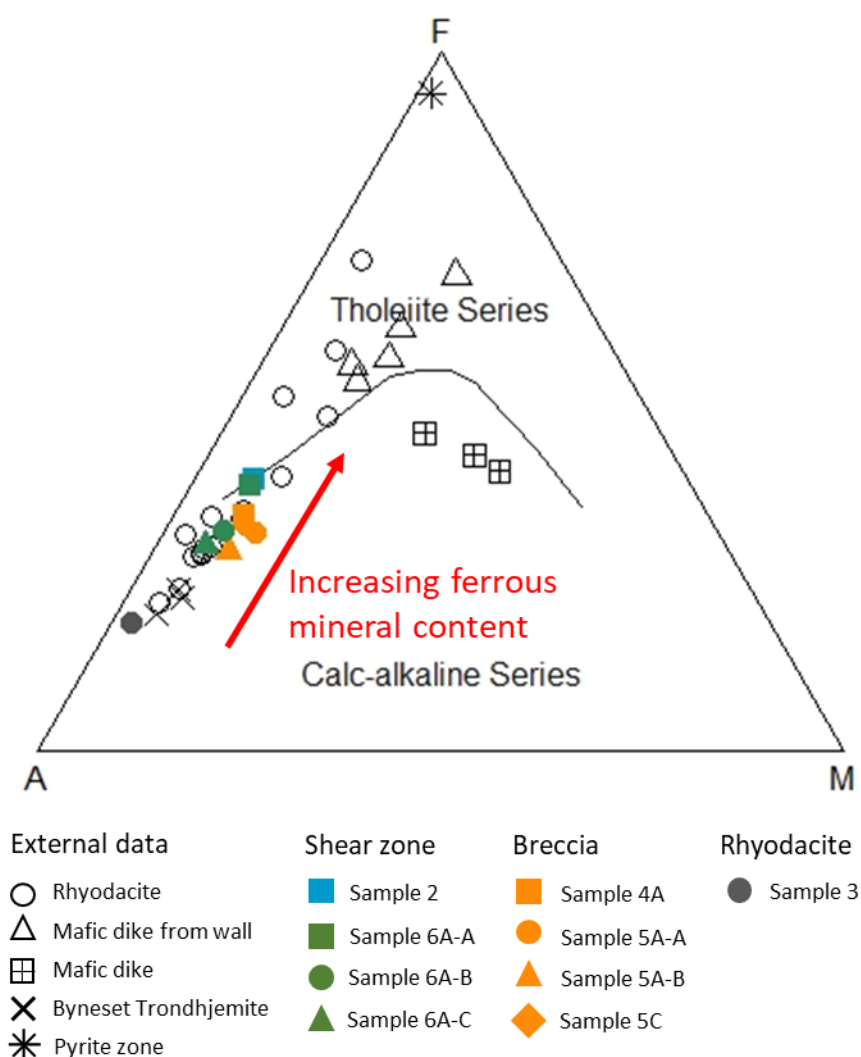


Figure 61: AFM diagram displaying internal variation between the Klemetsaunet samples, with increased scatter towards $\text{FeO}_{\text{Total}}$ (F), correlating to the increased mineral content of ferrous minerals.

To interpret the tectonic origin of my samples and the data from previous work, I used discrimination diagrams for granites (see Figure 58). For my samples the result was that they belong within the group, ocean ridge granites. This classification does relate to the model of Klemetsaunet being a part of the sequence in a volcanogenic massive sulphide-deposit. According to Slagstad (2003), high $\text{Y}/\text{Al}_2\text{O}_3$ ratios correlates a rock to having a oceanic origin. The Klemetsaunet rhyodacite exhibits a higher $\text{Y}/\text{Al}_2\text{O}_3$ ratio compared to the Byneset trondhjemite, which supports the established interpretation of the Klemetsaunet rhyodacite formed in an oceanic system. While the Byneset trondhjemite shows a typically subduction-related REE-pattern with indications of an increased arc influence during formation. While the REE-pattern of the Klemetsaunet rhyodacite and the plagiogranite of Løkken indicates that they are related.

6.6 Deformation

The relative geochronological assessment in the thesis is constrained by the absence of age dating and the limited observation of cross-cutting relationships. Nonetheless, it can be reasonably deduced that the mafic dikes and the Byneset trondhjemite are younger than the Klemetsaunet rhyodacite, given their intrusive nature within the rhyodacite as documented with the map and field observations. As a result, distinguishing the chronological sequence of the breccia, phyllonitic shear zone, and garnet-biotite shear zone becomes speculative. An assumption is that the garnet-biotite shear zone developed prior to the phyllonitic shear zone. This interpretation is supported by the presence of sinistral kinematic indicators, such as biotite mica fish and folded quartz veins, where both the garnet-biotite shear zone and the phyllonitic shear zone exhibit a consistent top-to-the-WNW orientation. However, observations in thin sections parallel to the foliation plane reveal a dextral shear sense towards the SSW in the phyllonitic shear zone (Figure 62). Therefore, it is inferred that the top-to-the-WNW orientation in the phyllonitic shear zone represents a preserved kinematic indicator, formed during the same deformation event as the garnet-biotite shear zone. Thus, implicating that there have been two distinct occurrences of deformation, indicating a potential reactivation. There was not identified any kinematic indicators for the breccia with respect to the shear zones.

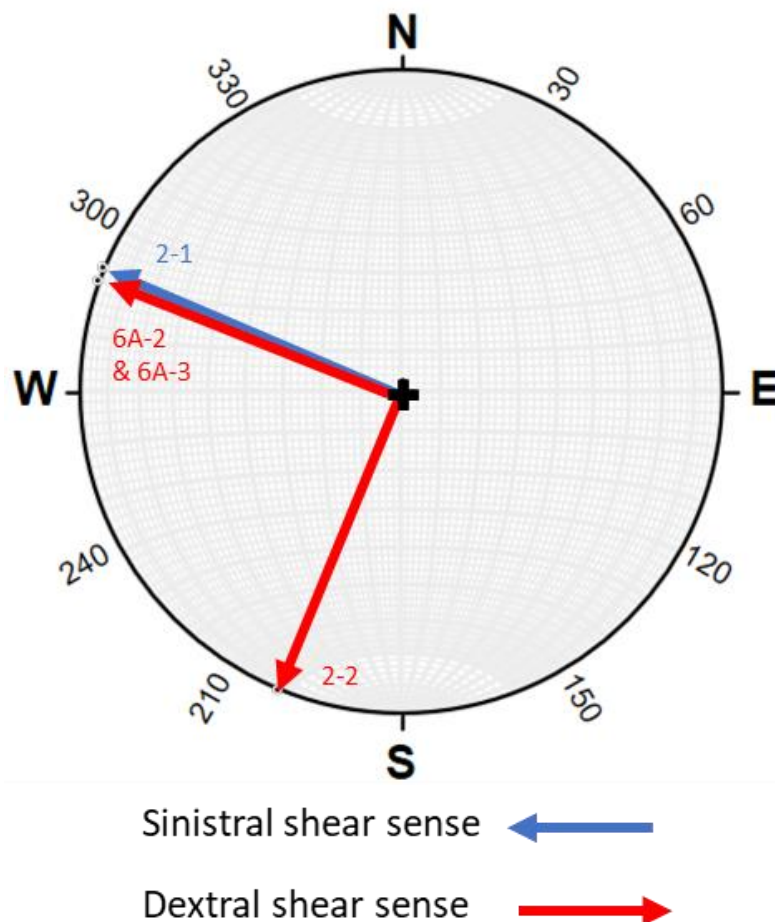


Figure 62: Summary of shear sense interpret from thin sections with kinematic indicators.

6.7 Metamorphism

From the amalgamated P-T estimates, the pressure conditions are lacking in representation. The used methods revolve more around the calculations of temperatures and can leave gaps in potential pressure conditions. It comes forth in Figure 63 that there are two groups for the estimates that gather around two different for P-T conditions. The chlorite- and the garnet-biotite geothermometers plots almost parallel to each other, where only the one of the three has specific pressure estimates. These P-T estimates are interpreted to represent two distinct events, reflected by the breccia's mineral assemblage and alteration, which suggests that it formed at cooler conditions compared to the shear zones.

The chlorite thermometry goes through the three metamorphic facies; hornfels, greenschist and blueschist, where there is a little constraint of the plausible pressure conditions. The temperatures remain within a small interval between 350-393°C for the pressure range of 1-9.5 kbar. In the other group of estimates, the KFMASH and biotite-muscovite geothermobarometers fits well into each other, while the span of temperature for grain boundary migration is a lot vaguer, since it doesn't give any information about the pressure. These thermobarometers display a temperature range ca. 500-580°C at 1-9.5 kbar, with the assumption of GBM being only slightly past the transition of SGR and GBM. The initial assumption for the KFMASH-estimate was that garnet, chlorite, and biotite were co-existing at an equilibrium. If this assumption holds true, then the estimate is considered valid. However, the lack of correlation between the temperature ranges of the chlorite thermometer and the KFMASH-grid suggests that chlorite, biotite, and garnet have not remained stable under the same petrophysical conditions. Therefore, it is unlikely that the KFMASH-grid is valid.

Also, the measured mineral chemistry of garnet is insufficient, as discussed in chapter 6.4, it can propose that the garnet-biotite thermometer is not accurate. Which comes forth when comparing the P-T estimates, where the temperature estimate of chlorite (Cathelineau, 1988) and garnet-biotite thermometer are within the same ranges.

According to Atherton (1968) when garnet is outside its stability field it easily interacts with hydrothermal fluids or melts. Which can lead to the formation of secondary phases, e.g., retrograde chlorite. That the chlorite is a formed as a secondary phase have been a suspicion for both shear zones and the breccia. This is due to chlorite penetrating the garnets, which is clear when looking at the SEM-results. Here it is observed how the chlorite cuts through the rim of garnets and even through its zonation. It has also been observed that chlorite intertwines with biotite and replacing it, as if being cannibalised. Chloritization of biotite involves the process of formation of chlorite by decomposing biotite, leading to increased concentrations of metallic ions in the hydrothermal fluids.

Dynamic recrystallisation of quartz have been observed in all samples, which suggests that all samples have experienced metamorphism around 500°C. Due to the presence of ductile deformation it can be assumed that metamorphism occurred at a depth below 20 km, where greenschist facies evolves (Fossen, 2016). This can be used to constrain the plausible P-T conditions for peak metamorphism when the syn-kinematic porphyroclasts of garnets grew. Resulting in a P-T estimate of 6-9.5 kbar at 520-580°C for peak metamorphism. Compared to the garnet-biotite thermobarometers of Slenes (2016) her application of Ferry and Spear (1978) yields similar results to that of mine, with 350°C at 0 kbar. However, her sampling point of the garnet were selected from the core and not the rim. Noticeably, one P-T estimate where garnet was measured at the rim and applied the

method of Ferry and Spear (1978), produces a higher temperature estimate of approximately 440°C at 0 kbar. The two other methods that she applied were Ganguly and Saxena (1984) and Hodges and Spear (1982), which produces P-T estimates that would correlate better to that of my peak temperature estimates, such as the muscovite-biotite thermometer (Wu, 2020).

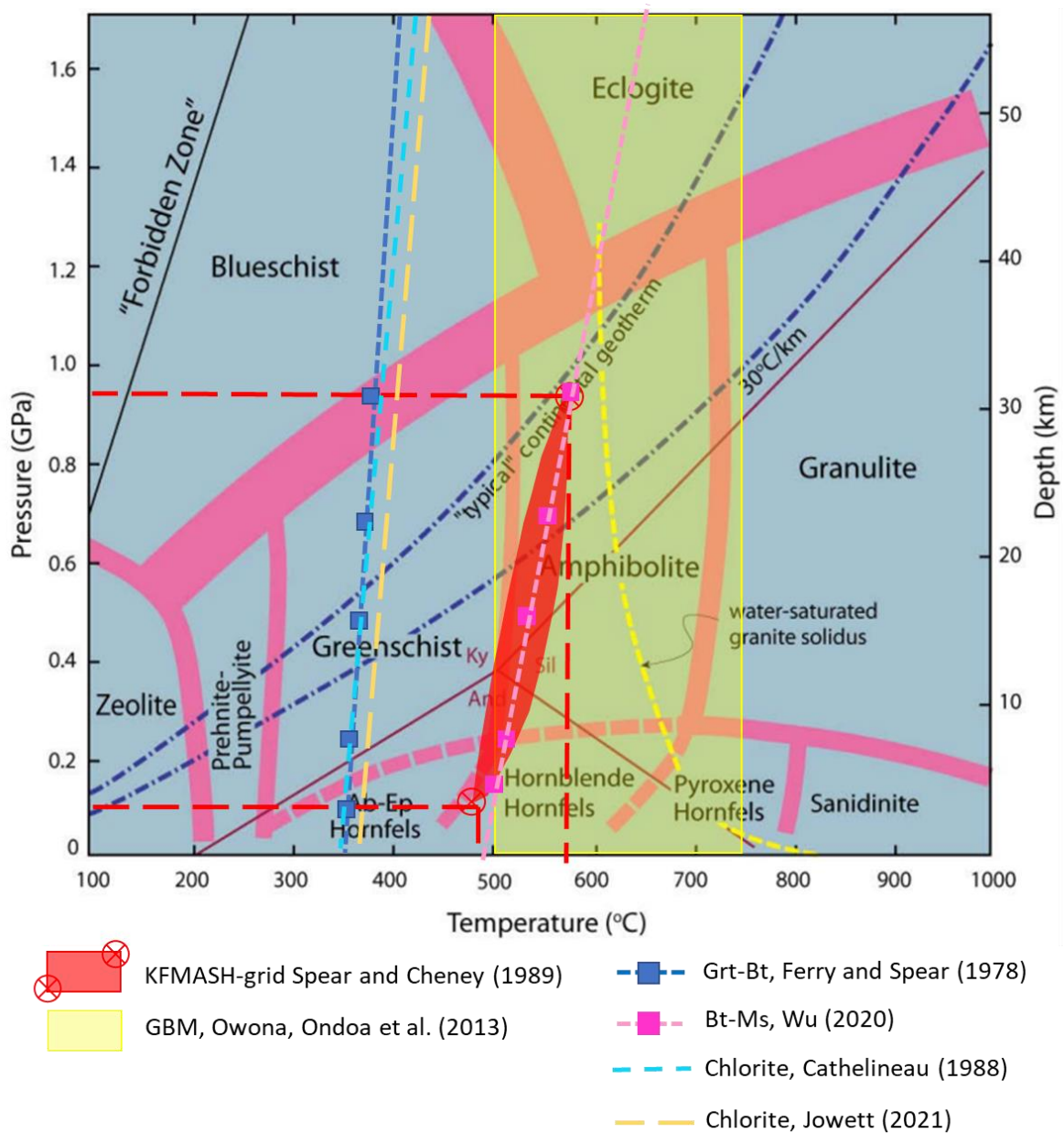


Figure 63: Metamorphic facies diagram from Winter (2013), the thermobarometers are based on data from microprobe analysis, mineral assemblages and mineral textures. All points represent estimated values, and their correspondingly drawn line is the linear trend. The KFMASH-grid and GBM estimate cover greater ranges, where the GBM has not limitation for pressure.

The presence of chlorite often indicates a low- to medium grade metamorphic grade, as it forms around 400°C and 3 kbar (Howie et al., 1992). The chlorite classification in Figure 53 can also be compared to the chlorite analysis of Slenes (2016) displayed in Figure 64. The chlorite found in the breccia samples (4A-1 and 5A-2), as well as the retrograde chlorite from the garnet-biotite shear zone sample (6A-2), exhibits a ferroan composition,

which is consistent with the blue/violet interference colour observed in the thin sections. In contrast the chlorite in the protolith and phyllonitic shear zone displays a clear brown interference colour. Suggesting that this chlorite are magnesian, though they were not analysed in this study their appearance are similar to chlorites analysed by Slenes (2016). To obtain more definitive data, it is essential to conduct additional EPMA measurements on chlorite grains. Without these measurements, the interpretation will have a more subjective aspect to it, potentially influenced by human error. The observed mineral assemblage in my samples enables the possibility for their alteration being related to regional metamorphism. In Figure 65 the peak metamorphic grade is estimated in the transitional states between greenschist- and amphibolite facies. If the occurrence of polymorph alumina-silicates such as andalusite, sillimanite, and/or kyanite then these could be used as indexes to denote more precise P-T conditions. However, the lack of those minerals is certainly due to metamorphic grade being lower than amphibolite facies, where the staurolite and kyanite zone occurs (Winter, 2013). Therefore, peak metamorphic grade of the Klemetsaunet rhyodacite correlates with the transitional grade. Though it's suspected lower amphibolite facies relates to peak deformation conditions which fits with the grain boundary migration of quartz.

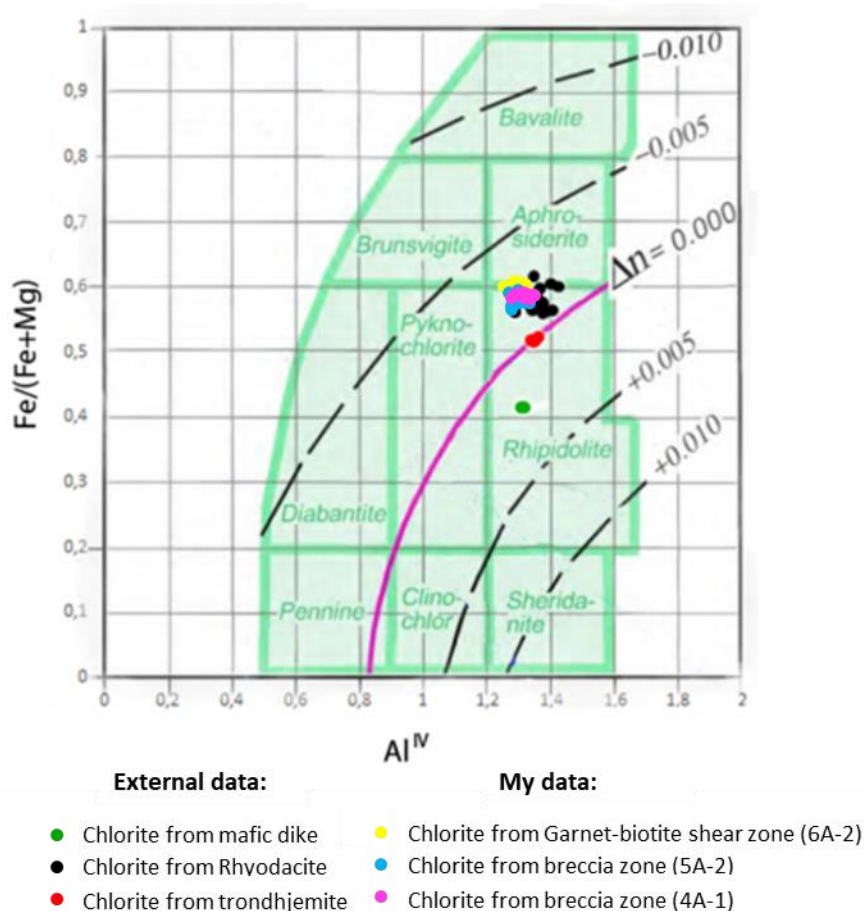


Figure 64: Classification after Tröger et al. (1968), figure from Slenes (2016). Chlorite samples plotting above the ratio line; $\Delta n = 0.000$ are more ferroan and has the characteristic masked blue/violet interference colour of chlorite. Magnesian chlorite below this ratio line will have a brown interference colour.

Metamorphic Grade →

Metamorphic Facies	Transitional States			Amphibolite		Granulite	
Albite							
Plagioclase > An ₁₂	Oligoclase					Andesine	
Epidote							
Actinolite							
Hornblende							
Augite							
Orthopyroxene							
Chlorite							
Garnet							
Biotite							
Quartz							
Phengite							
Cummingtonite							
Zone for associated metapelites	Chlorite Zone	Biotite Zone	Garnet Zone	Staurolite and Kyanite Zones	Sillimanite-Muscovite Zone	K-feldspar-Sillimanite Zone	Cordierite-Garnet Zone

Figure 65: Diagram for mineral assemblages during prograde metamorphism from Winter (2013). My samples fit into the metamorphic facies of “Transitional States” based on their mineral assemblage. This also correspond to the biotite- and garnet zone of regional metamorphism.

6.8 Metasomatism and Mineral Alteration

Normally plagiogranites are associated with a low K₂O content, while Na₂O and CaO being more abundant. By introducing volatiles such as H₂O and CO₂ into a system it enables chemical reactions between the rock composition and the composition of volatiles. Sea water is a common hydrothermal fluid for volcanic massive sulphides. Where the fluid phase is important for the alteration process, since sea water brings an influx of electrolytes such as Na⁺, K⁺, Ca²⁺, Mg²⁺, Cl⁻, HCO₃⁻, and SO₄²⁻ into the system (Marumo et al., 2003). Fractures and the damage zones in both the middle and lower crust where ductile deformation dominates act as conduits for fluid phases, leading to alteration typically by mobilizing alkali elements of the host rock (Fossen and Cavalcante, 2017). The alteration process is dependent on the properties of the wall rock and hydrothermal fluids, and the fluid/rock ratio. Properties of hydrothermal fluids are the composition, temperature, pH, and Eh, while the wall rock’s mineral assemblage is its main factor. If a system has a low temperature and a high fluid/rock ratio then the alteration of the mineral assemblage in the wall rock is largely controlled by the fluid phase, and vice versa (Robb, 2020). The degree of which elements are mobile during hydrothermal alteration or metamorphism can be evaluated by comparing the composition of the unaltered parent rock (Rollinson et al., 2021). Based on the P-T estimates of chlorite it is likely that the hydrothermal alteration has been either phyllic- or propylitic alteration. Where phyllic alteration occurs at temperatures between 300-450°C with the mineralisation of sericite and quartz, while propylitic alteration has a higher fluid/rock

ratio and a temperature range of 300-400°C. Additionally, propylitic alteration leads to formation of minerals such as chlorite, epidote, calcite, and albite.

Both the protolith, breccia, and Slenes's rhyodacite samples are relatively low in K₂O. Her samples averaging around 0,80 wt. % K₂O, while my protolith and breccia are below 0,5 wt. % K₂O. Correlating those samples to classify as oceanic plagiogranite according to Coleman and Peterman (1975). Figure 58 shows how samples with assumed a high fluid/rock ratio migrates away from the protolith in the ocean ridge granite field. Which is likely due to alteration of the parent rock. Leading to the assumption that phyllonitic shear zone has experienced the most hydrothermal activity, reflected by the elevated concentration in K₂O which likely stems for the abundance of muscovite. According to Robb (2020) the required amount of H₂O for the formation of muscovite is 8-10 wt. %, 3-5 wt. % for biotite, and 2-3 wt. % for hornblende.

As observed in the field the hand specimen from the phyllonitic shear zone disintegrates, likely related to its foliation where shear strength is controlled by the bands of phyllosilicates. Muscovite dominates the paragenesis of these phyllosilicate bands, with minor content of biotite and chlorite. From the field observations the transition between the phyllonitic shear zone and the protolith occurs abruptly, suggesting that hydrothermal activity was very localised. Where the fluid phases must have been plentiful due the formation of hydrothermal muscovite. Whereas the protolith does not have any sign of this abundant fluid flow. In contrast the protolith's hornblende vein relates to a lesser amount of hydrothermal activity, suggesting a lower influx of H₂O. These hornblende veins are found in several places at the outcrop and muscovite has been observed cutting through the hornblende veins. Suggesting that the hornblende veins occurred prior to the formation of muscovite, indicating that these two hydrothermal events are not related. As for the scattered hornblende all over Klemetsaunet, these hornblende grains do not align and could possibly stem from dehydration of the source melt where water concentrations were around 2-3 %. It's important to notify that this is a personal assumption and no samples with this feature have been studied in this thesis. The garnet-biotite shear zone there are substantially fewer mica bands than in the phyllonitic shear zone. Where biotite dominates, yet muscovite occurs in smaller proportions. Suggesting that either the influx of water have been lesser than in the phyllonitic shear zone or the P-T conditions were different, but further investigation needs to be carried out to determine if they are related events. Though the remnant shear sense indicator in the phyllonitic shear zone, suggest that the garnet-biotite shear zone formed first. Thus, these hydrothermal events would have occurred at different times. In the breccia it's reasonable to assume that the occurrence of chlorite is highly influenced by the interaction with fluid phases, as chlorite was precipitated into the fractures. Where magnetite grains have a great spatial association with the chlorite's presence. This neighbouring relationship makes it reasonable to assume that both chlorite and magnetite have been precipitated simultaneously under the same conditions. In these fractures there are also observed muscovite, but also in lesser amount compared to the phyllonitic shear zone.

All samples of the Klemetsaunet rhyodacite is suspected to have been altered by some hydrothermal alteration. This makes sense since the geochemistry of the Klemetsaunet rhyodacite which correlates to an oceanic setting, where great amount of saline fluids interacts with the rock. This relates to neocrystallisation of albite with decomposition of feldspars. It's recognized that albitization commonly occurs at a regional-scale numerous rock types and tectonic settings (Perez and Boles, 2005). Whereas the decomposition of albite when interacting with fluid phases and K⁺ leads to the formation of muscovite,

which is a plausible explanation for the muscovite found at Klemetsaunet (O'Hara, 1988). There are numerous types of veins penetrating Klemetsaunet, such as hornblende -, quartz -, and dolomite veins. Additionally Slenes (2016) reported the occurrence of biotite- and muscovite veins with an orientation to NE-SW. Tensile fractures or naturally occurring extensional fractures due to triaxial compression (Twiss and Moores, 1992). These fractures act as conduits for fluids phases where precipitation of mineral phases occurs. The vein types have vastly different paragenesis and physicochemical conditions should therefore be different. The aligned hornblende grains in the protolith correlates to those seen in the field, where metasomatism from underlying meta-gabbro could be a plausible source for Ca, Mg, and Fe. It's suspected that the dolomite-quartz-calcite veins related to the breccia formation.

The presence of both epidote and muscovite is believed to be associated with high hydrothermal activity, potentially influenced by the influx of seawater and the decomposition of Ca/K-bearing minerals. Enrichment in K_2O , Rb, Nb, Ba, Zn, V, Ga, and Ce can be seen as positive trend in the variation diagrams with respect to the protolith. Where the shear zones are the most enriched, especially the phyllonitic shear zone. Mobilisation of these elements have led to the increased concentration, by precipitation of new minerals. While the negative trends show how elements such as Co have been removed from the system. Immobile elements are such as Y, Sr, and TiO_2 show no trends. The occurrence of epidote is recognized as a typical mineral in hydrothermal systems, followed by chloritization (Jackson, 2005). Epidote is observed with the greatest quantity in phyllonitic shear zone, with only minor chlorite when compared to the breccia. From the EPMA analysis it can be seem that the hydrothermal chlorite in the breccia has a lesser Fe/Mg ratio compared to the chlorite in the garnet-biotite shear zone. This can be evident that the Fe and Mg in biotite and garnet remains in the chlorite from the chloritization. While the fracture infill in the breccia, the Fe/Mg ratio is not as high, probably due to the mineral assemblage of the wall rock. Which correlates to the mineral chemistry of chlorite being dependent on the decomposition of minerals interacting with the hydrothermal fluids.

7 Conclusion

Based on the findings of this study, it can be concluded that the Klemetsaunet rhyodacite falls under the classification of ocean ridge granites, as described by Frost and Frost (2008). The samples exhibit characteristics that align with the calc-alkaline series, commonly observed in subduction zones where the source melt originates from partial melting in an oceanic setting. Dehydration of the subduction slab has resulted in mixing of melts and introducing volatiles into the system, promoting oxidizing conditions and assisting to crystallization of ferric iron-bearing magnetite.

The Klemetsaunet rhyodacite exhibits a significant variation of lithologies altered through post-magmatic processes, showcasing its complex nature. Within the Klemetsaunet area, the predominant lithologies include rhyodacite, mafic dikes, and the Byneset trondhjemite. Additionally, localized areas of chalcophile enrichment, shear zones, and brecciation can be observed. The outcrops display a matrix characterized by a fine-grained matrix with an aphanitic texture, enclosing by porphyroclasts and porphyroblasts of garnet and hornblende. These porphyroclasts are distributed throughout the outcrops, displaying variations in concentration, type, vein alignment, and occasionally exhibiting a nematoblastic texture.

Based on the observed mineral assemblages, it is proposed that hydrothermal activity has played a crucial role in shaping the distinctive paragenesis of these lithologies. The matrix is predominantly composed of a combination of quartz and neocrystalline albite. Furthermore, it is interpreted that feldspars have undergone alteration, resulting in the formation of highly pure albite, likely influenced by a high fluid/rock ratio. However, in the most preserved rhyodacite (the protolith) there remains traces of the original magmatic texture, with interlocking of albite- and quartz grains.

The primary objective of the thesis was to document and analyse localised deformation zones along with their geochemical characteristics. The investigation led to the identification of three distinct zones: a phyllonitic shear zone, a garnet-biotite shear zone, and a breccia zone. These zones were thoroughly examined and compared to the least altered rhyodacite sample, which has been interpreted as the protolith of the Klemetsaunet area. The presence of hydrothermal fluids has resulted in the mobilization of major and trace elements. The shear zones and breccia exhibit enrichment in K_2O , MgO , Na_2O , Fe_2O_3 , Zn , Ga , Rb , Sr , Nb , Ba , while displaying depletion in SiO_2 , Cr , W .

Garnet grains found at Klemetsaunet exhibits a porphyroclastic- and poikiloblastic texture, with albite overgrowth and quartz inclusions. There are two identified garnet phases: almandine and Mn- and Ca-enriched almandine. Large prograde almandine grains display zonation with a transition from a Mn-enriched core with depletion towards the Fe-enriched rim. The zonation pattern is suspected to be diffusion limited, with a slow diffusion rate of major elements from the surrounding matrix relative to the mineral growth. Smaller grains are heterogeneous mixture of the two almandine phases, suggesting their immaturity. In the shear zones it's evident of retrograde chloritization of the garnet, where chlorite penetrates through the rim of core of zoned garnet. Which poses problems for reliability of P-T estimates including garnet.

Based on the analysis of geochemical and mineralogical data, it is evident that the rhyodacite in the study area has undergone regional metamorphism into a transitional stage between greenschist- and amphibolite facies. The observations reveal two distinct sets of pressure-temperature (P-T) estimates. The peak metamorphic conditions are estimated to be in the range of 6-9.5 kbar at 520-580°C. During this stage, dynamic recrystallization of quartz occurred, characterized by grain boundary migration, and the formation of syn-kinematic garnet, muscovite, and biotite. Subsequently, retrograde chloritization took place under cooler conditions, approximately 365-393°C, correlating to greenschist facies.

The kinematic indicators from the ductile shear zones indicate shear sense with top to the WNW. However, a few remnant shear sense indicators, perpendicular to the foliation plane of the phyllonitic shear zone, exhibit a shear sense towards the SSW. The absence of cross-cutting relationships and age dating, presents a challenging in distinguishing the geochronological sequence between the breccia and shear zones. However, it is assumed that the garnet-biotite shear zone formed prior to the phyllonitic shear zone based on the observed dextral shear sense seen in the latter, which cuts the dextral shear sense of the former. Furthermore, considering the chloritization that occurred at a retrograde stage in relation to the shear zones, it's inferred that the breccia represents the youngest feature.

8 Further work

Other recommendations for further work would be age dating of the breccia and both shear zones to distinguish when these events occurred. The application of age dating would help providing insight into the processes of formation, alteration, and deformation history. Radiometric dating is one of the plausible method, options are:

- U-Pb dating for either garnet, zircon, and/or apatite. Minerals that are resistant for alteration are suitable determining magmatic and metamorphic formation ages, where a corona texture represents the evolutionary sequence (Thomson et al., 2012, Bucher and Grapes, 2011). Although previous research conducted by Roberts et al. (2002) has addressed this aspect, its application could still be valuable in identifying potentially overlooked generations, specifically the garnet-biotite shear zone.
- In situ Rb-Sr dating of garnet is an option, can be particularly useful for dating of garnet formed during regional metamorphism (Inger and Cliff, 1994). Furthermore, there are ongoing developments in the field of in situ dating of white mica, hornblende, and other silicate minerals. These techniques involve the use of new reaction cells that allow for in situ Rb-Sr analysis to be conducted using LA-ICP-MS (Wang et al., 2022).
- Lu-Hf dating of garnets is appropriate to estimate the closure age of high-pressure metamorphic events for precis dating (Duchêne et al., 1997). The abundance of garnets in all samples can provide correlative evidence for both mineral growth and deformation event since most garnets show syn-kinematic structures.
- $^{40}\text{Ar}/^{39}\text{Ar}$ dating uses potassium bearing minerals such as micas and feldspars to determine geochronology. This method can be applied to find minimum age of hydrothermal alteration and mineralization, which is suited for my samples containing muscovite and biotite (Bird et al., 1990, Rollinson et al., 2021).

Despite the measurements of Lu and Pb is below the detection limits from the bulk analyses of trace elements (XRF and ICP-MS), the geochronometers could become feasible by utilizing either LA-ICP-MS and/or EPMA for the relevant elements.

9 Disclaimer for the Thesis

It should be remarked that not all the available data could be properly analysed, due to the shift in focus during the thesis. Initially 3D-modelling and creation of a database was the focus together with gathering geochemical- and mineralogical analyses of samples. However, limitations for progress and useability of the 3D-modelling caused the transition into performing more advanced analysis methods, that would provide greater benefits to the thesis. Therefore, microprobe analyses and SEM became prioritised at the end of February, to gain additional data for geochemistry and mineral chemistry. A summary of the aspects that were given lower priority due to time constraints:

- The 3D-modelling process received significant attention during the initial half of the thesis, with the generation of 3D models being conducted alongside analytical work in the laboratory. However, due to limited available data and time consumption, this aspect of 3D-modelling stopped by the end of January, following the completion of the basic model depicted in in **Feil! Fant ikke referanseilden..**
- The examination of fluid inclusions within a carbonate vein from the breccia was planned, and a doubly polished thin section was specifically prepared for this purpose. However, due to time limitations, planned fluid inclusion analysis had to be left aside because the thin section was delayed due to technical issues and lack of epoxy availability following the Corona epidemic.
- There was a desire to return to the field to acquire additional materials that could have aided in addressing the challenges of the thesis. However, given the already substantial amount of material to manage within the imposed time constraints, this plan was ultimately abandoned.

10 References

- AGISOFT, L. 2014. Agisoft PhotoScan user manual: professional edition. *St Petersburg, Russia: Agisoft LLC.*[Google Scholar].
- AHMED, A. H. 2014. Does anybody have a spreadsheet for calculating the chlorite formula? May 15, 2023 ed.
- ATHERTON, M. 1968. The variation in garnet, biotite and chlorite composition in medium grade pelitic rocks from the Dalradian, Scotland, with particular reference to the zonation in garnet. *Contributions to Mineralogy and Petrology*, 18, 347-371.
- BATANOVA, V., SOBOLEV, A. & MAGNIN, V. Trace element analysis by EPMA in geosciences: Detection limit, precision and accuracy. IOP Conference Series: Materials Science and Engineering, 2018. IOP Publishing, 012001.
- BEMIS, S. P., MICKLETHWAITE, S., TURNER, D., JAMES, M. R., AKCIZ, S., THIELE, S. T. & BANGASH, H. A. 2014. Ground-based and UAV-Based photogrammetry: A multi-scale, high-resolution mapping tool for structural geology and paleoseismology. *Journal of structural geology*, 69, 163-178.
- BEST, M. G. 2013. *Igneous and metamorphic petrology*, John Wiley & Sons.
- BIRD, M. I., CHIVAS, A. R. & MCDUGALL, I. 1990. An isotopic study of surficial alunite in Australia 2. Potassium-argon geochronology. *Chemical Geology: Isotope Geoscience Section*, 80, 133-145.
- BRAATHEN, A., NORDGULEN, Ø., OSMUNDSEN, P.-T., ANDERSEN, T. B., SOLLI, A. & ROBERTS, D. 2000. Devonian, orogen-parallel, opposed extension in the Central Norwegian Caledonides. *Geology*, 28, 615-618.
- BRAATHEN, A., OSMUNDSEN, P. T. & GABRIELSEN, R. H. 2004. Dynamic development of fault rocks in a crustal-scale detachment: An example from western Norway. *Tectonics*, 23.
- BUCHER, K. & GRAPES, R. 2011. *Petrogenesis of metamorphic rocks*, Springer Science & Business Media.
- CADDICK, M. J., KONOPÁSEK, J. & THOMPSON, A. B. 2010. Preservation of garnet growth zoning and the duration of prograde metamorphism. *Journal of Petrology*, 51, 2327-2347.
- CATHELINEAU, M. 1988. Cation site occupancy in chlorites and illites as a function of temperature. *Clay minerals*, 23, 471-485.
- COLEMAN, R. & PETERMAN, Z. 1975. Oceanic plagiogranite. *Journal of Geophysical Research*, 80, 1099-1108.
- CYGAN, R. T. & LASAGA, A. C. 1982. Crystal growth and the formation of chemical zoning in garnets. *Contributions to Mineralogy and Petrology*, 79, 187-200.
- DE CARITAT, P., HUTCHEON, I. & WALSHE, J. L. 1993. Chlorite geothermometry: a review. *Clays and clay minerals*, 41, 219-239.
- DEBON, F. & LE FORT, P. 1988. A cationic classification of common plutonic rocks and their magmatic associations: principles, method, applications. *Bulletin de Minéralogie*, 111, 493-510.
- DUCHÊNE, S., BLICHERT-TOFT, J., LUIS, B., TÉLOUK, P., LARDEAUX, J.-M. & ALBARÈDE, F. 1997. The Lu-Hf dating of garnets and the ages of the Alpine high-pressure metamorphism. *Nature*, 387, 586-589.
- DUTROW, B. L. & CLARK, C. M. 2012. X-ray powder diffraction (XRD). *Geochemical Instrumentation and Analysis*, 1-2.
- EIDE, E. & LARDEAUX, J.-M. 2002. A relict blueschist in meta-ophiolite from the central Norwegian Caledonides—discovery and consequences. *Lithos*, 60, 1-19.
- EL AZZOUZI, M., KHOUCHEF, L. & ACHAHBAR, A. 2017. Monte Carlo study of the interaction volume changes by the beam skirt in Vp-Sem. *Acta Physica Polonica A*, 132, 1393-1398.

- FERRY, J. T. & SPEAR, F. 1978. Experimental calibration of the partitioning of Fe and Mg between biotite and garnet. *Contributions to mineralogy and petrology*, 66, 113-117.
- FOSSEN, H. 2016. *Structural geology*, Cambridge university press.
- FOSSEN, H. & CAVALCANTE, G. C. G. 2017. Shear zones—A review. *Earth-Science Reviews*, 171, 434-455.
- FROST, B. R. & FROST, C. D. 2008. A geochemical classification for feldspathic igneous rocks. *Journal of Petrology*, 49, 1955-1969.
- GANGULY, J. & SAXENA, S. K. 1984. Mixing properties of aluminosilicate garnets: constraints from natural and experimental data, and applications to geothermobarometry. *American mineralogist*, 69, 88-97.
- GASSER, D., GRENNÉ, T., CORFU, F., BØE, R., RØHR, T. S. & SLAGSTAD, T. 2022. Concurrent MORB-type and ultrapotassic volcanism in an extensional basin along the Laurentian Iapetus margin: Tectonomagmatic response to Ordovician arc-continent collision and subduction polarity flip. *Bulletin*, 134, 1635-1659.
- GEE, D. 1977. TECTONIC MODEL FOR CENTRAL PART OF SCANDINAVIAN CALEDONIDES-REPLY. *American Journal of Science*, 277, 657-665.
- GEE, D. G., JUHLIN, C., PASCAL, C. & ROBINSON, P. 2010. Collisional orogeny in the Scandinavian Caledonides (COSC). *Gff*, 132, 29-44.
- GRANSETH, A. U. 2015. *Deformation, Phyllonitization and Associated Element Mobilization of Granitoid Rocks: -A geochemical study of the Fagervika granitoid, Norway*. NTNU.
- GRENNÉ, T., IHLEN, P. & VOKES, F. 1999. Scandinavian Caledonide metallogeny in a plate tectonic perspective. *Mineralium Deposita*, 34, 422-471.
- HACKER, B. R. & GANS, P. B. 2005. Continental collisions and the creation of ultrahigh-pressure terranes: Petrology and thermochronology of nappes in the central Scandinavian Caledonides. *Geological Society of America Bulletin*, 117, 117-134.
- HENDERSON, P. 2013. *Rare earth element geochemistry*, Elsevier.
- HENRIKSEN, L. H. 2022. *Mineralogical assessment of rocks of hydropower tunnels subjected to swelling*. NTNU.
- HERMANN, J. & RUBATTO, D. 2003. Relating zircon and monazite domains to garnet growth zones: age and duration of granulite facies metamorphism in the Val Malenco lower crust. *Journal of Metamorphic Geology*, 21, 833-852.
- HEY, M. H. 1954. A new review of the chlorites. *Mineralogical Magazine and Journal of the Mineralogical Society*, 30, 277-292.
- HODGES, K. & SPEAR, F. S. 1982. Geothermometry, geobarometry and the Al₂SiO₅ triple point at Mt. Moosilauke, New Hampshire. *American mineralogist*, 67, 1118-1134.
- HOLTEDAHL, O. 1920. Paleogeography and diastrophism in the Atlantic-Arctic region during Paleozoic time. *American Journal of Science*, s4-49, 1-25.
- HOWIE, R., ZUSSMAN, J. & DEER, W. 1992. *An introduction to the rock-forming minerals*, Longman London, UK.
- INGER, S. & CLIFF, R. 1994. Timing of metamorphism in the Tauern Window, Eastern Alps: Rb-Sr ages and fabric formation. *Journal of metamorphic Geology*, 12, 695-707.
- INOUE, A., INOUE, S. & UTADA, M. 2018. Application of chlorite thermometry to estimation of formation temperature and redox conditions. *Clay Minerals*, 53, 143-158.
- JACKSON, J. A. 2005. *Glossary of geology*.
- JOWETT, E. C. 2021. Fitting iron and magnesium into the hydrothermal chlorite geothermometer. *Available at SSRN 3863523*.
- KELLEY, K. A. & COTTRELL, E. 2009. Water and the oxidation state of subduction zone magmas. *Science*, 325, 605-607.
- KÜRZL, H. 1988. Exploratory data analysis: recent advances for the interpretation of geochemical data. *Journal of Geochemical Exploration*, 30, 309-322.
- LINDER, W. & LINDER, W. 2009. Example 3: Some special cases. *Digital Photogrammetry: A Practical Course*, 111-140.

- LLOYD, G. E. & FREEMAN, B. 1994. Dynamic recrystallization of quartz under greenschist conditions. *Journal of Structural Geology*, 16, 867-881.
- MARUMO, K., URABE, T. & NAKASHIMA, M. Geochemistry and mineralogy of the hydrothermal system at Suiyo Seamount. Japan Earth and Planetary Science Joint Meeting, B002-001, 2003.
- MICHELETTI, N., CHANDLER, J. & LANE, S. 2015. Structure from Motion (SfM) Photogrammetry. British Society for Geomorphology, Geomorphological Techniques. *Online Edition (ISSN 2047-0371)*.
- MOHAMMED, A. & ABDULLAH, A. Scanning electron microscopy (SEM): A review. Proceedings of the 2018 International Conference on Hydraulics and Pneumatics—HERVEX, Băile Govora, Romania, 2018. 7-9.
- MOORE, S., CARLSON, W. & HESSE, M. 2013. Origins of yttrium and rare earth element distributions in metamorphic garnet. *Journal of Metamorphic Geology*, 31, 663-689.
- MÜLLER, G. & SCHNEIDER, A. 1971. Chemistry and genesis of garnets in metamorphic rocks. *Contributions to Mineralogy and Petrology*, 31, 178-200.
- NATIONAL OCEANIC AND ATMOSPHERIC ADMINISTRATION. n.d. *Magnetic Field Calculators* [Online]. Available: <https://www.ngdc.noaa.gov/geomag/calculators/magcalc.shtml?#declination> [Accessed 30.09.2022 2022].
- NGU 2023. Berggrunn WMS3. <https://kartkatalog.geonorge.no/metadata/berggrunn-wms3/51243d4e-e86e-474b-baf8-b7ccfb59fe8e>.
- O'HARA, K. 1988. Fluid flow and volume loss during mylonitization: an origin for phyllonite in an overthrust setting, North Carolina USA. *Tectonophysics*, 156, 21-36.
- OSBORN, E. F. 1959. Role of oxygen pressure in the crystallization and differentiation of basaltic magma. *American Journal of Science*, 257, 609-647.
- OSMUNDSSEN, P. T., EIDE, E., HAABESLAND, N., ROBERTS, D., ANDERSEN, T., KENDRICK, M., BINGEN, B., BRAATHEN, A. & REDFIELD, T. 2006. Kinematics of the Høybakken detachment zone and the Møre-Trøndelag Fault Complex, central Norway. *Journal of the Geological Society*, 163, 303-318.
- OWONA, S., ONDOA, J. M. & EKODECK, G. E. 2013. Evidence of quartz, feldspar and amphibole crystal plastic deformations in the paleoproterozoic Nyong Complex Shear Zones under Amphibolite to Granulite conditions (west Central African Fold Belt, SW Cameroon). *Journal of Geography and Geology*, 5, 186.
- PASSCHIER, C. W. & TROUW, R. 2005a. Deformation mechanisms. *Microtectonics*, 25-66.
- PASSCHIER, C. W. & TROUW, R. A. 2005b. *Microtectonics*, Springer Science & Business Media.
- PEARCE, J. A. & CANN, J. R. 1973. Tectonic setting of basic volcanic rocks determined using trace element analyses. *Earth and planetary science letters*, 19, 290-300.
- PEARCE, J. A., HARRIS, N. B. & TINDLE, A. G. 1984. Trace element discrimination diagrams for the tectonic interpretation of granitic rocks. *Journal of petrology*, 25, 956-983.
- PEREZ, R. J. & BOLES, J. R. 2005. An empirically derived kinetic model for albitization of detrital plagioclase. *American Journal of Science*, 305, 312-343.
- RAGAN, D. M. & RAGAN 1985. *Structural geology*, John Wiley & Sons.
- RAZA, M. Q., ABSAR, N., PANDALAI, H. & PATEL, S. 2021. Chlorite thermometry and fluid inclusion studies on vein-type Tintini copper deposit, Eastern Dharwar Craton, India: Ore genetic implications. *Ore Geology Reviews*, 131, 104058.
- ROBB, L. 2020. *Introduction to ore-forming processes*, John Wiley & Sons.
- ROBERTS, D. 2003. The Scandinavian Caledonides: event chronology, palaeogeographic settings and likely modern analogues. *Tectonophysics*, 365, 283-299.
- ROBERTS, D., WALKER, N., SLAGSTAD, T., SOLLI, A. & KRILL, A. 2002. U-Pb zircon ages from the Bymarka Ophiolite, near Trondheim, central Norwegian Caledonides, and regional implications. *Norsk Geologisk Tidsskrift*, 82, 19-30.

- RÓG, M. & RZONCA, A. 2021. The impact of photo overlap, the number of control points and the method of camera calibration on the accuracy of 3D model reconstruction. *Geomatics and Environmental Engineering*, 15, 67-87.
- ROLLINSON, H. R. 2014. *Using geochemical data: evaluation, presentation, interpretation*, Routledge.
- ROLLINSON, H. R., ROLLINSON, H. & PEASE, V. 2021. *Using geochemical data: To understand geological processes*, Cambridge University Press.
- RUESSINK, B. & HARVILLE, D. Quantitative analysis of bulk mineralogy: The applicability and performance of XRD and FTIR. SPE Formation Damage Control Symposium, 1992. OnePetro.
- SCIENCE EDUCATION RESOURCE CENTER, S. 2009. *Excel Template for Ternary Diagrams* [Online]. Available: <http://serc.carleton.edu/details/files/19001.html> [Accessed May 8, 2023 2023].
- SELEN, L., PANTHI, K. K. & VISTNES, G. 2020. An analysis on the slaking and disintegration extent of weak rock mass of the water tunnels for hydropower project using modified slake durability test. *Bulletin of Engineering Geology and the Environment*, 79, 1919-1937.
- SERANNE, M. 1992. Late Palaeozoic kinematics of the Møre-Trøndelag Fault Zone and adjacent areas, central Norway. *Norsk Geologisk Tidsskrift*, 72, 141-158.
- SHEARER, C. & PAPIKE, J. 1989. Is plagioclase removal responsible for the negative Eu anomaly in the source regions of mare basalts? *Geochimica et Cosmochimica Acta*, 53, 3331-3336.
- SKORA, S., BAUMGARTNER, L. P., MAHLEN, N. J., JOHNSON, C. M., PILET, S. & HELLEBRAND, E. 2006. Diffusion-limited REE uptake by eclogite garnets and its consequences for Lu-Hf and Sm-Nd geochronology. *Contributions to Mineralogy and Petrology*, 152, 703-720.
- SLAGSTAD, T. 2001. The Bymarka Ophiolite - Field Trip Guide. *Norsk Geologisk Forening*.
- SLAGSTAD, T. 2003. Geochemistry of trondhjemites and mafic rocks in the Bymarka ophiolite fragment, Trondheim, Norway: petrogenesis and tectonic implications. *Norsk Geologisk Tidsskrift*, 83, 167-185.
- SLENES, T. M. 2016. *Metamorfose og metasomatiske prosesser i tonalittiske og mafiske gangbergarter på Klemetsaunet, Trondheim*. NTNU.
- SPEAR, F. S. 1993. Metamorphic phase equilibria and pressure-temperature-time paths. *Mineralogical Society of America Monograph*, 352-356.
- SPEAR, F. S. & CHENEY, J. T. 1989. A petrogenetic grid for pelitic schists in the system SiO₂-Al₂O₃-FeO-MgO-K₂O. *Contributions to Mineralogy and Petrology*, 101, 149-164.
- SPECIALE, P. A., TOKLE, L. & BEHR, W. M. 2022. Feldspar and orthopyroxene piezometers constrained using quartz-feldspar and olivine-orthopyroxene mineral pairs from natural mylonites. *Journal of Structural Geology*, 154, 104495.
- STEPHENS, M., GEE, D. & STURT, B. 1985. A tectonic model for the evolution of the eugeoclinal terranes in the central Scandinavian Caledonides. *The Caledonide Orogen—Scandinavia and Related Areas*, 2, 953-978.
- TERRY, M. P., ROBINSON, P., HAMILTON, M. A. & JERCINOVIC, M. J. 2000. Monazite geochronology of UHP and HP metamorphism, deformation, and exhumation, Nordøyane, Western Gneiss Region, Norway. *American Mineralogist*, 85, 1651-1664.
- THOMSON, S. N., GEHRELS, G. E., RUIZ, J. & BUCHWALDT, R. 2012. Routine low-damage apatite U-Pb dating using laser ablation-multicollector-ICPMS. *Geochemistry, Geophysics, Geosystems*, 13.
- TRÖGER, W. E., BAMBAUER, H. U., TABORSZKY, F. & TROCHIM, H. D. 1968. *Optische Bestimmung der gesteinbildenden Minerale*, E. Schweizerbart'sche Verlagsbuchhandlung.
- TWISS, R. J. & MOORES, E. M. 1992. *Structural geology*, Macmillan.
- VEDELER, S. 2013. *Structural and Petrological Study of the Klemetsaunet plagiogranite, Trondheim, Norway*. Institutt for geologi og bergteknikk.

- VIDAL, O., PARRA, T. & TROTET, F. 2001. A thermodynamic model for Fe-Mg aluminous chlorite using data from phase equilibrium experiments and natural pelitic assemblages in the 100 to 600 C, 1 to 25 kb range. *American journal of Science*, 301, 557-592.
- WANG, C., ALARD, O., LAI, Y.-J., FOLEY, S. F., LIU, Y., MUNNIKHUIS, J. & WANG, Y. 2022. Advances in in-situ Rb-Sr dating using LA-ICP-MS/MS: applications to igneous rocks of all ages and to the identification of unrecognized metamorphic events. *Chemical Geology*, 610, 121073.
- WESTOBY, M. J., BRASINGTON, J., GLASSER, N. F., HAMBREY, M. J. & REYNOLDS, J. M. 2012. 'Structure-from-Motion' photogrammetry: A low-cost, effective tool for geoscience applications. *Geomorphology*, 179, 300-314.
- WHITNEY, D. L. & EVANS, B. W. 2010. Abbreviations for names of rock-forming minerals. *American mineralogist*, 95, 185-187.
- WINTER, J. D. 2013. *Principles of igneous and metamorphic petrology*, Pearson education.
- WU, C.-M. 2020. Calibration of the biotite-muscovite geobarometer for metapelitic assemblages devoid of garnet or plagioclase. *Lithos*, 372, 105668.
- XIAO, B. & CHEN, H. 2020. Elemental behavior during chlorite alteration: New insights from a combined EMPA and LA-ICPMS study in porphyry Cu systems. *Chemical Geology*, 543, 119604.
- XU, H., JIN, S. & NOLL, B. C. 2016. Incommensurate density modulation in a Na-rich plagioclase feldspar: Z-contrast imaging and single-crystal X-ray diffraction study. *Acta Crystallographica Section B: Structural Science, Crystal Engineering and Materials*, 72, 904-915.
- YUGUCHI, T., SASAO, E., ISHIBASHI, M. & NISHIYAMA, T. 2015. Hydrothermal chloritization processes from biotite in the Toki granite, Central Japan: Temporal variations of the compositions of hydrothermal fluids associated with chloritization. *American Mineralogist*, 100, 1134-1152.

Appendix

Appendix A – Overview of samples and which have been analysed

Appendix B – Description of hand specimen

Appendix C – Thin sections

Appendix D – Modal mineralogy

Appendix E – XRD diffractograms

Appendix F – XRF, major elements

Appendix G – XRF, trace elements

Appendix H – ICP-MS

Appendix I – EBS-images and mineral maps from SEM

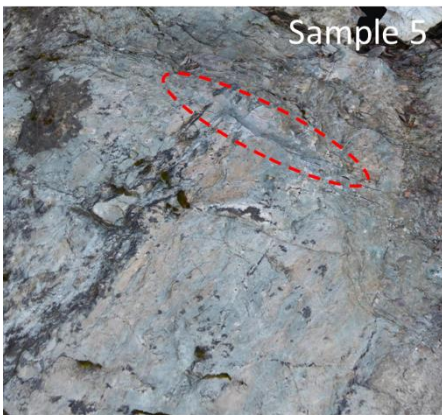
Appendix J – EPMA, data and stoichiometry

Appendix K – Quartz analysis, grain size and angles

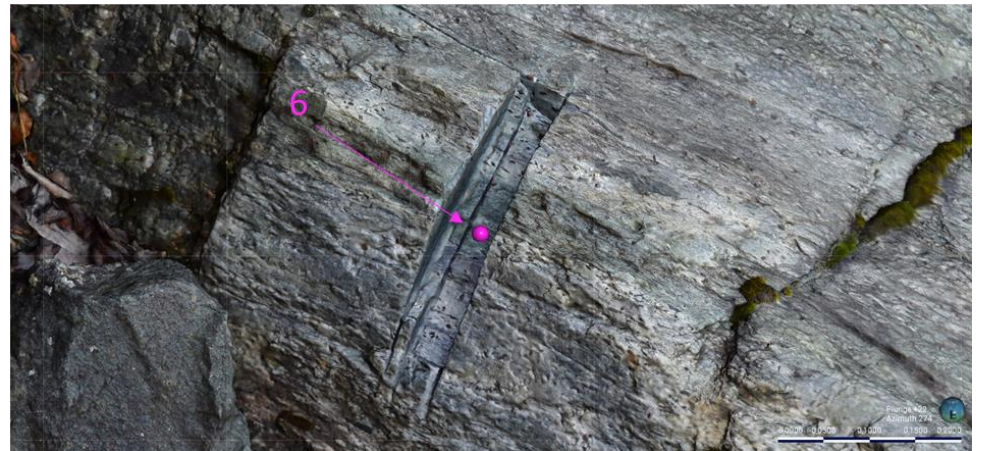
Appendix A: Overview of samples and which have been analysed

Sample ID				Thin sections and analyses performed on them					Geochemical- and mineralogical analyses on crushed samples						
Field ID	Location (WGS 84 / UTM zone 32N (EPSG:32632))			Thin section ID	Type	SEM		EPMA	ID		XRF, Major	XRF, Trace	XRD	ICP-MS	
	X	Y	Z (m)			Overview	Detailed		Personal ID	Journal number					
1A	562215.335	7036675.285	2.775												
1B	562215.338	7036675.28	2.768												
2	562215.4	7036675	2.737	2-1	Polished				2	220899	x	x	x	x	
				2-1B	Polished										
				2-2	Polished	x	2-2d1 & 2-2d2								
3	562215.437	7036675.2	2.673	3	Polished	x			3	220900	x	x	x	x	
4A	562187.6	7036679	3.462	4A-1	Polished	x		x	4A	220901	x	x	x	x	
				4A-1B	Polished										
				4A-2	Polished	x									
4B	562187.729	7036679.266	3.451												
5A	562190.2	7036679	3.377	5A-1	Polished				5A-A	220902	x	x	x	x	
				5A-1V	Liquid										
				5A-2	Polished	x	5A-2d	x	5A-B	220903	x	x	x	x	
5B	562190.134	7036679.454	3.314												
5C	562190.01	7036679.528	3.23	5C	Polished	x			5C	220905	x	x	x	x	
6A	562202.8	7036677	3.085	6A-1	Polished	x			6A-A	220906	x	x	x	x	
				6A-2	Polished	x	6A-2d	x	6A-B	220907	x	x	x	x	
				6A-2B	Polished										
				6A-3	Polished				6A-C	220908	x	x	x	x	
6B	562202.859	7036676.45	3.026												
6-XRD	562202.783	7036676.519	3.059												

The cells that contain information and are highlighted with the lightest colour shades of either blue, yellow and/or green indicate which samples have been relevant for an analysis. Not highlighted samples weren't investigated further than being inspected at a macro level after they were sampled from the field.

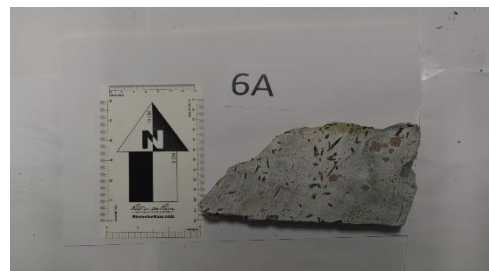
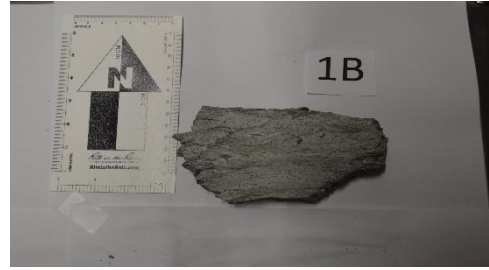


All sampling locations and close-ups from 3D-models created with ContextCapture.



Hand specimens of all collected samples





Appendix B: Description of hand specimen

Phyllonitic shear zone

The samples and their locations can be seen in **Feil! Fant ikke referanseilden.** and Appendix A. Sample 1A and 1B are fragments from the same piece and was located at the very top above sample 2 and 3. The samples were disintegrating and has a pronounced schistosity, porphyritic texture and with an aphanitic groundmass. The matrix of 1A has a white colour and is entwined by multiple bands of a dark grey material. Downwards the sample it becomes more greenish and greyer in its matrix. There are phenocrysts of hornblende, garnet and chalcophile minerals with a grain size ranging from 1-5mm. The hornblende crystals are the most dominant phenocrysts and seemingly have a random orientation. In sample 1B the hand specimen has a greyer and more greenish coloured matrix compared to 1A. In the whole specimen there are the same dark bands as in 1A, but they occur more often and forming lenses. 1B contains fewer phenocrysts, but they remain around the same grain size. Hornblende still dominates, but garnet and chalcophile minerals are scarce. Else, the sample is like 1A by its schistosity, porphyritic texture, and aphanitic groundmass.

Sample 2 has a green coloured matrix and is fragile with moderate schistosity. It displaces a porphyritic texture with an aphanitic groundmass with few phenocrysts of hornblende, garnet and chalcophile minerals ranging from a fine- (<1mm) to medium grained (1-5mm) grain size that can only be observed in some parts of the specimen. There is a flow pattern in the hand specimen that is visible due to foliation between layers with a light grey colour and layers that have a darker hue to its grey colour. The crosscut of the sample reveals thinner layers that are more parallel to each other, forming a more regular flow pattern. Also, in Figure 23 there can be seen a garnet with zonation at a macro level, where the core has a darker red colour in contrast to the brighter red coloured rim.

Protolith

Sample 3 is an intact sample with a white to light grey coloured matrix, found at the bottom of sampled area below sample 2. Porphyritic texture with an aphanitic groundmass with a moderate number of phenocrysts of hornblende and garnet ranging from a fine- (<1mm) to medium grained (1-5mm) grain size. The garnets are scattered all around in the groundmass, but the distribution of the hornblende grains is uneven. The medium grained hornblende grains are located at the top of the sample, while the fine-grained hornblende grains are systematically found along planes. These fine grains forms planes that doesn't always go through the whole specimen but can be easily observed in cross-sections of the sample.

Breccia zone

Sample 4A and 4B shows two lithologies one looks like the typical rhyodacite commonly found at Klemetsaunet, such as sample 3. However, this facies contains darker minerals forming an irregular pattern, almost like a webbing through the matrix and there are brown veins penetrating the rock. The other facies are a white rhyodacite with brown spots scattered around its matrix, the boundary is often sharp to the typical rhyodacite. It is also

observed that the facies with the brown spots contains garnets that has depletion halos where these brown spots cannot be found near them.

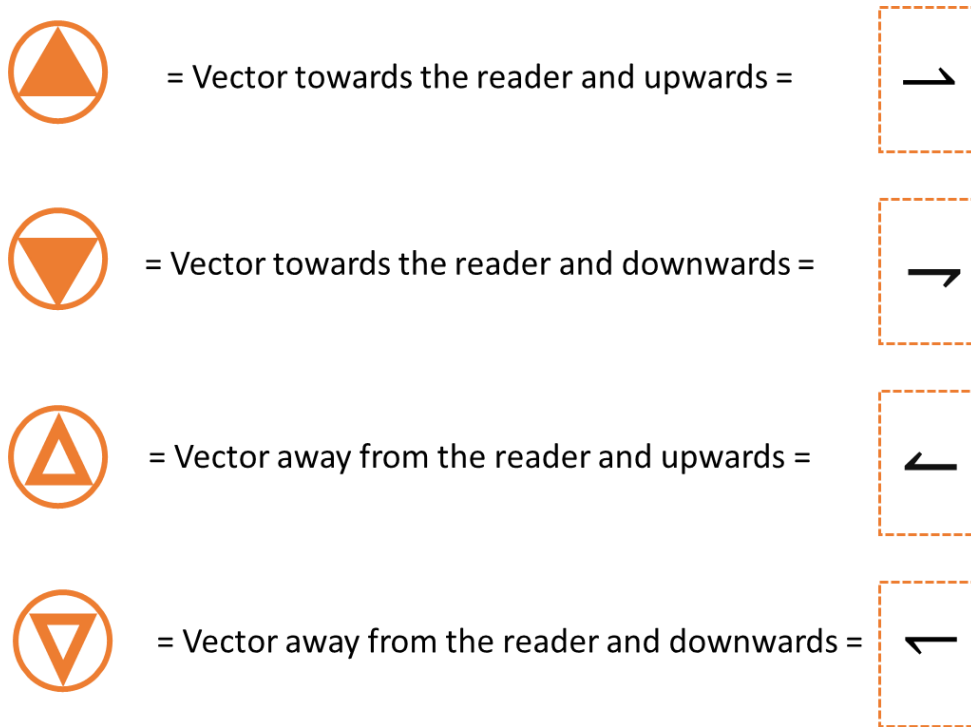
Sample 5 show a cataclastic texture, with angular grey fragments in a dark grey matrix. Inside the sample it's larger pieces of rhyodacite that contains garnets with depletion halos. The pieces themselves has a brighter with colour, with a brown-reddish tint to them. There are also hornblende grains that align themselves along one plane, that also has a depleted area around those grains.

Garnet-Biotite shear zone

The hand specimen of sample 6 is solid and remained intact, in contrast to sample 1 and 2. The slab shows localization of dark grey matrix in the middle that contains lots of garnets and few hornblende grains. Above and below this area the concentration of hornblende grains increases by a lot, while the number of garnets diminishes, and the matrix gets a lighter white colour. Continuing further above and below within the hand specimen the grey matrix returns, but without the presence of garnets.

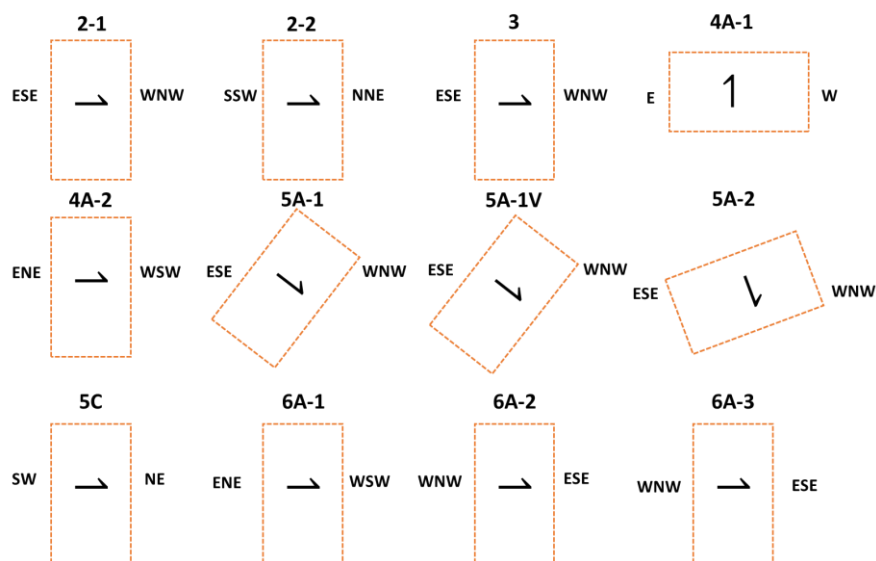
Appendix C: Thin sections

Symbolization for orientation of thin sections. A grey vector should be present of the thin sections to indicate which direction is up and to the right. If no vector is present, then one of the following symbols should be present.

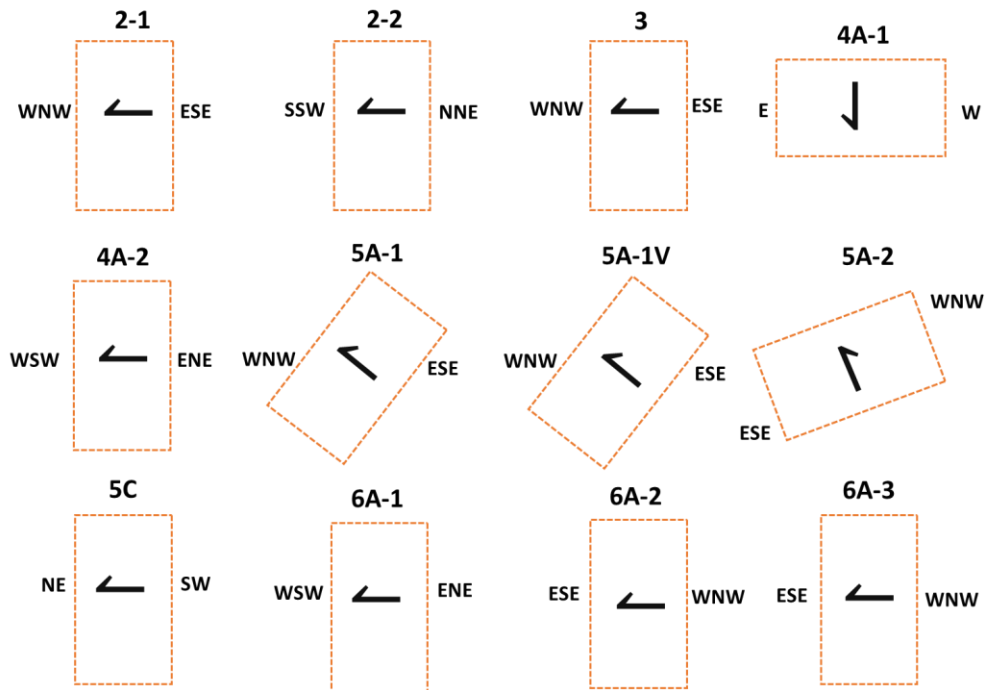


The placement of thin sections on the sample surfaces on the hand specimen to be investigated even further.

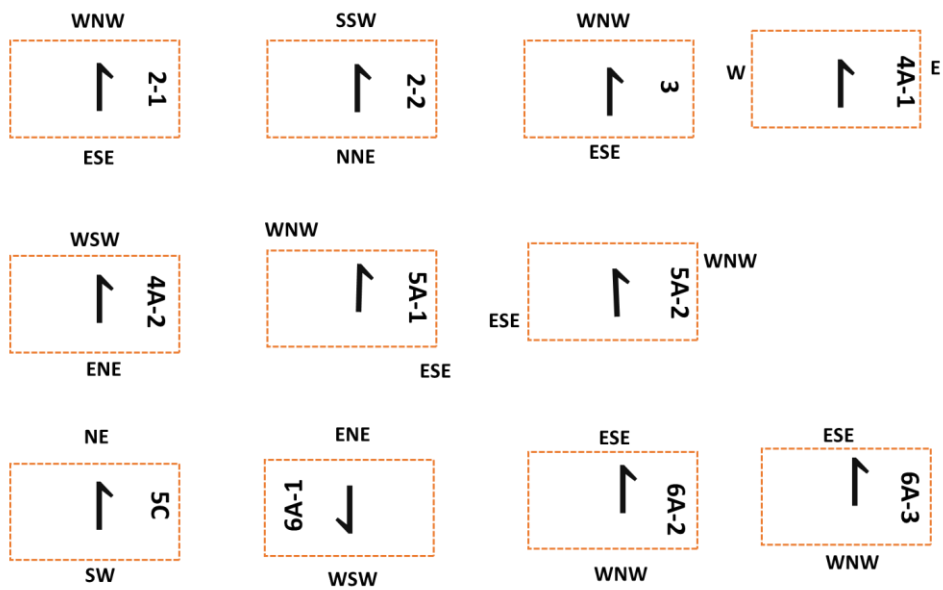
Thin section placement on hand specimen



Corrected orientation of thin sections



Scans: Orientation of thin sections



Phyllonitic shear zone

2-1



2-1B



Thin section 2-1 and 2-1B are parallel to each other and displayed in PPL with the polarizer rotated by 90° and XPL at 45°.

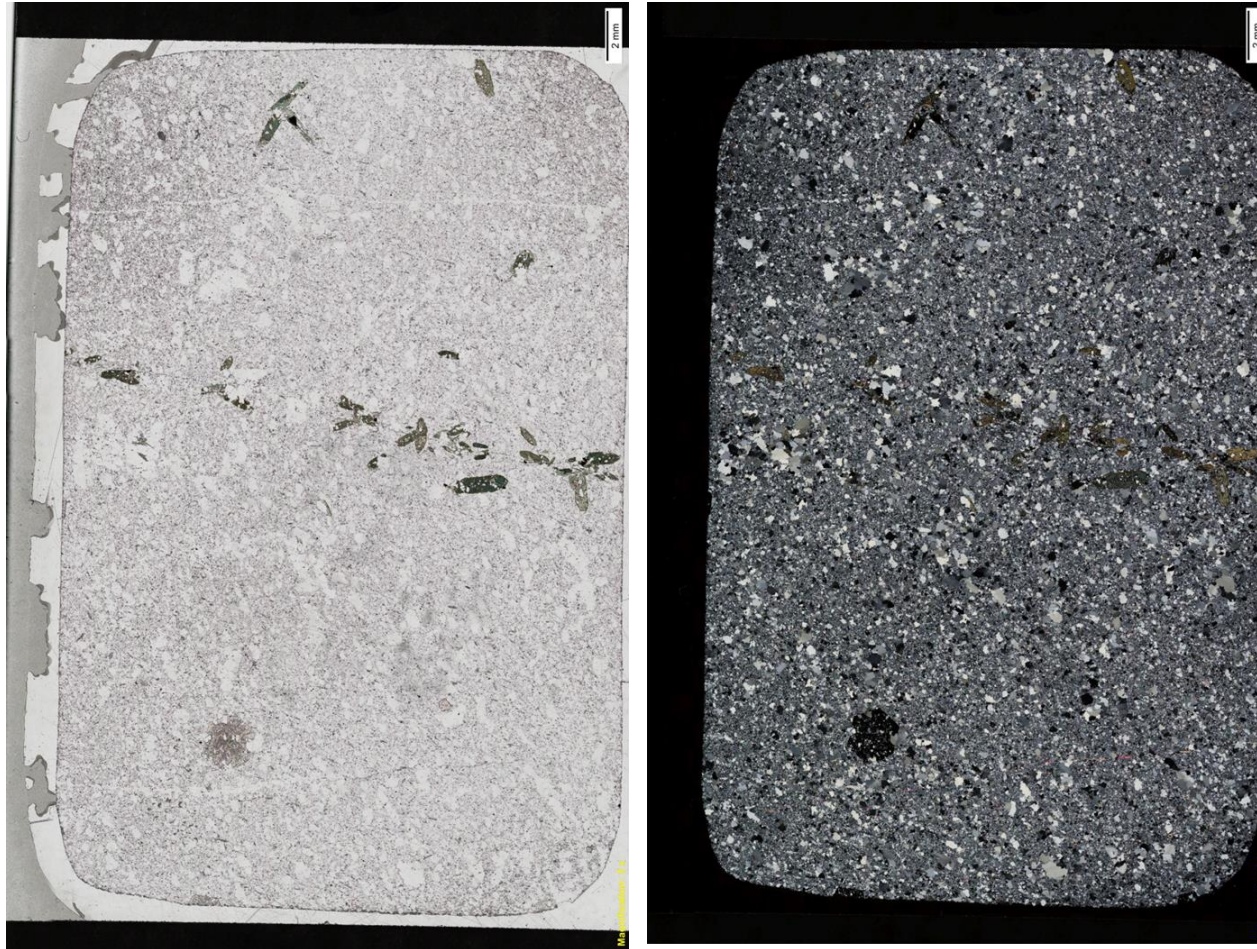
2-2



Thin section 2-2 displayed in PPL with the polarizer rotated by 90° and XPL at 45°. The whole thin section was analysed with SEM, creating an overview map and the red rectangles represents the area for the detailed maps.

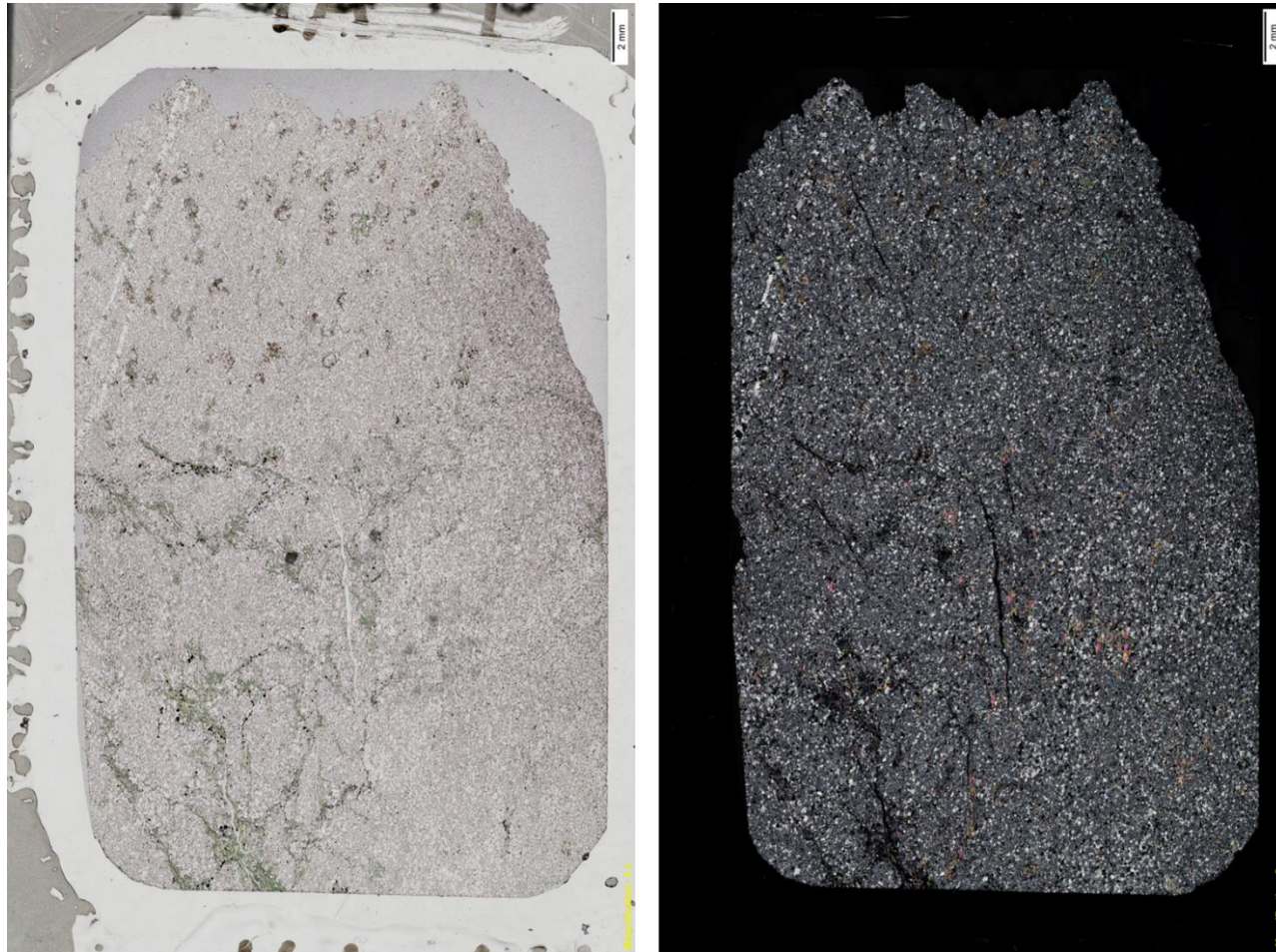
Protolith

3



Thin section 3 displayed in PPL with the polarizer rotated by 90° and XPL at 45°.

4A-1



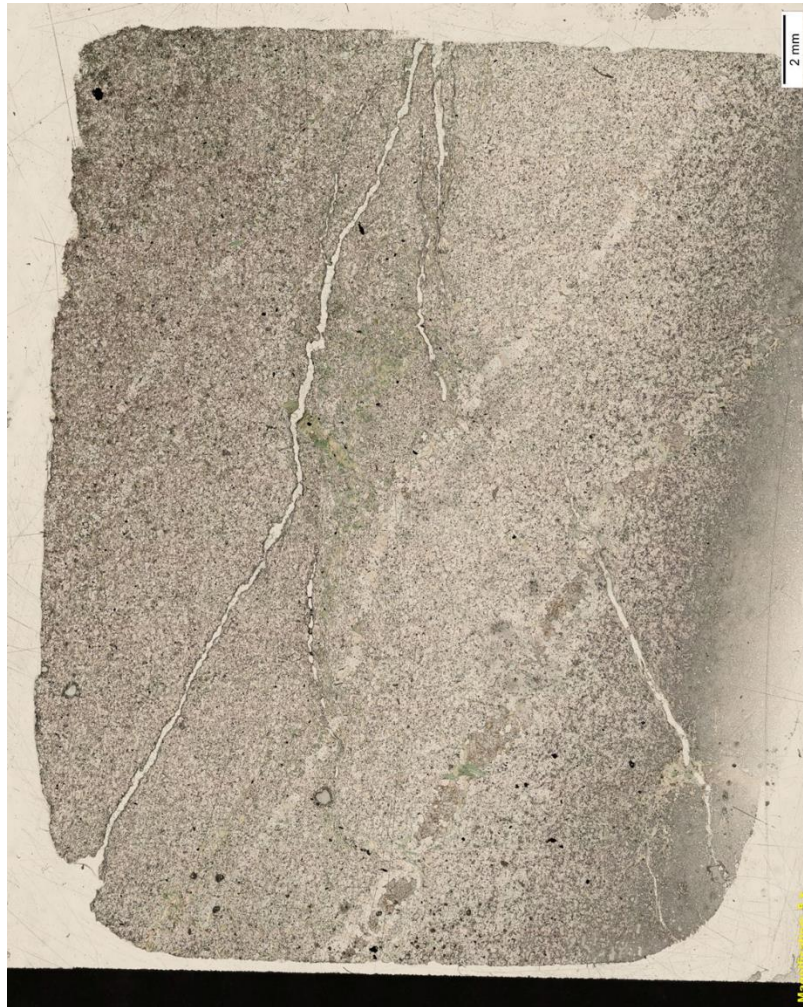
Thin section 4A-1 displayed in PPL with the polarizer rotated by 90° and XPL at 45°.

4A-2



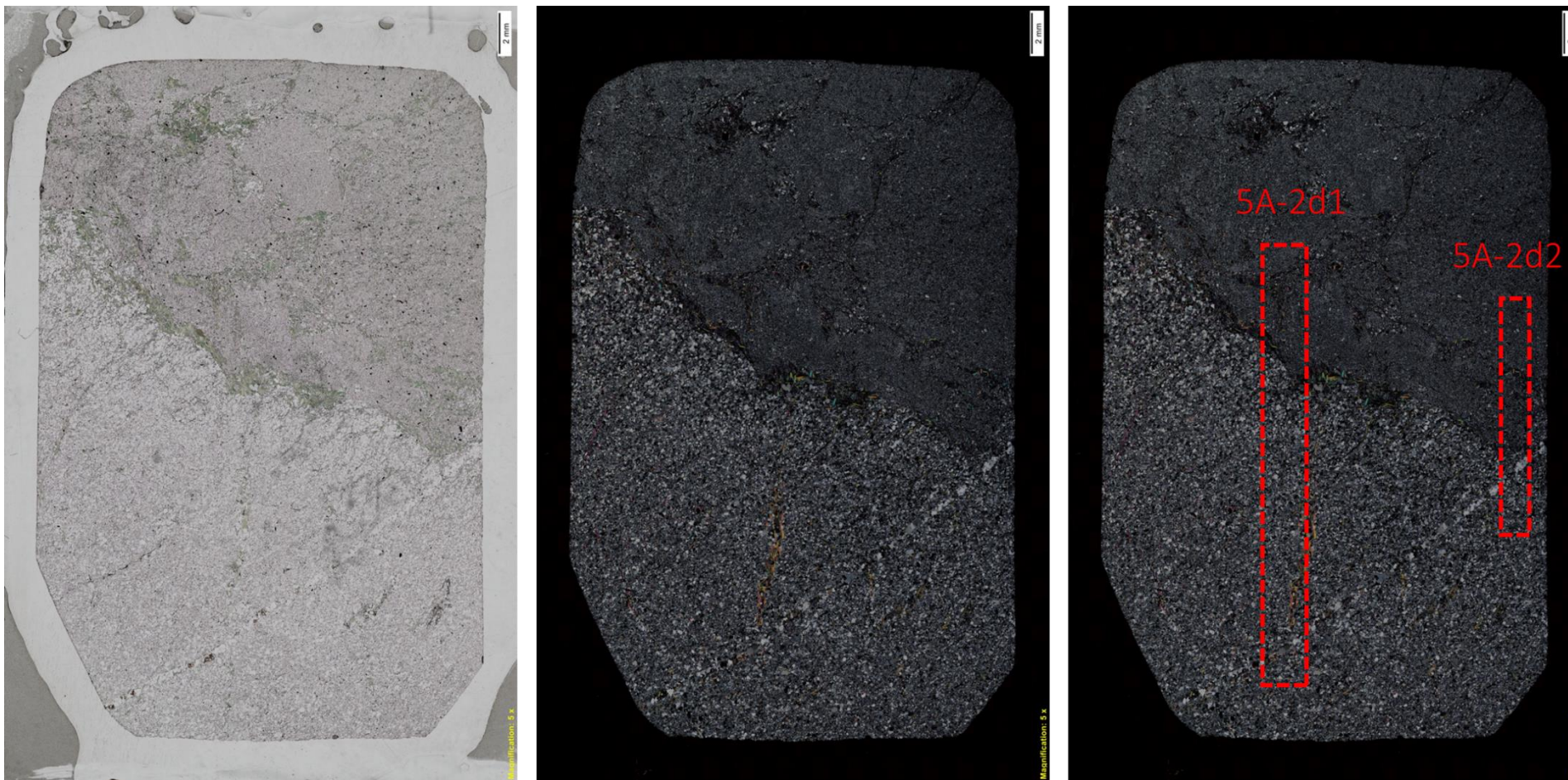
Thin section 4A-2 displayed in PPL with the polarizer rotated by 90° and XPL at 45°.

5A-1



Thin section 5A-1 displayed in PPL with the polarizer rotated by 90° and XPL at 45°.

5A-2



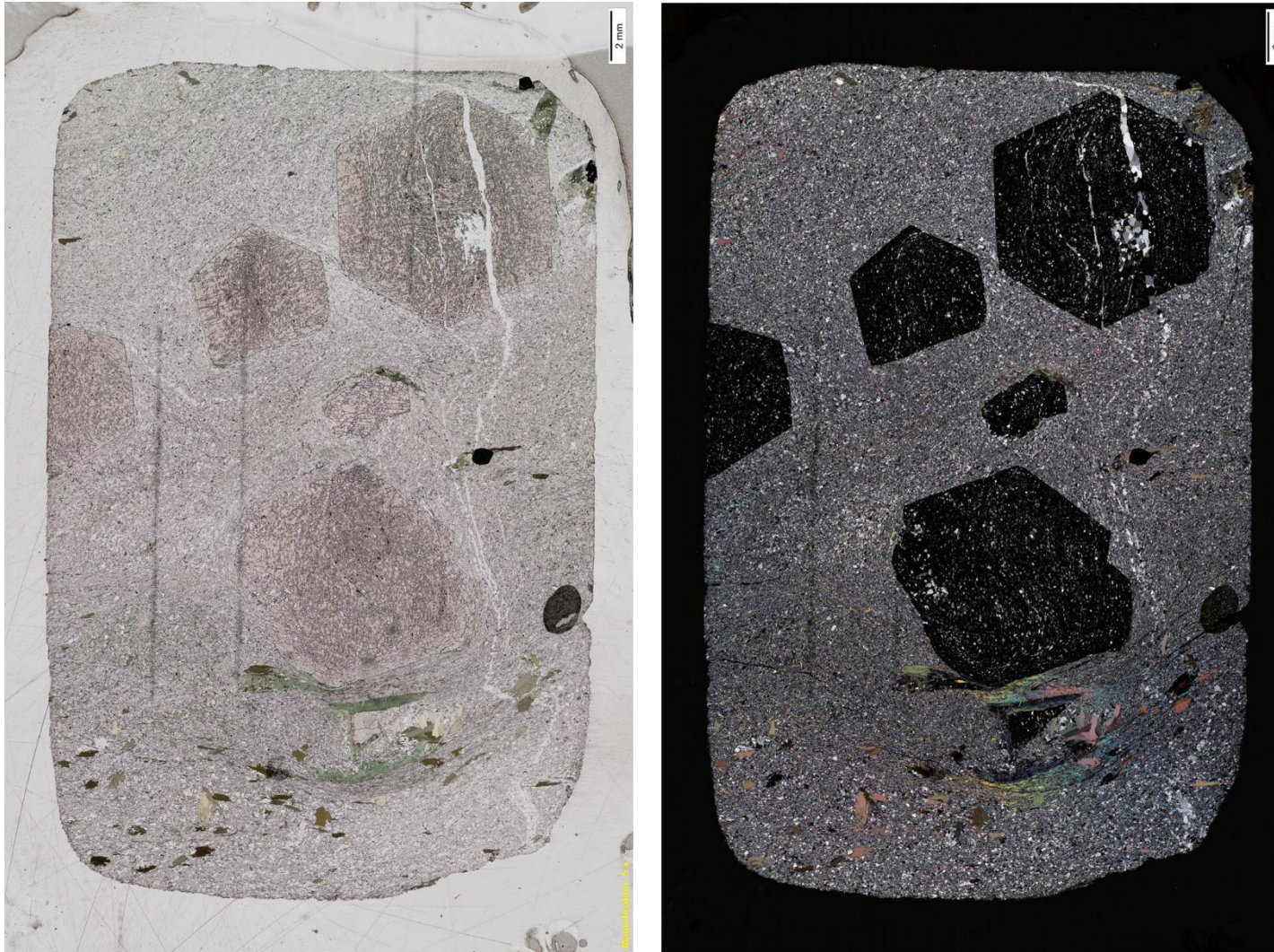
Thin section 5A-2 displayed in PPL with the polarizer rotated by 90° and XPL at 45°. The whole thin section was analysed with SEM, creating an overview map and the red rectangles represents the area for the detailed maps.

5C



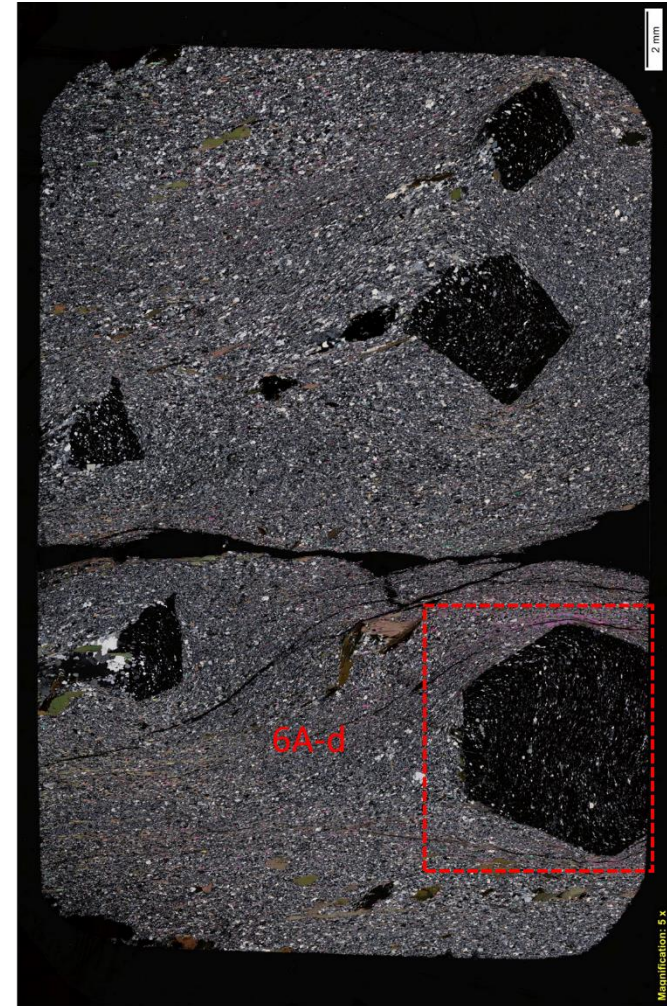
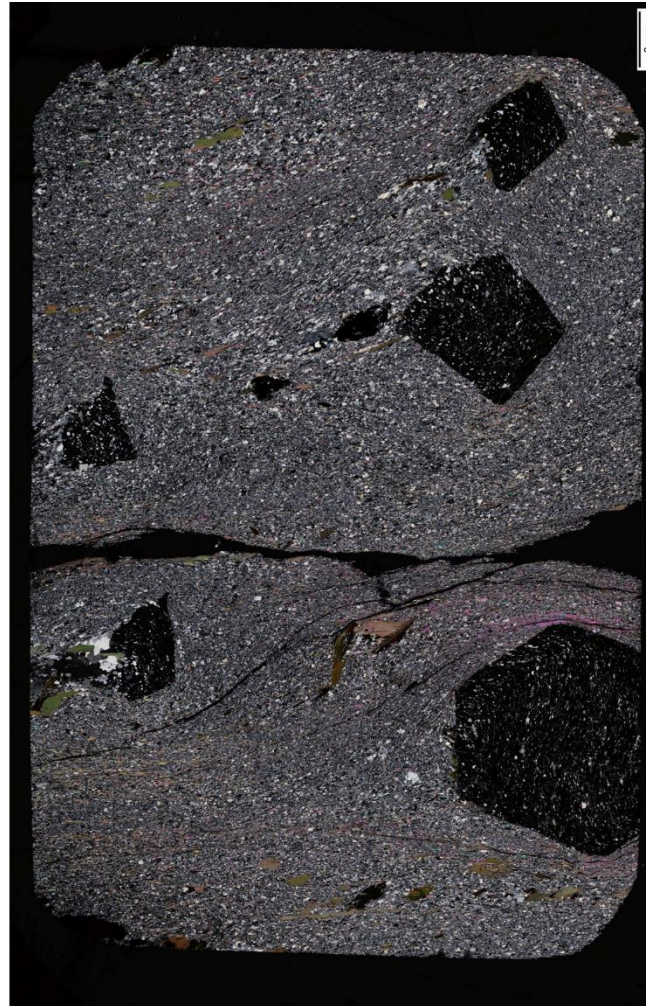
Thin section 5C displayed in PPL with the polarizer rotated by 90° and XPL at 45°.

6A-1



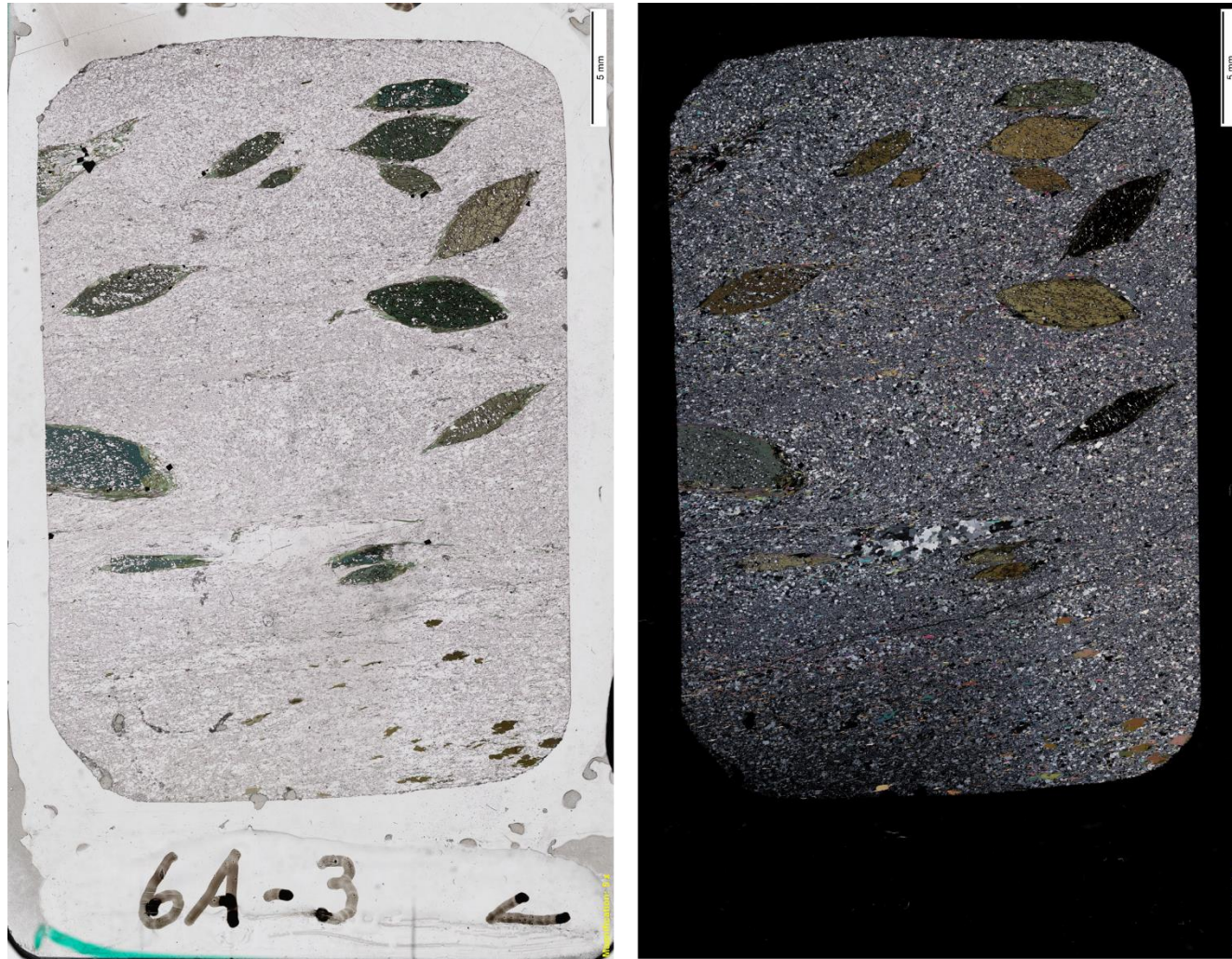
Thin section 6A-1 displayed in PPL with the polarizer rotated by 90° and XPL at 45°.

6A-2



Thin section 6A-2 displayed in PPL with the polarizer rotated by 90° and XPL at 45°. The red rectangles represent the area for the detailed SEM map.

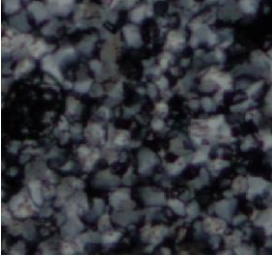
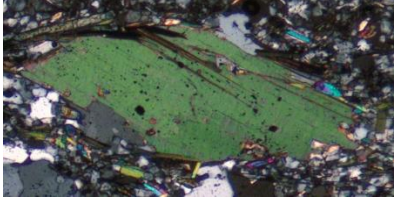
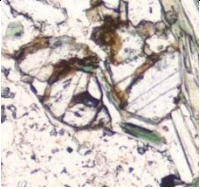

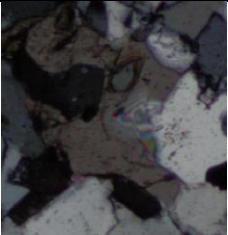
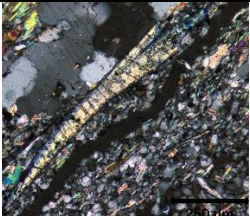
6A-3

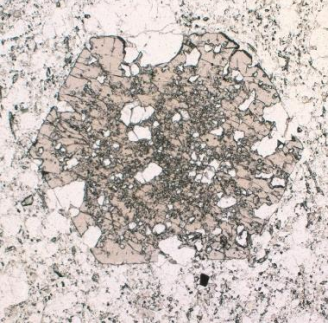
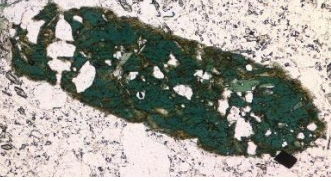
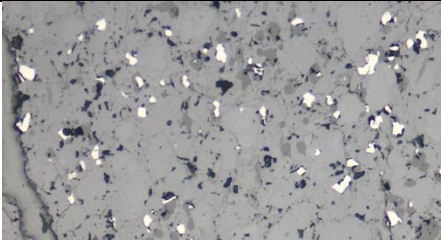
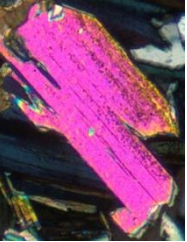
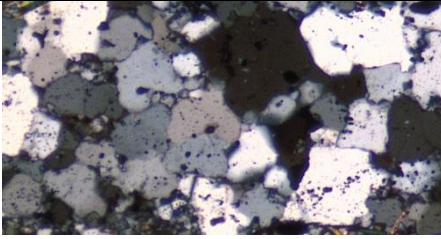


Thin section 6A-3 displayed in PPL with the polarizer rotated by 90° and XPL at 45°.

Appendix D: Modal mineralogy

Common minerals found in most of the samples and some of their mineralogic properties.

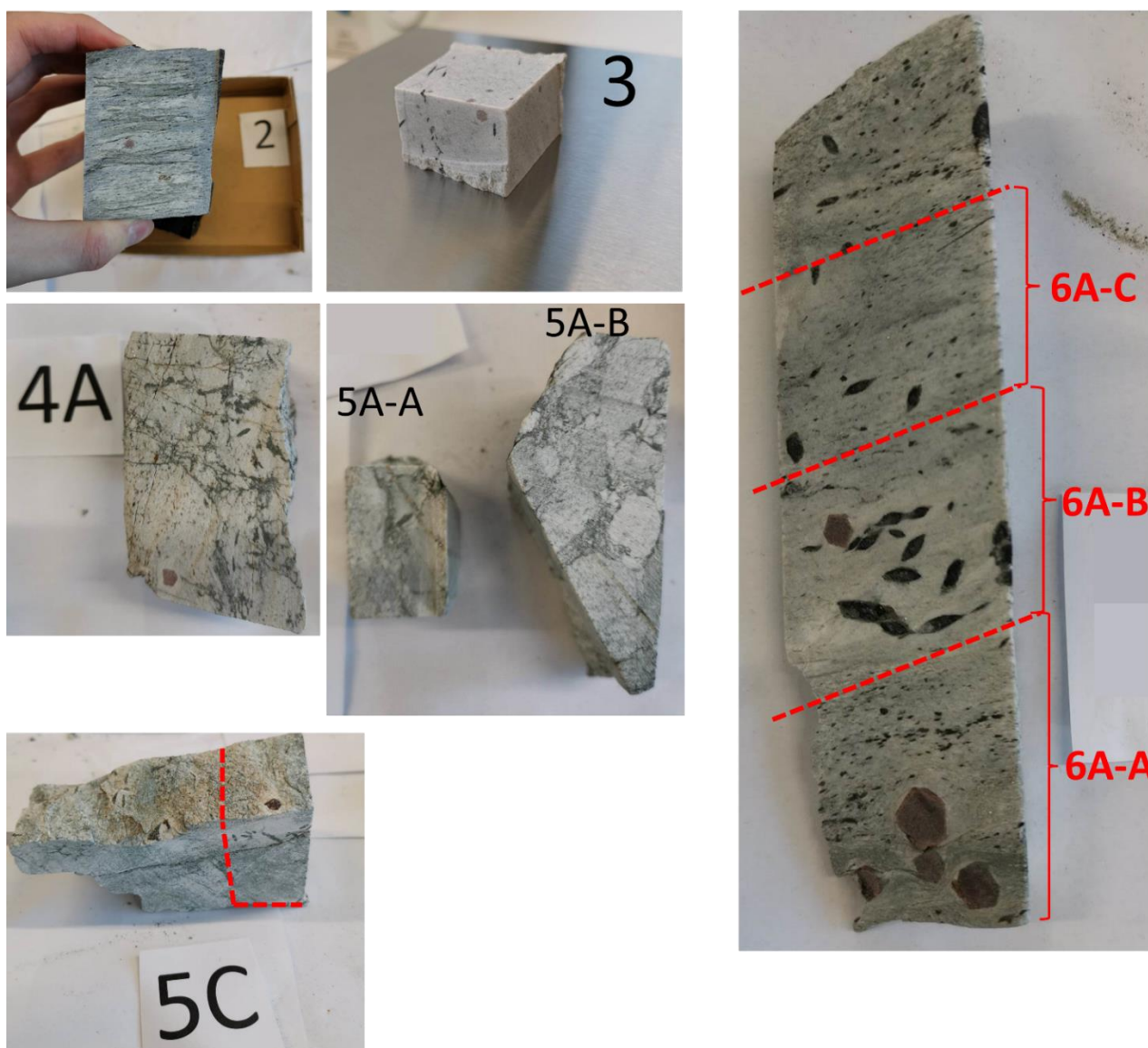
Mineral	Image	Shape (Habitus /contour)	Colour	Interference colour
Albite		Anhedral	Colourless	1.order grey - white
Biotite		An- /subhedral	Brown - Colourless	3.order green - pink
Calcite		Anhedral	Colourless with brown specks	Masked colour - 5.order pink/ turquoise
Chlorite		Sub- /Euhedral	Light green	1. order brown - masked interference colour
Dolomite		Anhedral	Colourless	Masked colour - 5.order pink/ turquoise
Epidote		Euhedral	Yellow/ Grey	

Garnet		Euhedral	Grey	Isotropic
Hornblende		Subhedral	Dark green – Light green	
Magnetite		Anhedral	Opaque	Opaque
Muscovite		Sub- /Euhedral	Colourless	3. order blue - purple
Quartz		Anhedral	Colourless	1.order white

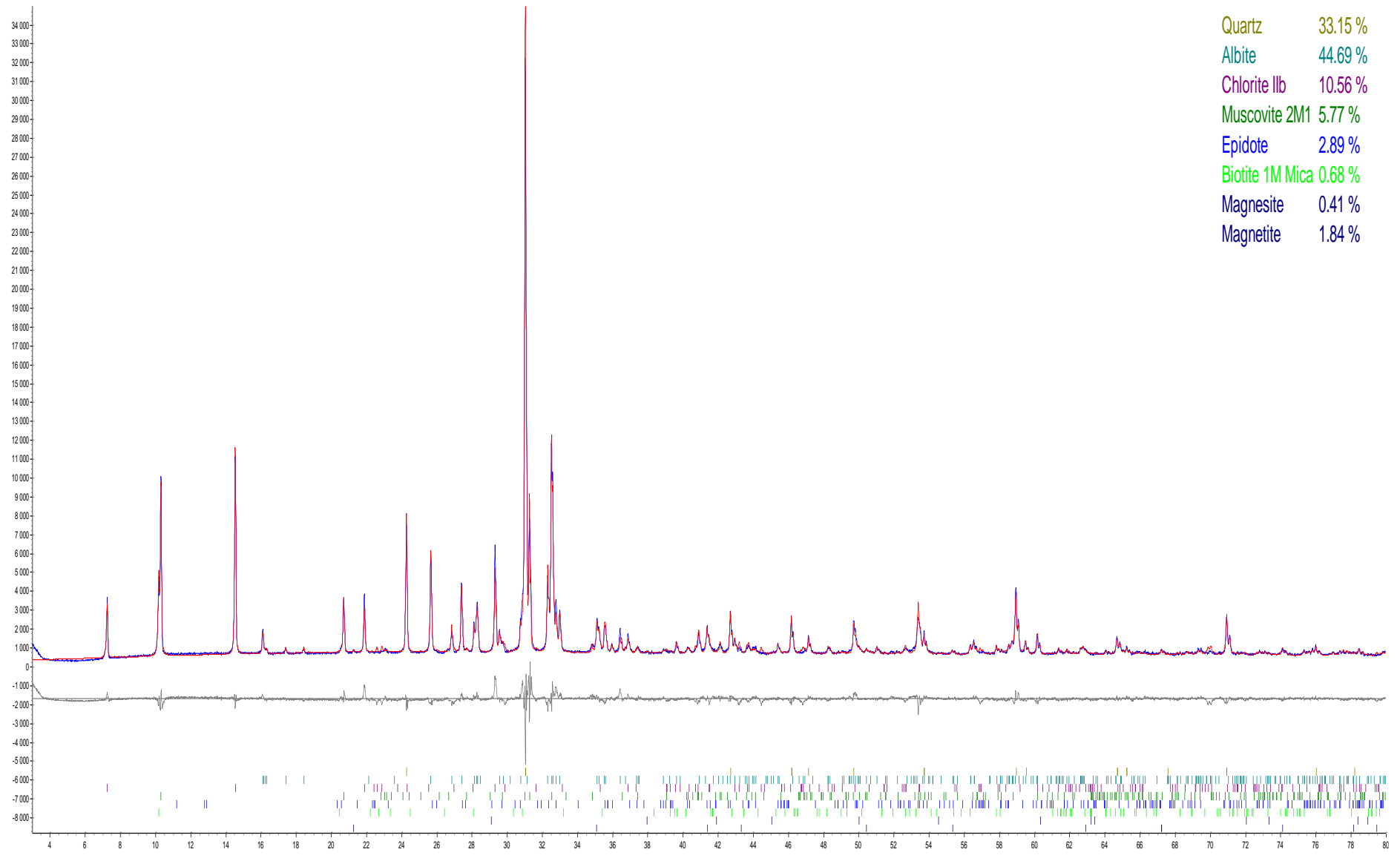
Appendix E: XRD diffractograms

Journal number (J.No)	Sample name for geochemical analyses
220899	2
220900	3
220901	4A
220902	5A-A
220903	5A-B
220905	5C
220906	6A-A
220907	6A-B
220908	6A-C

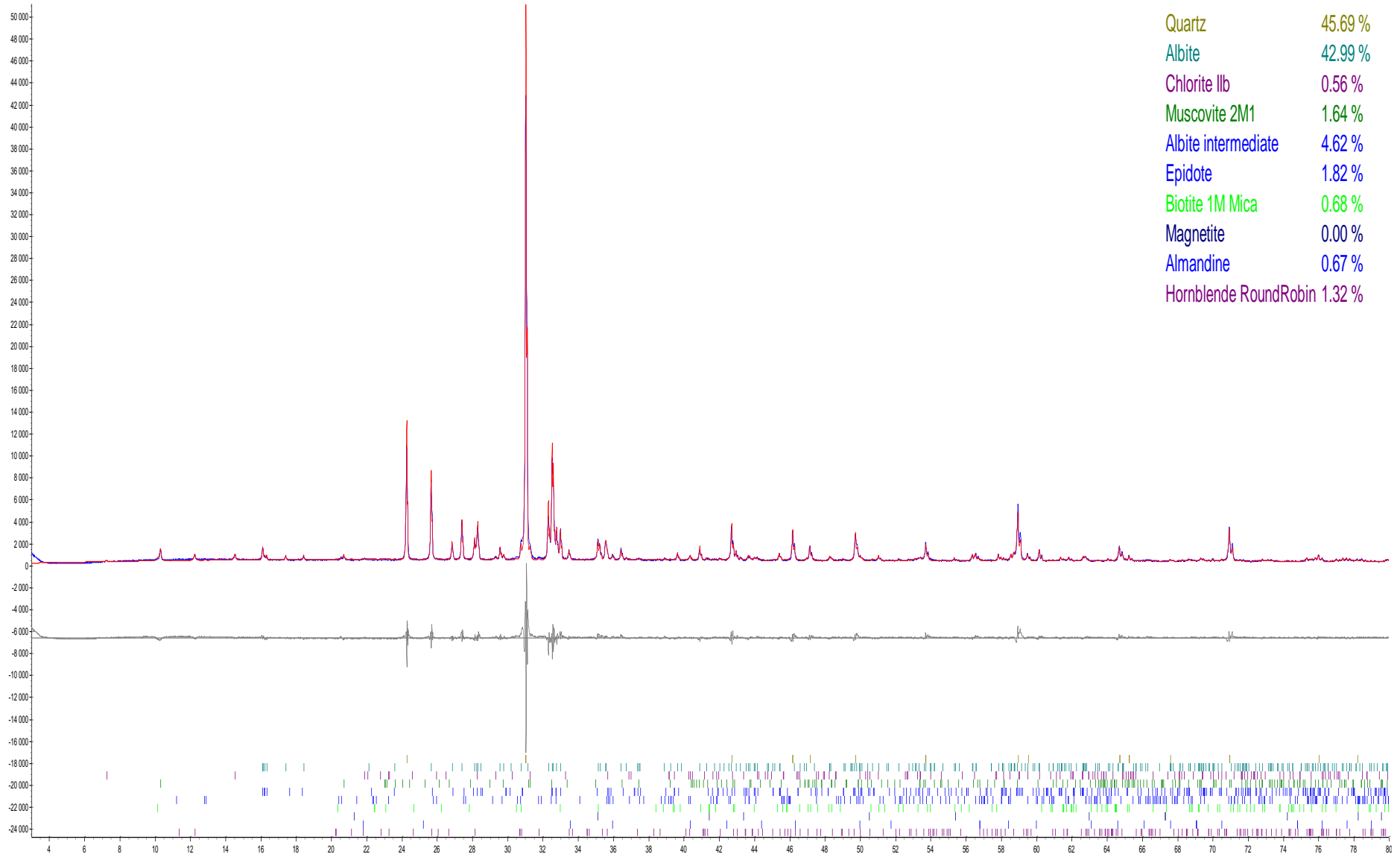
Hand specimens for bulk chemistry



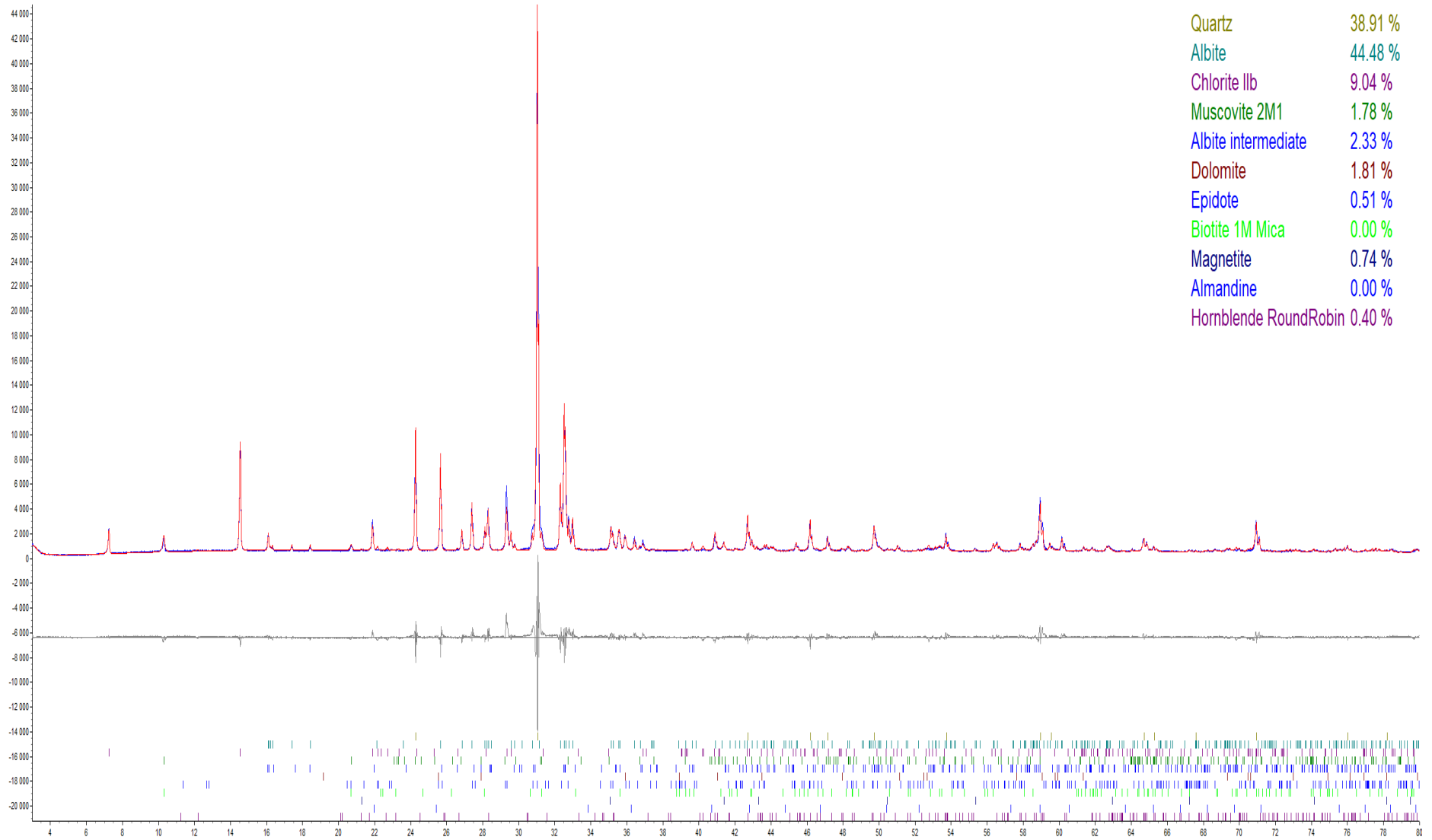
220899: 2



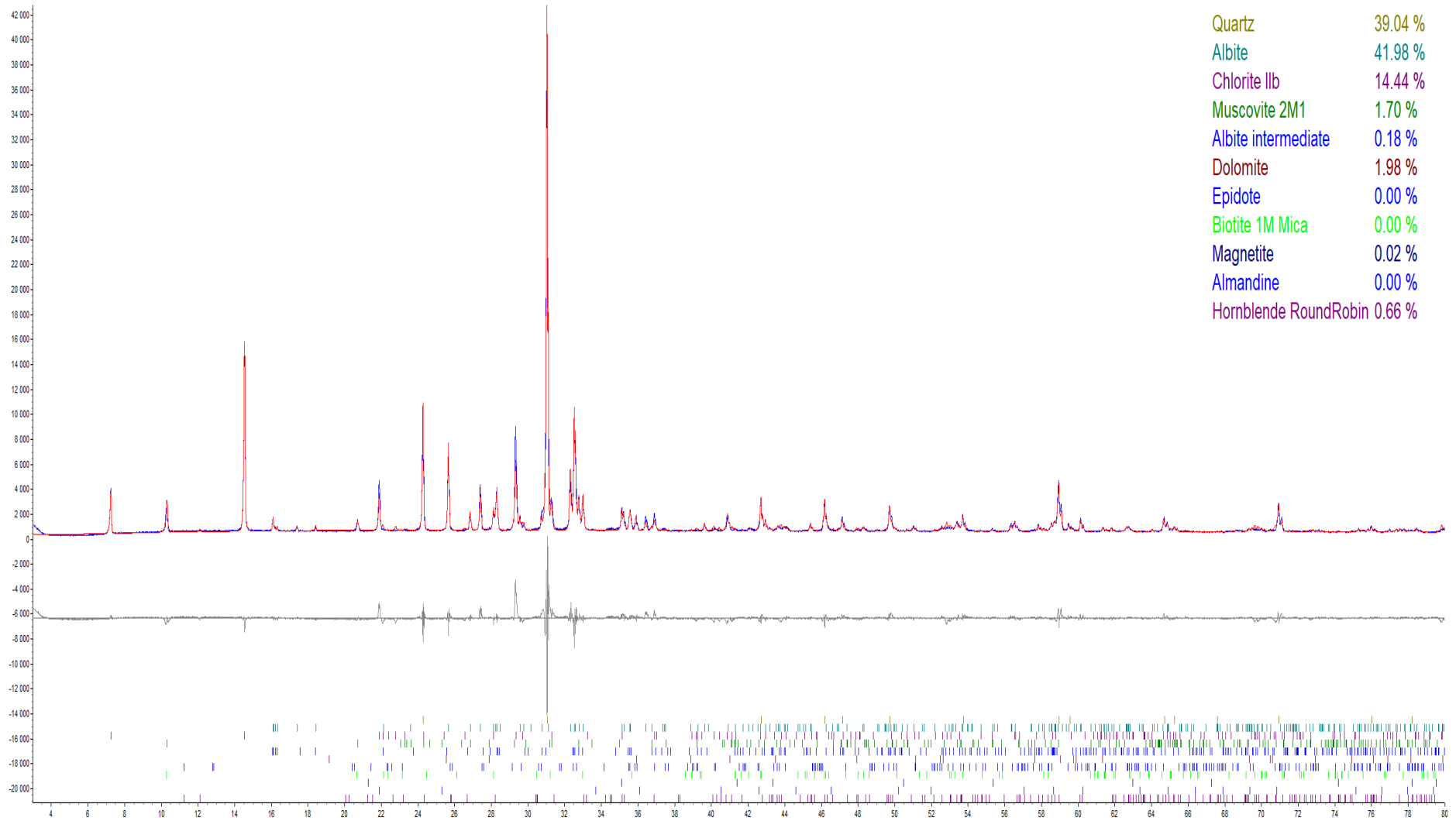
220900: 3



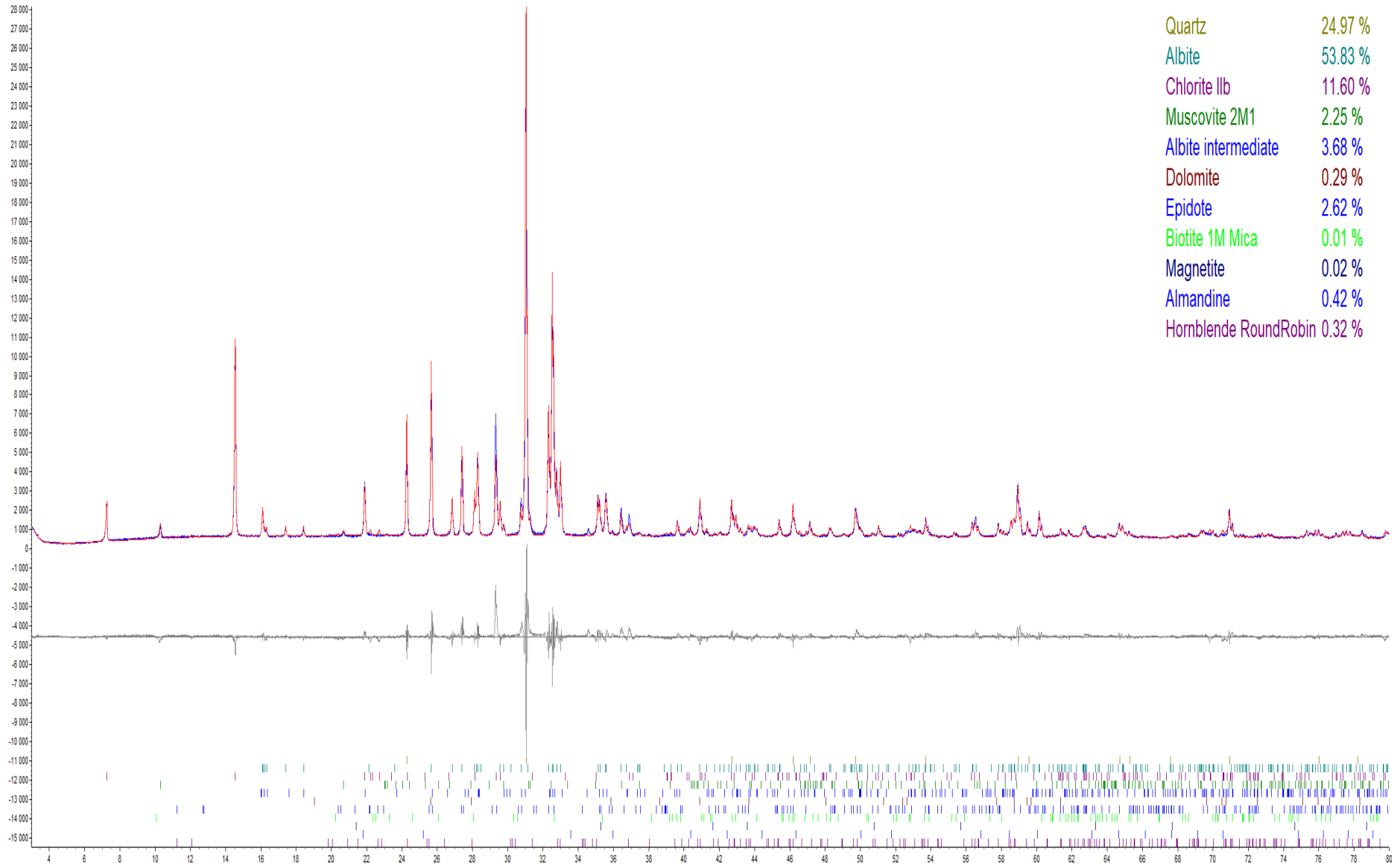
220901: 4a



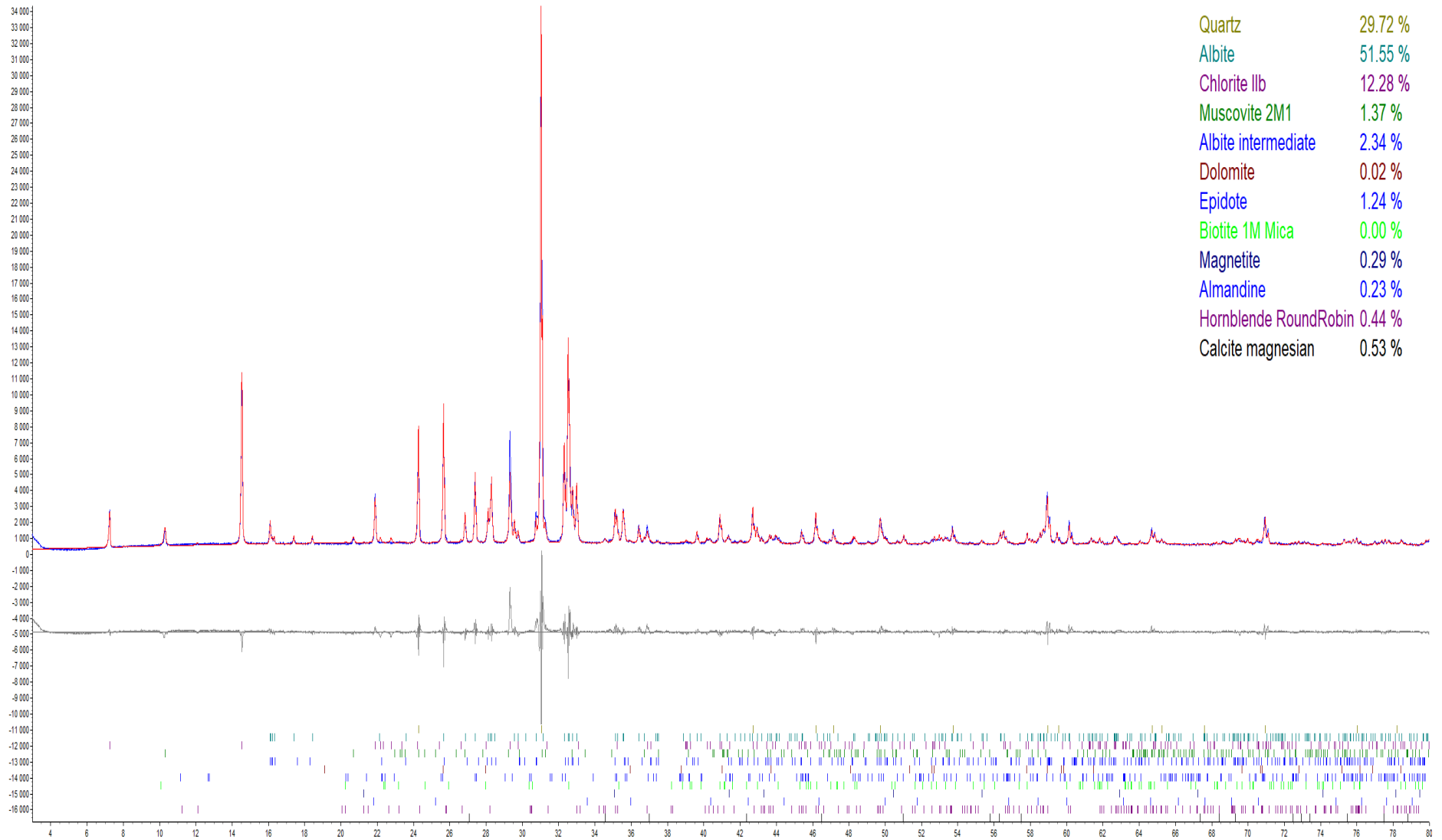
220902: 5a-a



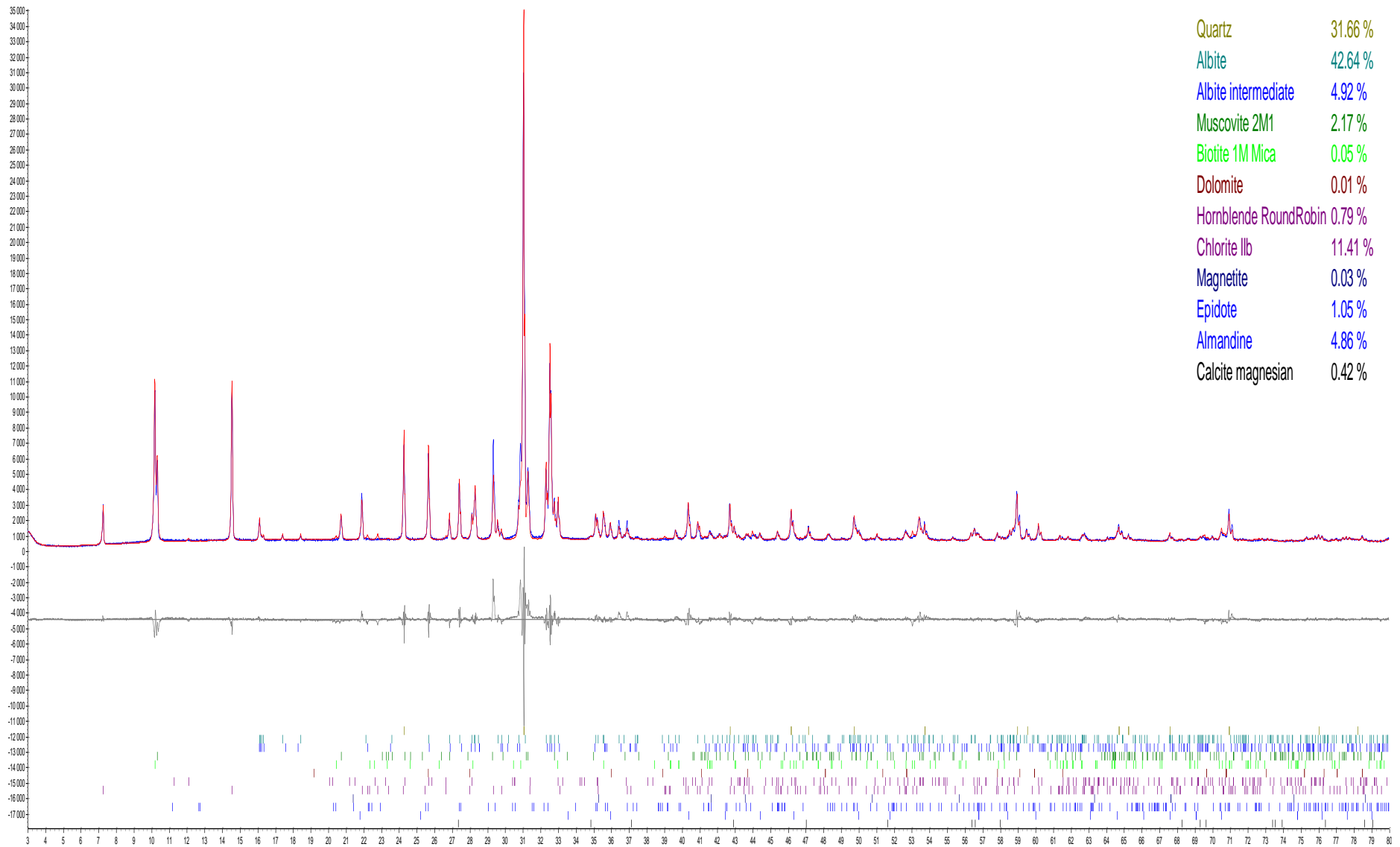
220903: 5a-b



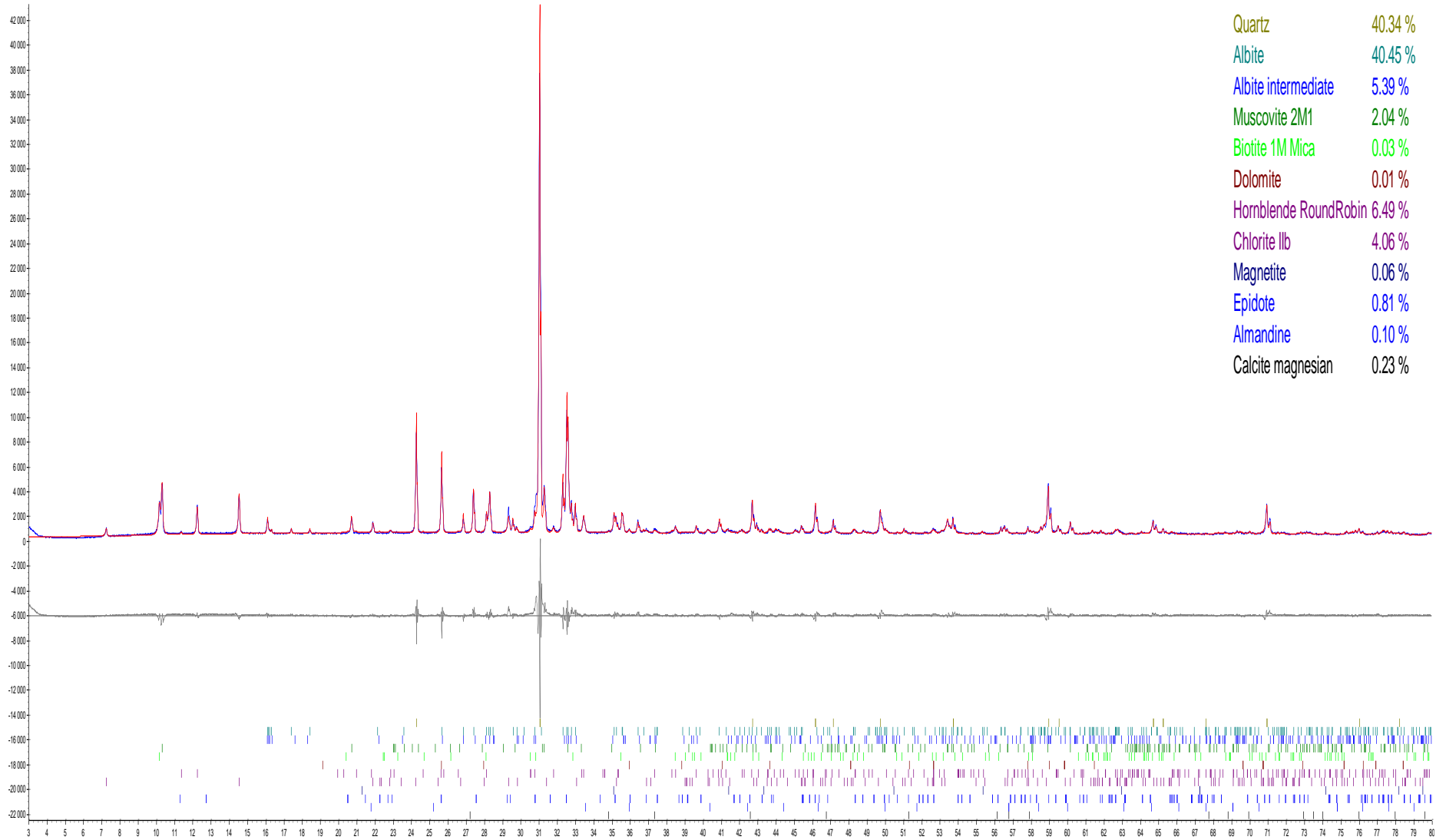
220905: 5c



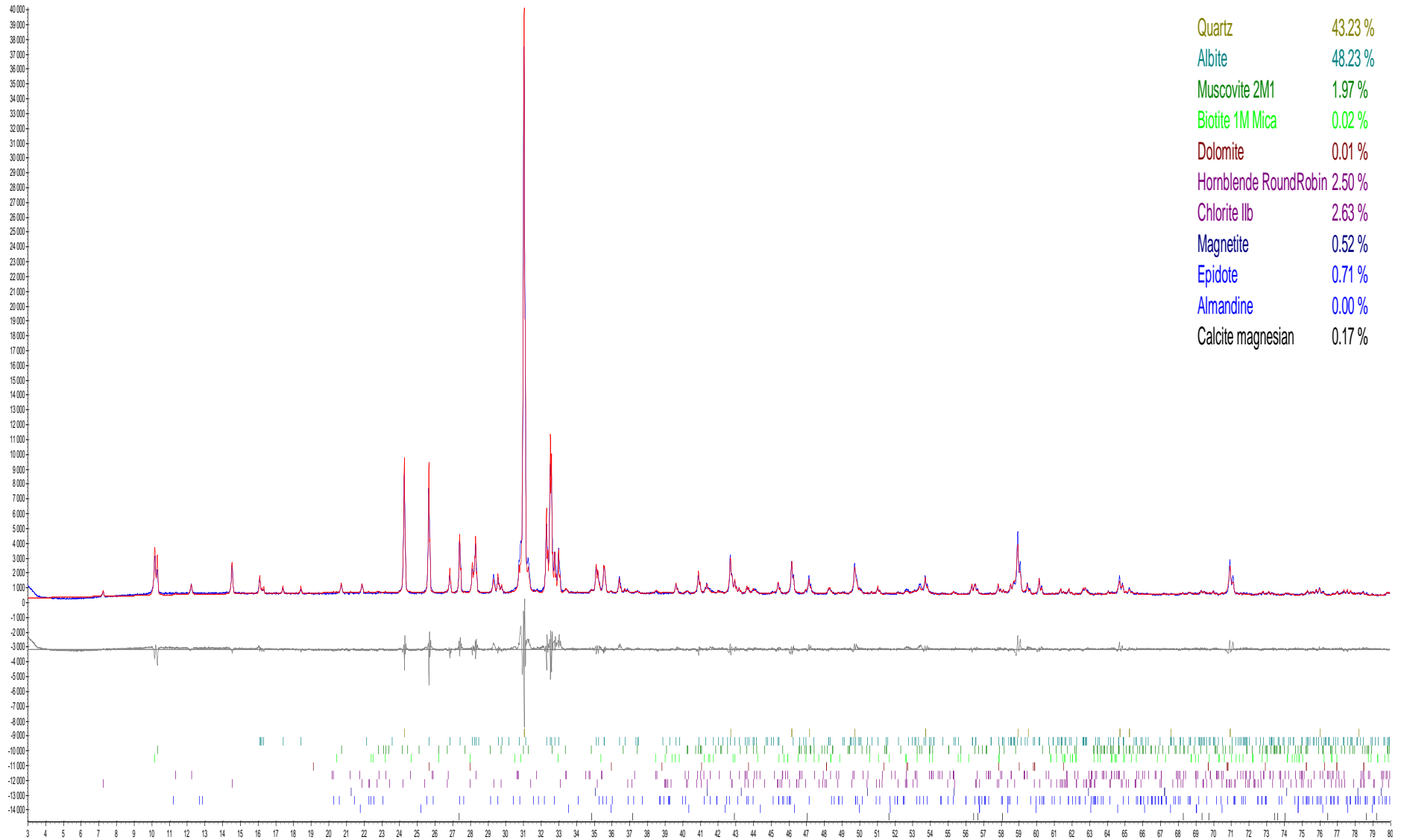
220906: 6A-A



220907: 6A-B



220908: 6A-C



Appendix F: XRF, Major elements

J.No.		22089	22090	22090	22090	22090	22090	22090	22090	22090
Sample		9	0	1	2	3	5	6	7	8
		2	3	4A	5A-A	5A-B	5C	6A-A	6A-B	6A-C
K ₂ O	(wt. %)	1.25	0.223	0.310	0.460	0.296	0.348	0.957	0.682	0.704
MgO	(wt. %)	0.870	0.144	0.895	1.15	1.13	1.08	0.894	0.702	0.608
Mn ₃ O ₄	(wt. %)	0.045	0.068	0.059	0.071	0.066	0.065	0.350	0.053	0.026
Na ₂ O	(wt. %)	5.13	4.54	5.50	5.30	7.12	6.42	5.53	5.38	5.68
P ₂ O ₅	(wt. %)	<0.00	<0.00	<0.00	<0.00	<0.00	<0.00	<0.00	<0.00	<0.00
SiO ₂	(wt. %)	3	3	3	3	3	3	3	3	3
TiO ₂	(wt. %)	70.7	82.8	74.8	73.7	70.3	71.7	71.1	75.5	75.9
Al ₂ O ₃	(wt. %)	0.182	0.101	0.143	0.157	0.191	0.164	0.159	0.138	0.147
CaO	(wt. %)	13.6	9.00	11.1	11.7	14.6	13.6	13.9	11.8	11.9
Fe ₂ O ₃	(wt. %)	0.999	0.770	0.901	1.06	0.517	0.553	0.670	0.943	0.558
NiO	(wt. %)	5.15	1.23	3.79	3.49	3.79	4.16	5.03	3.49	3.24
PbO	(wt. %)	<0.00	<0.00	<0.00	<0.00	<0.00	<0.00	<0.00	<0.00	<0.00
SO ₃	(wt. %)	2	2	2	0.005	2	2	2	2	2
SrO	(wt. %)	<0.00	<0.00	<0.00	<0.00	<0.00	<0.00	<0.00	<0.00	<0.00
V ₂ O ₅	(wt. %)	9	9	9	9	9	0.011	9	9	9
ZnO	(wt. %)	<0.00	<0.00	<0.00	<0.00	<0.00	<0.00	<0.00	<0.00	<0.00
ZrO ₂	(wt. %)	2	2	2	2	2	2	2	2	2
BaO	(wt. %)	0.011	0.001	0.018	0.020	0.021	0.022	0.015	0.013	0.012
Cr ₂ O ₃	(wt. %)	0.053	0.026	0.037	0.041	0.057	0.045	0.048	0.040	0.041
CuO	(wt. %)	0.019	0.005	0.009	0.009	0.008	0.011	0.032	0.020	0.021
HfO ₂	(wt. %)	<0.00	<0.00	<0.00	<0.00	<0.00	<0.00	<0.00	<0.00	<0.00
LOI 1000°C	(%)	3	3	3	3	3	3	3	3	3
Sum	(wt. %)	<0.00	<0.00	<0.00	<0.00	<0.00	<0.00	<0.00	<0.00	<0.00
	(wt. %)	1	1	1	1	1	1	1	1	1
	(wt. %)	<0.00	<0.00	<0.00	<0.00	<0.00	<0.00	<0.00	<0.00	<0.00
	(wt. %)	3	3	3	3	3	0.005	3	3	3
	(wt. %)	1.29	0.27	1.66	2.02	1.24	1.22	0.60	0.53	0.52
	(wt. %)	99.30	99.15	99.13	99.11	99.26	99.36	99.21	99.35	99.30

Loss of ignition (LOI) for all samples before analysing the content of major elements with XRF

J.No.	Weight of crucible (g)	Weight of crucible + sample weight (g)	Weight of crucible + sample weight after ignition (g)	Weight of sample (g)	Weight of sample after ignition (g)	Loss of mass (g)	LOI (%) 1000° C
220899	17.5062	20.0115	19.9791	2.5053	2.4729	0.0324	1.29
220900	16.4692	18.9702	18.9634	2.5010	2.4942	0.0068	0.27
220901	16.9142	19.4519	19.4098	2.5377	2.4956	0.0421	1.66
220902	16.3121	18.8231	18.7723	2.5110	2.4602	0.0508	2.02
220903	16.0268	18.5389	18.5078	2.5121	2.4810	0.0311	1.24
220905	15.39	17.8931	17.8625	2.5031	2.4725	0.0306	1.22
220906	13.9299	16.4287	16.4136	2.4988	2.4837	0.0151	0.60
220907	16.1437	18.6456	18.6323	2.5019	2.4886	0.0133	0.53
220908	17.2877	19.7843	19.7714	2.4966	2.4837	0.0129	0.52

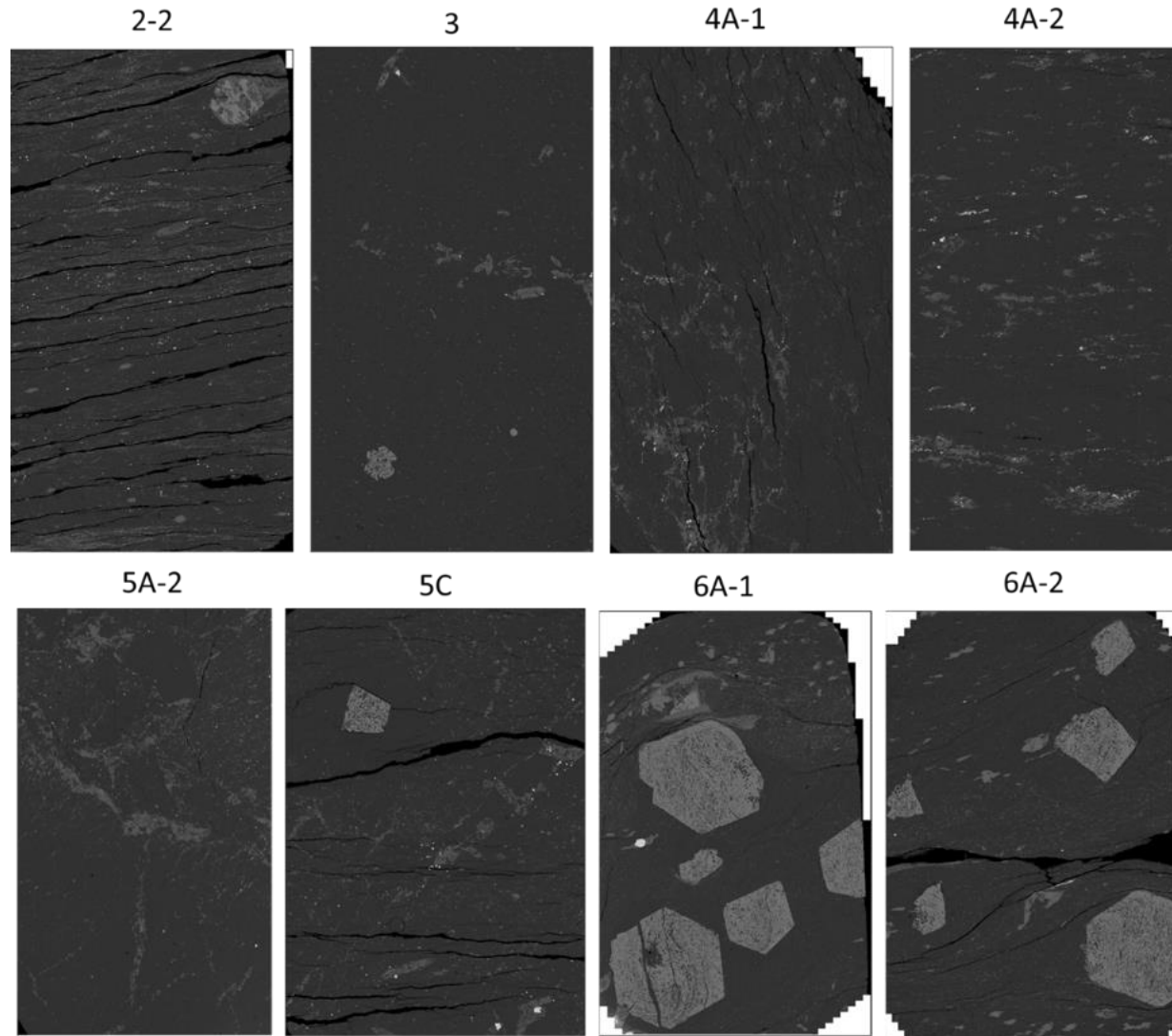
Appendix G: XRF, Trace elements

J.No. Sample marked	2208 99	2209 00	2209 01	2209 02	2209 03	2209 05	2209 06	2209 07	2209 08
	2	3	4A	5A-A	5A-B	5C	6A-A	6A-B	6A-C
Sc (ppm)	4.5	2.5	3.6	4.2	5.4	5	4.3	4	3.8
V (ppm)	8.8	1.7	<1.5	2	2.4	2.3	3.9	2.9	2.8
Cr (ppm)	<1.3	7.3	<1.3	3.3	<1.3	<1.3	<1.3	1.3	<1.3
Mn (ppm)	284	367	475	539	423	414	1936	316	165
Co (ppm)	32	50	32.1	21.7	18.7	19	34	40.4	37.7
Ni (ppm)	3.2	2.2	2.1	1.8	2.3	1.7	2	1.8	2
Cu (ppm)	10.3	4.9	<0.8	2.6	1.6	0.9	2.7	1.6	<0.8
Zn (ppm)	88.1	13.3	138.1	134.8	159.9	164.8	114.6	105.1	91.6
Ga (ppm)	23.7	10.7	20.1	22.5	25.6	24.9	25.3	22.6	22.2
Ge (ppm)	0.4	0.6	0.2	0.2	0.3	0.6	0.7	0.6	0.4
As (ppm)	5.1	5.4	5.3	4	<2.5	4.5	5	5.6	3.9
Se (ppm)	<0.5	1.2	1	<0.5	<0.5	<0.5	<0.5	0.7	0.8
Br (ppm)	<0.5	<0.5	0.5	<0.5	<0.5	0.5	<0.5	<0.5	<0.5
Rb (ppm)	12.4	1.7	2.9	4.1	2.3	3	9.2	5.8	6.5
Sr (ppm)	74.6	45.3	49.1	60.6	67.8	63.8	35.4	50.4	46.4
Y (ppm)	102	90.8	105	87.2	138	96.9	104	96.7	98.1
Zr (ppm)	389	221	302	319	416	347	361	298	301
Nb (ppm)	7.1	3.8	5.6	6	7.1	5.8	7.5	6	6.3
Mo (ppm)	1.4	1	1.2	1.3	1.5	1.1	1.1	1	1.1
Ag (ppm)	6.3	5.4	5.9	5.2	6.1	6.2	6.2	6	6.8
Cd (ppm)	7.2	5.6	6.8	6.6	6.6	6.2	7.7	7.3	6.6
Sn (ppm)	2	<1.5	1	1.7	<1.5	3.1	1.7	4	2.3
Sb (ppm)	<1.6	<1.6	<1.6	<1.6	<1.6	<1.6	<1.6	<1.6	<1.6
Te (ppm)	<1.8	<1.8	<1.8	<1.8	<1.8	<1.8	<1.8	<1.8	<1.8
I (ppm)	2.8	2.7	<2.0	3.1	<2.0	2	<2.0	2.3	2.7
Cs (ppm)	<4.0	<4.0	<4.0	<4.0	<4.0	<4.0	<4.0	<4.0	<4.0
Ba (ppm)	167	23.8	37.7	65.9	34.6	50.7	244	136	145
La (ppm)	13.5	9.4	6.4	<6.0	16.8	12.2	10.7	17.7	17.2
Ce (ppm)	38.5	22.1	25.9	22.3	45.3	42	30.6	42.6	34.1
Nd (ppm)	28	22.8	27.5	19.5	40.9	38.2	26.8	35.1	33.1
Sm (ppm)	6.7	8.8	13.6	10.3	15.7	10.2	8.2	13.8	13.6
Yb (ppm)	7.6	7.5	6.2	6.5	10.8	10.3	8.1	6.4	6.6
Hf (ppm)	16.5	10.4	14.4	14.1	17	15	15.3	12.5	13.5
Ta (ppm)	<1.3	<1.3	<1.3	<1.3	<1.3	<1.3	<1.3	<1.3	<1.3
W (ppm)	242	383	257	157	123	138	227	297	285
Tl (ppm)	<0.8	<0.8	<0.8	<0.8	<0.8	<0.8	<0.8	<0.8	<0.8
Pb (ppm)	0.9	<0.8	<0.8	<0.8	<0.8	<0.8	<0.8	<0.8	<0.8
Bi (ppm)	<1.0	<1.0	<1.0	<1.0	<1.0	<1.0	<1.0	<1.0	<1.0
Th (ppm)	14	12.9	13.7	13.7	14.1	13.4	13.2	13.4	13.6
U (ppm)	2.5	2.4	1.8	2.1	2.1	2.4	1.9	2.3	2

Appendix H: ICP-MS

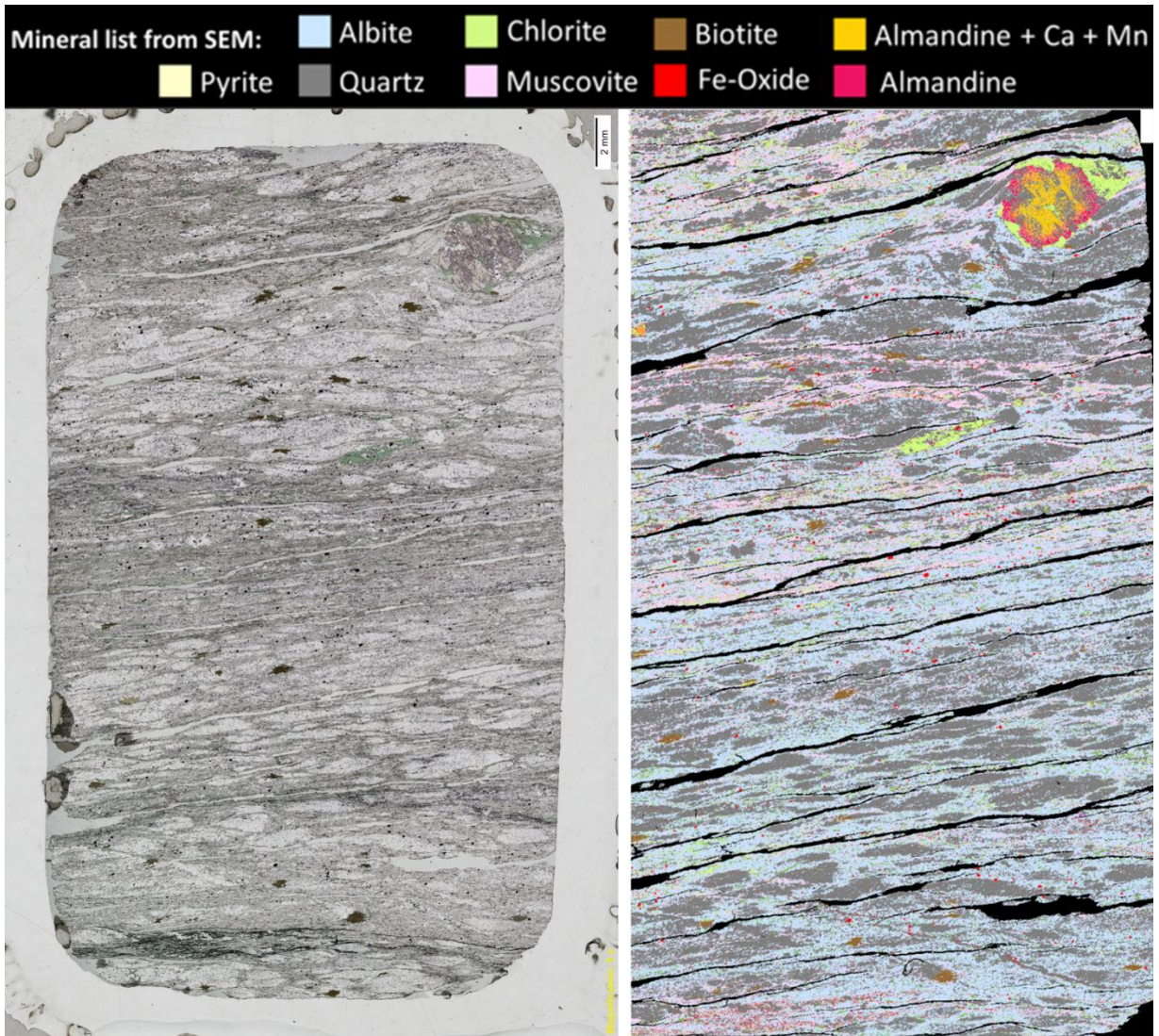
			2208	2209	2209	2209	2209	2209	2209	2209	2209
		J.No	99	00	01	02	03	05	06	07	08
		Sample	2	3	4A	5A-A	5A-B	5C	6A-A	6A-B	6A-C
Element	Mass	Detection Limit	mg/kg	mg/kg	mg/kg	mg/kg	mg/kg	mg/kg	mg/kg	mg/kg	mg/kg
P	31	20	298	375	278	222	278	368	184	265	358
K	39	0.3	8030	2260	2550	3680	2610	3170	6400	5100	5240
Ti	48	0.5	1070	603	861	865	1160	1030	995	852	865
Rb	85	2	12.2	2.78	2.92	4.09	< 2	2.18	8.43	4.83	5.62
Sr	87	8	85.5	58	53.8	62.1	83.8	80.1	47.2	62.7	59
Y	89	2	111	100	117	95	156	109	125	114	115
Zr	90	0.2	231	144	192	190	248	218	220	184	187
Nb	93	3	5.87	< 3	4.57	5.06	6.55	5.85	6.85	5.21	5.24
Ba	138	0.2	159	35.4	46.1	78.2	42.4	55.2	240	158	163
La	139	0.3	16.7	20.9	13.9	9.41	22	20.6	14	19.6	17.7
Ce	140	0.08	47.7	45.7	41	27.2	61.1	60.7	44.2	57.2	55.1
Pr	141	0.6	7.62	6.3	7	4.09	9.19	9.33	6.94	8.82	8.48
Nd	142	10	36.5	27.4	33.7	20.4	42.9	42.7	33.4	40.4	39.7
Sm	152	7	12.8	10.1	12.1	8.3	15.2	15.5	12	15.3	14.6
Eu	153	2	2.37	< 2	2.53	< 2	3.52	2.88	2.18	2.94	3.15
Gd	158	1	14.5	12	16.2	10.7	18.2	17.5	13.7	16.7	16.6
Tb	159	2	3.16	2.78	3.21	2.4	3.71	3.37	3.08	3.22	3.72
Dy	164	1	12	10.2	12.3	9.68	14.8	12.2	12.4	12.4	12.5
Ho	165	2	4.21	3.98	4.28	3.55	5.47	4.27	4.56	4.36	4.39
Er	166	6	12.5	12.6	13.2	10.1	17	12.8	13.9	12.4	12.4
Tm	169	3	< 3	< 3	< 3	< 3	< 3	< 3	< 3	< 3	< 3
Yb	174	3	12.1	11.4	10.5	8.61	15.1	12.7	14.7	10.2	10.1
Lu	175	2	< 2	< 2	< 2	< 2	2.15	< 2	2.28	< 2	< 2
Hf	180	5	11.6	6.85	9.63	9.59	12.4	10.8	10.7	9.48	8.96
Ta	181	3	< 3	< 3	< 3	< 3	< 3	< 3	< 3	< 3	< 3
Th	232	0.5	1.75	1.39	1.56	1.24	1.86	1.79	1.79	1.61	1.62

Appendix I: EBS-images and mineral maps from SEM



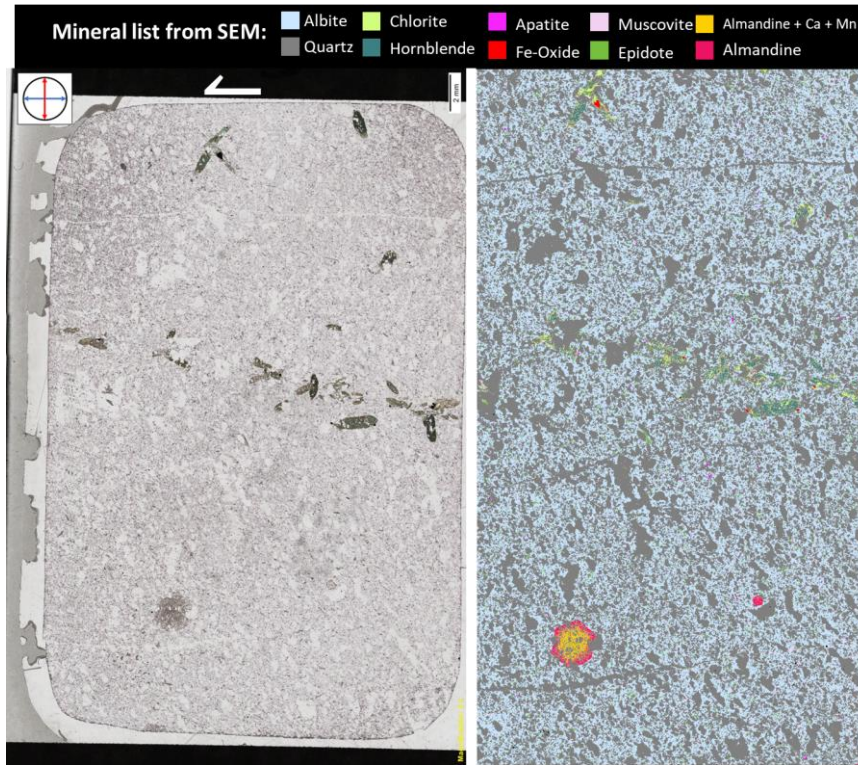
Phyllonitic shear zone

2-2



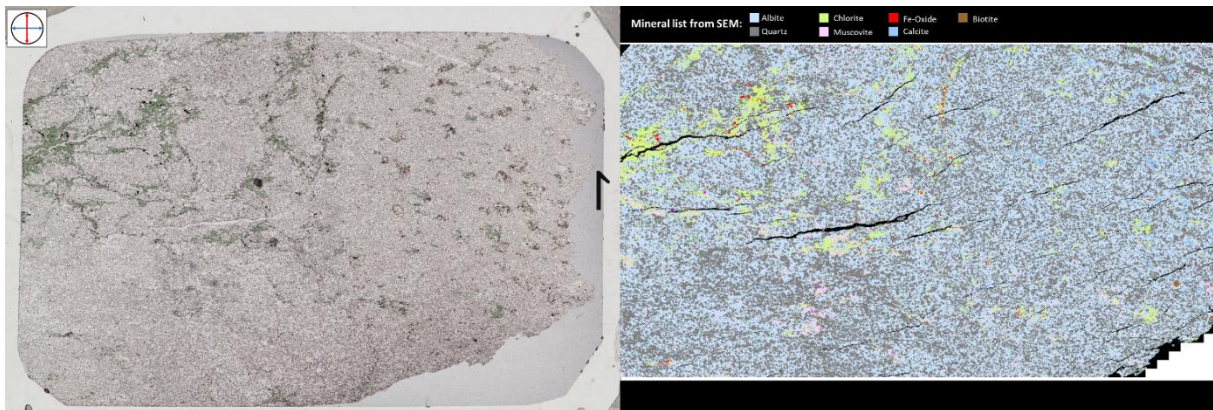
Protolith

3

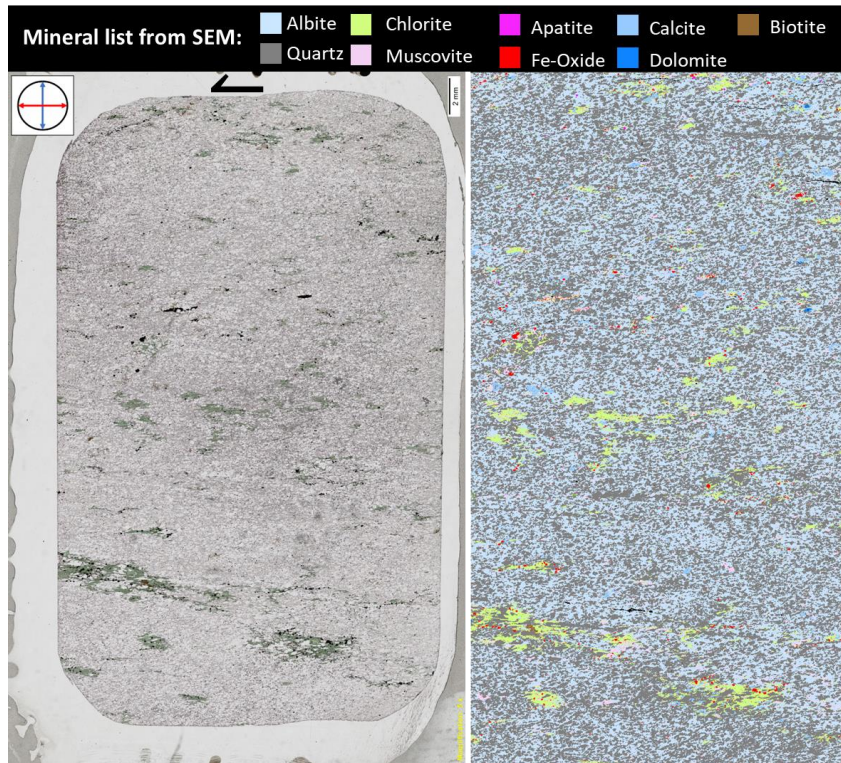


Breccia zone

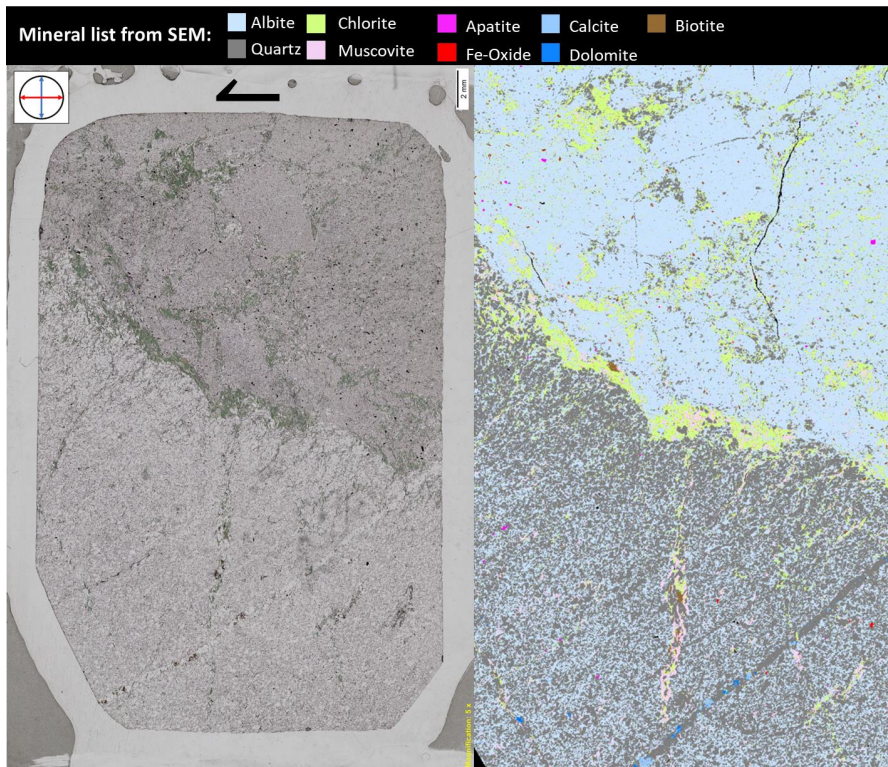
4A-1



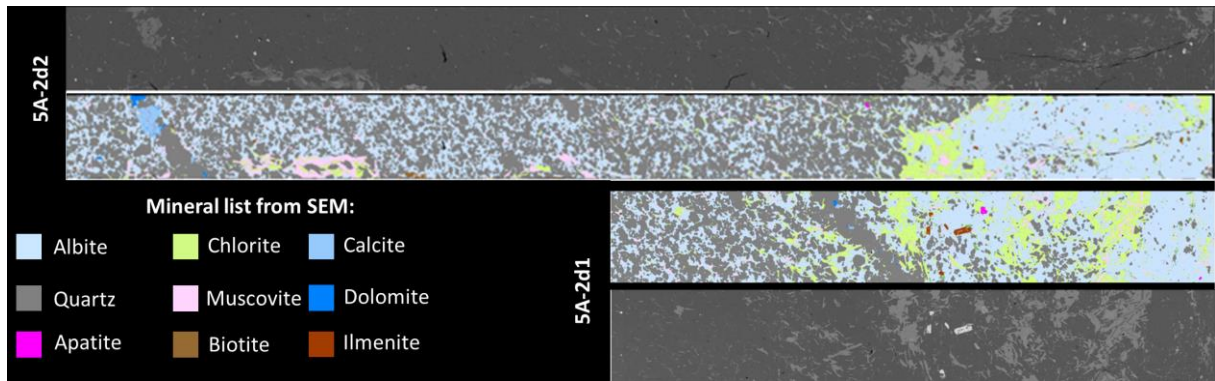
4A-2



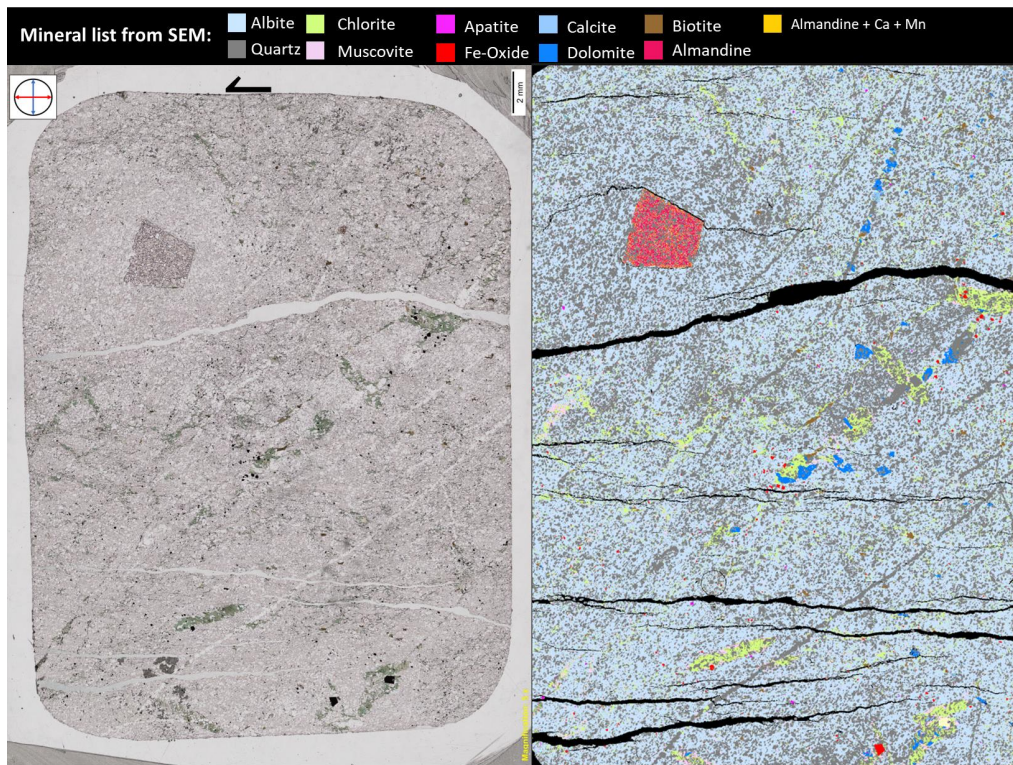
5A-2



5A-2d

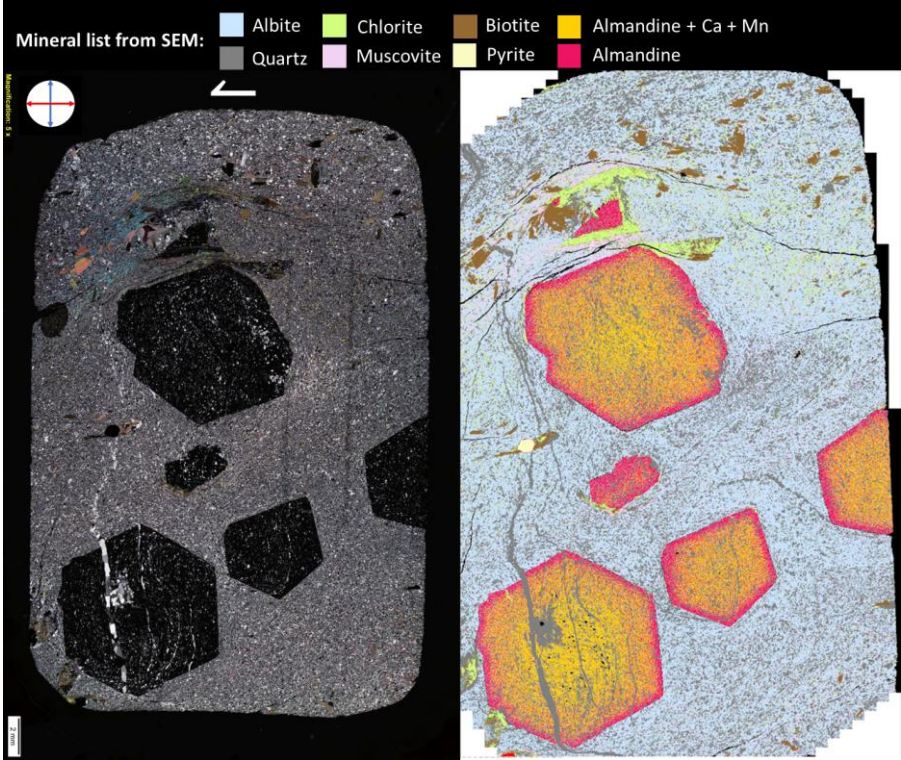


5C

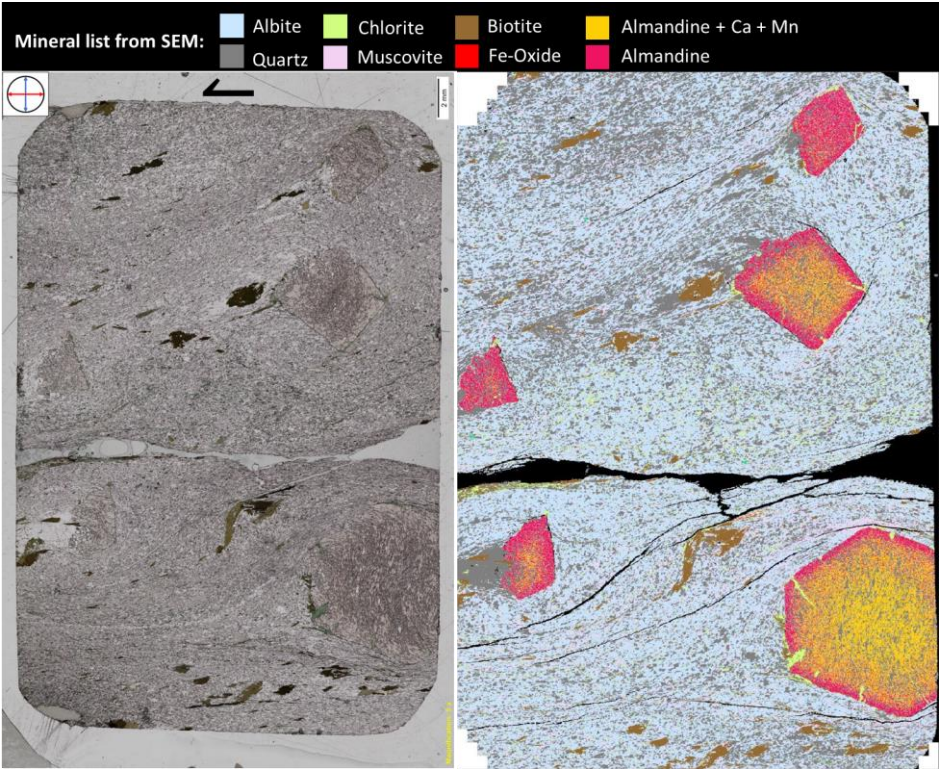


Garnet-Biotite shear zone

6A-1



6A-2



Appendix J: EPMA, data and stoichiometry

Mineral chemistry of the rim of garnets in thin section 6A-2. Mineral formula normalised to 12 oxygen, Fe³⁺ was not analysed. Sample size = 15.

EPMA analysis								
Sample	MgO (wt. %)	SiO ₂ (Wt. %)	Al ₂ O ₃ (Wt. %)	MnO (Wt. %)	FeO (Wt. %)	TiO ₂ (Wt. %)	CaO (Wt. %)	Total (Wt. %)
6A-2_Grt_007	1.24	36.83	25.84	2.27	33.31	0.06	5.88	105.42
6A-2_Grt_008	1.35	36.67	25.95	2.14	33.68	0.06	5.61	105.45
6A-2_Grt_009	1.25	36.67	25.90	2.41	33.38	0.06	5.59	105.27
6A-2_Grt_010	1.23	36.69	25.84	2.63	33.51	0.06	5.42	105.37
6A-2_Grt_011	1.25	36.82	25.87	2.25	33.21	0.05	5.83	105.27
6A-2_Grt_013	1.26	37.06	25.67	2.22	33.17	0.04	5.81	105.24
6A-2_Grt_014	1.15	36.83	25.74	2.73	32.77	0.07	6.04	105.32
6A-2_Grt_015	1.20	36.84	25.73	2.63	33.15	0.06	5.59	105.20
6A-2_Grt_016	1.15	36.84	25.57	2.92	32.68	0.06	5.89	105.10
6A-2_Grt_017	1.23	36.84	25.78	2.39	32.68	0.06	5.84	104.82
6A-2_Grt_018	1.25	36.93	25.96	2.17	32.81	0.04	5.87	105.02
6A-2_Grt_019	1.28	36.98	25.86	2.03	33.07	0.05	5.84	105.11
6A-2_Grt_020	1.05	36.93	25.71	3.55	31.20	0.08	6.28	104.79
6A-2_Grt_021	1.28	37.02	25.91	2.31	33.04	0.05	5.53	105.12
6A-2_Grt_022	1.00	36.80	25.46	3.97	31.26	0.10	6.07	104.66
Average	1.21	36.85	25.79	2.57	32.86	0.06	5.80	105.14

Stoichiometry								
Sample	Si ⁴⁺	Ti ⁴⁺	Al ³⁺	Fe ²⁺	Mn ²⁺	Mg ²⁺	Ca ²⁺	Total
6A-2_Grt_007	2.81	0.00	2.32	2.12	0.15	0.14	0.48	8.03
6A-2_Grt_008	2.80	0.00	2.33	2.15	0.14	0.15	0.46	8.03
6A-2_Grt_009	2.80	0.00	2.33	2.13	0.16	0.14	0.46	8.03
6A-2_Grt_010	2.80	0.00	2.33	2.14	0.17	0.14	0.44	8.03
6A-2_Grt_011	2.81	0.00	2.33	2.12	0.15	0.14	0.48	8.02
6A-2_Grt_013	2.83	0.00	2.31	2.12	0.14	0.14	0.47	8.02
6A-2_Grt_014	2.81	0.00	2.32	2.09	0.18	0.13	0.49	8.03
6A-2_Grt_015	2.82	0.00	2.32	2.12	0.17	0.14	0.46	8.02
6A-2_Grt_016	2.82	0.00	2.31	2.09	0.19	0.13	0.48	8.02
6A-2_Grt_017	2.82	0.00	2.33	2.09	0.15	0.14	0.48	8.01
6A-2_Grt_018	2.82	0.00	2.34	2.09	0.14	0.14	0.48	8.01
6A-2_Grt_019	2.82	0.00	2.33	2.11	0.13	0.15	0.48	8.01
6A-2_Grt_020	2.83	0.00	2.32	2.00	0.23	0.12	0.51	8.01
6A-2_Grt_021	2.82	0.00	2.33	2.11	0.15	0.15	0.45	8.01
6A-2_Grt_022	2.83	0.01	2.30	2.01	0.26	0.11	0.50	8.02
Average	2.82	0.00	2.32	2.10	0.17	0.14	0.48	8.02

Mineral chemistry of the core of garnets in thin section 6A-2. Mineral formula normalised to 12 oxygen, Fe³⁺ was not analysed. Sample size = 7.

EPMA analysis								
Sample	MgO (wt. %)	SiO ₂ (Wt. %)	Al ₂ O ₃ (Wt. %)	MnO (Wt. %)	FeO (Wt. %)	TiO ₂ (Wt. %)	CaO (Wt. %)	Total (Wt. %)
6A-2_Grt_001	0.69	36.40	25.74	6.09	29.88	0.12	5.98	104.89
6A-2_Grt_002	0.64	36.50	25.39	6.99	29.32	0.11	5.94	104.89
6A-2_Grt_003	0.63	36.29	25.30	7.28	28.99	0.10	5.39	103.99
6A-2_Grt_004	0.65	36.61	25.44	6.27	29.83	0.11	6.02	104.93
6A-2_Grt_005	0.73	36.63	25.40	5.25	30.67	0.10	5.97	104.76
6A-2_Grt_006	0.87	36.59	25.57	4.79	31.14	0.11	6.03	105.09
6A-2_Grt_012	0.72	36.88	25.23	5.61	30.89	0.08	5.73	105.14
Average	0.71	36.56	25.44	6.04	30.10	0.10	5.87	104.81

Stoichiometry								
Sample	Si ⁴⁺	Ti ⁴⁺	Al ³⁺	Fe ²⁺	Mn ²⁺	Mg ²⁺	Ca ²⁺	Total
6A-2_Grt_001	2.80	0.01	2.33	1.92	0.40	0.08	0.49	8.03
6A-2_Grt_002	2.81	0.01	2.30	1.89	0.46	0.07	0.49	8.03
6A-2_Grt_003	2.82	0.01	2.31	1.88	0.48	0.07	0.45	8.02
6A-2_Grt_004	2.82	0.01	2.31	1.92	0.41	0.07	0.50	8.03
6A-2_Grt_005	2.82	0.01	2.30	1.97	0.34	0.08	0.49	8.02
6A-2_Grt_006	2.81	0.01	2.31	2.00	0.31	0.10	0.50	8.03
6A-2_Grt_012	2.83	0.00	2.28	1.98	0.37	0.08	0.47	8.02
Average	2.81	0.01	2.31	1.94	0.39	0.08	0.48	8.03

Mineral chemistry of chlorite from thin section 6A-2. Mineral formula normalised to 14 oxygen (10 O + 8 OH), Fe³⁺ was not analysed. Sample size = 18.

EPMA analysis																
Sample	Na2O (Wt. %)	F (Wt. %)	MgO (Wt. %)	SiO2 (Wt. %)	Al2O3 (Wt. %)	MnO (Wt. %)	Cr2O3 (Wt. %)	TiO2 (Wt. %)	FeO (Wt. %)	SrO (Wt. %)	BaO (Wt. %)	Cl (Wt. %)	H2O (Wt. %)	CaO (Wt. %)	H2O (Wt. %)	Total (Wt. %)
6A-2-Ch_003	0.00	0.13	11.87	23.79	19.31	0.29	0.02	0.07	30.76	0.01	0.00	0.02	0.01	0.03	13.00	93.30
6A-2-Ch_004	0.00	0.00	11.43	24.23	19.86	0.33	0.00	0.05	31.17	0.00	0.00	0.03	0.01	0.02	13.00	100.11
6A-2-Ch_005	0.00	0.00	11.47	24.23	19.83	0.34	0.00	0.04	30.88	0.00	0.00	0.01	0.00	0.01	13.00	98.61
6A-2-Ch_008	0.00	0.05	11.73	24.45	20.00	0.25	0.00	0.08	30.55	0.01	0.00	0.01	0.04	0.01	13.00	100.17
6A-2-Ch_009	0.01	0.00	11.99	24.04	19.09	0.28	0.00	0.02	30.72	0.00	0.00	0.02	0.01	0.00	0.01	93.19
6A-2-Ch_010	0.00	0.00	11.81	24.40	19.69	0.27	0.00	0.05	30.55	0.00	0.00	0.01	0.06	0.01	13.00	100.15
6A-2-Ch_011	0.00	0.00	11.71	24.49	19.85	0.28	0.01	0.07	31.13	0.01	0.00	0.00	0.01	0.01	13.00	100.56
6A-2-Ch_012	0.00	0.00	11.70	24.18	20.06	0.29	0.00	0.05	30.90	0.00	0.00	0.01	0.01	0.02	13.00	100.22
6A-2-Ch_013	0.00	0.00	11.75	24.49	20.25	0.23	0.01	0.04	30.74	0.00	0.00	0.01	0.00	0.02	13.00	100.75
6A-2-Ch_014	0.00	0.15	11.50	24.08	19.56	0.32	0.00	0.06	30.77	0.00	0.00	0.01	0.01	0.02	13.00	98.50
6A-2-Ch_015	0.02	0.11	11.78	24.17	19.11	0.30	0.00	0.06	30.73	0.00	0.00	0.02	0.01	0.03	13.00	99.33
6A-2-Ch_016	0.00	0.00	11.74	24.23	19.68	0.35	0.02	0.08	31.38	0.00	0.00	0.01	0.01	0.00	13.00	100.07
6A-2-Ch_017	0.00	0.12	11.49	23.89	18.70	0.32	0.00	0.02	31.04	0.01	0.00	0.02	0.02	0.03	13.00	98.66
6A-2-Ch_018	0.01	0.00	11.60	24.40	19.81	0.36	0.00	0.04	32.15	0.00	0.00	0.00	0.00	0.01	13.00	101.37
6A-2-Ch_019	0.00	0.00	11.74	24.23	19.68	0.35	0.02	0.08	31.38	0.00	0.00	0.01	0.01	0.00	13.00	100.07
6A-2-Ch_020	0.00	0.00	11.69	24.15	20.09	0.33	0.00	0.07	31.45	0.00	0.00	0.01	0.01	0.01	13.00	101.02
6A-2-Ch_021	0.00	0.00	11.52	23.97	19.44	0.29	0.00	0.02	31.61	0.00	0.00	0.01	0.01	0.00	13.00	99.87
6A-2-Ch_022	0.00	0.00	11.61	24.05	19.59	0.31	0.00	0.03	31.77	0.00	0.00	0.01	0.01	0.00	13.00	100.89
Average	0.00	0.03	11.64	24.21	19.61	0.31	0.00	0.05	31.14	0.00	0.00	0.01	0.01	0.00	13.00	100.94

Stoichiometry																
Sample	Si4+	Ti4+	Al3+	Fe2+	Mn2+	Mg2+	Ca2+	Na+	K+	Cr3+	Sr2+	Ba2+	Total cations	OH	F	Cl
6A-2-Ch_003	2.65	0.01	2.54	1.87	0.03	1.97	0.00	0.00	0.00	0.00	0.00	0.00	10.07	7.95	0.04	0.00
6A-2-Ch_004	2.67	0.00	2.58	1.87	0.03	1.88	0.00	0.00	0.00	0.00	0.00	0.00	10.04	7.99	0.00	0.00
6A-2-Ch_005	2.70	0.00	2.56	1.86	0.03	1.86	0.00	0.00	0.00	0.00	0.00	0.00	10.01	8.00	0.00	0.00
6A-2-Ch_008	2.68	0.01	2.58	1.89	0.02	1.92	0.00	0.00	0.01	0.00	0.00	0.00	10.02	7.98	0.02	0.00
6A-2-Ch_009	2.68	0.00	2.51	1.99	0.03	1.99	0.00	0.00	0.00	0.00	0.00	0.00	10.07	8.00	0.00	0.00
6A-2-Ch_010	2.68	0.00	2.55	1.84	0.02	1.94	0.00	0.00	0.01	0.00	0.00	0.00	10.04	8.00	0.00	0.00
6A-2-Ch_011	2.69	0.00	2.56	1.89	0.03	1.91	0.00	0.00	0.00	0.00	0.00	0.00	10.03	8.00	0.00	0.00
6A-2-Ch_012	2.66	0.00	2.60	1.92	0.04	1.92	0.00	0.00	0.00	0.00	0.00	0.00	10.04	8.00	0.00	0.00
6A-2-Ch_013	2.69	0.00	2.60	1.89	0.02	1.91	0.00	0.00	0.00	0.00	0.00	0.00	10.01	8.00	0.00	0.00
6A-2-Ch_014	2.68	0.00	2.56	1.86	0.03	1.90	0.00	0.00	0.00	0.00	0.00	0.00	10.01	7.95	0.04	0.00
6A-2-Ch_015	2.69	0.00	2.51	1.86	0.03	1.95	0.00	0.00	0.00	0.00	0.00	0.00	10.05	7.96	0.04	0.00
6A-2-Ch_016	2.68	0.00	2.52	1.93	0.04	1.88	0.00	0.00	0.00	0.00	0.00	0.00	10.06	8.00	0.00	0.00
6A-2-Ch_017	2.65	0.00	2.48	1.93	0.03	1.93	0.00	0.00	0.00	0.00	0.00	0.00	10.07	7.95	0.04	0.00
6A-2-Ch_018	2.66	0.00	2.55	1.89	0.03	1.89	0.00	0.00	0.00	0.00	0.00	0.00	10.05	8.00	0.00	0.00
6A-2-Ch_019	2.68	0.01	2.55	1.89	0.03	1.92	0.00	0.00	0.00	0.00	0.00	0.00	10.06	8.00	0.00	0.00
6A-2-Ch_020	2.64	0.00	2.59	1.89	0.03	1.90	0.00	0.00	0.00	0.00	0.00	0.00	10.06	8.00	0.00	0.00
6A-2-Ch_021	2.66	0.00	2.54	1.93	0.03	1.91	0.00	0.00	0.00	0.00	0.00	0.00	10.07	8.00	0.00	0.00
6A-2-Ch_022	2.65	0.00	2.55	1.93	0.03	1.91	0.00	0.00	0.00	0.00	0.00	0.00	10.07	8.00	0.00	0.00
Average	2.67	0.00	2.55	1.92	0.03	1.92	0.00	0.00	0.00	0.00	0.00	0.00	10.05	7.99	0.01	0.00

Mineral chemistry of chlorite from thin section 5A-2. Mineral formula normalised to 14 oxygen (10 O + 8 OH), Fe³⁺ was not analysed. Sample size = 14.

EPMA analysis																
Sample	Na2O (Wt. %)	F (Wt. %)	MgO (Wt. %)	SiO2 (Wt. %)	Al2O3 (Wt. %)	MnO (Wt. %)	Cr2O3 (Wt. %)	TiO2 (Wt. %)	FeO (Wt. %)	SrO (Wt. %)	BaO (Wt. %)	Cl (Wt. %)	H2O (Wt. %)	CaO (Wt. %)	H2O (Wt. %)	Total (Wt. %)
5A-2-Ch_001	0.00	0.04	11.42	23.43	19.59	0.18	0.01	0.07	29.72	0.00	0.00	0.01	0.05	0.01	13.00	98.22
5A-2-Ch_002	0.02	0.05	11.12	23.99	20.50	0.19	0.01	0.06	29.86	0.00	0.00	0.02	0.01	0.02	13.00	98.73
5A-2-Ch_003	0.00	0.14	11.70	23.44	20.08	0.19	0.00	0.06	29.18	0.00	0.00	0.02	0.03	0.02	13.00	97.87
5A-2-Ch_004	0.00	0.09	12.03	23.16	19.53	0.20	0.00	0.06	29.18	0.00	0.00	0.01	0.02	0.01	13.00	97.80
5A-2-Ch_005	0.00	0.05	11.84	23.99	19.83	0.17	0.00	0.05	29.38	0.00	0.00	0.02	0.02	0.01	13.00	97.67
5A-2-Ch_006	0.00	0.02	11.43	23.52	19.90	0.17	0.00	0.06	29.46	0.00	0.00	0.02	0.01	0.02	13.00	97.62
5A-2-Ch_007	0.00	0.05	11.73	23.42	19.63	0.19	0.00	0.08	28.52	0.00	0.00	0.02	0.02	0.02	13.00	97.08
5A-2-Ch_008	0.00	0.09	11.29	23.12	20.76	0.17	0.02	0.06	29.24	0.00	0.00	0.01	0.00	0.02	13.00	98.82
5A-2-Ch_009	0.01	0.09	11.57	23.76	19.82	0.18	0.02	0.07	29.48	0.00	0.00	0.02	0.00	0.02	13.00	98.66
5A-2-Ch_010	0.03	0.13	11.33	23.30	19.80	0.18	0.02	0.04	29.49	0.00	0.00	0.02	0.01	0.02	13.00	97.37
5A-2-Ch_011	0.00	0.11	11.66	23.54	19.60	0.17	0.01	0.07	29.09	0.00	0.00	0.02	0.04	0.03	13.00	97.54
5A-2-Ch_012	0.00	0.00	10.85	24.31	20.11	0.21	0.00	0.08	29.19	0.00	0.00	0.01	0.03	0.01	13.00	98.17
5A-2-Ch_013	0.01	0.17	11.57	23.82	20.01	0.17	0.00	0.07	28.04	0.00	0.00	0.03	0.02	0.02	13.00	96.94
5A-2-Ch_015	0.00	0.11	11.85	23.46	19.46	0.13	0.00	0.08	29.60	0.00	0.00	0.03	0.06	0.00	13.00	98.21
Average	0.01	0.08	11.56	23.62	20.03	0.18	0.01	0.07	29.20	0.00	0.00	0.02	0.02	0.02	13.00	97.80

Stoichiometry																
Sample	Si4+	Ti4+	Al3+	Fe2+	Mn2+	Mg2+	Ca2+	Na+	K+	Cr3+	Sr2+	Ba2+	Total cations	OH	F	Cl
5A-2-Ch_001	2.63	0.01	2.63	1.79	0.02	1.98	0.00	0.00	0.00	0.00	0.00	0.00	10.05	7.98	0.01	0.00
5A-2-Ch_002	2.66	0.01	2.69	1.78	0.02	1.84	0.00	0.00	0.00	0.00	0.00	0.00	10.00	7.98	0.02	0.00
5A-2-Ch_003	2.66	0.01	2.66	1.78	0.02	1.96	0.00	0.00	0.00	0.00	0.00	0.00	10.03	7.95	0.05	0.00
5A-2-Ch_004	2.63	0.01	2.61	1.77	0.02	2.03	0.00	0.00	0.00	0.00	0.00	0.00	10.06	7.96	0.03	0.00
5A-2-Ch_005	2.63	0.00	2.64	1.77	0.02	1.99	0.00	0.00	0.00	0.00	0.00	0.00	10.05	7.98	0.02	0.00
5A-2-Ch_006	2.65	0.01	2.64	1.78	0.02	1.92	0.00	0.00	0.00	0.00	0.00	0.00	10.02	7.99	0.01	0.00
5A-2-Ch_007	2.65	0.01	2.62	1.74	0.02	1.98	0.00	0.00	0.00	0.00	0.00	0.00	10.03	7.98	0.02	0.00
5A-2-Ch_008	2.67	0.01	2.71	1.86	0.03	1.86	0.00	0.01	0.00	0.00	0.00	0.00	10.08	7.97	0.03	0.00
5A-2-Ch_009	2.64	0.01	2.68	1.74	0.02	1.92	0.00	0.00	0.00	0.00	0.00	0.00	10.01	7.96	0.03	0.00
5A-2-Ch_010	2.68	0.00	2.65	1.80	0.02	1.92	0.00	0.00	0.00	0.00	0.00	0.00	10.03	7.90	0.03	0.00
5A-2-Ch_011	2.66	0.01	2.61	1.75	0.02	1.97	0.00	0.00	0.01	0.00	0.00	0.00	10.03	7.96	0.04	0.00
5A-2-Ch_012	2.69	0.01	2.73	1.70	0.02	1.99	0.00	0.00	0.00	0.00	0.00	0.00	9.94	8.00	0.00	0.00
5A-2-Ch_013	2.69	0.01	2.66	1.69	0.02	1.95	0.00	0.00	0.00	0.00	0.00	0.00	9.98	7.93	0.06	0.00
5A-2-Ch_015	2.68	0.01	2.60	1.71	0.01	2.00	0.00	0.00	0.01	0.00	0.00	0.00	10.00	7.98	0.02	0.00
Average	2.65	0.01	2.66	1.76	0.02	1.93	0.00	0.00	0.00	0.00						

Mineral chemistry of biotite in thin section 6A-2. Mineral formula normalised to 11 oxygen (10 O + 2 OH), Fe³⁺ was not analysed. Sample size =22.

Sample	EPMA analysis															
	Na2O (Wt. %)	F (Wt. %)	MgO (Wt. %)	SiO2 (Wt. %)	Al2O3 (Wt. %)	MnO (Wt. %)	Cr2O3 (Wt. %)	TiO2 (Wt. %)	FeO (Wt. %)	SrO (Wt. %)	BaO (Wt. %)	Cl (Wt. %)	K2O (Wt. %)	CaO (Wt. %)	H2O (Wt. %)	Total (Wt. %)
6A-2_Bt_001	0.07	0.16	8.54	36.21	16.56	0.14	0	1.68	27.27	0	0.14	0.02	9.77	0.01	4.00	104.57
6A-2_Bt_002	0.04	0.15	8.64	35.81	16.11	0.13	0.00	1.59	27.56	0	0.12	0.02	9.67	0.02	4.00	103.88
6A-2_Bt_003	0.02	0.19	8.42	35.90	15.99	0.13	0.01	1.76	26.98	0	0.15	0.02	9.72	0.02	4.00	103.32
6A-2_Bt_004	0.04	0.13	8.52	35.84	16.03	0.11	0	1.69	27.33	0.01	0.12	0.02	9.76	0.02	4.00	103.61
6A-2_Bt_005	0.07	0.11	8.67	35.70	15.73	0.11	0.01	1.65	27.29	0	0.14	0.01	9.56	0.03	4.00	103.10
6A-2_Bt_006	0.08	0.17	8.56	35.83	16.14	0.12	0.03	1.55	27.26	0	0.14	0.04	9.75	0	4.00	103.67
6A-2_Bt_007	0.09	0.22	8.56	36.05	16.21	0.12	0.00	1.75	27.57	0	0.15	0.03	9.85	0	4.00	104.49
6A-2_Bt_008	0.09	0.16	8.57	35.91	16.12	0.10	0.01	1.58	27.53	0	0.14	0.05	9.83	0	4.00	104.09
6A-2_Bt_009	0.14	0.11	8.53	35.81	16.18	0.14	0.02	1.69	27.13	0	0.14	0.07	9.82	0	4.00	103.77
6A-2_Bt_010	0.14	0.18	8.55	35.92	15.98	0.17	0	1.69	27.66	0	0.13	0.05	9.79	0	4.00	104.26
6A-2_Bt_011	0.08	0.15	8.57	36.01	16.20	0.16	0.02	1.53	27.36	0	0.15	0.04	9.86	0	4.00	104.12
6A-2_Bt_012	0.09	0.24	8.69	36.27	16.25	0.13	0	1.68	27.11	0	0.15	0.01	9.82	0	4.00	104.43
6A-2_Bt_013	0.10	0.15	8.52	36.00	16.21	0.13	0.00	1.62	27.24	0.01	0.13	0.02	9.83	0	4.00	103.97
6A-2_Bt_014	0.02	0.09	7.33	35.93	16.22	0.15	0	1.11	28.66	0	0.13	0.03	9.67	0.02	4.00	104.37
6A-2_Bt_015	0.04	0.10	7.42	35.80	16.54	0.17	0	1.82	28.69	0	0.12	0.02	9.68	0.02	4.00	104.43
6A-2_Bt_016	0.02	0.16	7.32	35.52	15.98	0.20	0	1.76	29.62	0	0.14	0.03	9.40	0.02	4.00	104.16
6A-2_Bt_017	0.10	0.19	8.52	35.78	16.03	0.17	0	1.56	26.60	0	0.13	0.01	9.69	0	4.00	102.66
6A-2_Bt_018	0.06	0.21	8.39	35.67	15.42	0.13	0	1.47	25.77	0	0.13	0.01	9.34	0	4.00	100.60
6A-2_Bt_019	0.06	0.18	8.62	36.04	16.13	0.14	0.03	1.57	26.51	0	0.12	0.01	9.69	0	4.00	103.09
6A-2_Bt_020	0.11	0.23	8.42	36.00	16.44	0.13	0	1.62	26.67	0	0.12	0.01	9.51	0	4.00	103.25
6A-2_Bt_021	0.04	0.12	8.50	35.96	16.66	0.08	0	1.41	26.54	0	0.13	0.02	9.70	0	4.00	103.15
6A-2_Bt_022	0.06	0.18	8.57	36.01	16.44	0.13	0.02	1.54	26.59	0	0.12	0.02	9.56	0	4.00	103.14
Average	0.07	0.16	8.38	35.91	16.16	0.14	0.01	1.65	27.31	0.00	0.13	0.02	9.69	0.01	4.00	103.64

Sample	Stoichiometry															
	Si4+	Ti4+	Al3+	Fe2+	Mn2+	Mg2+	Ca2+	Na+	K+	Cr3+	Sr2+	Ba2+	Total cations	OH	F	Cl
6A-2_Bt_001	2.72	0.10	1.47	1.72	0.01	0.96	0.00	0.01	0.94	0.00	0.00	0.00	7.92	1.96	0.04	0.00
6A-2_Bt_002	2.73	0.09	1.44	1.75	0.01	0.96	0.00	0.01	0.94	0.00	0.00	0.00	7.94	1.96	0.04	0.00
6A-2_Bt_003	2.74	0.10	1.44	1.72	0.01	0.96	0.00	0.00	0.95	0.00	0.00	0.00	7.92	1.95	0.05	0.00
6A-2_Bt_004	2.73	0.10	1.44	1.74	0.01	0.97	0.00	0.01	0.95	0.00	0.00	0.00	7.93	1.97	0.03	0.00
6A-2_Bt_005	2.73	0.10	1.42	1.75	0.01	0.99	0.00	0.01	0.93	0.00	0.00	0.00	7.94	1.97	0.03	0.00
6A-2_Bt_006	2.73	0.09	1.45	1.73	0.01	0.97	0.00	0.01	0.95	0.00	0.00	0.00	7.94	1.95	0.04	0.01
6A-2_Bt_007	2.72	0.10	1.44	1.74	0.01	0.96	0.00	0.01	0.95	0.00	0.00	0.00	7.94	1.97	0.03	0.00
6A-2_Bt_008	2.72	0.09	1.44	1.75	0.01	0.97	0.00	0.01	0.95	0.00	0.00	0.00	7.95	1.96	0.04	0.01
6A-2_Bt_009	2.72	0.10	1.45	1.72	0.01	0.97	0.00	0.02	0.95	0.00	0.00	0.00	7.94	1.96	0.03	0.01
6A-2_Bt_010	2.72	0.10	1.43	1.75	0.01	0.97	0.00	0.02	0.95	0.00	0.00	0.00	7.95	1.95	0.04	0.01
6A-2_Bt_011	2.73	0.09	1.45	1.73	0.01	0.97	0.00	0.01	0.95	0.00	0.00	0.00	7.94	1.96	0.04	0.01
6A-2_Bt_012	2.73	0.10	1.44	1.71	0.01	0.98	0.00	0.01	0.94	0.00	0.00	0.00	7.93	1.94	0.06	0.00
6A-2_Bt_013	2.73	0.09	1.45	1.73	0.01	0.96	0.00	0.02	0.95	0.00	0.00	0.00	7.94	1.96	0.03	0.00
6A-2_Bt_014	2.73	0.12	1.45	1.82	0.01	0.83	0.00	0.00	0.94	0.00	0.00	0.00	7.90	1.97	0.02	0.00
6A-2_Bt_015	2.71	0.10	1.48	1.82	0.01	0.84	0.00	0.01	0.94	0.00	0.00	0.00	7.91	1.97	0.02	0.00
6A-2_Bt_016	2.72	0.10	1.44	1.89	0.01	0.83	0.00	0.00	0.92	0.00	0.00	0.00	7.92	1.96	0.04	0.00
6A-2_Bt_017	2.74	0.09	1.45	1.70	0.01	0.97	0.00	0.01	0.94	0.00	0.00	0.00	7.92	1.95	0.05	0.00
6A-2_Bt_018	2.78	0.09	1.42	1.68	0.01	0.98	0.00	0.01	0.93	0.00	0.00	0.00	7.89	1.95	0.05	0.00
6A-2_Bt_019	2.74	0.09	1.45	1.69	0.01	0.98	0.00	0.01	0.94	0.00	0.00	0.00	7.92	1.96	0.04	0.00
6A-2_Bt_020	2.74	0.09	1.47	1.70	0.01	0.95	0.00	0.02	0.92	0.00	0.00	0.00	7.90	1.94	0.06	0.00
6A-2_Bt_021	2.73	0.08	1.49	1.69	0.01	0.96	0.00	0.01	0.94	0.00	0.00	0.00	7.91	1.97	0.03	0.00
6A-2_Bt_022	2.74	0.09	1.47	1.69	0.01	0.97	0.00	0.01	0.93	0.00	0.00	0.00	7.91	1.96	0.04	0.00
Average	2.73	0.09	1.45	1.74	0.01	0.95	0.00	0.01	0.94	0.00	0.00	0.00	7.93	1.96	0.04	0.00

Mineral chemistry of muscovite in thin section 6A-2. Mineral formula normalised to 22 oxygen (20 O + 4 OH), Fe³⁺ was not analysed. Sample size =11.

Sample	EPMA analysis															
	Na2O (Wt. %)	F (Wt. %)	MgO (Wt. %)	SiO2 (Wt. %)	Al2O3 (Wt. %)	MnO (Wt. %)	Cr2O3 (Wt. %)	TiO2 (Wt. %)	FeO (Wt. %)	SrO (Wt. %)	BaO (Wt. %)	Cl (Wt. %)	K2O (Wt. %)	CaO (Wt. %)	H2O (Wt. %)	Total (Wt. %)
6A-2_Ms_001	0.51	0.02	1.71	47.27	29.52	0.02	0.00	0.19	5.50	0.01	0.14	0.01	4.01	0.01	4.00	100.01
6A-2_Ms_002	0.51	0.01	1.71	47.27	29.52	0.02	0.00	0.19	5.50	0.01	0.14	0.01	4.01	0.01	4.00	100.01
6A-2_Ms_003	0.49	0.00	1.66	46.94	29.41	0.01	0.00	0.28	5.83	0.00	0.49	0.00	10.59	0.00	4.00	99.60
6A-2_Ms_004	0.51	0.06	1.68	47.23	29.84	0.01	0.04	0.26	5.57	0.00	0.29	0.00	10.16	0.00	4.00	99.56
6A-2_Ms_005	0.73	0.08	1.55	46.07	28.97	0.00	0.00	0.15	5.58	0.00	0.23	0.00	10.20	0.00	4.00	99.54
6A-2_Ms_006	0.83	0.00	1.69	47.30	29.43	0.03	0.00	0.23	5.16	0.04	0.35	0.00	9.91	0.01	4.00	98.56
6A-2_Ms_007	0.49	0.00	1.70	46.68	29.24	0.01	0.00	0.29	5.41	0.00	0.48	0.00	10.65	0.00	4.00	98.85
6A-2_Ms_008	0.48	0.06	1.59	47.24	30.30	0.01	0.00	0.17	5.57	0.00	0.41	0.01	10.48	0.00	4.00	100.32
6A-2_Ms_009	0.94	0.03	1.47	46.39	30.47	0.04	0.01	0.25	5.08	0.00	0.40	0.15	10.07	0.01	4.00	99.31
6A-2_Ms_010	0.71	0.09	1.80	47.81	29.85	0.00	0.01	0.21	5.49	0.01	0.25	0.00	10.01	0.00	4.00	100.14
6A-2_Ms_011	0.80	0.11	1.80	47.74	29.49	0.02	0.00	0.24	5.41	0.00	0.30	0.00	10.06	0.00	4.00	99.97
Average	0.65	0.06	1.73	47.46	29.69	0.02	0.01	0.23	5.43	0.01	0.36	0.02	10.05	0.00	4.00	99.71

Sample	Stoichiometry															
	Si4+	Ti4+	Al3+	Fe2+	Mn2+	Mg2+	Ca2+	Na+	K+	Cr3+	Sr2+	Ba2+	Total cations	OH	F	Cl
6A-2_Ms_001	6.57	0.02	4.70	0.61	0.00	0.39	0.00	0.14	1.36	0.00	0.00	0.01	18.81	0.91	0.09	0.00
6A-2_Ms_002	6.44	0.03	4.74	0.62	0.00	0.35	0.00	0.14	1.80	0.00	0.00	0.02	14.13	4.00	0.00	0.00
6A-2_Ms_003	6.42	0.03	4.74	0.62	0.00	0.34	0.00	0.10	1.85	0.00	0.00	0.03	14.16	4.00	0.00	0.00
6A-2_Ms_004	6.41	0.03	4.78	0.60	0.00	0.34	0.00	0.21	1.76	0.00	0.00	0.02	14.15	3.98	0.02	0.00
6A-2_Ms_005	6.51	0.02	4.62	0.63	0.00	0.39	0.00	0.19	1.76	0.00	0.00	0.01	14.14	3.97	0.03	0.00
6A-2_Ms_006	6.46	0.02	4.74	0.62	0.00	0.34	0.00	0.10	1.85	0.00	0.00	0.03	14.16	4.00	0.00	0.00
6A-2_Ms_007	6.42	0.03	4.74	0.62	0.00	0.35	0.00	0.11	1.87	0.00	0.00	0.03	14.17	3.97	0.03	0.00
6A-2_Ms_008	6.39	0.02	4.83	0.63	0.00	0.32	0.00	0.13	1.81	0.00	0.00	0.02	14.15	3.95	0.01	0.03
6A-2_Ms_009	6.34	0.03	4.91	0.58	0.00	0.30	0.00	0.25	1.76	0.00	0.00	0.02	14.19	3.96	0.04	0.00
6																

Mineral chemistry of albite in thin section 6A-2. Mineral formula normalised to 8 oxygen. Sample size = 7.

EPMA analysis								
Sample	Na2O(Mass%)	SiO2(Mass%)	Al2O3(Mass%)	BaO(Mass%)	SrO(Mass%)	K2O(Mass%)	CaO(Mass%)	Total(Mass%)
6A-2_Ab_001	9.96	69.05	19.75	0.00	0.01	0.08	0.08	98.92
6A-2_Ab_002	10.79	67.09	18.72	0.05	0.00	0.09	0.07	96.80
6A-2_Ab_003	10.68	67.11	18.98	0.05	0.00	0.09	0.07	96.97
6A-2_Ab_006	10.61	66.51	19.27	0.00	0.02	0.08	0.46	96.95
6A-2_Ab_007	10.78	67.16	19.03	0.00	0.00	0.11	0.04	97.12
6A-2_Ab_008	10.41	66.62	18.78	0.00	0.00	0.16	0.04	96.02
6A-2_Ab_010	10.69	66.98	19.12	0.00	0.01	0.07	0.03	96.91
Average	10.56	67.22	19.09	0.01	0.01	0.10	0.11	97.10

Stoichiometry								
Sample	Si4+	Al3+	Ca2+	Na+	K+	Sr2+	Ba2+	Total
6A-2_Ab_001	3.02	1.02	0.00	0.85	0.00	0.00	0.00	4.89
6A-2_Ab_002	3.02	0.99	0.00	0.94	0.01	0.00	0.00	4.96
6A-2_Ab_003	3.01	1.00	0.00	0.93	0.01	0.00	0.00	4.95
6A-2_Ab_006	2.99	1.02	0.02	0.92	0.00	0.00	0.00	4.96
6A-2_Ab_007	3.01	1.00	0.00	0.94	0.01	0.00	0.00	4.96
6A-2_Ab_008	3.02	1.00	0.00	0.91	0.01	0.00	0.00	4.94
6A-2_Ab_010	3.01	1.01	0.00	0.93	0.00	0.00	0.00	4.95
Average	3.01	1.01	0.01	0.92	0.01	0.00	0.00	4.95

Mineral chemistry of albite in thin section 5A-2. Mineral formula normalised to 8 oxygen. Sample size = 10.

EPMA analysis								
Sample	Na2O(Mass%)	SiO2(Mass%)	Al2O3(Mass%)	BaO(Mass%)	SrO(Mass%)	K2O(Mass%)	CaO(Mass%)	Total(Mass%)
5A-2_Ab_006	10.72	64.87	18.63	0.03	0.00	0.06	0.10	94.41
5A-2_Ab_007	10.71	65.04	18.47	0.00	0.00	0.07	0.05	94.35
5A-2_Ab_008	10.66	64.82	18.66	0.00	0.00	0.06	0.13	94.33
5A-2_Ab_009	10.78	64.66	18.50	0.00	0.00	0.05	0.06	94.05
5A-2_Ab_010	10.68	65.33	18.71	0.01	0.00	0.05	0.04	94.82
5A-2_Ab_011	10.67	65.22	18.71	0.00	0.00	0.07	0.03	94.70
5A-2_Ab_012	10.77	65.02	18.39	0.00	0.00	0.06	0.08	94.32
5A-2_Ab_013	10.70	65.03	18.70	0.00	0.00	0.08	0.12	94.63
5A-2_Ab_014	10.61	65.22	18.78	0.00	0.00	0.06	0.05	94.72
5A-2_Ab_015	10.74	65.11	18.75	0.00	0.00	0.05	0.08	94.73
Average	10.70	65.03	18.63	0.00	0.00	0.06	0.07	94.51

Stoichiometry								
Sample	Si4+	Al3+	Ca2+	Na+	K+	Sr2+	Ba2+	Total
5A-2_Ab_006	3.00	1.01	0.00	0.96	0.00	0.00	0.00	4.98
5A-2_Ab_007	3.00	1.01	0.00	0.96	0.00	0.00	0.00	4.97
5A-2_Ab_008	3.00	1.02	0.01	0.95	0.00	0.00	0.00	4.98
5A-2_Ab_009	3.00	1.01	0.00	0.97	0.00	0.00	0.00	4.98
5A-2_Ab_010	3.00	1.01	0.00	0.95	0.00	0.00	0.00	4.97
5A-2_Ab_011	3.00	1.01	0.00	0.95	0.00	0.00	0.00	4.97
5A-2_Ab_012	3.00	1.00	0.00	0.96	0.00	0.00	0.00	4.98
5A-2_Ab_013	3.00	1.02	0.01	0.96	0.00	0.00	0.00	4.98
5A-2_Ab_014	3.00	1.02	0.00	0.95	0.00	0.00	0.00	4.97
5A-2_Ab_015	3.00	1.02	0.00	0.96	0.00	0.00	0.00	4.98
Average	3.00	1.01	0.00	0.96	0.00	0.00	0.00	4.98

Mineral chemistry of albite in thin section 4A-1. Mineral formula normalised to 8 oxygen. Sample size = 3.

EPMA analysis								
Sample	Na2O(Mass%)	SiO2(Mass%)	Al2O3(Mass%)	BaO(Mass%)	SrO(Mass%)	K2O(Mass%)	CaO(Mass%)	Total(Mass%)
4A-1-Ab_001	10.78	66.92	19.08	0.00	0.00	0.06	0.05	96.89
4A-1-Ab_004	10.78	67.38	19.00	0.04	0.02	0.06	0.05	97.32
4A-1-Ab_005	10.91	66.95	18.60	0.02	0.00	0.06	0.14	96.68
Average	10.82	67.08	18.89	0.02	0.01	0.06	0.08	96.96

Stoichiometry								
Sample	Si4+	Al3+	Ca2+	Na+	K+	Sr2+	Ba2+	Total
4A-1-Ab_001	3.01	1.01	0.00	0.94	0.00	0.00	0.00	4.96
4A-1-Ab_004	3.01	1.00	0.00	0.93	0.00	0.00	0.00	4.96
4A-1-Ab_005	3.02	0.99	0.01	0.95	0.00	0.00	0.00	4.97
Average	3.01	1.00	0.00	0.94	0.00	0.00	0.00	4.96

Mineral chemistry of calcite. Mineral formula normalised to 6 oxygen. Fe³⁺ was not analysed, sample size from 4A-1 = 9 and 5A-2 n = 7.

EPMA analysis							
Sample	MgO(Mass%)	FeO(Mass%)	MnO(Mass%)	SrO(Mass%)	CaO(Mass%)	C(Mass%)	Total(Mass%)
4A-1_Cal_001	9.72	19.35	1.88	0.03	28.28	41.00	100.26
4A-1_Cal_002	10.78	18.64	0.90	0.05	28.45	41.00	99.82
4A-1_Cal_003	8.11	20.36	2.63	0.09	27.86	41.00	100.05
4A-1_Cal_004	0.00	0.22	0.02	0.00	0.15	41.00	41.39
4A-1_Cal_005	9.78	19.72	2.19	0.10	27.68	41.00	100.47
4A-1_Cal_006	9.63	20.76	1.75	0.04	27.94	41.00	101.12
4A-1_Cal_007	10.41	17.81	1.27	0.00	28.96	41.00	99.45
4A-1_Cal_008	10.60	19.19	0.72	0.05	28.44	41.00	100.00
4A-1_Cal_009	9.88	20.27	1.65	0.09	27.57	41.00	100.46
5A-2_Cal_001	7.63	22.07	1.69	0.03	27.59	41.00	100.01
5A-2_Cal_002	8.56	20.50	1.90	0.03	26.78	41.00	98.77
5A-2_Cal_003	10.66	18.18	1.46	0.02	27.20	41.00	98.52
5A-2_Cal_004	8.69	20.35	1.61	0.02	27.13	41.00	98.80
5A-2_Cal_005	10.19	18.38	1.11	0.03	27.26	41.00	97.96
5A-2_Cal_006	9.40	20.44	1.72	0.09	26.62	41.00	99.27
5A-2_Cal_007	9.86	19.91	1.40	0.03	26.43	41.00	98.63
Average	8.99	18.51	1.49	0.04	25.90	41.00	95.94

Stoichiometry						
Sample	Mg ²⁺	Ca ²⁺	Mn ²⁺	Fe ²⁺	Sr ²⁺	Total
4A-1_Cal_001	0.54	0.95	0.05	0.47	0.00	2.00
4A-1_Cal_002	0.59	0.94	0.02	0.44	0.00	2.00
4A-1_Cal_003	0.46	0.96	0.07	0.51	0.00	2.00
4A-1_Cal_004	0.00	0.96	0.07	0.97	0.00	2.00
4A-1_Cal_005	0.54	0.93	0.05	0.47	0.00	2.00
4A-1_Cal_006	0.53	0.93	0.04	0.50	0.00	2.00
4A-1_Cal_007	0.57	0.97	0.03	0.43	0.00	2.00
4A-1_Cal_008	0.58	0.94	0.02	0.46	0.00	2.00
4A-1_Cal_009	0.55	0.92	0.04	0.49	0.00	2.00
Average	0.48	0.95	0.04	0.52	0.00	2.00
5A-2_Cal_001	0.44	0.96	0.04	0.55	0.00	2.00
5A-2_Cal_002	0.50	0.94	0.05	0.52	0.00	2.00
5A-2_Cal_003	0.60	0.92	0.04	0.44	0.00	2.00
5A-2_Cal_004	0.50	0.95	0.04	0.51	0.00	2.00
5A-2_Cal_005	0.58	0.94	0.03	0.45	0.00	2.00
5A-2_Cal_006	0.53	0.92	0.04	0.51	0.00	2.00
5A-2_Cal_007	0.56	0.91	0.04	0.49	0.00	2.00
Average	0.53	0.93	0.04	0.50	0.00	2.00

Mineral chemistry of dolomite from thin section 5A-2. Mineral formula normalised to 6 oxygen. Fe³⁺ was not analysed, sample size = 6.

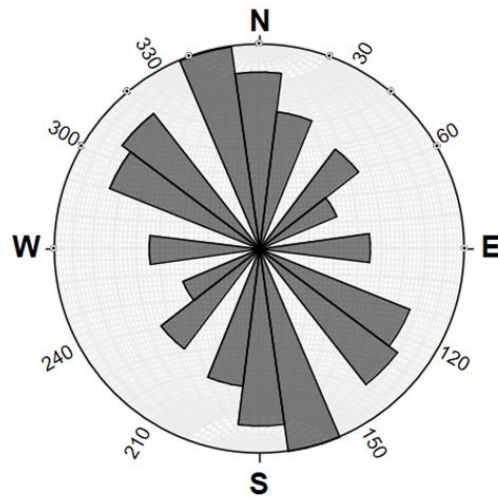
EPMA analysis							
Sample	MgO(Mass%)	FeO(Mass%)	MnO(Mass%)	SrO(Mass%)	CaO(Mass%)	C(Mass%)	Total(Mass%)
5A-2_Dol_001	1.24	5.95	1.03	0.03	50.53	58.78	100.26
5A-2_Dol_002	1.68	6.72	0.90	0.08	49.59	58.97	99.82
5A-2_Dol_003	1.40	7.69	0.97	0.08	49.38	59.52	100.05
5A-2_Dol_004	1.39	6.41	0.93	0.06	49.54	58.33	41.39
5A-2_Dol_005	1.49	6.14	0.91	0.03	48.36	56.94	100.47
5A-2_Dol_006	1.39	6.28	0.93	0.07	48.89	57.56	101.12
Average	1.43	6.53	0.95	0.06	49.38	58.35	116.70

Stoichiometry						
Sample	Mg ²⁺	Ca ²⁺	Mn ²⁺	Fe ²⁺	Sr ²⁺	Total
5A-2_Dol_001	0.07	1.75	0.03	0.15	0.00	2.00
5A-2_Dol_002	0.10	1.71	0.02	0.17	0.00	2.00
5A-2_Dol_003	0.08	1.70	0.02	0.19	0.00	2.00
5A-2_Dol_004	0.08	1.73	0.02	0.16	0.00	2.00
5A-2_Dol_005	0.09	1.73	0.02	0.16	0.00	2.00
5A-2_Dol_006	0.08	1.73	0.02	0.16	0.00	2.00
Average	0.08	1.73	0.02	0.16	0.00	2.00

Appendix K: Quartz analysis, grain size and angles

Quantification of quartz grains in the protolith, compared to the phyllonitic shear zone (thin section 2-2), with a rose diagram of shear zone's quartz grain orientation.

3, Protolith		2-2, Quartz lenses				Diameters	3, Protolith	2-2, Quartz lenses
Diameters	Amount	Diameters	Amount	Corrected angle	Amount	<50 μm , %	10.30	4.76
<50 μm	31	<50 μm	5	90	2	50-80 μm , %	26.25	26.67
50-80 μm	79	50-80 μm	28	60	4	80-130 μm , %	27.24	42.86
80-130 μm	82	80-130 μm	45	40	9	>130 μm , %	36.21	25.71
130< μm	109	130< μm	27	20	11	Sum, %	100.00	100.00
Sum	301	Sum	105	0	18			
					340			
					320			
					300			
					270			
					Sum			105





 **NTNU**

Norwegian University of
Science and Technology